Electrical and thermal transport coefficients of CoFe thin films deposited on a microcalorimeter

Dissertation
zur Erlangung des Doktorgrades der Naturwissenschaften
(Dr. rer. nat.)
der Fakultät für Physik
der Universität Regensburg

vorgelegt von
Sasmita Srichandan
aus
Bhubaneswar, Indien

November 2016

Die Arbeit wurde von Prof. Dr. Christoph Strunk angeleitet.
Das Promotionsgesuch wurde am 08.07.2016 eingereicht.
Das Kolloquium fand statt am 22.12.2016.

Prüfungsausschuss: Vorsitzender: Prof. Dr. Karsten Rincke

1. Gutachter: Prof. Dr. Christoph Strunk

2. Gutachter: Prof. Dr. Christian Back

Weiterer Prüfer: PD Dr. Tobias Korn

To

my parents

ACKNOWLEDGEMENTS

My journey in completing this thesis has been a long one but it has been made pleasant and enriching one due to several people who have helped me in various capacities and here I must acknowledge them. In the last 5 year, I have learned a lot to move ahead in career, made friends and acquaintances, gained further teaching and mentoring experience and last but not the least experienced the culture and tradition of Germany. There have been a lot of people involved in this process whom I cannot name all but would like to address to most of them.

First of all I am ever grateful to my supervisor Prof. Dr. Christoph Strunk for the opportunity to carry out my PhD degree in his group and also for all the support in the experiment and the discussions. I thank my co-supervisor Prof. Dr. Christian Back for letting me use his labs. I have greatly benefited from the collaboration with his group and from his inputs and encouragements.

I extend my gratitude to the thesis committee members, Prof. Dr. Karsten Rincke and PD Dr. Tobias Korn for evaluation and their useful comments. I thank Prof. Dr. Hubert Ebert in Ludwig-Maximilians University in Munich and his student Sebastian for assisting in the theoretical calculations for our project. I thank Prof. Dr. Christoph Sürgers in Karlsruhe institute of technology for helping with the XRD measurements. I thank Prof. Dr. Günter Reiss in Bielefeld University for allowing us to visit his labs and for the discussion on experimental results. I am especially thankful to our chair head, Prof. Dr. Dieter Weiss for providing infrastructure in the clean-room for sample preparation and characterization and also labs for the conduct of the experiments. I am grateful to Prof. Dr. Josef Zweck for helping with the TEM characterization of thin films. I am also grateful to Prof. Barry Zink from University of Denver for the fruitful discussions on thermal transport.

I thank all my co-authors who have all been very helpful. Special thanks to my colleagues from my department, Max, Matthias and Michael in the group of Prof. Dr. Christian Back for the work on the projects, also for letting me carpool to all the workshops and conferences. I thank Timo, Daniel and Jan-Michael from the group of Prof. Dr. Günter. Reiss in Bielefeld for the excellent collaboration.

I thank my colleague Daniel for helping me with testing and running our flow cryostat. Special thanks to Sofia, Nicole and Paul for helping me without hesitation every time I needed to cool-down the set-up. For my

experiments, there are several colleagues in the group of Prof. Dr. Christian Back that I am thankful to. I thank George for discussion on the magnet design. I thank Matthias for deposition and XPS characterization of numerous batches of CoFe films, also for giving his ideas on measurements. I thank Thomas for doing XPS on the later samples. I thank Michael Zimmerman for doing AFM characterization of the CoFe thin films. Thanks to Bernhard for doing the COMSOL simulations. I thank Helmut for doing the magnetic characterizations in SQUID system. I thank Jean-Yves and Tobias for helping with the MOKE measurements. I thank Johannes for helping me with the flow cryostat. I thank Bernhard Endres for initial discussions on flow cryostat design and operation. I also greatly appreciate the help I received from the colleagues in the group of of Prof. Dr. Josef Zweck, Johannes and Felix for the TEM measurements,

In my work from the instrumentation side of the set-ups, I have received a lot of help especially from two people, our technician Tom Haller and electronic workshop head Dieter Riedl. While setting up the flow cryostat, Tom helped in the design and setting up of the cryostat base and the magnet. I always ran to him whenever an unforeseen service was required by the set-up. Somehow he always knew what to do. Dieter and his team helped in design and preparation of the sample holder. I understood the working of small detail of various electronic instruments after discussion with him. I am also thankful to the other technicians, Conny, Uli, Daniel and Michael for the help in the clean-room and other technical help. I also appreciate all the help from our university helium liquefier team, Christian Haimerl and Thomas Solleder for the smooth conduct of our low temperature measurements.

I can not thank enough our secretaries Claudia and Elke especially in taking care of the complicated bureaucratic obligations. This made my journey as an international student much easier. Discussion on non-academic topic has been so much fun too.

I have enjoyed the company of my colleagues in my group who have always helped me in my work or outside work-space too. To name a few here, first are the people from our generation in our group, Ina, Masoumeh, Matthias, Maurice, Klaus, Daniel, Paul, Michael, people I shared office space with Daniel, Nicola, Sofia and Alois, people from the previous generation are Markus, Andi, David. I have also had good time with the younger generation people, colleagues from Dr. Hüttel's group during the group meetings, seminars. I thank the colleagues from the group of Prof. Dr. Dieter Weiss for the numerous introductions and help with various instruments and the fun time during chair outings.

I specially thank my friend and colleagues Ajay for helping me with device fabrication, labview script writing and experiments as well as for the quality time. I also thank my friend Jeongsu for his valuable comments on the introduction chapter of my thesis and for taking time for coffee break to discuss wordly affairs. I appreciate Denis for his academic and non-academic discussions.

Finally I am indebted to my parents, for granting me such freedom to choose my path and always encouraging me also my sister and brother for being not so hasty. Last but not the least, I am glad to be with my husband, Amartya, who stood by me for all these years and cheered me up. I also thank him for proof-reading my entire thesis.

LIST OF PUBLICATIONS

This thesis is based on the following papers and preprints:

- Transverse spin Seebeck effect versus anomalous and planar Nernst effects in Permalloy thin films, M. Schmid, S. Srichandan, D. Meier, T. Kuschel, J.-M. Schmalhorst, M. Vogel, G. Reiss, C. Strunk, and C. H. Back, *Phys. Rev. Lett.* **111**, 187201 (2013)
- Magnon scattering in the transport coefficients of CoFe alloys, S. Srichandan, S. Wimmer, M. Kronseder, M. Vogel, M. Zimmermann, H. Ebert, C. H. Back and C. Strunk (to be submitted).

Abstract

Interaction of spin, charge and heat currents in micro/nano structures opens opportunities for improving the performance of thermoelectric devices and future generation memory devices. For example, in magnetic insulators, coupled interaction of magnons with heat current generates the so called spin-Seebeck effect while magnon degree of freedom is utilized to transmit and process information in the sub-field of magnonics. In parallel, in magnetic metals, the charge carrying electrons interact with magnons and phonons to generate effects such as spin transfer torque and spin-dependent Seebeck effect. In the heart of the research on future generation thermoelectric and memory devices, lies the interplay of electrons, phonons and magnons along with external parameters of magnetization and thermal current. In this thesis, the roles played by the electrons, phonons and magnons in generating various electrical, thermal and magneto-thermal transport properties has been studied in ferromagnetic alloy thin films. Emphasis has been given to the development and utilization of SiN_x membrane based suspended microcalorimeter. In Co_xFe_{1-x} thin films, resistivity, thermopower and thermal conductivity were measured in the temperature range of 25 K-296 K. Contribution of electron scattering from phonons and magnons to these transport coefficients has been separated. The change of sign of the magnon drag contribution to thermopower from Co-rich to Fe-rich side of the material has been discussed. Additionally simultaneous measurement of resistivity and thermal conductivity has facilitated studying the validity of Wiedemann-Franz law in these films. In a second alloy of $Ni_{80}Fe_{20}$, observation of transverse magneto-thermoelectric effects in the presence of in-plane temperature gradient and magnetization has been discussed. Various competing effects have been separated depending on their angular dependencies. Together with the results from bulk substrates (see PhD thesis by M. Schmid), the existence of transverse spin Seebeck effect has been discarded.

Contents

List of Figures

List of Tables

Chapter 1

Introduction

1.1 Introduction and motivation

Reversible thermoelectric effects such as the Seebeck and the Peltier effects have been the driving force behind many industrial developments that have taken place in electronics, semiconductor, automobile, refrigeration, cooling industry and so on. The Seebeck effect, first observed by Thomas Johann Seebeck in 1821 [1], offers a unique opportunity to utilize the thermal energy which is otherwise lost in dissipation during various mechanical and electrical processes [2, 3]. The Seebeck effect opens up new vistas in the context of overcoming obstacles in future development of device miniaturization set by Moore's law [4]. As predicted already in 1965 by Moore *et al*. [5, 6], the size of the devices has been shrinking at a rate of 100% every two years with ever increasing technological boom, but this trend cannot last forever.

As we approach the limit of Moore's law, an alternative solution is required to sustain the growing demand for smaller and smaller device sizes. One such solution is offered by spintronics [7–9], which deals with the spin of the electrons along with its charge and can be used for storage and transmission of data. The use of the spin degree of freedom of the electrons not only increases the processing speed but also reduces the electric power consumption. Memory storage industry has progressed along with spintronics. Magnetoresistive random access memory (MRAM) devices and their future generation devices [10] use electron spin to store data in a nonvolatile manner [11], yet they suffer from dissipative losses since charge current is used to create magnetic field in order to write the data [8, 12]. This is where another breakthrough is needed. Therefore it is imperative that we develop methods to reduce the dissipation losses and thereby improve their performance. In this regard recently discovered (longitudinal) spin Seebeck effect in magnetic insulators [13–24] is one of the most promising prospects, which involves the generation of pure spin current in a magnetized material in the presence of uneven temperature distribution along the length or the height of the film. The integration of this effect will help recycle the dissipated thermal energy in conventional electronic industry and potential spintronics devices. For this reason, the spin Seebeck effect has garnered a lot of interest from both theoreticians and experimentalists [25, 26] and has several potential applications in proposal [27, 28] already. Magnonics [29]

is another growing field where dissipation-less transmission of information can be achieved using the magnons in nano-structures. Needless to say that the collective interplay of charge, spin, magnetic field and temperature in magnetic materials can bring forth phenomena which can be used in nano-devices to a great effect.

While the field of spintronics is evolving, a parallel solution to improve the performance of electronic devices is to improve the overall device quality. This includes enhanced nano-scale fabrication techniques and sophisticated patterning [30], adjusting material property to suitability by alloying or layering [31–34] etc. One such quality index is the thermoelectric figure of merit, $ZT = \sigma S^2 T/\kappa$, [32, 35–37], where T is the temperature of operation, σ is the thermal conductivity, S is the thermopower and κ is the thermal conductivity of the material in use. Higher ZT is achieved by improving the Seebeck coefficient and reducing the thermal conductivity. However, electrical and thermal conductivity in most cases go hand in hand, therefore studying the classical transport coefficients and the processes affecting them such as scattering and polarization, even in the field of magnetism, has much significance. Solid state devices with high thermoelectric figure of merit could be more useful in re-utilizing heat lost during operation in industry as well as in automotive applications. While semiconducting alloys with high ZT values are predominantly used in the electronics research both in industry and academia, metals play an equally important part, for example, as interconnects in semiconductor industry or as spin valves in MRAM devices. Therefore we study the transport coefficients in a metallic ferromagnetic system which can assist in improving material properties.

In the wake of such overwhelming interest in the fields of spintronics or spin-based thermoelectricity industry, the one of the open questions that remains to be satisfactorily answered is, what is the role played by the electrons, phonons and magnons in generating and transmitting heat, current, spin current etc. at a fundamental level. One should notice that the various quasi-particles play an important role in the origin of novel effects dominating the field of spin-caloritronics which is currently being investigated by several groups in various materials, using newly developed techniques. For example, several reports have emerges claiming to have observed transverse spin Seebeck effect in metals [13, 38–44] as well as semiconductors [45]. The origin of the said effect has been variously claimed to be due to the chemical potentials of the spin up and spin down electrons [38], phonons in the substrate [14, 45, 46] or a phonon-magnon drag effect [47]. Besides, competing classical effects such as planar Nernst effect [48] or anomalous Nernst effect [49] exist in case of metallic ferromagnetic films. Furthermore in lateral spin valve structures prepared with metallic ferromagnets, the spin dependent thermoelectric effects have been shown to be caused by the temperature difference between electrons and magnons [50, 51]. Regarding magnetic insulators, several reports have come out claiming the origin of longitudinal spin Seebeck effect [13–21, 23, 24] to be the temperature gradient between the electrons in the normal metal and the magnons in the insulating magnetic film [46, 52, 53] or magnonic spin currents due to temperature gradient [54]. Among the various aspects, we make contribution to ongoing research by studying the role played by electrons, phonons, magnons and the scattering mechanisms in transporting heat and electricity in metallic ferromagnetic system.

For the experimental determination of both spin dependent as well as independent thermal transport coefficients, it is crucial to know both the absolute temperature and the temperature difference across the sample as accurately as possible. Here we explain the suitability of membrane based suspended microcalorimeter to measure thermal and electrical transport coefficients of thin films. Several measurement techniques involve external

heaters or heater structures to generate a temperature gradient on the sample plane in order to measure either thermopower, thermal conductivity, Nernst coefficients. These techniques often underestimate the temperature gradient on the actual film as the sample substrate acts as a heat sink, usually at least 100 times thicker than the film itself [41, 162]. Now that the devices are in the shape of either film or wire in the nanometer to micrometer scale range, the presence of such thick substrates posses serious questions to the accuracy of the measureables. Also while using external thremocouples, bad thermal contact between the thermocouple and the sample could also be a source of error. On the other hand for the determination of thermal conductivity, 3ω technique [55–57] or 3ω-Völklein techniques [58,59] are quite popular since they do not involve direct measurement of temperature gradient. However, they requires precise knowledge of the substrate dimensions and the background offset to be subtracted. On top of that, the techniques are model dependent for retrieving relevant parameters. Opto-electric methods of thermal conductivity measurement have on the other hand their own limitations in the form of precise measurement of temperature gradients [35]. For deeper understanding of the nano-scale thermal transport issues, refer to the review articles [60, 61]. Hence after weighing all the options and considering suitability to our objectives, in this thesis work we have used SiN_x membrane platform technique to do transport study of metallic ferromagnetic films. SiN_x Membranes of thicknesses 100 nm and 500 nm have been used which not only provide minimal contribution of substrate to the heat current but also facilitate creating larger temperature gradient on the plane of the film.

Finally we elaborate the manifold motivation for selecting CoFe alloy as our choice of material for the study of transport coefficients. Firstly an alloy system suppresses phonon drag effects so that the contribution of individual scattering events are not overshadowed. Secondly by varying the composition, the Fermi level can be varied systematically. By measuring electrical resistivity, the effect of band structure can be directly mapped. Simultaneously CoFe being ferromagnetic, the electron-magnon scattering contribution to transport coefficients can be separately studied. CoFe and related material such as CoFeB are important in spintronics applications due to high Curie temperature and saturation magnetization. CoFe is well documented in terms of magnetic property study (see Chapter 2) but not transport study. Our study can narrow such gap. Additionally we have carried out theoretical calculations to help separate the various contributions. Therefore, we present a systematic study of transport coefficients with systematic variation composition which has not been done on this material so far.

1.1.1 Thesis arrangement

The thesis work is broadly divided into two parts, part one is regarding the study of transverse magneto thermoelectric power studied in Py/Pt bi-layer and part two regards the study of classical transport coefficients in CoFe alloys. The thesis is arranged as follows. Chapter 1 introduces the content of the thesis, beginning with the motivation. Chapter 2 consists of detailed introduction to transport coefficients and magneto-thermoelectric effects observed on metallic ferromagnets. Basic information on the transport properties with and without external magnetic field, temperature dependence, equations governing the transport in a metal, interactions involving the spin degree of freedom etc. are elaborated. This is needed to achieve an understanding or appreciate the motivation, experiments as well as the results produced in this work. Chapter 3 and 4 describe the first part of

the thesis. In Chapter 3, we describes the measurement techniques, sample preparation, characterization and set-up designs for the $Ni_{80}Fe_{20}$ films for magneto-thermoelectric study. In chapter 4 we discuss the results of the magneto thermoelectric effect study mainly focusing on our attempt to measure transverse spin Seebeck effect in $Ni_{80}Fe_{20}$. The results of this particular study are best understood from the complete study done on both bulk and SiN_x membranes. However, since the work on the bulk substrate system are part of another thesis [62], in this thesis we only take credit for our contribution i.e. the work and result studied on thin SiN_x membranes. Since the conclusion for the entire study can only be drawn by putting the picture of both bulk and membrane results together, only the final results from the bulk samples are here included.

Chapter 5 and 6 constitute the bulk of the thesis and describe the second part of the thesis. In Chapter 5, the device fabrication and measurement schemes for the Co_xFe_{1-x} samples for classical transport coefficient study are described. Chapter 6 elaborates the main results of transport coefficients measured on Co_xFe_{1-x} alloys of different compositions on SiN_x based microcalorimeter. Systematic study of the evolution of transport properties on ferromagnetic alloy systems with varying composition in such a large temperature range has not been done before. Hence this work not only holds the potential to broaden range of our existing knowledge of transport in ferromagnetic alloys but also provide us with the basic understanding of the roles played by different transport carriers involved in the transport which has so far been not studied in detail. Our results are complemented by the theoretical calculations provided by the group of Prof. H. Ebert in Munich. Finally we finish with conclusions and future aspect on the work described in Chapter 7. The appendix chapter further gives overview on the measurement instruments and scripts in labview as well as the list of devices.

Chapter 2

Theory

2.1 Introduction

This chapter provides the basic theoretical background necessary to understand the motivation behind our research and results obtained in this thesis. We begin with a short overview of the theory of band ferromagnetism and a review of the existing scientific literature on the electronic, structural, magnetic and thermal properties of Co_xFe_{1-x} and related alloy systems. Next we discuss various classical transport models and how they are applicable to our problem. We further include a discussion on the contribution of electrons, phonons and magnons to the transport coefficients. We conclude the chapter with a description of the magneto-thermoelectric effects, useful for the TSSE section of the thesis.

2.2 Ferromagnetism in transition metals

Ferromagnetism in the transition metals can be described in terms of the Stoner-Hubbard itinerant electron model for magnetism [63,64]. The non-localized electrons in narrow unfilled d-bands in the transition metals and correlation effects make the picture rather complicated. In the band ferromagnetism model [65,66], the electronic conduction takes place in two bands with spin up electrons $N_\uparrow$ and spin down electrons $N_\downarrow$. The Hamiltonian in each band contains the usual one electron approximation term along with another term for on-site Coulomb repulsion represented by parameter U. The energy dispersion curves are spin dependent and are given by

$$\varepsilon_{k\uparrow} = \varepsilon(K) + U\frac{N_\downarrow}{N} + \mu_0\mu_B H, \tag{2.1}$$

$$\varepsilon_{k\downarrow} = \varepsilon(K) + U\frac{N_\uparrow}{N} - \mu_0\mu_B H, \tag{2.2}$$

where the total number of electrons is $N = N_\uparrow + N_\downarrow$. Even though the two bands though have the same density of states (DOS) at the Fermi level $D(\varepsilon_F)$, they are split due to exchange interaction by an amount $\frac{U}{N} \times (N_\downarrow - N_\uparrow)$.

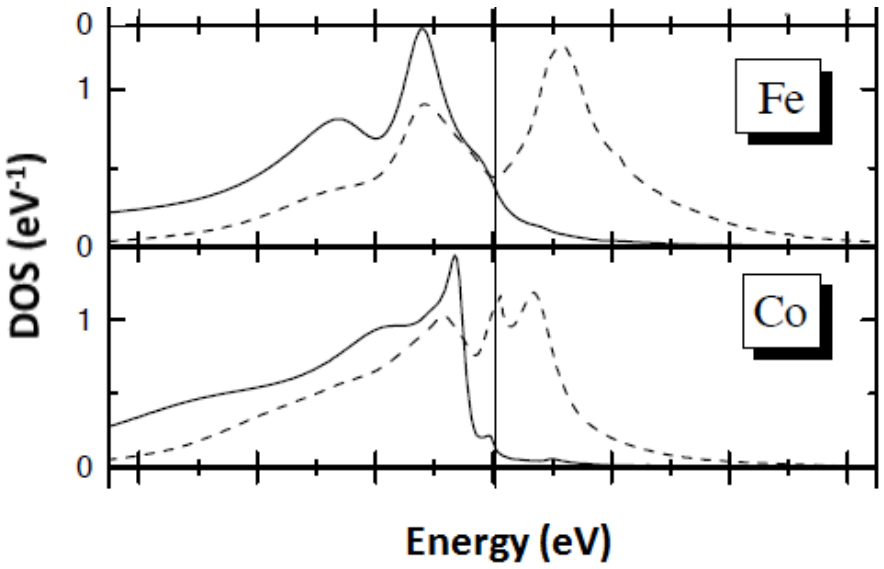

Figure 2.1: 3d-band density of state of spin up (solid line) and spin down (dotted line) electrons for Fe and Co at T=750 K. Source [67].

In other words

$$N_{\downarrow} - N_{\uparrow} = \frac{\mu_B H D(\varepsilon_F)}{1 - 0.5\frac{D(\varepsilon_F)U}{N}}. \tag{2.3}$$

It is known that the Stoner condition for the onset of band ferromagnetism is very high Pauli susceptibility which is proportional to the density of state, i.e.,

$$\frac{1}{2}\frac{D(\varepsilon_F)}{N}U > 1. \tag{2.4}$$

As an example, the 3d-band density of states of spin-up and spin-down electrons are calculated for Fe and Co in first principle local-density approximation scheme with dynamical mean field theory method by Lichtenstein *et al*. [67] as shown in Fig. 2.1. The correlation effects are rendered with large exchange splitting, minimum near Fermi energy for Fe and multiple-peaks in the minor DOS in Co.

2.3 Review on CoFe film alloy

The extensive study on CoFe has begun at early 20th century. In 1912, Preuss [68] and Weiss [69] separately reported high saturation magnetization values for $CoFe_2$ alloy . The CoFe itself was discovered as $Co_{50}Fe_{50}$ in 1927 by Ellis [70] and 1929 by Elmen [71] and is one of the most commonly studied alloy. It has been named Permendur [72] due to its high saturation magnetization in spite of high permeability. It was later alloyed with 2% Vanadium in 1932 by White and Wahl [73] which reduced its brittleness to assist in low temperature applications. Much of the published study concern CoFe-V and its variants. The alloy $Co_{50}Fe_{50}$-V is called

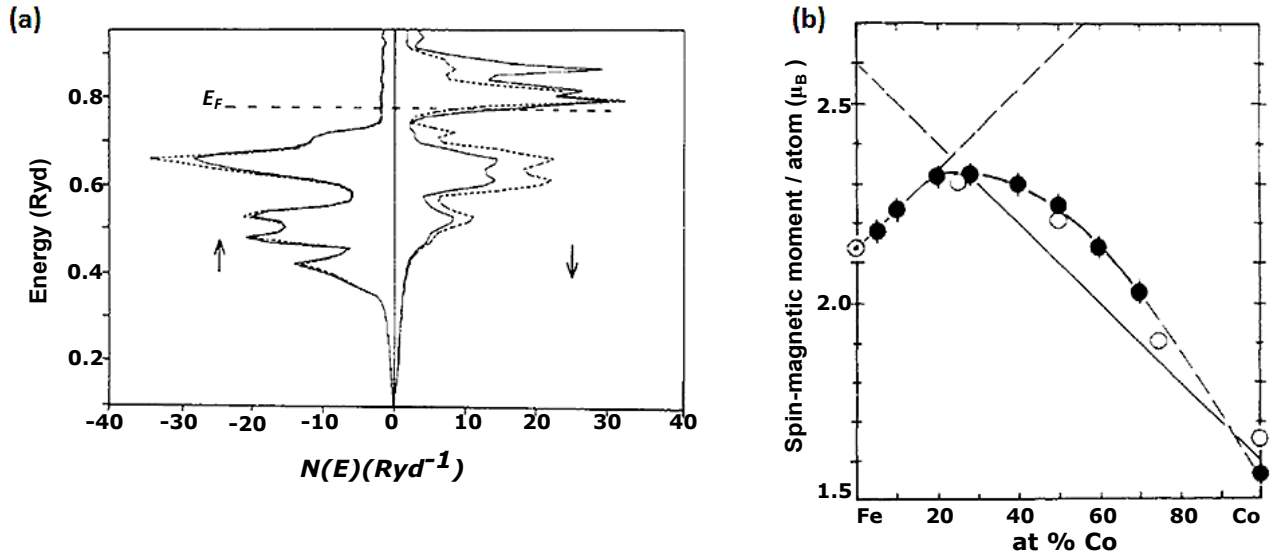

Figure 2.2: (a) Site and spin projected DOS for $Co_{50}Fe_{50}$ in CsCl structure ([75], also see [76] and [77]. (b) Part of Slater-Pauling curve of CoFe [75]. The measured spin magnetic moments by Bardos *et al*. [78] (black dots), calculated values by Schwarz *et al*. [75] (open circles). The lines are from the theoretical study of Berger *et al*. [79].

supermendur due to its superior qualities [74].

Next we discuss pure Co_xFe_{1-x} system since this is the system of interest for us and explain why this system holds such importance in various magnetism and spintronics applications [80–86]. It has the highest magnetostriction of all 3-d transition metal alloys, about 82 ppm in polycrystalline state [86], 150 ppm for annealed bulk single crystal $Co_{50}Fe_{50}$ alloys [87], the highest saturation magnetization-about 2.3 T [88], high mean Curie temperature of 1043-1500 K [76], low magnetocrystalline anisotropy, high uniaxial anisotropy in distorted structure [81]. These properties in soft ferromagnet materials of CoFe and related alloys are interesting in memory devices and other spintronics applications. Its magnetic properties are well studied over time, both experimentally and theoretically [75–78, 86, 87, 89–101]. The magnetic property that makes it less ideal for sensor applications is its high coercivity when studied on as-deposited films. Due to this reason the alloy is often subjected to different heating and cooling treatments afterwards, such as annealing, cold quenching, slow cooling and so on. A study by Cooke *et al*. [91], shows the effect of thermal treatment on magneto-sputtered 50% CoFe film. After annealing, the coercivity drops by a factor of 30, magnetostriction increases by a factor of 1.3, the grain size for film deposited on Si increases from 20-80 nm to 40-400 nm. The magnetic properties were also observed to be dependent on the substrate. Out of plane anisotropy has been achieved by depositing CoFe on Pd, Rh(001) or Pt films. The same effect can be achieved also by increasing thickness. Strong magnon softening has been theoretically calculated for CoFe deposited on Pd, Rh(001) or Pt substrates [84]. The Fig. 2.2(a) shows the spin projected density of states of $Co_{50}Fe_{50}$. The DOS for majority spin up band corresponds to that of bcc Fe but the minority band shows increased effect of Co due to the presence of one more electron than Fe [75–77]. Figure 2.2(b) shows the Slater-Pauling curve for CoFe. The black circles represent experimental work by Bardos *et al*. [78], the open circles represent theoretical work by Schwarz *et al*. [75] and the lines are

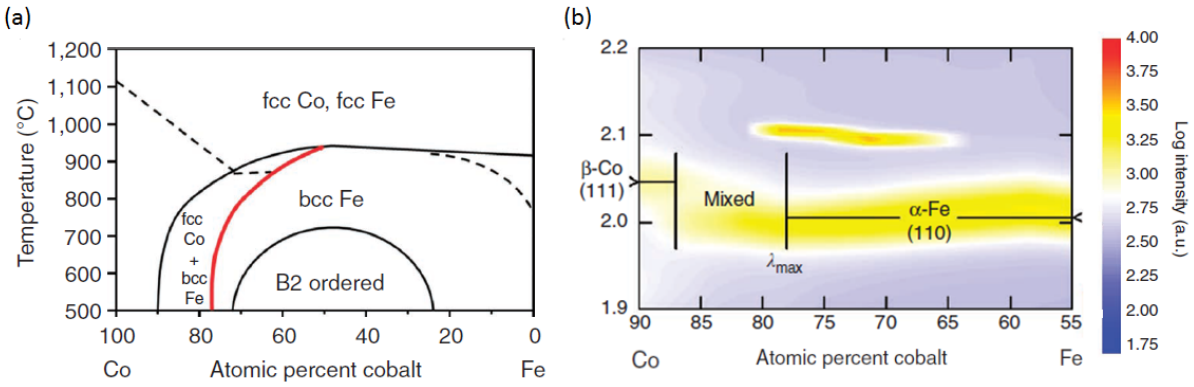

Figure 2.3: (a) Co-Fe phase diagram. (b) Synchrotron micro-diffraction of as-deposited CoFe film. The density plot shows measured d-spacing in $\AA$ as a function of Co atomic percent. The color scheme represents diffraction intensity. Source [86].

from the theoretical study by Berger *et al*. [79]. It shows good agreement between theory and experiments on the spin magnetic moment of the alloy as a function of Co concentration. In 2006, Ortiz *et al*. [90] did theoretical calculation and found that the magnetic moment is insensitive to the crystal structure and depend only on the volume and atomic concentration.

As to the crystal structure, several reports suggest towards its dependence on substrate choice and post deposition treatment. From early study on crystal structure [102–104], it was shown that the CoFe system at ambient temperatures and lower, is mostly in bcc structure for Co 0-78%, in fcc structure for Co between 78-95 % and finally in hcp structure for Co higher than 95%. This is also seen in the crystal lattice parameter which has been shown to remain close to 2.86 $\AA$ for Co from 0-30%, decrease nearly linearly to 2.83 $\AA$ until 78% Co and then remain constant upto 100% Co [83]. The system exhibits interesting order-disorder phase transition at 730° C above which the system is in ordered B2 CsCl structure and below in bcc disordered structure. However, there is an anomalous phase change at 550° C [80, 105, 106], the origin of which is still under dispute [107, 108]. The phase diagram by Ohnuma in treated CoFe is shown in Fig. 2.3(a). Pain *et al*. [97] in 1994 studied 200 nm ion-beam (with neutral Ar^+ or reactive N^+/N_2^+) sputtered CoFe onto Si wafers. They found that the films have fibrous structure throughout the film thickness. Those grown with neutral Ar^+ turned out to be in Fe bcc state with average grain size of 10-15 nm. However, Fe β phase was observed for N_2 reacted films due to the formation of Fe-N bonds.

The structure has been theoretically studied as well. In the study of Oritz *et al*. [90], it was showed that the B2 phase is ordered, and further found additional ground states. In 2011, in the experimental study by Hunter *et al*. [86], synchrotron X-ray micro-diffraction was performed on both treated and untreated CoFe samples. Since in our experiments, we study only as-deposited samples, for the sake of comparison the density plot for as-deposited sample from [86] is shown in Fig. 2.3(b). For untreated sample it was shown that below 912 ° C, the system is in α Fe bcc phase for Co less than 78%.

Finally we also review the available literature on the transport properties of the CoFe system. Most literature is available for heat treated samples since this process. Berger *et al*. [109] in 1987 measured the resistivity

of furnace cooked and quenched alloys which are ordered and disordered respectively at 4.2 K. The resistivity has a peak near Co 20% and then it drops monotonously as more cobalt is added and there is a small effect of ordering most prominent at 50% concentration. There are other reported electrical resistivity e.g. in spin-valve device [110]. Some resistivity studies have been done at higher temperature across the order-disorder transition [109, 111]. The specific heat behavior has been predicted near the order-disorder transition region which would captures the 550° C anomaly [111] and has been measured between 5 and 300 K [112]. There are no more studies of other transport coefficients for this system at least not in the temperature region of 4-300 K.

2.4 Transport phenomena in metals

2.4.1 Drude model of transport

The initial understanding of transport in metals came from the Drude model [113].

This model is based on certain assumptions such as the electrons with average mass m^* in solid are like free electron gas with no long range interaction with other charged bodies except local collisions with stationary ions cores within a mean relaxations time of τ. The outcome of the model is summarized to the derivation of the electrical conductivity σ given by the expression

$$\sigma = \frac{ne^2}{m^*}\tau, \tag{2.5}$$

where e and n are the charge and number density of electron.

2.4.2 Boltzmann theory and transport coefficients

The Boltzmann transport equations describe the dynamics inside a macroscopic system not in equilibrium. Considering more intuitively, for transport to occur, i.e., for the fluxes of momentum, energy, charge, number of particles etc. to flow from one region to the other, existence of a non-equilibrium distribution is a requirement. Relations dealing with such transport phenomena are put forth in the Boltzmann theory.

The current charge current density J_e and the heat current density J_Q under the weak electric and temperature gradients are first defined respectively as

$$J_e = \frac{2e}{8\pi^3}\int \upsilon_k f_k dk, \tag{2.6}$$

$$J_Q = \frac{2e}{8\pi^3}\int \upsilon_k \left[\varepsilon - \mu\right] f_k dk. \tag{2.7}$$

Here e, ε, υ_k and μ represent electron charge, electron energy, electron velocity and chemical potential respectively. f_k is the electron population distribution function under perturbations of weak electric field and temperature gradient.

At steady state, the current densities are converted to simplified forms

$$J_{\mathrm{e}} = e^2 K_0 E + \frac{eK_1}{T}(-\nabla T), \tag{2.8}$$

$$J_{\mathrm{Q}} = eK_1 E + \frac{K_2}{T}(-\nabla T). \tag{2.9}$$

Here the K_{n} is an integral defined as

$$K_{\mathrm{n}} = \frac{\tau_{\mathrm{k}}}{4\pi^3\hbar}\int\int(\upsilon_{\mathrm{k}})^2(\varepsilon-\mu)^n\left(\frac{-\partial f_{\mathrm{k}}^0}{\partial\varepsilon}\right)\frac{ds'}{\mid\upsilon_{\mathrm{k}}\mid}d\varepsilon, \tag{2.10}$$

where the volume integral dk has been converted to surface integral of surface s' with energy ε. In the absence of temperature gradient, the electrical current is just the 1st term of equation (2.8). In a pure metal the velocity of electrons is $\upsilon = hk_{\mathrm{F}}/m^*$ and hence the integral K_0 when calculated over the Fermi surface produces the electrical current density as

$$J_{\mathrm{e}} = \frac{ne^2\tau}{m^*}\cdot\mathbf{E} = \sigma\cdot\mathbf{E}, \tag{2.11}$$

where σ is the electrical conductivity which is nothing but the value calculated from Drude's model in equation (2.5) which is not surprising since we know that only the electrons near the Fermi surface contribute to electrical conduction.

To calculate the thermal conductivity, $J_{\mathrm{e}} = 0$ condition is set and equations (2.8) and (2.9) are solved simultaneously for J_{Q} which then is given by

$$J_{\mathrm{Q}} = \frac{1}{T}\left[K_2 - K_1^2K_0^{-1}\right] \approx K_2\left(-\nabla T\right) = k\left(-\nabla T\right). \tag{2.12}$$

The term $K_1^2K_0^{-1}$ is negligible for metals and hence the electronic contribution of the thermal conductivity is simply K_2/T or κ_{el}. K_2 is related to K_0 via the relation $K_2 = K_0\left(\pi^2/3\right)(k_{\mathrm{B}}T)^2$. Then this simplifies our κ_{el} to be

$$\kappa_{\mathrm{el}} = \frac{K_2}{T} = \frac{\pi^2k_{\mathrm{B}}^2T}{3}K_0 = \frac{\pi^2}{3}\left(\frac{k_{\mathrm{B}}}{e}\right)^2 T\sigma. \tag{2.13}$$

This is the Wiedemann-Franz relation [114] which relates the electric thermal conductivity and the electric conductivity as $\kappa/\sigma = L_0T$ where $L_0 = (\pi^2/3)\,(k_{\mathrm{B}}/e)^2$ is the Sommerfeld value of the Lorenz number, i.e., $L_0 = 2.45\times10^{-8}$ WΩ/K^2. The value of the Lorenz number changes when other scattering events contribute to the thermal conductivity such as e-phonon drag, i.e., in U and N processes which are dominant in the intermediate temperatures. Hence the Wiedemann-Franz law holds only at the low (when phonons freeze out) and the high temperature (e-phonon and phonon-phonon interactions saturate) regimes and in the intermediate temperatures Lorenz number deviates from L_0. Further discussion on Lorenz number has been done shortly in the scattering section.

Finally we can also calculate the Seebeck coefficient or thermopower (S) from the Boltzmann equation by

putting null value for J_e in equation (2.8) and solving we get

$$\mathbf{E} = \frac{K_0^{-1}K_1}{eT}\nabla T = S\nabla T. \tag{2.14}$$

We can use the relation between K_1 and K_0, i.e., $K_1 = \left(\pi^2/3\right)(k_B T)^2 \left[\partial K_0/\partial\varepsilon\right]_{\varepsilon=\varepsilon_F}$ to finally arrive at the relation for the thermopower as

$$S = \frac{\pi^2 k_B^2 T}{3e}\left[\frac{1}{\sigma}\frac{\partial\sigma(\varepsilon)}{\partial\varepsilon}\right]_{\varepsilon=\varepsilon_F} = \frac{\pi^2}{3}\left(\frac{k_B}{e}\right)k_B T\left[\frac{\partial ln\sigma(\varepsilon)}{\partial\varepsilon}\right]_{\varepsilon=\varepsilon_F}. \tag{2.15}$$

This is the famous Mott relation for thermopower which relates Seebeck coefficient to electrical conductivity via the derivative of electrical conductivity with respect to energy on the Fermi surface.

2.4.3 Onsager reciprocal relations

Reciprocity has been observed among the coefficients of reversible and irreversible thermoelectric transport effects, i.e., the Seebeck, the Peltier and the Thomson effects. Per definition, the application of temperature difference at the ends of a film generates Seebeck voltage and on the same sample if a potential difference is maintained across the ends then a temperature difference appears due to the Peltier effect. Such intuitive arguments led Lord Kelvin to put the reciprocity among these effects in mathematical forms [115]. The first Kelvin relation states the relation between Seebeck (S) and Peltier (Π) coefficients as

$$\Pi = ST. \tag{2.16}$$

The reciprocity among the thermoelectric effects predict the following form for the Thomson coefficient (Π)

$$\sigma_T = T\frac{\partial S}{\partial T} = -S + \frac{\partial\Pi}{\partial T}, \tag{2.17}$$

where T stands for the temperature. Such reciprocity has also been observed in mechanics, fluid dynamics and thermodynamics under the discussion of applied force and the corresponding movement effects.

Following the same logic, Onsager argued that similar reciprocity also exists among other transport coefficients. Onsager put the thermoelectric effects in perspective along with irreversible thermodynamic processes such as Joule heating and thermal conduction and published in his 1931 publication [116] the famously known Onsager reciprocal relations.

Onsager considered electric potential, temperature difference, momentum or particle number difference as the force factors and correspondingly electric current, heat current, electron diffusion as the flow terms. Since external forces are involved obviously the system under study has to be away from equilibrium yet close, i.e., within first order of Boltzmann distribution. The resulting phenomenological reciprocal relations obtained as the

following.

$$J_{\mathrm{e}} = -\frac{L_{11}}{T}\nabla\mu - \frac{L_{12}}{T^2}\nabla T, \tag{2.18}$$

$$J_{\mathrm{Q}} = -\frac{L_{21}}{T}\nabla\mu - \frac{L_{22}}{T^2}\nabla T, \tag{2.19}$$

with $L_{12} = L_{21}$ from Kelvin's relations. The application of the Onsager relations in transport coefficients take the following forms.

$$J_{\mathrm{e}} = -\frac{\sigma}{e^2}\nabla\mu + \frac{S\sigma}{|\,e\,|}\nabla T, \tag{2.20}$$

$$J_{\mathrm{Q}} = \frac{ST\sigma}{|\,e\,|}\nabla\mu - (k + TS^2\sigma)\nabla T, \tag{2.21}$$

where σ, e, μ, S, κ and T are the electrical conductivity, electron charge, chemical potential, Seebeck coefficient, thermal conductivity of the material and temperature respectively. These relations state the obvious that the transport coefficients are dependent on each other. This is no surprise as we have seen already in the equations from (2.8) and (2.9) that the electrical and thermal currents can be generated by both electric and thermal gradient fields. One more important take away from the above equations is that not only the transport coefficients are related to each other but also they all are dependent on the temperature. However, the temperature dependence of the various transport coefficients in different temperature regime is not so simple to calculate since they are highly dependent on the scattering processes among the charge and heat carriers. This topic is addressed in the next sections mostly stating qualitative results without mathematical derivations. Such dependencies are very important for understanding the experimental work done this study.

2.4.4 Scattering processes and Lorenz number

The Onsager reciprocal relations nicely tie all the electronic transport coefficients together. However, with varying external factors such as temperature, pressure or magnetic field, i.e with the variation of the population of different particles, it becomes important to give proper importance to the scattering mechanisms involved. The scattering processes can involve electron-electron processes (e-e), electron-impurity processes (e-imp), electron-phonon interactions (e-ph), electron-magnon interactions (e-mag) or any other additional effects. One or more of the scattering events can affect the transport of heat or charge across a system and not only that, each process has different temperature dependencies in different temperature region. The overall effect is therefore reflected in the temperature dependence of the transport coefficients. A good measure in this regards is the so called Lorenz number, which is the ratio of two transport coefficients, the thermal conductivity (κ) and the electronic conductivity (σ). The Lorenz number is equal to the Sommerfeld value of 2.45×10^{-8} WΩ/K^2 if scattering mechanisms contribute equally to heat and charge transport. This occurs, for example, in degenerate gas systems such as monovalent metals at temperatures higher than the Debye temperature or at temperature much lower than the Debye temperature. However, in the intermediate temperature range or for other materials with the presence of strong scattering mechanisms, deviation from Wiedemann-Franz law is observed, i.e., the Lorenz number

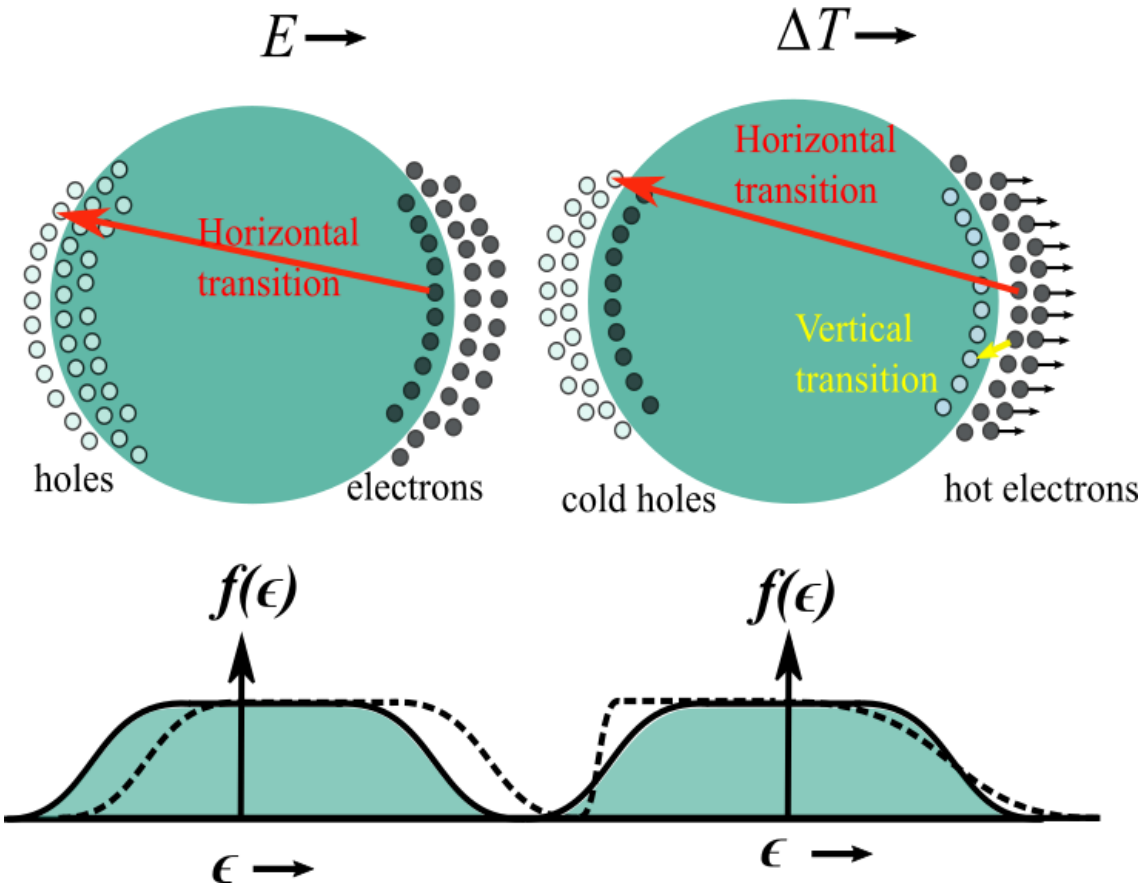

Figure 2.4: Horizontal (large angle) vs vertical (small angle) scatterings affecting the Fermi surface and electron distribution function under electric field and temperature difference.

deviates from the Sommerfeld value [73, 117].

To understand the difference in the electron scattering events for charge and heat transport, we refer to Fig. 2.4. In a normal metal, the behavior of electron scattering casts two different pictures under electric field gradient and temperature gradient. Figure 2.4 shows the Fermi sea as the edge of the sphere around which the electrons are scattered. In the left figure, the electric field simply displaces electrons residing just outside the Fermi surface whereas electrons embedded deep within the valence band are not affected. As a consequence, equal number of holes also get displaced but around the opposite surface. The sketch at the bottom shows the electron number distribution as a function of electric energy. After the electric field has been removed, the electrons have to relax back by taking the long angle scattering path and hence, it is called large angle scattering or horizontal scattering (indicated by red arrow). On the other hand, an application of temperature gradient drags electrons from hot region to cold region. Additionally some electrons in the valence band acquire enough thermal energy to overcome the Fermi energy. The distribution of electron and hole densities appear as seen in the right figure. Now if the external heat source is removed, the electrons can either relax by again taking the long route by scattering horizontally or can make small vertical jumps otherwise known as small angle scattering (indicated by yellow

arrow). These vertical scattering are inelastic in nature and contribute only to the thermal transport in the lattice. In case the electrons make several small vertical jumps, the scattering time is increased by a factor dependent on the average scattering angle which in turn is a function of temperature. At very low temperature, due to the scarcity of phonons, electrons scatter elastically following horizontal scattering and then the Wiedemann-Franz law is valid. Similarly at very high temperature, there is abundance of phonon, the scattering of phonon-impurity and phonon-phonon average out and the electron thermal transport is limited by large angle electron-phonon elastic scattering. Only in the intermediate temperature range, the phonon scattering length decreases and they no longer scatter electrons at large angles. Electrons relax via inelastic vertical processes using additional channels and the relaxation time in thermal process decreases, thus deviation from Wiedemann-Franz law is observed. In other words, the Lorenz number is no longer the Sommerfeld value. The established asymptotic relations are

$$L \approx 1, for\ T \geq \Theta_D, \tag{2.22}$$

$$L \propto T^2, for\ T \ll \Theta_D, \tag{2.23}$$

where Θ_D is the Debye temperature. Therefore, the direct determination of Lorenz number provides with the information on dominance of particular scattering events or presence of contributing non-electronic quasi-particles.

2.4.5 Resistivity

Resistivity in non-magnetic metal and alloys

The resistivity of a metal is aptly put by A. Matthiessen in 1864 in his empirical rule as

$$\rho = \rho_0 + \rho_{\mathrm{el-ph}}(T). \tag{2.24}$$

Here ρ_0 is the residual resistivity of the metal which is nothing but the contribution coming from the defects and impurities, each scattering mechanism considered independently. The temperature dependent resistivity ($\rho_{\mathrm{el-ph}}$(T)) is purely metallic in character arising from the electron-phonon interactions. Although this simple rule caters to all the metals at high temperatures, small deviations are normally observed at low temperatures. At low temperatures the scatterings from phonons and defects are more complicated and the mean free path is no longer independent of the phase space vector and hence the residual resistivity is no longer a constant with respect to temperature.

In terms of temperature dependence of the total resistivity of non-magnetic material, it has been shown that at high temperatures, i.e., at temperatures higher than the Debye temperature Θ_{D}, electrons scatter from phonons. This produces a direct proportionality of ρ to temperature [118], i.e.,

$$\rho \propto T, T \geq \Theta_D. \tag{2.25}$$

But at temperatures T $\ll \Theta_{\mathrm{D}}$, the electron-phonon interactions give rise to T^5 temperature dependence which

can be explained by the Bloch-Grüneisen relation [118, 119] in the framework of Boltzmann transport theory as

$$\rho_{\mathrm{el-ph}}(T) = \alpha_{\mathrm{el-ph}}\Big(\frac{T}{\Theta_{\mathrm{R}}}\Big)^5 \int_0^{\frac{\Theta_{\mathrm{R}}}{T}} \frac{x^5 dx}{(e^x-1)(1-e^{-}x)}, \tag{2.26}$$

where $\alpha_{\mathrm{el-ph}}$ is material dependent electron-phonon interaction constant and Θ_{R} is Bloch-Grüneisen temperature. Θ_{R} is not exactly same as the Debye temperature but the characteristic temperature of the metal characterizing its intrinsic electrical resistivity same way as Debye temperature characterizes its lattice specific heat [242]. The Θ_{R} is given by

$$\Theta_{\mathrm{R}} = \frac{2\hbar \upsilon_{\mathrm{s}} K_{\mathrm{F}}}{k_{\mathrm{B}}}, \tag{2.27}$$

where υ_{s}, K_{F} and k_{B} are the sound velocity, Fermi wave vector and Boltzmann constant respectively.

The coefficient $\alpha_{\mathrm{el-ph}}$ is proportional to the electron-phonon coupling constant (λ) [120] via the relation

$$\alpha_{\mathrm{e-ph}} = \frac{4\pi\lambda\omega_{\mathrm{D}}}{\varepsilon_0\omega_{\mathrm{P}}^2} = \frac{8\pi^2\upsilon_{\mathrm{s}}m^*}{n^{2/3}e^2}\lambda, \tag{2.28}$$

where ω_{D} and ω_{P} are the Debye frequency and the Drude plasma frequency respectively. Equation (2.28) can be simplified within the simple Drude model by writing $\omega_{\mathrm{D}} = \Theta_{\mathrm{D}}k_{\mathrm{B}}/\hbar$.

During the discussion of resistivity and its dependence of temperature, the temperature coefficient of resistivity (TCR) as an intrinsic quantity deserves to be discussed as well. For metals, in the range of temperature where resistivity changes linearly with temperature, the TCR is calculated using the relation

$$TCR = \frac{1}{\rho_0}\frac{\partial\rho}{\partial T}, \tag{2.29}$$

where ρ_0 is the lowest measured resistivity. For most metals the TCR is positive.

Resistivity in ferromagnetic metals (transition metal) and alloys

According to Mott and Stevens, transition metals have in general higher resistivity compared to normal metals due to the presence of vacant d-bands [121–123]. The vacant d-bands allow s electrons to jump to these states and hence reduce electrical conductivity. Mott put forth a simple relation in the following form

$$\frac{1}{\tau_{\mathrm{s}}} = \frac{1}{\tau_{\mathrm{s-d}}} \propto N_{\mathrm{d}}(\varepsilon)_{\varepsilon=\varepsilon_{\mathrm{F}}}, \tag{2.30}$$

where N_{d} is the density of state of d band. The high N_{d} is used to explain the high ρ of transition metals and alloys compared to non-transition metal alloys.

Signature of magnon scattering in ρ

In ferromagnetic materials, collective spin excitation, i.e., magnons also contribute to transport properties. The fundamental quantity to look out for is the magnon number N_{mag} which in the low temperature limit can be calculated analytically from the magnon dispersion relation. The magnon dispersion relation in three dimensional cubic lattice is given by

$$\hbar\omega = 2Js[1-\cos(k.a)], \tag{2.31}$$

where J, s, k and a are the exchange coupling constant, electron spin, wave number and lattice constant respectively. At low temperature only low energy magnon near $k = 0$ are excited, then the dispersion relation simplifies to

$$\hbar\omega = (Jsa^2)k^2 = D^{'}k^2, \tag{2.32}$$

here $D^{'}$ is called the spin wave stiffness constant. Now the number of magnons in mode k and at temperature T is given by the relation,

$$< n_{\mathrm{k}} >= \frac{1}{e^{\frac{\hbar\omega_{\mathrm{k}}}{k_{\mathrm{B}}T}} - 1}. \tag{2.33}$$

The total number of magnons is then $\sum_{\mathrm{k}} n_{\mathrm{k}} = \int d\omega D(\omega) < n(\omega) >$, where $D(\omega)$ is the magnon density of states, i.e., the number of magnon modes per unit frequency range. The number of modes of wave vector per unit volume less than k is $\left(1/2\pi\right)^3\left(4/3\pi k^3\right)$. The total number of magnon modes per frequency interval is given by

$$D(\omega)d\omega = \left(\frac{1}{2\pi}\right)^3(4\pi k^2)\left(\frac{dk}{d\omega}d\omega\right) = \frac{1}{4\pi^2}\left(\frac{\hbar}{D^{'}}\right)^{3/2}\sqrt{\omega}. \tag{2.34}$$

For $k_{\mathrm{B}}T \ll Js$, the total number of magnons is obtained by using equation (2.34) in equation (2.33) and integrating from 0 to ∞ resulting in,

$$N_{\mathrm{Mag}} = \sum_k n_{\mathrm{k}} = 2.315 \times \left(k_{\mathrm{B}}/D^{'}\right)^{3/2} T^{3/2}. \tag{2.35}$$

These low energy magnons scatter from the electrons and contribute to the total electrical resistivity in the low temperature regime (i.e. $\mathrm{T} < \Theta_{\mathrm{D}}$). The electron-magnon scattering time is proportional to the magnon number density and hence the resistivity due to electron-magnon scattering is expected to vary as $T^{3/2}$. But according to the study by Raquet *et al*. [226], the temperature dependence of the resistivity due to electron-magnon scattering has a complicated temperature dependence.

However at much lower temperatures i.e. $\mathrm{T} < 15$ K, according to the work of Mannari *et al*. [124], an appreciable contribution of electron-magnon scattering to the resistivity of ferromagnetic material has been reported which is given by a quadratic temperature dependence, i.e., $\rho = BT^2$ where

$$B = \frac{3\pi^2 S\hbar}{16e^2K_{\mathrm{F}}}\left(\frac{\mu_{\mathrm{m}}}{m^*}\right)^2\frac{[k_{\mathrm{B}}TNJ(0)]^2}{\varepsilon_{\mathrm{F}}^4}. \tag{2.36}$$

Here s(=1/2) is the electron spin, μ_{m}, m^* are the effective magnon mass and electron mass respectively, $\varepsilon_{\mathrm{F}}, K_{\mathrm{F}}$

and N are the Fermi energy, Fermi wave vector and number of spins in the respective order, and finally $NJ(0)$ is the strength of the s-d scattering.

To calculate magnon scattering contribution to ρ at higher temperatures, the phonon scattering contribution has to be subtracted from the total ρ. At $T > 100$ K, i.e, at intermediate and high temperature, resistivity due to phonon scattering is better approximated by Bloch-Wilson relation [118] instead of Bloch-Grüneisen relation. The T^3 dependence corresponds to the substantial s-d scattering in these metals.

$$\rho(T) = \rho_0 + \alpha_{\mathrm{el-ph}}\Big(\frac{T}{\Theta_\mathrm{D}}\Big)^3 \int_0^{\Theta_\mathrm{D}/T} \frac{x^3 dx}{(e^x-1)(1-e^{-}x)}. \tag{2.37}$$

Hence one practical way to separate the magnon contribution $\rho_{\mathrm{mag}}(T)$ at high temperatures is to fit the measured resistivity with Bloch-Wilson function only upto 100 K and then extrapolate to the highest temperature. The difference between the measured and the extrapolated resistivity gives the $\rho_{\mathrm{mag}}(T)$ at high temperature [125].

2.4.6 Thermal conductivity

Thermal conductivity of a material is the property which describes how well heat energy is transferred across the material [126]. In the simplest form, thermal conductivity (κ) is the rate of flow of heat per unit area (A) per unit temperature gradient (∇T) across a material, i.e.,

$$\kappa = -\frac{\dot{Q}}{A\nabla T}. \tag{2.38}$$

The total thermal conductivity in a ferromagnetic metal is written as the sum of the contributions from scattering with various quasi-particles and defects, i.e.,

$$\kappa = \kappa_\mathrm{e} + \kappa_{\mathrm{ph}} + \kappa_{\mathrm{mag}} + additional, \tag{2.39}$$

where κ_e corresponds to the electronic contribution, κ_{ph} to the lattice thermal conductivity or the phononic contribution and κ_{mag} to the magnon scattering contribution to the total thermal conductivity.

Each contribution can be written in terms of its corresponding scattering time (τ), velocity (υ) and specific heat per unit volume (C). For example the electronic thermal conductivity can be written as,

$$\kappa_\mathrm{e} = \frac{1}{3} C_\mathrm{e} \upsilon_\mathrm{e}^2 \tau_\mathrm{e} \tag{2.40}$$

And from Matthiessen's rule we already know that the scattering times are additive. An example of τ_e contributing to κ_e is as follows

$$\frac{1}{\tau_\mathrm{e}} = \frac{1}{\tau_{\mathrm{e-e}}} + \frac{1}{\tau_{\mathrm{e-ph}}} + \frac{1}{\tau_{\mathrm{e-mag}}} + c, \tag{2.41}$$

where the additional terms c comes from the electron-impurity scattering and so on.

Next we discuss the temperature dependence of thermal conductivity. Examples at room temperature and be-

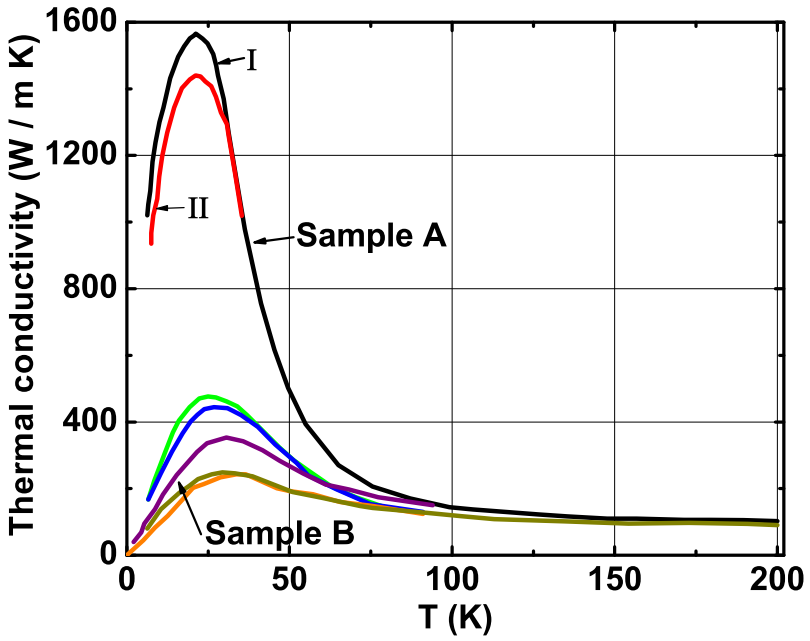

Figure 2.5: Thermal conductivity of Fe in different purity as a function of temperature. The κ of Fe has been collected from the study by Arajs *et al*. (black, red and dark yellow lines) [129], Kemp *et al*. (orange line) [130], Kemp *et al*. (green and blue lines) [131] and Rosenberg *et al*. (purple line). The Umklapp peak is observed in all graphs at temperature 20-31 K. Data collected from source [129] and replotted.

low are reviewed in [127]. This dependency arises from the temperature dependency of the scattering times [128]. Usually the electronic thermal conductivity is larger than the lattice thermal conductivity due to the higher electronic velocity compared to the velocity of sound. However, at higher temperatures the phonon number increases with temperature and then it becomes a competition between the various scattering processes. That is the reason why the total thermal conductivity does not increase monotonically with temperature but decreases or rather is suppressed at higher temperatures. At low temperature, i.e., $T < \Theta_D$, electrons undergo large angle elastic horizontal scattering from impurity centers [118]. Since the residual resistivity is temperature independent, according to Wiedemann-Franz law the thermal conductivity which is mostly electronic, is proportional to temperature, i.e., $\kappa \propto T$. At high temperatures, $T > \Theta_D$, again the inelastic vertical jumps are not important in phonon scattering and is limited by the maximum possible spread of the Fermi distribution of the order of $k_B T$. Since the electrical conductivity is inversely proportional to temperature, according to Wiedemann-Franz, the thermal conductivity κ tends to remain constant. At temperature much lower than Θ_D, the phonon wavelength reduces and the relaxation time for thermal conductivity follows the relation $\tau \propto \Theta_D^4/T^3$.

The phonon-phonon scattering also contributes to transport at the intermediate temperatures. This process can be either the normal process known as the N-process or the Umklapp process, i.e., the U-process. In case of pure metals at intermediate temperatures, its not the electron-phonon drag rather the phonon-phonon drag effect,

i.e., the U-process which dominates often seen as a peak in the thermal conductivity graph around temperature $\Theta_D/5$. Before the peak, the lattice thermal conductivity has a T^3 temperature dependence due to scattering at the boundaries and defects whereas immediately after the peak the κ varies exponentially as $e^{\Theta_D/T}$. At higher temperature, the U-process contributes to κ with $1/T$ temperature dependence. As an illustration, Fig. 2.5 shows the large Umklapp peak in the thermal conductivity of Fe in different purities. The graph shows κ of Fe studied by Arajs *et al*. (black, red and dark yellow lines) [129], Kemp *et al*. (orange line) [130], Kemp *et al*. (green and blue lines) [131] and Rosenberg *et al*. [132] (purple line).

However, in case of alloys, the scattering from the various scattering centers limit the phonon mean free path and the U-process is suppressed.

2.4.7 Thermoelectric effects - Seebeck, Peltier and Thomson effects

The fist thermoelectric effect was discovered in a thermocouple structure in 1821 by Thomas Johann Seebeck [1] and thus the name Seebeck effect. When two dissimilar metals were joined to form a loop structure, Seebeck observed that heating or cooling one junction produced voltage difference of appropriate sign at the other junction. Seebeck initially thought it to be an thermo-magnetic effect but was later corrected by Hans Oersted to be a thermoelectric effect. The Seebeck coefficient, put in a simple formula, is given by,

$$S = \lim_{\Delta T \to 0} \frac{\Delta V}{\Delta T}, \tag{2.42}$$

where the ΔV is measured with a voltmeter with polarity aligned in the temperature gradient direction. The Seebeck coefficient can have either positive or negative sign. Going by convention, the sign of the Seebeck coefficient indicates the potential of the cold side with respect to the hot side. If in a metal, electrons diffuse from the hot side to the cold side then the Seebeck coefficient carries negative sign. Of course it is assumed here that the metal follows Drude's free electron model, i.e., the mean free path and mean velocity increase with increasing electron thermal energy. However, in reality the scattering processes do intervene and then the sign of the Seebeck coefficient is no longer accounted for by the free electron model.

We discuss the sign of absolute thermopower with the following example. At the junction of a thermocouple with two metals, the electron flux is given by [133]

$$\Gamma \approx -\frac{\lambda^2}{\tau}(\Delta n) - \frac{n\lambda}{2\tau}(\Delta\lambda) + \frac{n\lambda^2}{2\tau}(\Delta ln\tau), \tag{2.43}$$

where λ, τ and n are the mean free path, scattering time and electron number density respectively. Hence depending on the strength of the energy dependence of either of these quantities, the electrons can flow in either direction. For example if the mean free path in a metal is strongly dependent on the energy then the $\Delta\lambda$ is negative which in turn makes Γ positive, i.e., the electrons diffuse from hot to cold end of the metal with a negative thermopower. On the other hand, if for some metals the λ decreases with increasing energy then the direction of flow of the electrons will be from the cold to the hot end or in other words the metal has a positive

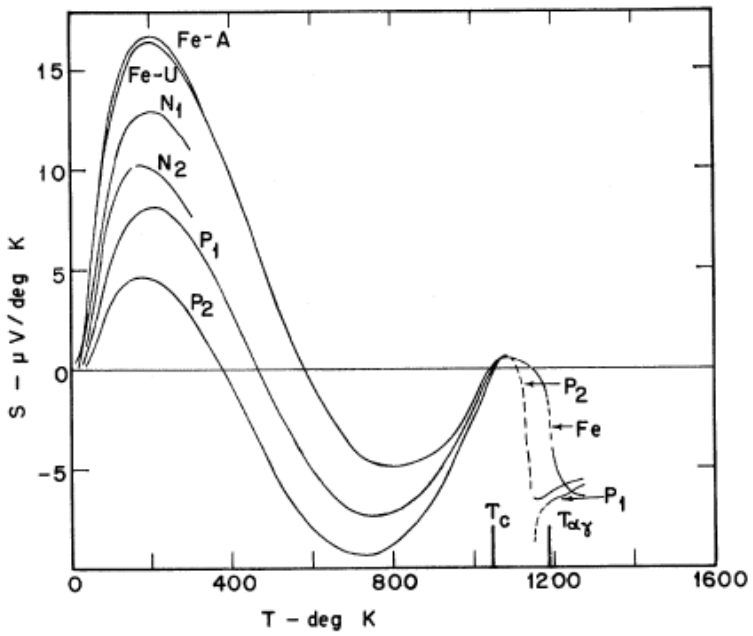

Figure 2.6: Thermopower vs temperature in Fe and its dilute alloys. The magnon drag peak for pure annealed (Fe-A) and un-annealed Fe (Fe-U) near 200 K. Source [135].

thermopower. Hence, the sign of the thermopower is strongly dictated by not only the scattering mechanisms but also by the energy dependence of these scatterings.

Mott and Cutler arrived at the general Mott formula for thermopower [64, 134],

$$S = -\frac{1}{|e|T}\frac{\int(\varepsilon-\varepsilon_F)\sigma(\varepsilon)\frac{\partial f_0}{\partial \varepsilon}d\varepsilon}{\int\sigma(\varepsilon)\frac{\partial f_0}{\partial \varepsilon}d\varepsilon}, \tag{2.44}$$

where the symbols have usual meaning. For diffusion thermopower, this equation boils down to the simpler Mott formula (2.15) which elegantly conveys the sensitivity of the thermopower to the curvature of the band structure near Fermi surface and hence the scattering with the electrons.

Signature of magnon scattering in S

The electron-magnon scattering contribution or otherwise called the magnon drag effect in the thermopower of Fe and its dilute alloys (with Ni) was reported as early as in 1967 by Blatt *et al*. [135]. As shown in Fig. 2.6, magnon drag peak in pure annealed Fe (Fe-A) and un-annealed Fe (Fe-U) was observed at 200 K. The drag contribution was smaller but finite for dilute alloys. The total thermopower was fitted to a function $S = \alpha T + \beta T^{3/2}$ in the temperature range of 15 - 81 K. The linear in temperature term corresponds to diffusion thermopower whereas the $T^{3/2}$ dependent term represents magnon drag component. The coefficients found in this study [135] were $\alpha = -0.01\ \mu$V/K^2 and $\beta = 0.016\ \mu$V/K$^{5/2}$, implying that the total thermopower before

the magnon drag peak consisted of a diffusion term of negative sign and a drag contribution of opposite sign in pure Fe. In 1976, magnon drag contribution was reported in the Peltier coefficient of $Ni_{66}Cu_{34}$ and $Ni_{69}Fe_{31}$ alloys at 4.2 K and in the presence of magnetic field by Grannemann *et al*. [136]. Several decades later the topic was picked up again and magnon drag effect was studied in $Ni_{80}Fe_{20}$ alloy in a thermopile structure in 2011 [137]. The growing interest in magnon based transport phenomenon has triggered further research interest in magnon drag effects. Very recently the magnon drag effect in thermopower was studied both theoretically and experimentally, in pure ferromagnetic metals of Fe, Co and Ni by Watzman *et al*. [138]. Two separate theories were proposed to understand the theory of magnon drag thermopower. One is a hydrodynamic theory based on non-relativistic spin preserving electron-magnon scattering and the other is based on spin motive force. The sign of the drag component is assigned by the sign of the Hall coefficient of the materials. Both models provide similar results and the magnon drag thermopower $S_{\mathrm{M-drag}}$ is given by

$$S_{\mathrm{M-drag}} = \frac{2}{3}\frac{C_{\mathrm{m}}}{n_{\mathrm{e}}e}\left(\frac{1}{1+\frac{\tau_{\mathrm{em}}}{\tau_{\mathrm{m}}}}\right), \tag{2.45}$$

where C_{m}, τ_{em} and τ_{m} are the magnon specific heat per unit volume, electron-magnon scattering time and magnon mean free time respectively. The magnon specific heat is given by [139]

$$C_{\mathrm{m}} = 0.113 k_{\mathrm{B}}\left(\frac{k_{\mathrm{B}}T}{D}\right)^{3/2}, \tag{2.46}$$

where D is the spin stiffness constant. The results on Fe thermopower by Blatt *et al*. [135] are experimentally reproduced in this study [138] and compared with theoretical model results. We discuss these results in more detail.

Figure (2.7) shows the thermopower in Fe and Co, measured data in filled circles and theory result as lines [138]. The dashed line represents theoretically calculated magnon drag thermopower contribution calculated from equation (2.45) and the solid line represents total calculated thermopower including magnon drag and diffusion thermopower. The diffusion thermopower is calculated from $S_{\mathrm{D}} = (\pi k_{\mathrm{B}})^2 T/3e\varepsilon_{\mathrm{F}}$ where ε_{F} is the Fermi energy. See [138] for detail on the input parameters in the model calculation. In Fig. 2.7(a), both single crystal (black) and dense sintered polycrystal (red) Fe, exhibit magnon drag contributions. The magnon drag peak is observed at 200 K. Unlike the study by Blatt *et al*., both the diffusion and drag contributions to thermopower are positive in sign. The reason for positive diffusion component is the positive slope of s and p bands' density of state the the Fermi energy used as input parameter in the model calculation. In case of Co, as shown in Fig. 2.7(b), the drag contribution was observed from 150 K up to 600 K (red). In this case, both the contributions to Co thermopower are negative in sign. Additional measurement on a porous Co sample (blue) shows suppression of phonon drag contribution while retaining the magnon drag contribution.

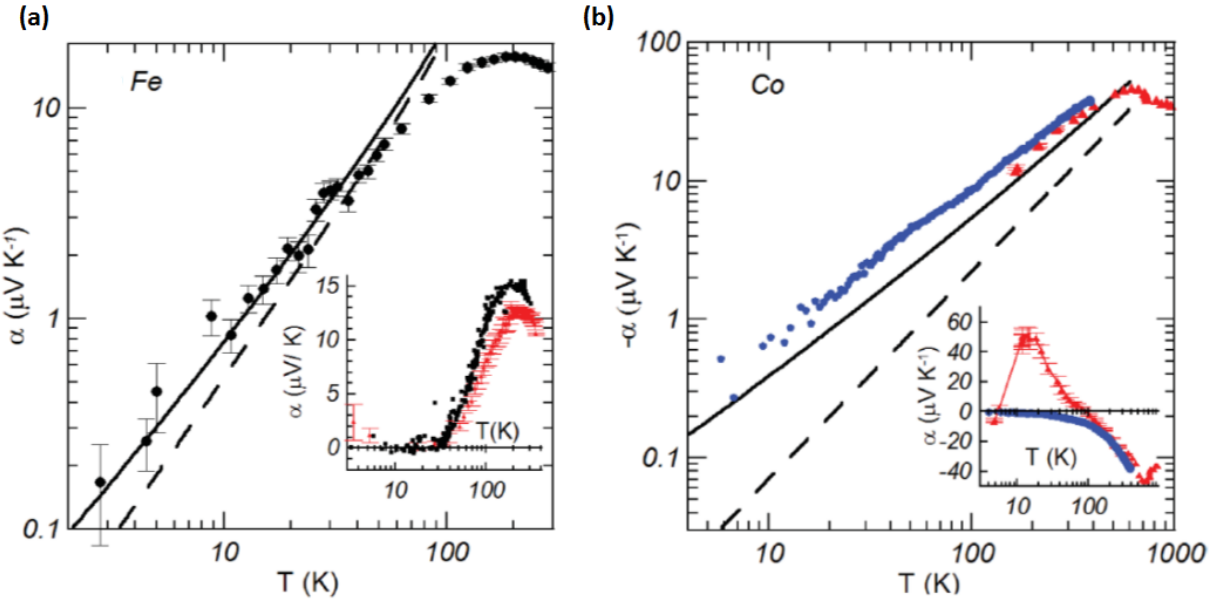

Figure 2.7: Thermopower vs temperature in log-log scale. The measured data are shown as closed circles an triangles, magnon-drag thermopower from model calculation is shown as dashed line and theoretically calculated total thermopower is shown as solid line in (a) single crystal Fe (black) and 95% sintered polycrystalline Fe (red). The inset shows the same result in linear scale. (b) polycrystalline Co ingot (red) and porous sample (blue). Source [138]

2.4.8 Thermoelectric figure of merit

The so called thermoelectric figure of merit of a material quantifies its power generation and cooling capabilities [32, 35–37]. This quantity is calculated from the expression

$$ZT = \frac{S^2 T}{\rho \kappa} = \frac{S^2 \sigma T}{\kappa}, \tag{2.47}$$

where S, ρ, σ and κ bear the regular meanings, i.e., they stand for thermopower, electrical resistivity, electrical conductivity and thermal conductivity respectively. ZT is dimensionless and is usually calculated for temperatures higher than room temperature since that would imply to be the operational temperature of such devices. Higher the ZT, higher the efficiency of the material. Thus materials which can potentially exhibit high thermopower, high electrical conductivity and lower thermal conductivity are the focus of research in many groups. But as we have discussed the transport coefficients in detail already, these coefficients are not independent of each other, therefore manufacturing such materials possesses great challenges. Usually $ZT > 3$ is considered ideal and ≥ 1 is achievable with thermoelectric high band gap or nano-structured materials at high temperatures. The examples are bismuth chalcogenids [140], lead telluride [141–143], silicides [144], skutterudites [145] etc.

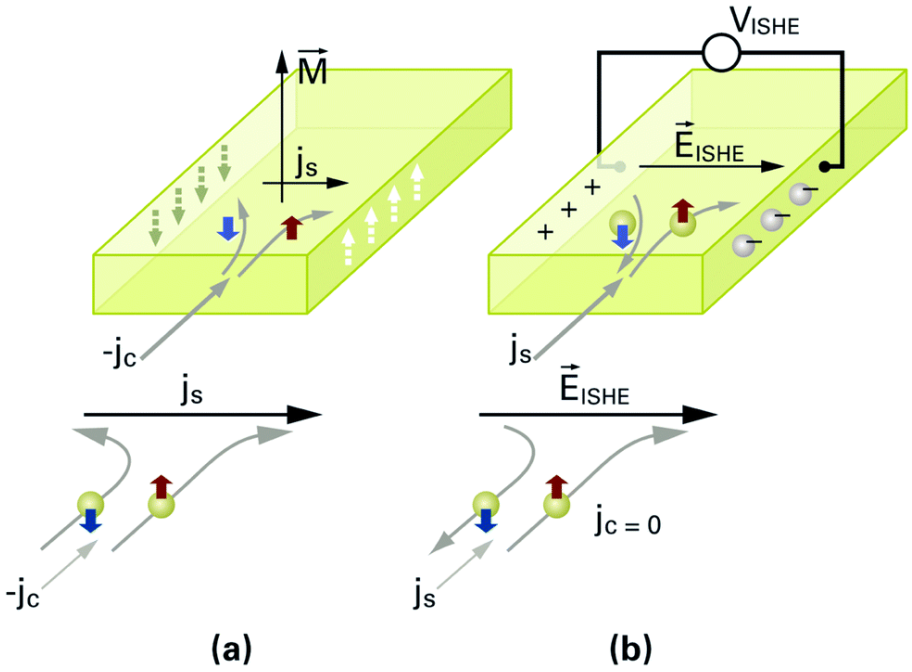

Figure 2.8: (a) Spin Hall effect (b) inverse spin Hall effect [26].

2.5 Transport properties involving magnetization in metals

2.5.1 Spin Hall effect and inverse spin Hall effect

In a normal conductor, in the presence of an out of the plane magnetic field, an in-plane flow of electric charge gets deflected owing to the Lorenz force. This is the well known Hall effect discovered by E. Hall in 1897 [146]. In the absence of such a magnetic field inside a paramagnet, the electron spins constituting the charge current deflect in opposite directions due to spin-orbit interactions. This effect is called the spin Hall effect (SHE) [147–153], the term coined by Hirsch in 1999 [151]. As shown in the illustration in Fig. 2.8, electrons with spin in the upward direction accumulate at one edge of the film and the spin down electrons accumulate at the other edge thus creating a pure spin current perpendicular to the direction of applied charge current. Now if this applied charge current is unpolarized then equal number of spin up and spin down electrons accumulate at the opposite edges of the film and the electrical detection of the pure spin current becomes impossible. To solve this issue polarized current is passed through the magnetic film. This current then creates a charge imbalance which is electrically detectable. Although SHE was proposed in the 70s' [148, 149] it was not until 2006 that the effect was actually successfully observed [150]. As origin of SHE, both extrinsic and intrinsic mechanisms have been proposed. Extrinsic mechanisms involve spin orbit mediated scattering such as skew scattering (deflection of the trajectory of the electron at the scattering event) [123] and side jump scattering (displacement of the trajectory at the scattering event) [154] whereas intrinsic mechanism originates from topological band structure. However, the actual mechanism governing the SHE is still under debate.

The reverse effect of SHE namely the generation of charge current (J_c) by application of pure spin current (J_s) has also been observed [155] and is called the inverse spin Hall effect (ISHE). The ISHE generates charge current which is spin polarized with polarized vector σ. The charge current can be expressed as

$$J_c = D_{ISHE} J_s \times \sigma, \tag{2.48}$$

where D_{ISHE} is the inverse spin Hall coefficient of the specific material.

2.5.2 Anisotropic magneto resistance, (anisotropic) Magneto thermoelectric power

Unlike non-magnetic metals, the electrical and thermal transport in a ferromagnet is spin dependent. As a simple example, the electrical resistance in a non-magnetic metal increases with increasing magnetic field ($\vec{B}$) and the transverse magnetoresistance is larger than the longitudinal magnetoresistance [156, 157]. While in case of a ferromagnet additionally the resistance is anisotropic with respect to the direction of the magnetization and current. This is known as the anisotropic magneto resistance (AMR) effect [158]. The origin of this effect lies in the spin orbit coupling [159, 160] and opposite to the case of non-magnetic metals, the longitudinal magneto resistance is larger than the transverse magnetoresistance. This is understood in terms of the scattering cross section encountered by the electrons for different orientation of the magnetization [158]. We explain the magnetoresistance effect in some detail here.

The electric field in a ferromagnet according to Ohm's law is given by the following expression

$$E_i = \sum_j \rho_{ij} J_j. \tag{2.49}$$

The resistivity tensor for a material with magnetization in the Z direction but otherwise isotropic in the plane takes the form

$$[\rho_{ij}] = \begin{bmatrix} \rho_\perp & -\rho_H & 0 \\ \rho_H & \rho_\perp & 0 \\ 0 & 0 & \rho_\parallel \end{bmatrix}, \tag{2.50}$$

where $\rho_\parallel$ and $\rho_\perp$ are the longitudinal and transverse resistivities respectively and ρ_H is the extraordinary Hall resistivity otherwise known as the anomalous Hall resistivity from anomalous Hall effect [161]. $\rho_{12} = -\rho_{21} = \rho_H$ is due to microscopic time invariant symmetry associated with spin-rotational symmetry also confirmed by Onsager reciprocal relations. The electric field can then be expanded as

$$\vec{E} = \rho_\perp \vec{J} + [\rho_\parallel - \rho_\perp][\vec{m} \cdot \vec{J}]\vec{m} + \rho_H \vec{m} \times \vec{J}. \tag{2.51}$$

The first term is known as the Lorenz magnetoresistance, the next term is the anisotroic magnetoresistance effect which also includes the planar Hall effect and the final term is nothing but the extraordinary Hall effect. The anisotropic magnetoresistance itself is defined as the term $\rho_\parallel - \rho_\perp$ but in order to compare different materials

the dimensionless AMR ratio as follows is more useful, i.e.,

$$\frac{\Delta\rho}{\rho} = \frac{\rho_{\parallel} - \rho_{\perp}}{\rho_0} = \frac{\rho_{\parallel} - \rho_{\perp}}{\frac{\rho_{\parallel}}{3} + \frac{2\rho_{\perp}}{3}}. \tag{2.52}$$

Among the various studied features, one of the characteristic of AMR is its angular dependence, i.e.,

$$\rho = \rho_0 + \rho_{\text{aniso}} \cos^2\theta, \tag{2.53}$$

where quite obviously θ stands for the angle between the current and magnetization directions.
In such an isotropic material the transport coefficients obey the Onsager relations and are written as

$$\begin{pmatrix} \vec{J}_{\text{e}} \\ \vec{J}_{\text{Q}} \end{pmatrix} = \begin{pmatrix} -\frac{\hat{\sigma}}{q} & -\hat{\sigma}\hat{S} \\ -\hat{\lambda} & -\hat{\Pi} \end{pmatrix} \begin{pmatrix} \vec{\nabla}\mu \\ \vec{\nabla}T \end{pmatrix}, \tag{2.54}$$

where $\hat{\lambda}$ and $\hat{\sigma}$ stand for the heat and the charge conductivity tensors respectively. $\hat{S}$ and $\hat{\pi}$ are respectively the Seebeck and the Peltier tensors where the Peltier tensor can be put in terms of other transport coefficient tensors as $\hat{\pi} = -T\hat{\sigma}\hat{S}$. In a polycrystal the electric field due to the heat current follow Ohm's law in a similar fashion as the field due to the charge current, i.e.,

$$E_{\text{i}} = \sum_j S_{\text{ij}} \nabla T_{\text{j}}. \tag{2.55}$$

The Seebeck tensor S is represented as follows

$$S_{\text{ij}} = \begin{pmatrix} S_{\perp} & S_{\text{N}} & 0 \\ -S_{\text{N}} & S_{\perp} & 0 \\ 0 & 0 & S_{\parallel} \end{pmatrix}, \tag{2.56}$$

where $S_{\parallel}$ and $S_{\perp}$ are the isothermal thermopowers in the parallel and perpendicular geometries and S_{N} is the Nernst coefficient. The total electric field can then be written in an analogous form as in case of equation (2.51),

$$\vec{E} = S_{\perp}\vec{\nabla}T + (S_{\parallel} - S_{\perp})(\hat{m}\cdot\vec{\nabla}T)\cdot\hat{m} + S_{\text{n}}\vec{m}\times\vec{\nabla}T. \tag{2.57}$$

We have seen already that the AMR effect exhibits an angular dependence of $\cos^2\theta$ with respect to the direction of charge current and magnetization. Similarly the electric fields arising due to the temperature gradient in an isotropic film also yields several angular dependencies. Here we begin with laying out a very general scenario where magnetization which we will consider as an unit vector in polar coordinates and temperature gradient having components in all three dimensions, are written as below

$$\hat{m} = \sin\theta\cos\phi\hat{x} + \sin\theta\sin\phi\hat{y} + \cos\theta\hat{z}, \tag{2.58}$$

$$\vec{J} = J_{\text{x}}\hat{x} + J_{\text{y}}\hat{y} + J_{\text{z}}\hat{z}. \tag{2.59}$$

Inserting the vectors $\hat{m}$ and $\vec{J}$ in equation (2.57), the generalized electric fields in three dimensions is written in the matrix form as below

$$\begin{pmatrix} E_x \\ E_y \\ E_z \end{pmatrix} = (S_\parallel - S_\perp) \begin{pmatrix} \sin^2\theta\cos^2\phi & -\sin^2\theta\sin\phi\cos\phi & -\sin\theta\cos\theta\cos\phi \\ -\sin^2\theta\sin\phi\cos\phi & \sin^2\theta\sin^2\phi & \sin\theta\cos\theta\sin\phi \\ -\sin\theta\cos\theta\cos\phi & \sin\theta\cos\theta\sin\phi & \cos^2\theta \end{pmatrix} \begin{pmatrix} \nabla T_x \\ \nabla T_y \\ \nabla T_z \end{pmatrix} + \tag{2.60}$$

$$\begin{pmatrix} S_\perp & -S_N\cos\theta & S_N\sin\theta\sin\phi \\ S_N\cos\theta & S_\perp & -S_N\sin\theta\cos\phi \\ -S_N\sin\theta\sin\phi & S_N\sin\theta\cos\phi & S_\perp \end{pmatrix} \begin{pmatrix} \nabla T_x \\ \nabla T_y \\ \nabla T_z \end{pmatrix}. \tag{2.61}$$

For a special situation of magnetization lying in the plane of the film, i.e., $m_z = 0$ and vanishing Nernst coefficient $S_N = 0$, the electric field can now be written as

$$\begin{pmatrix} E_x \\ E_y \\ E_z \end{pmatrix} = (S_\parallel - S_\perp) \begin{pmatrix} \cos^2\phi & \sin\phi\cos\phi & 0 \\ \sin\phi\cos\phi & \sin^2\phi & 0 \\ 0 & 0 & 0 \end{pmatrix} \begin{pmatrix} \nabla T_x \\ \nabla T_y \\ \nabla T_z \end{pmatrix} + S_\perp \mathbb{I} \begin{pmatrix} \nabla T_x \\ \nabla T_y \\ \nabla T_z \end{pmatrix}. \tag{2.62}$$

This matrix which contains the spin dependent as well as independent transport coefficients in the convenient matrix form, can be referred to, to calculate the effects of a single or a combination of external fields rendered on a film. This knowledge comes to our aid in our study on metallic $Ni_{80}Fe_{20}$ film with applied magnetic field in search for spin Seebeck effect where such effects are competing.

2.5.3 Anisotropic magneto-thermopower or Planar Nernst effect

The first Nernst-Ettinghausen effect or simply the Nernst effect is one of the classical effects observed in magnetic films owing to the spin dynamics. When an external magnetic field (B_z) and temperature gradient ∇T_x each normal to the other are present on a metallic or semiconducting magnetic film, then it is observed that an electric field E_y is generated in a direction perpendicular to both the B_z and ∇T_x. i.e

$$\mathbf{E}_y = \frac{|N|}{B_z}\frac{dT}{dx}, \tag{2.63}$$

where N represents the Nernst coefficient of the magnetic material.

However, in 1961 in the study by Ky *et al*. [48] in $Ni_{80}Fe_{20}$ films, in the presence of magnetization and temperature gradient in the plane of the film, an effect was detected in the plane but transverse to both the magnetization and temperature gradient direction. This effect was called the planar Nernst effect (PNE) due to its geometrical analogy with the planar Hall effect. In addition, planar Nernst effect is also the thermal analog of anisotropic magneto-resistance and is otherwise known as the transverse anisotropic magneto thermopower

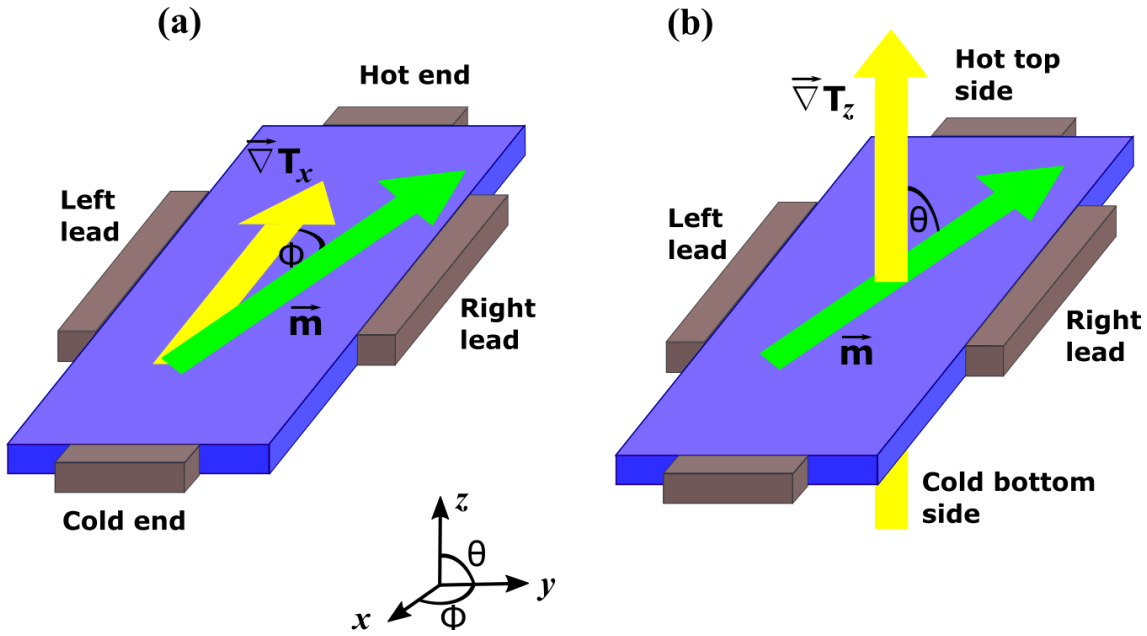

Figure 2.9: (a) Planar Nernst effect geometry, both $\vec{m}$ and $\nabla\vec{T}_x$ on the plane of the film. (b) Anomalous Nernst effect geometry. $\vec{m}$ on the plane of the film but $\nabla\vec{T}_z$ is out of the plane. Figure source [25]

(AMTEP). This comes as no surprise as the two effects bear the same microscopic origin involving anisotropic scattering rate. Since then this effect remained quite unexplored until 2006 when the group of J. Shi did experiments on the semiconducting GaMnAs films [41] and observed the same angular dependence of the planar Nernst effect on the angle between $\vec{m}$ and ∇T, as observed by Ky *et al*. [48] in $Ni_{80}Fe_{20}$ film. An additional observation emerged that the PNE is independent of the strength of the applied magnetic field but depends on the magnetization in the film instead.

The transverse anisotropic magneto thermopower effect has been explained here referring to a simple schematic as shown in Fig. 2.9(a). The blue block represents a metallic or semiconducting ferromagnetic film with available charge carriers. The magnetization $\vec{m}$ (green arrow) and temperature gradient $\nabla\vec{T}_x$ (yellow arrow) lie in the plane of the film and make an angle of ϕ with each other. Due to the anisotropic scattering of the charge carriers, a voltage is developed when measured between the left and right side of the film which is called the transverse signal E_y. According to equation (2.63) this transverse voltage is given by

$$\mathbf{E}_y = J_y \sin\phi\cos\phi(S_\parallel - S_\perp), \tag{2.64}$$

where $S_\parallel$ and $S_\perp$ are the longitudinal and the transverse thermopowers respectively. Worth noticing is the angular dependence of the planar Nernst effect which is given by

$$\mathbf{E}_{PNE} \propto \sin 2\phi. \tag{2.65}$$

This angular dependence between the direction of in-plane magnetization and temperature gradient is unique to

planar Nernst effect and is distinguishable among such thermo-magnetic effects.

2.5.4 Anomalous Nernst effect

We have already encountered Nernst effects which are named so due to their analogy to various Hall effects. In case of the Hall effects the dynamics exist between magnetization and electrical current. Whereas in case of Nernst effects, the dynamics is between magnetization and thermal currents. There exists a thermal analogy to anomalous Hall effect and this is called the anomalous Nernst effect. The anomalous Nernst effect can be explained referring to Fig. 2.9(b). The magnetization $\hat{m}$ has been maintained in the plane of the film but the $\vec{\nabla T}$ instead of being in the plane of the film, now lies in the out of the plane direction (∇T_z). The anomalous Nernst effect generates an electric field between the left and right edges of the magnetic film. The anomalous Nernst signal thus detectable is given by

$$\vec{\mathbf{E}}_{\mathrm{ANE}} = -\alpha_{\mathrm{ANE}} \hat{m} \times \vec{\nabla} T_z \tag{2.66}$$

where α_{ANE} is the anomalous Nernst coefficient of the magnetic material. Looking back to equation 2.63, it is seen that the anomalous Nernst effect signal has a $\cos\phi$ dependence between the magnetization and temperature gradient where ϕ is the angle the in plane $\hat{m}$ makes with the X-axis.

These angular dependencies are crucial while working with thin films deposited on bulk substrates. Usually the thickness of the bulk substrates are at least 3 orders of magnitude larger than the thin films in which case even though temperature gradient is intended to lie in the plane of the thin film, there always arises an out of the plane temperature gradient component. Depending on the anomalous Nernst coefficient of the material the contribution from the anomalous Nernst effect could be big enough to act as a competing effect to other thermo-electric effects arising due to an in-plane temperature gradient. Then arises the question of how to distinguish between the two effects, the ones generated due to an intended in-plane temperature gradient and an undesirable parasitic effect due to a non-negligible out of the plane temperature gradient. The simplest way the distinction is recognized is via the angular dependencies of the effects. In a metallic ferromagnetic film, the planar Nernst effect and anomalous Nernst effect can be separated with the prior knowledge that the planar Nernst effect has a $\cos 2\phi$ relation while the later has a $\cos\phi$ dependency, ϕ being the angle between temperature gradient and magnetization lying on the plane of the magnetic film.

2.5.5 Spin Seebeck effect

The spin Seebeck effect (SSE) is a relatively new effect. It is proposed that the spin Seebeck effect generates spin imbalance in a single magnetic material in the presence of an in-plane magnetization (using external magnetic field) and an out of the plane temperature gradient. This spin imbalance generates spin accumulation at the end of such a film. The flow of such pure spin current can be detected by attaching strips of noble metal with high spin orbit angle such as Pt where owing to the inverse spin Hall effect the pure spin current is converted to electronically observable charge current according to equation 2.49. This novel technique of generating pure spin current using heat lost in nano-systems can help to push the size limit further towards the desired dimen-

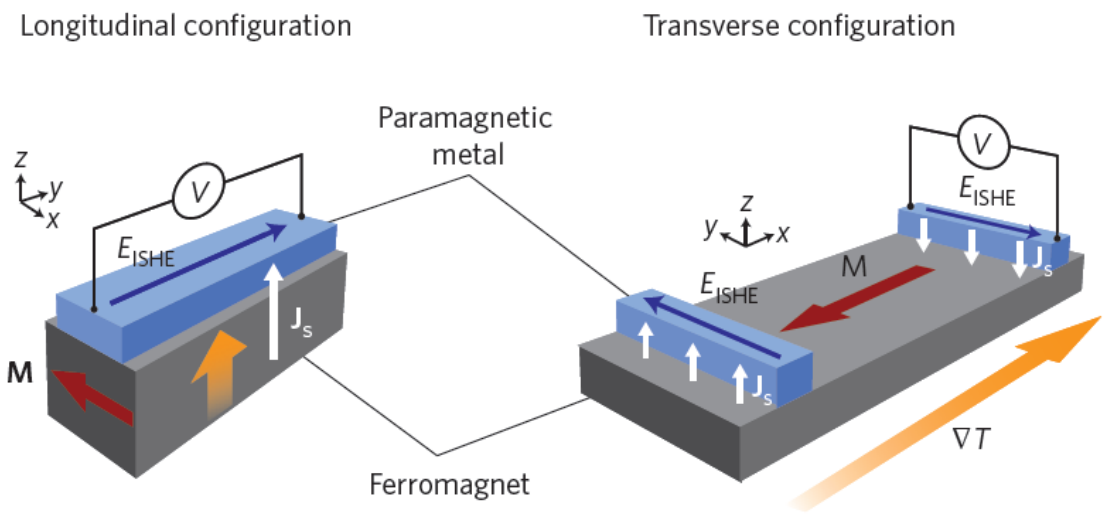

Figure 2.10: Measurement geometry for longitudinal spin Seebeck effect and proposed transverse spin Seebeck effect. Source [25].

sions. One of the proposed application of SSE is the spin thermoelectric (STE) coating which by the dint of the SSE will be capable of converting spurious heat looses into electric energy and promises advantages in terms of application due to convenient scaling capability and simple fabrication methods involved. Another proposed application is to use spin Seebeck effect to build thermopower conversion devices.

Originally the spin Seebeck effect was reported in two different geometries, transverse and longitudinal. The distinguishing feature lied in the geometry and the way the magnetization and temperature gradient are positioned with respect to each other. When the ∇T lied in the plane of the film as in Fig. 2.10(a) then the effect was called the transverse spin Seebeck effect (TSSE) and on the other hand if the ∇T was directed out of the plane as shown in Fig. 2.10(b), then the corresponding effect was called the longitudinal spin Seebeck effect (LSSE) all the while keeping the magnetization in the plane of such a film. The transverse spin Seebeck effect has been claimed to have been observed in metallic films of Py, Ni, Fe, Co2MnSi and semiconducting films of GaMnAs while the longitudinal spin Seebeck effect has been observed in insulators like YIG on GGG substrates.

Since the first part of our study largely involves the search for the transverse spin Seebeck effect, a mention of the earlier evolution of this effect is included here. The first report on TSSE by Uchida *et al*. [38] was made on Py deposited on sapphire substrate with two Pt strips. The transverse Seebeck signal was reported as

$$V \approx \frac{\theta_{\mathrm{Pt}} \eta_{\mathrm{Py-Pt}} L_{\mathrm{Pt}} S_{\mathrm{S}} \Delta T}{2 d_{\mathrm{Pt}}}, \tag{2.67}$$

where θ_{Pt} is the spin Hall angle of Pt, $\eta_{\mathrm{Py-Pt}} L_{\mathrm{Pt}}$ is the spin injection efficiency at the interface, L_{Pt} and d_{Pt} are the length and thickness of the Pt strip respectively, S_{S} is the spin Seebeck coefficient of Py and finally ΔT is the temperature difference between the ends of the Py film. This experiment [38] described a few distinct features unique to the transverse spin Seebeck effect which had been used later by several other groups to recognize this

effect in their measurements. The Seebeck coefficient had been observed to change sign with the change of the direction of ∇T. Next the transverse voltage varied linearly with the applied ∇T and finally the Seebeck signal had a $\cos\phi$ dependency where ϕ represents the angle between the in-plane magnetization and temperature gradient ∇T.

Immediately after, a number of research groups reported the observation of TSSE. In the experiment by Jaworski *et al*. [45] the TSSE was reported on semiconductor GaMnAs on GaAs substrate with the recognizable features typical to TSSE. The role played by the phonons in the substrate was discussed. Another study by Uchida *et al*. [44] reported the transverse spin Seebeck effect in Ni and Fe as well. Bosu *et al*. [39] also reported TSSE on Heusler material Co2MnSi. But most of these reports were published from the same research group of E. Saitoh and co-authors and were not reproduced in other groups. We stop the discussion on the history of TSSE here and the current state of the art on TSSE is described in more detail in Chapter 4.

On the other hand, the longitudinal spin Seebeck effect effect is more popular among the researchers as far as the agreement among the various groups go. This effect is measured on insulating magnetic material in the presence of in-plane magnetization and out of the plane temperature gradient. Unlike the case with the metals, the absence of electronic charge carriers prevent the generation of spurious effects affecting the detection of transverse spin Seebeck effect. The longitudinal spin Seebeck effect has been detected in ferromagnetic, ferrimagnetic as well as anti-ferromagnetic materials. The examples of such materials are YIG (Yttrium iron garnet $Y_3Fe_5O_{12}$) [15, 18, 19, 88, 155], various garnets such as $Y_{3-x}R_xFe_{5-y}M_yO_{12}$ (R = Gd, Ca; M=Al, Mn, V, Ir, Zr) [23], $NiFe_2O_4$ [22], Mn-Zn ferrites [(Mn, Zn) Fe_2O_4] [23], Bi doped YIG [21] and so on. Moreover the origin of this effect is now well established to be magnonic currents due to temperature gradient.

Chapter 3

TSSE Sample preparation, measurement set-ups and methods

3.1 Introduction

In this chapter, the device preparation and measurement scheme for TSSE samples are described. All the magneto-thermoelectric effects are measured on 20 nm thick $Ni_{80}Fe_{20}$ films deposited on 100 nm thin SiN_x membranes. These membranes are manufactured by Silson Ltd. The advantage of using suspended membrane substrate over bulk substrate for the study transverse magneto-thermoelectric effects is described in the introduction section in Chapter 2. The details of the micro-structuring and how it is different from the bulk sample preparation and measurement is explained.

3.1.1 TSSE Py/Pt bi-layer sample

At the beginning of this work, the origin and the existence of TSSE was under dispute. Several research groups had failed to reproduce the results published in the first report on TSSE by Uchida *et al*. [38]. Our task was to verify whether TSSE existed and whether phonons in the substrate had any roles to play. For the sake of consistency, our sample design follows the basic structure used in the literature. Here we provide a short overview of the sample design by various published authors so that the fabrication steps of our TSSE sample are better comprehended.

For the observation of the proposed TSSE, a metallic ferromagnetic film is prepared on an insulating substrate. The most literature work on the TSSE has been performed on bulk substrates such as sapphire [38], Si/SiO_2 [41], GaAs [45], GGG [13, 15] or $NiFe_2O_4$ [15, 22]. At one end or at both ends of this ferromagnetic film, Pt strips of thickness 10 nm or less are deposited. The Pt strip is used to convert spin current into detectable charge current via inverse spin Hall effect. On such bulk substrate samples, an in-plane temperature gradient is produced by using external means, i.e., either by using a heater wire wound around the region where one end

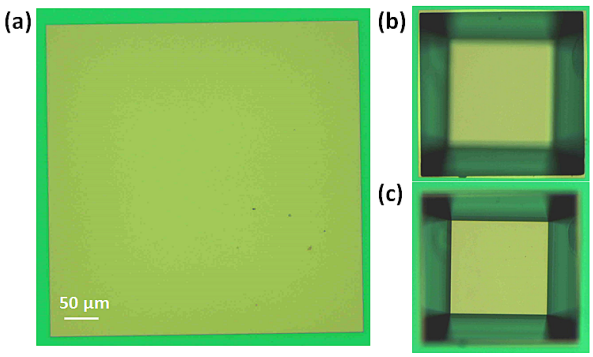

Figure 3.1: (a) Optical image of membrane top side. The membrane area 500 μm $\times$500 μm. (b) and (c) images from the bottom, focusing the Si substrate first and then the back side of the membrane.

of the sample is located or mounting the sample on a Peltier element. On the other hand, in the experimental study by Avery *et al*. [162], 500 nm thick SiN_x membrane has been used as a substrate and patterned heater wire design was implemented. Once temperature gradient is produced on the plane of the film, it is proposed that it will generate accumulation of spins at the ends of such film, i.e., electrons with spin in the upward direction gather at one end and the spin down electrons occupy the other end of the film. These spin accumulation will later diffuse into the Pt strip. This pure spin current is detected by the attached Pt strips, Pt with its high spin orbit angle facilitates conversion of pure spin current to charge current via inverse spin Hall effect. Instead of measuring this charge current, the voltage is measured using a DC voltmeter, a nanovoltmeter in most cases, at both ends of each Pt strip and hence it is called the transverse voltage. Our SiN_x membrane sample design basically follows the above description. The steps for sample fabrication on SiN_x membrane are described next.

The chips used in our experiment are manufactured in the form of a frame with 16 such chips in one frame and each chip having the dimension 6 mm $\times$ 6 mm. Individual chips have to be carefully cut from the frame using a diamond cutter. They are cleaned in acetone followed by iso-propanol and dried by blowing with nitrogen gas. Always care has to be taken while cleaning the chips or using the spin-coater since rough and vigorous handling can cause either immediate breakage or induce stress which breaks the central suspended membrane later in the process. Figure 3.1 gives a clearer idea about the appearance of an individual chip. Figure 3.1:(A) shows the top side of the chip which looks flat and undergoes patterning and metal deposition. Figure 3.1:(B) and (C) are of the back side of the chip, taken with the chip flipped upside down so that the suspended part of the membrane is clearly visible. Any residual resist or glue stuck at the corners on this side can also break the membrane.

Next we discuss the steps involved in device patterning. See Fig. 3.2 for the fabrication steps and Fig. 3.4 for a scanning electron microscopy image of a finished device. As a first step of lithography, a square of the dimension 500 μm $\times$ 500 μm is patterned on the central suspended membrane area via photo-lithography. We use a positive photo-resist (S1805) which is spin-coated at a speed of 4500 rpm for 30 seconds followed by soft-baking on a hot plate at 90° C for 2 minutes (Fig. 3.2(b)). In the mask-aligner, the sample is exposed under UV light for 40 seconds (Fig. 3.2(c)). The development is done in NaoH (buffered AR-300-26) and H_2O solution (in 1:3 ratio) for 43 seconds after which the exposed area on the membrane has no resist and the

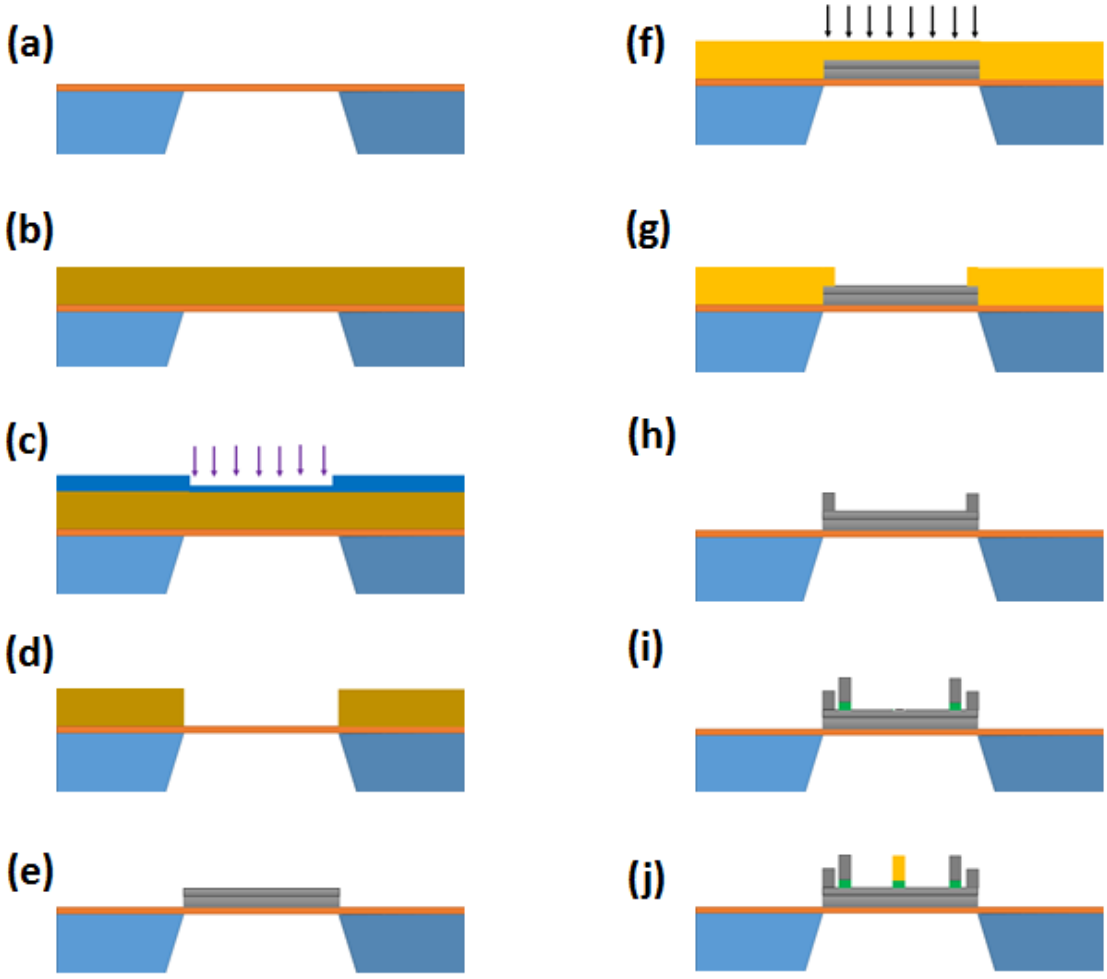

Figure 3.2: (a) Cleaned membrane chip of area 500 μm $\times$ 500 μm. (b) Optical resist coating (c) Exposure under UV light using photo mask (top blue cover)(d) After development (e) Py/Pt bi-layer deposition and lift-off. (f) E-beam resist coating and e-beam lithography (g) after development (h) after dry etching, Pt remains only on the sides as two strips. Step (e,g) are repeated to make Pt contacts to these stripes and deposit 40 nm thick Pt. (i) Repetition of step (e,g) for thermometers and deposition of 40 nm thick Al_2O_3(green) followed by 40 nm thick Pt and lift-off. (j) Repeat steps from (e) to (g) to make heater structure. Again deposit 40 nm thick Al_2O_3, 5 nm Ti, 40 nm Au(yellow) and lift off.

rest of the surface on the chip is covered with the photo-resist (Fig. 3.2(d)). Next we deposit Py/Pt bi-layer in a sputter deposition chamber. The deposition of both the layers takes place in-situ, i.e., one deposition after the other without breaking the vacuum. The 20 nm Py film is sputtered first and then the 10 nm Pt film (Fig. 3.4:B). This technique of depositing the two films together ensures good interface between the films for spin pumping purposes. This is unlike some of the other experiments one encounters in literature where Py film is deposited first and before Pt is deposited, an additional etching step is included [38, 162]. Typically, first a Py film was deposited. Py being prone to oxidation had to be cleaned via Ar^+ ion etching or RF sputtering before depositing Pt. The cleaning step affects the surface raising questions on the quality and transparency of the interface between the two films, which is crucial for spin pumping purposes [13, 163]. All the initial studies suggested that the interface was important for the observation of spin Seebeck effect. Our method ensures that both the films are deposited together without breaking the vacuum. In case of bulk substrate samples, a shadow mask was used for the deposition of Pt immediately after Py [62], in the same deposition session.

After deposition, the sample is immersed in acetone and put on a hot plate maintained at 60° C. After a waiting time of 15-30 minutes, lift-off is done carefully. The sample at this stage corresponds to Fig. 3.2(e). Next an e-beam lithography is performed to create Pt strip structures. An e-beam resist, 250 K-7% (a chlorobenzine based solution) is spin-coated on the device. This lithography step creates two rectangular strip structures of dimension 20 μm $\times$ 500 μm at either end of the Py/Pt bi-layer area. Subsequent development step leaves e-beam resist only on top of these two strips. This implies that if the sample undergoes an etching process, then the Pt shall be etched from everywhere except from the top of these two strips protected by the thick resist. The sample is mounted in a dry etcher in order to etch 10 nm Pt.

Before we proceed to the result of the etching process, a short review on the etching process is included here. Sputter etching is one of the dry etching methods where a gas is introduced inside a vacuum chamber with the sample glued onto a holder. A bias voltage generates plasma inside the chamber which physically knocks the material out of the surface. To remove Pt we have used Ar and O_2 gas which forms the plasma

$$Ar + e^- -> Ar^+ + 2e^-, \tag{3.1}$$

$$O_2 + e^- -> O_2^+ + 2e^-. \tag{3.2}$$

Etching is done for 2 minutes at a source power of 30 W, sufficient to remove 10 nm Pt from the rectangular area. After the sample is removed from the etching chamber, the remaining resist is then dissolved away with acetone followed by the usual cleaning with iso-propanol and N_2 blow drying. This produces a device which has 20 nm of Py and two 10 nm thick Pt strips at both ends as shown in Fig. 3.2(h). In some of the later designs, only one detector strip has been patterned.

In order to electrically measure transverse signal on the Pt strips, contact leads are required which are patterned in another step of e-beam lithography. These patterns are deposited with 40 nm thick Pt (Fig. 3.4:C, D). Naturally this deposition step is followed by another lift-off and cleaning process. Following which we have to pattern structures that are required to generate and sense temperature gradient on the film. In case of bulk substrates, conventionally, the sample holder inside the measurement device are so designed that a heater wire

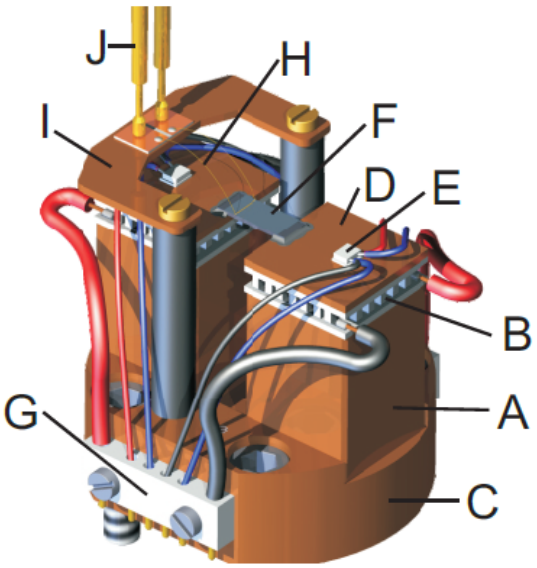

Figure 3.3: A home made copper holder (A,C) built in a shape of two pillars to support the gray rectangular sample. Two Peltier elements(B) provide temperature gradient on the film which is detected by two Pt 100 thermometers attached on top of the Peltier elements. Transverse signal is detected from the ends of the Pt strip by using gold wires (H) leading to the pogo pins (J). Source: PhD thesis by M. Schmid [62]

or Peltier element and thermocouple can be attached externally to apply and measure temperature difference between the ends of the film (see Fig. 3.3 for example [62]).

However, such global application of temperature gradient is no longer a practical approach in our case. Our small area of the Py film needs a local heater structure and on-chip patterned thermometers for the accurate determination of the actual temperature difference between the two ends. Therefore in the next e-beam lithography step, a meander heater structure is patterned at the center of the Py film with width 3 μm and total length of 3 mm. The purpose of the meander design in the heater structure ensures that a large resistive of the structure lies on the Py film. Thus a relatively small electrical current would be sufficient to generate necessary temperature gradient for our experiment. However, a metal can not be directly deposited over the Py film, as it will create an electrical short between the heater and the underlying metallic film. Therefore a 40 nm thick insulating layer of Al_2O_3 is first deposited using an atomic layer deposition (ALD) system. In an ALD system, a sample plate is maintained at a high temperature on top of which the sample is to be placed. A control software allows two different gases or so called precursors to be introduced into the chamber one after the other with prefixed time interval. In our case we have used H_2O and Trimythelynaluminum (TMA) gases. After each gas pulse is allowed into the chamber, a spike in the chamber pressure is observed. Each gas reacts with the surface and forms a monolayer, e.g., after H_2O is introduced, O+ ions form a monolayer on the sample. Next when TMA is allowed into the chamber, it undergoes a chemical reaction and forms a single atomic layer of Al_2O_3 on the sample surface. This cycle is repeated to achieve the desired thickness of uniform insulating layer on the sample, which is 40 nm in our case.

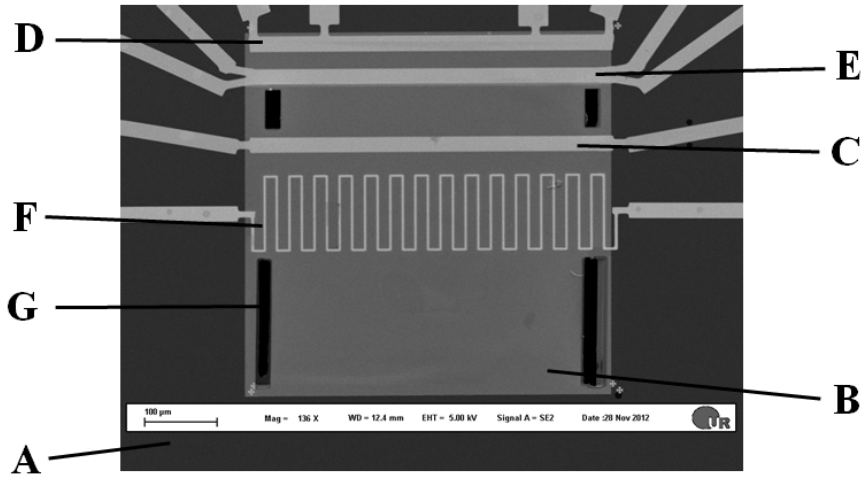

Figure 3.4: (A) represents Si chip or the heat sink, (B) the total 500 μm $\times$ 500 μm membrane with 20 nm/10 nm Py/Pt bi-layer. (C), (D) are the hot and cold end Pt strips respectively. Similarly (E) and (F) represent the thermometer and heater respectively. Finally (G) shows the trenches etched using FIB.

After Al_2O_3 has been deposited, without doing lift-off, the sample is directly transferred to a thermal evaporator where 40 nm thick gold is deposited along with 5 nm of Ti adhesion layer. After lift-off, the sample has now a gold meander heater at the center, electrically isolated from the underlying Py by insulating Al_2O_3 layer (Fig 3.4:F). Finally for the thermometer structures, two strips of width 20 μm with four leads are patterned. Again a 40 nm thick insulating layer of Al_2O_3 is first deposited in the ALD system followed by sputter deposition of 40 nm Pt (Fig. 3.4: E). This completes the patterning and deposition steps as shown in Fig. 3.2(j).

However, we are yet to complete the device fabrication process. From the look of the sample at this stage, it is clear that the heat generated at the heater structure will flow in all possible directions and most of it will be dissipated at the sink. Hence in order to prevent the heat loss, as a final step, the sample is inserted in a focused ion beam (FIB) system where trenches are cut from both left and right edges of the Py film including the underlying membrane so that the middle region is being suspended and isolated from the silicon sink sides (Fig. 3.4:G). This step not only reduces the heat loss to the silicon sink but also defines the desired direction of temperature gradient on the film, i.e., in a direction perpendicular to the length of Pt detector strips.

3.2 Characterization of Py films

The Permalloy ($Ni_{80}Fe_{20}$) used in our experiments has been deposited in the sputter chamber in the lab of Prof. C. Back. Saturation magnetization of this Py is close to the standard value of 1 T. A few examples of experiments using this particular Py can be found in the published works by Back *et al*., e.g., inverse spin Hall effect experiment in Obstbaum *et al*., [164] and AC and DC inverse spin Hall effect experiment in Dahai *et al*., [165].

A systematic ferromagnetic resonance (FMR) study was done by us on Si chip to study the spin pumping

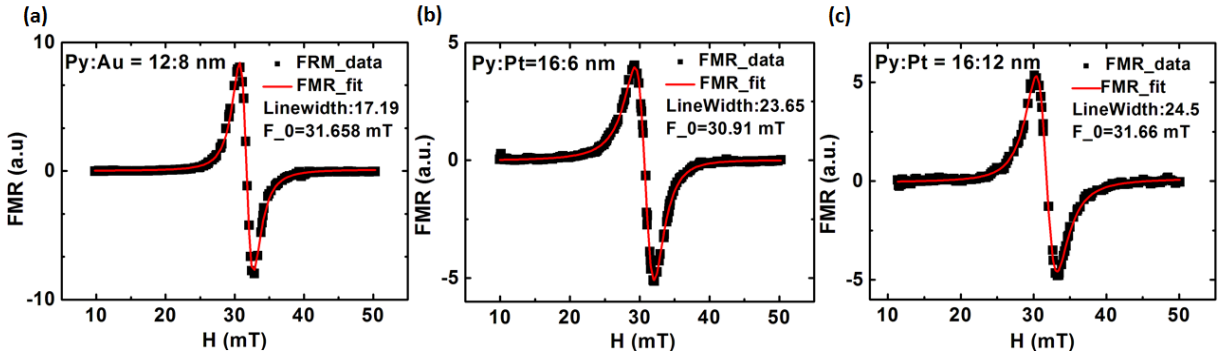

Figure 3.5: Measured ferromagnetic resonance curves vs magnetic field swept from -10 mT to 50 mT for film (a) Py 12 nm on Au 8 nm, (b) Py 16 nm on Pt 6 nm (c) Py 16 nm on Pt 12 nm.

effect in Py/Au or Py/Pt of varying thickness. Figure 3.5 shows the FMR in arbitrary units as a function of external field along the co-planar waveguide for three different samples with Py/Au=12 nm/8 nm, Py/Pt=16 nm/6 nm and Py/Pt=16 nm/12 nm. The quantity to look at is the linewidth which are 17.19 mT, 23.65 mT and 24.5 mT for the above three samples respectively. The linewidth is defined as

$$\Delta H = \frac{4\pi\alpha f^{'}}{H_{\text{eff}}\gamma}, \tag{3.3}$$

where α is the damping coefficient (as referred in Landau-Lifshitz equation [166]), $f^{'}$ is the frequency of linewidth measurement, γ is the gyromagnetic ratio and H_{eff} is the effective magnetic field. The linewidth is proportional to α and according to Landau-Lifshitz equation, the magnetization precession inside the ferromagnet causes the Gilbert damping which injects spin from ferromagnetic metal into the noble metal. Larger the linewidth larger is the spin pumping effect from Py into the top noble metal. From the figures Fig. 3.5(a)-(c), there is an indication that Pt is a better material compared to Au [152, 167–169] for the purpose of spin pumping due to the high spin Hall angle, suitable for the study of spin Seebeck effect. However, since the line width broadening is also proportional to the frequency, a frequency dependent FMR study is necessary for confirming the above conclusion. Such a frequency dependent study has not been carried out as part of this thesis work, however, the experimental work by Obstbaum *et al*. [164] can be used as a good reference for a frequency dependent FMR study on this Permalloy film.

3.2.1 TSSE measurement set-up and method

Set-up

A vacuum chamber capable of going to base pressure of $\approx 10^{-6}$ mbar and operable only at room temperature is used for the measurements performed in our experiments. The TSSE sample is mounted on a custom made 20 pin sample holder using a high temperature glue. Bonding between the pads on the chip and the pads on the sample holder is done with aluminum wire of diameter 100 μm. The sample holder is placed onto the suitable

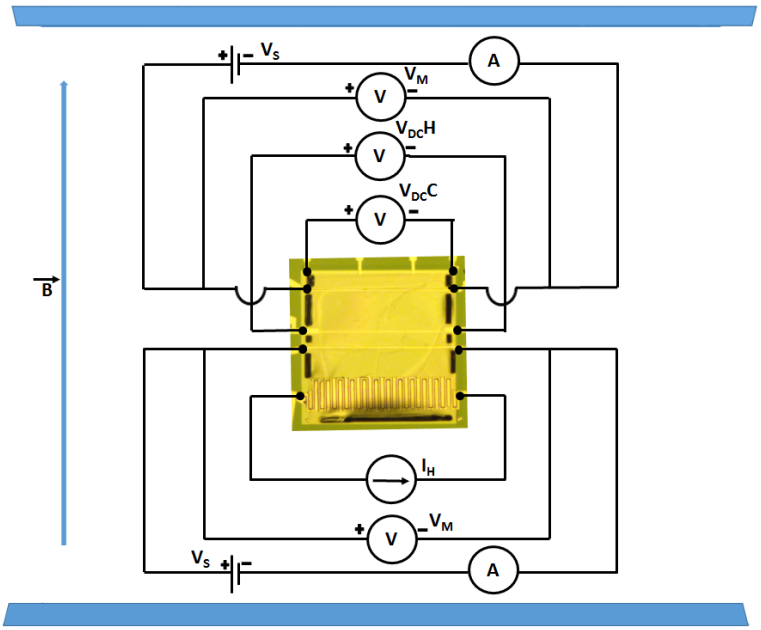

Figure 3.6: Heater current I_H is applied using an analog DC current current supplier. The transverse voltages $V_{DC}H$ and $V_{DC}C$ are measured using Agilent nanovoltmeters in the presence of in-plane magnetic field $\vec{B}$. The thermometer resistances are measured separately as explained in the text using two Keithley sourcemeters. Current I_S is applied and the corresponding voltage V_M is measured on the thermometer.

chip carrier inside the vacuum chamber. A rotatable Helmholtz coil is fixed around the chamber with the plane of the field aligned horizontally with the sample plane. The coil sits on a rotatable circular plate attached with grooves indicating angles with resolution of 0.5° which is operated manually. The wiring from the chamber go to a breakout box from where cables are connected to the current source for heater and to a nanovoltmeter for voltage signal measurement. The current source is custom built analog current source with a sensitivity of 1 μA and the nanovoltmeter is manufactured by Agilent. The wiring from the Helmholtz coil to Kepco magnet power supply are done independently.

Method

The measurement method involving instrumentation is illustrated using Fig. 3.6. In order to generate temperature gradient on the film, DC current (I_H) upto 1 mA, was applied to the heater structure using the current source. The transverse voltage (V_{DC}) was measured using nano-voltmeter. Care was taken to maintain the consistency of the polarity of the nano-voltmeter connections for different Pt strips on the sample and for all the samples. For samples where both the Pt strips were utilized simultaneously, the voltages at the hot end and the cold end were measured using both the channels of the nanovoltmeter and the transverse voltages are labeled as $V_{DC}H$ and $V_{DC}C$ respectively. The change of resistance of the thermometers was recorded using two sourcemeters. Current I_S was applied and voltage V_m was measured using the sourcemeter, which when later compared with a standard calibration done in a different chamber provided the temperature difference between the ends

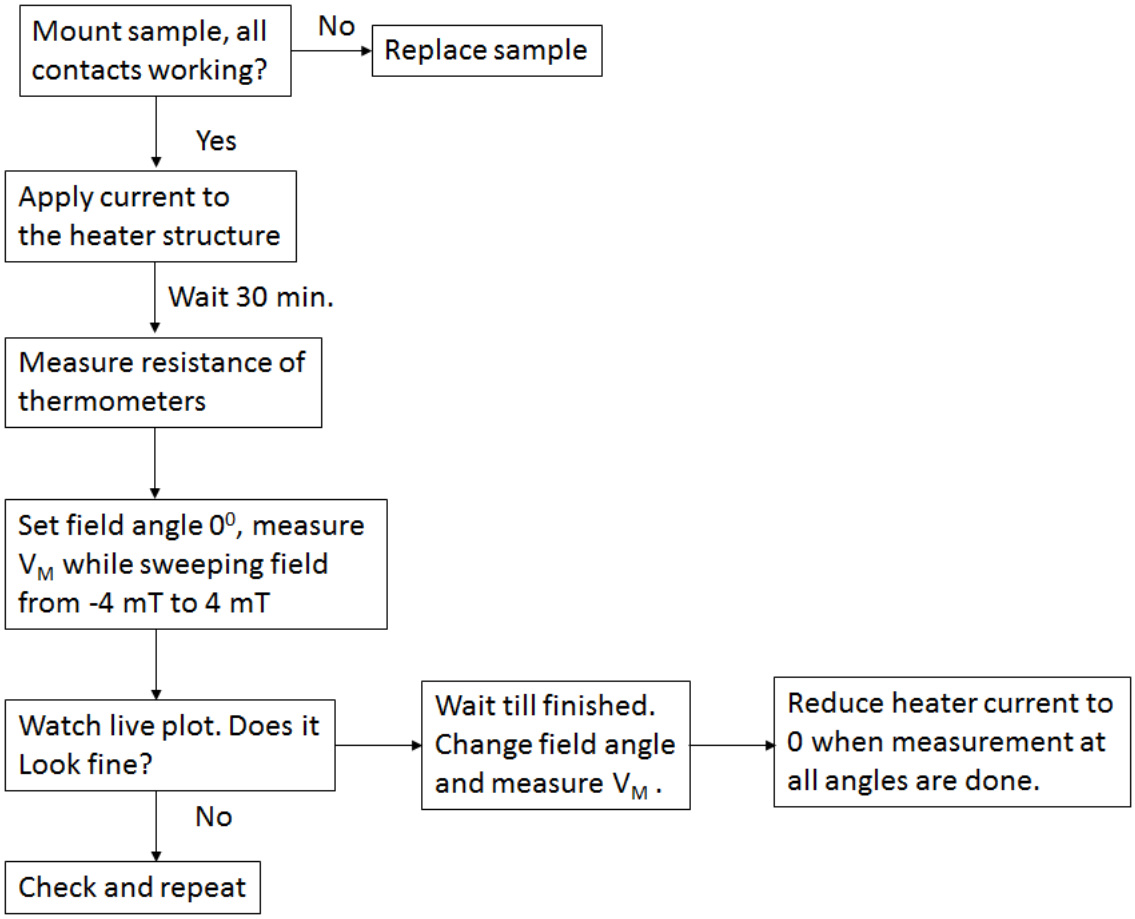

Figure 3.7: Flow diagram for the measurement of the transverse voltage.

of the sample. During the process of measurement with heater current upto 1 mA, the temperature fluctuation recorded directly from the chamber thermometer was maximum 0.5 K.

Rotating the Helmholtz coil as well as applying current to the heater structure could only be done manually. A waiting time of around half hour was given between applying the heater current and starting the measurement so as to allow sufficient time for the film to reach steady state. After the steady state was achieved, transverse signal was measured as a function of sweeping external magnetic field from -4 mT to +4 mT in steps of 0.2 mT. For a particular angle of the Helmholtz coil, 5-8 such field sweeps were done and averaged over. After finishing with one angle, the coil was rotated to the next angle and the measurement process was repeated. We had used angle intervals of 45° from 0° to 360°. The whole measurement process could take upto 30 hours to finish. Only at the end of the measurement, the heater current was reduced to 0. The sweeping of the magnetic field, doing average over several runs and the data acquisition were automated via a labview script. The flow diagram in Fig. 3.7 summarizes the measurement steps.

3.3 Summary

We have developed the SiN_x platforms for the measurement of magneto-thermoelectronic properties of Py. The sample design follows similar design as has been used for the measurement of proposed TSSE in bulk samples. With a bit of precaution, 100% yield is achievable notwithstanding the several steps of lithography. The measurement techniques are discussed in detail.

Chapter 4

Transverse thermoelectric power results on Py/Pt bi-layer

4.1 Introduction

In this chapter, we describe in detail the results on the transverse thermopower measurement and experimental results in TSSE sample. Data from another membrane sample where Pt strip has been replaced by gold point contacts are reported. The focus on the bulk sample results are limited since it is part of another thesis [62] but nevertheless the measurement values are mentioned for comparison with our membrane sample results. The primary motivation behind studying both the bulk and membrane substrate samples is to study the effect of the substrate. Unlike the membrane sample, an applied in-plane temperature gradient in a bulk substrate sample also produces an out of the plane temperature gradient. In the presence of an in-plane magnetization, several contributions are expected in the transverse thermopower which can be separated from their angular dependence. In this chapter, we analyze the data obtained and discuss the conclusions that can be drawn based on our observations. Finally, we put in context our results comparing them with studies from other groups to give an overview of the current state of the art of the spin Seebeck effect. The longitudinal spin Seebeck effect has not been discussed since it lies out of the scope of the current work.

4.2 Membrane sample

4.2.1 Results

In Fig. 4.1 the transverse voltage $V_y(\vec{H})$ measured on a Pt strip at the hot end of a membrane sample as a function of varying angles θ is shown. At each θ the external magnetic field H has been swept from -4 mT to + 4 mT in the presence of constant temperature gradient $\nabla_x T$ of around 280 K/mm. Angle 360° data is included for the sake of the completion of a sinusoidal cycle.

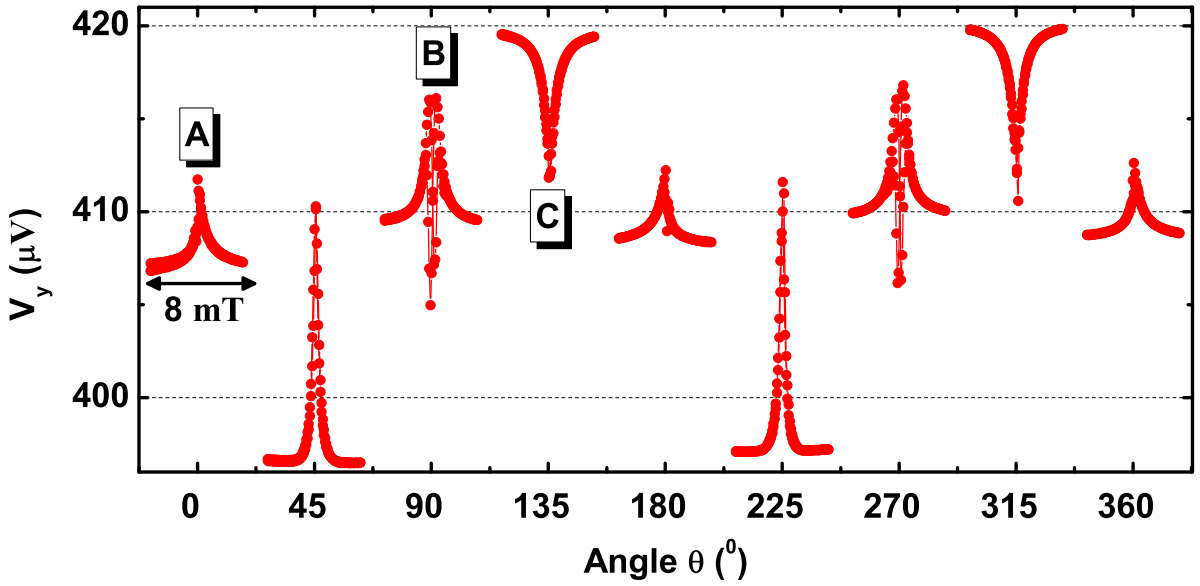

Figure 4.1: Voltage $V_y(\vec{H})$ (plotted along Y axis) vs magnetic field $\mu_0 H$ for different angles θ (on the X axis) is shown. The magnetic field is swept from left at -4 mT to right upto +4 mT for membrane sample at the hot side. See text for the description of the labels 'A', 'B' ad 'C'.

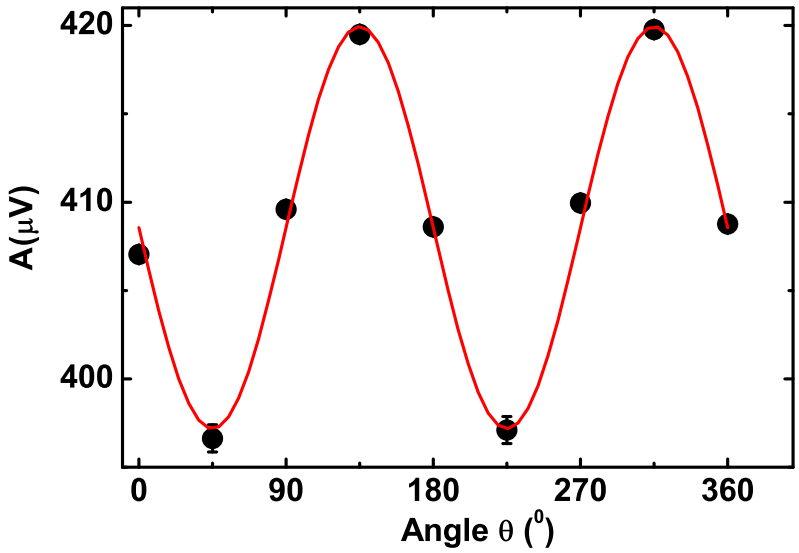

Figure 4.2: Average of left and right saturation values of $V_y(\vec{H})$ plotted Vs angle θ as black dots and the fit to the equation (4.5) is shown as the red curve. The error bars correspond to twice the standard deviation.

Next we discuss the features observed in this Fig. 4.1. We first notice the distinct feature of sharp peak or dip structures near $\mu_0 H$=0 mT. The peak structures appear for angles $\theta = 0°, 45°, 180°, 225°$ and 360° (labeled structure 'A' in Fig. 4.1) while dip structures are at angles 135° and 315° (labeled structure 'C' in Fig. 4.1). The peak heights for angles 45° and 225° are the largest. At angles 90° and 270°, prominent dip structures are sandwiched between peak structures (labeled structure 'B' in Fig. 4.1).

The next feature that one can observe is a background envelope that passes through the saturation values at each of the angles. These saturation values V^+ and V^- are calculated by

$$V^+ = \left\langle V_y\left(\mu_0 H \geq 3.6mT\right)\right\rangle, \tag{4.1}$$

$$V^- = \left\langle V_y\left(\mu_0 H \leq -3.6mT\right)\right\rangle. \tag{4.2}$$

In our experiments, the V^+ and V^- are not the same. The average of the saturation values on both sides of the hysteresis loop is called the A signal, i.e.,

$$A(\theta) = \frac{V^+ + V^-}{2}. \tag{4.3}$$

The signal A is plotted as a function of θ as shown in Fig. 4.2. The signal has what appears to be a sinusoidal form with amplitude 11.2 μV with maxima at angles $\theta = 135°$ and 315° and minima at angles 45° and 225°.

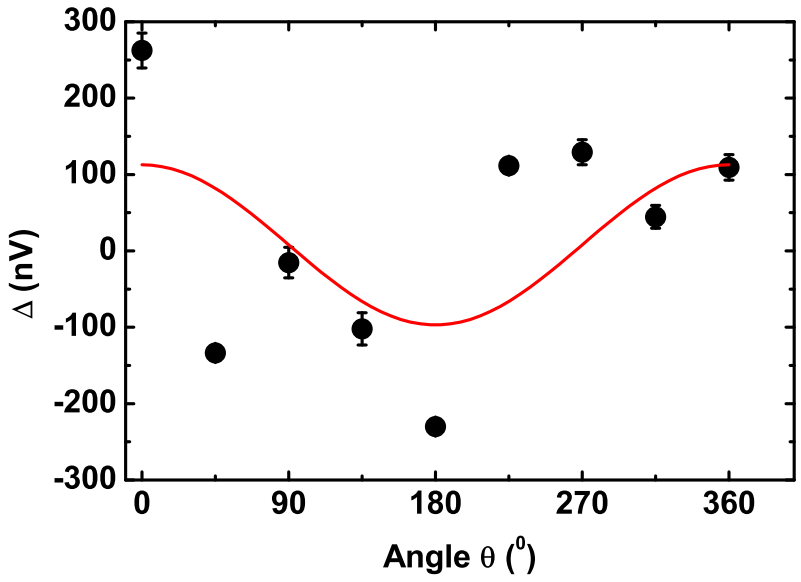

Figure 4.3: The $\Delta(\theta)$ signal is plotted Vs θ shown as black dots and the fit to the function (4.4) is the red line. The error bars correspond to twice the standard deviation of the original data.

The small asymmetry between V^- and V^+ is called the difference signal $\Delta(\theta)$, i.e.,

$$\Delta(\theta) = V^- - V^+ \propto \cos\theta, \tag{4.4}$$

In Fig. 4.3, $\Delta(\theta)$ is plotted versus angle. We observe data points lie within a scatter of the order of 200 nV around 0 value.

4.2.2 Discussion

Since the peak and the dip structures observed around $\mu_0 H = 0$ are the most prominent features, we will begin with the description of these structures in the context of changes of in-plane magnetization direction and its interplay with the temperature gradient.

The peak and dip structure can be explained in terms of AMTEP effect or PNE. The off diagonal elements of the AMTEP tensor relates the transverse electric field E_y with the local temperature gradient $\nabla_x T$. The peak and dip structures are periodic by 180° inside the background envelope which we call the AMTEP signal. From equation (2.64), it appears as the natural consequence of AMTEP that the $V_y(H)$ should vanish for angles θ=0°, 90°, 180° or 270°. The maximum amplitude should be observed at 45° and 225° and the minimum at 135° and 315°. The complex peak and dip structures appearing at θ=90° and 270° can be explained in the context of the competition between anisotropy energy and Zeeman energy. At angles θ=0° and 180° in Fig. 4.1, the

magnetization makes sharp switch instead of rotating in competition with the magnetic field, as evidenced by the small peak heights. This indicates that the direction of anisotropy in our Py films lies in the direction of θ=0° or 180°. Therefore at angle 90° (270°), during the magnetization reversal process from negative to positive saturation state, the magnetization begins to align along the direction of anisotropy θ=0° (180°) at $\mu_0 H = 0$, flips along the opposite direction θ=180° (θ=0°) and finally rotates once magnetic field is increased. In order to quantify the AMTEP contribution to the $V_y(\vec{H})$, we refer to Fig. 4.2 first. As explained in the Chapter 2, this average signal which is seen as the background envelope in Fig. 4.1 is nothing but the AMTEP signal and should follow a $\sin\theta\cos\theta$ dependence from equation (2.64), i.e.,

$$A(\theta) = 2A_0 \sin\theta\cos\theta + c, \tag{4.5}$$

where A_0 is the amplitude and c is a θ-independent constant. From the V_y plotted in Fig. 4.1, the average $A(\theta)$ is calculated at each θ angle, then fitted to the above equation (red fit line) and plotted as a function of θ as Fig. 4.2. The amplitude of the AMTEP signal from Fig. 4.2 turns out to be $A_0 = 11.2$ μV and the constant c has a value of 6.3 μV. The $V_y(\vec{H})$ has a huge offset of 406 μV which comes from the ordinary thermopower of the long cables and wiring (inside cryostat) used in the set-up but this offset does not affect our AMTEP amplitude.

Comparison of PNE signal between groups					
Group	A_0	∇T_x	t	l	C_{PNE}
V. D. Ky(1966)	1.5 μV	150 K/mm	139 nm	0.6 cm	23×10^{-14}
A. Avery *et al.*(2013)	82 nV	62.5 K/mm	20 nm	35 μm	74×10^{-14}
Our membrane (Schmid *et al.*)	11.2 μV	280 K/mm	20 nm	500 μm	16×10^{-13}
Bulk MgO substrate (Schmid *et al.*)	1.2 μV	3.6 K/mm	20 nm	8 mm	83×10^{-14}

Table 4.1: The coefficients A_0 and C_{PNE} for various groups with additional information on the geometry of sample and applied ∇T_x. Citations from top to bottom are from [48], [162] and [43].

We can compare the measured AMTEP or PNE signal with other values reported in literature including the one measured on the bulk MgO substrate as another part of the project [62]. For comparison since different groups have used different sample geometry, temperature gradient, magnetic field value and even Py material, it is not wise just to compare the AMTEP amplitudes rather a coefficient which is normalized with respect to parameters involved. So we calculate a quantity which we denote as C_{PNE} defined as,

$$C_{PNE} = \frac{A(\theta)t}{\nabla T l}, \tag{4.6}$$

where $A(\theta)$, ∇T, t and l are the AMTEP amplitude, absolute value of temperature gradient, thickness and length of the Pt strip or the width of the sample along which the transverse signal has been measured respectively. We put the result in the form of a table (table 4.1) where the unit of the coefficient C_{PNE} is V/(K/mm).

We see that the measured coefficient C_{PNE} for the membrane sample falls quite close to measured C_{PNE}

values for Py on different substrates and by various groups. The coefficient in case of our membrane sample is a bit higher, the origin of which could be the underestimation of the actual ΔT measured on the sample.
Moving on to the difference signal $\Delta(\theta)$, it is fitted to $\cos\theta$ function. Although it is not an exact fit, one can estimate an upper limit of the amplitude of the order of 50 nV. The $\cos\theta$ fit would have signified the presence of either TSSE or ANE signal since they both follow the same angular symmetry. If we discard the ANE contribution entirely on the basis that the thickness of the membrane is too small to sustain any appreciable out of the plane temperature gradient $\nabla_z T$, then we can assign an upper limit for the contribution of the TSSE to be 50 nV. This value when compared to the previously reported values of TSSE [38] is at least 2 orders of magnitude smaller. In the study by Uchida *et al*. [38], the spin Seebeck coefficient is calculated using the equation

$$S_S = \frac{2\Delta V_y d_{Pt}}{\theta_{Pt}\eta_{Pt} l_{Pt}\Delta T}, \tag{4.7}$$

where d_{Pt} and l_{Pt} are the thickness and length of the Pt strip, $\eta_{Py} = 0.2$ and $\theta_{Pt} = 0.0037$. The expected TSSE signal using this equation for the membrane sample would yield 1 μV which is clearly orders of magnitude larger than what we have observed. The $\Delta(\theta)$ signal however, is not due to random artifact. This aspect has been discussed later in this chapter.

4.2.3 Membrane sample with gold point contacts

The detection of SSE utilizes Pt strip contact on top of ferromagnetic film where the spin Seebeck current is converted to charge current via ISHE. In order to verify that the observed signal in suspended samples is purely a classical effect, i.e., intrinsic to the ferromagnetic film and to eliminate any contribution from TSSE, gold point contacts were used instead of Pt strip contacts on another membrane substrate. The two pairs of gold point contacts were positioned where the Pt strip should have been and had the same thickness of 10 nm as the Pt strip contacts had in the previous samples. The measured transverse voltage at the cold end of the Py film in the presence of $\nabla_x T$ of the same order as in the with Pt strip sample as a function of θ is shown in Fig. 4.4.

The shape of the curves at each angle θ can again be explained as the result of an interplay between the temperature gradient and the magnetization direction, influenced by the external applied field and the anisotropy present on the Py film. The difference from the earlier sample with Pt strip is that now the direction of anisotropy lies around $\theta = 135°$, or $\theta = 315°$, since at these angles, the magnetization makes small jump around $\mu_0 H$ =0 unlike the cases for other angles. The shape of the curve at $\theta = 0°$ now looks like that of at $\theta = 90°$ in the previous case and can be explained by similar logic.

It is clear from the first glance, that the transverse signal is dominated by AMTEP signal. We calculate the average of the saturation values of $V_y(\vec{H})$ which can be plotted separately.

As shown in Fig. 4.5, the amplitude of the average voltage A_0 is 44.2 μV which is 4 times larger than that of the previous case while in the presence of similar ∇T. This can be explained by the fact that the presence of a Pt strip contact partially shorts the transverse voltage which is prevented in case of gold point contacts and therefore a larger transverse voltage is detected. Pt with its high spin Hall angle facilitates conversion of spin

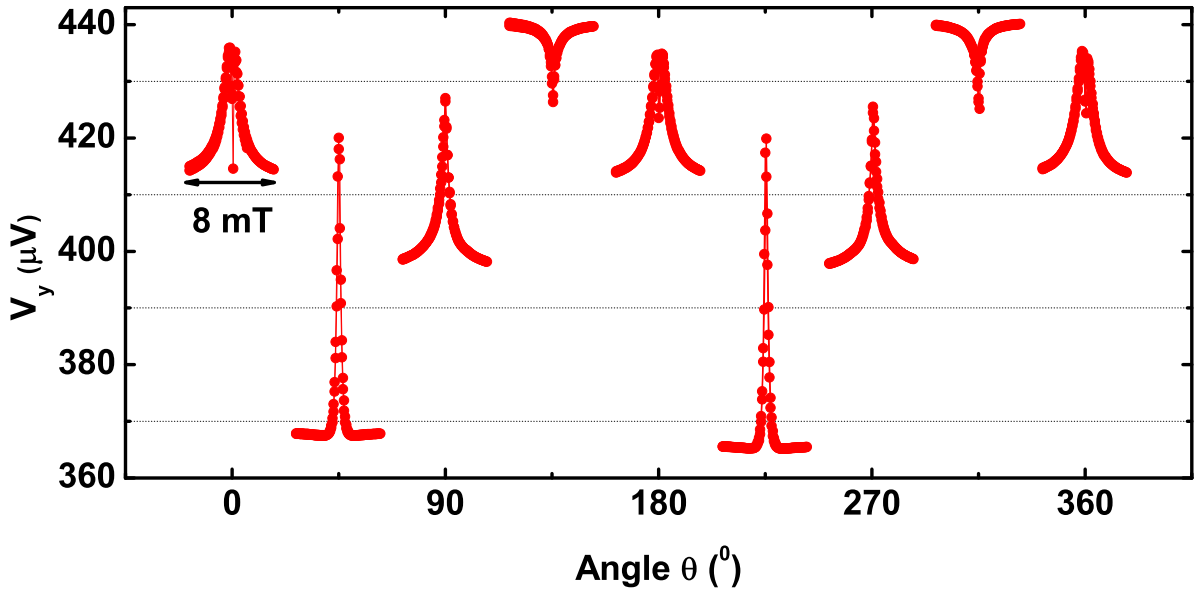

Figure 4.4: $V_y(\vec{H})$ swept from -4 mT on the left to +4 mT on the right is plotted as a function of angle θ starting at 0° at an interval of 45°.

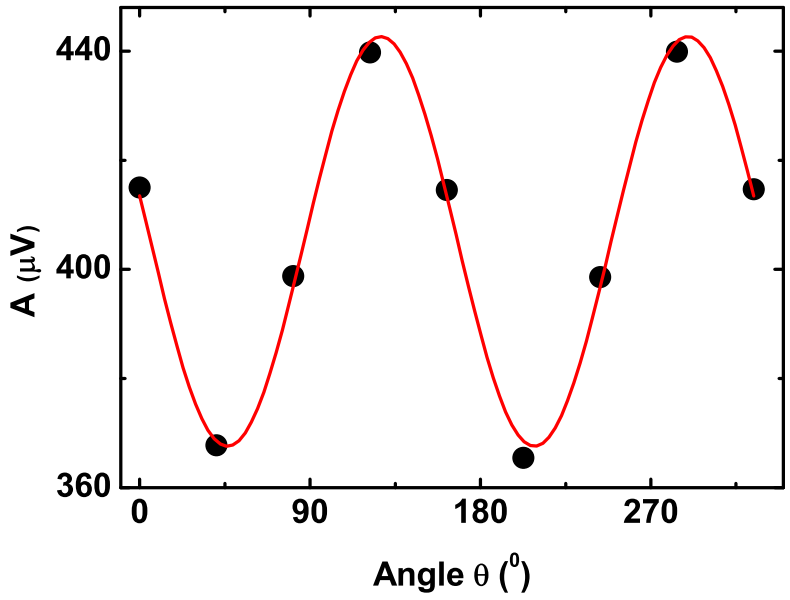

Figure 4.5: The black dots corresponds to data points collected at the average saturation values and the red curve is the fit function to the equation (4.5). The amplitude A_0 is 4 times larger than the case with Pt strip contacts.

current to measurable charge current. We have replaced Pt with Au whose spin Hall angle is at least 1 to 2 orders of magnitude smaller than Pt. The point contacts hinder the detection of TSSE. Hence we do not expect any $\Delta(\theta)$ that could be related to TSSE here. We plotted the $\Delta(\theta)$ for this sample nevertheless and tried to fit as a cosine function as shown in Fig. 4.6.

In this sample again the difference voltage $\Delta(\theta)$ shows data points scattered within 700 nV and do not exhibit a clear $\cos\theta$ relation. This verifies that the observed transverse signal is purely a classical effect which has the same origin as the anisotropic magneto resistance and has no relation with spin transport.

4.2.4 Discussion on features of asymmetry in $V_y(\vec{H})$, $\Delta(\theta)$

The difference voltage $\Delta(\theta)$ signal in both the suspended samples (one with Pt strip and other with Au point contacts) could not be fitted to $\cos(\theta)$ function. It might look featureless at first glance but it turns out that they have a consistent shape and this shape can be explained in terms of parasitic magnetic field present in the measurement set-ups. This feature has also been observed in case of the bulk samples [62] and has been worked out in detail by doing measurements in the presence of permanent magnets. The detailed study on this using MgO bulk substrate can be found in the study by Shestakov *et al*., [170].

To begin the analysis, we attempt to fit the $\Delta(\theta)$ voltage (as shown in Fig. 4.5) on SiN_x membrane is fitted

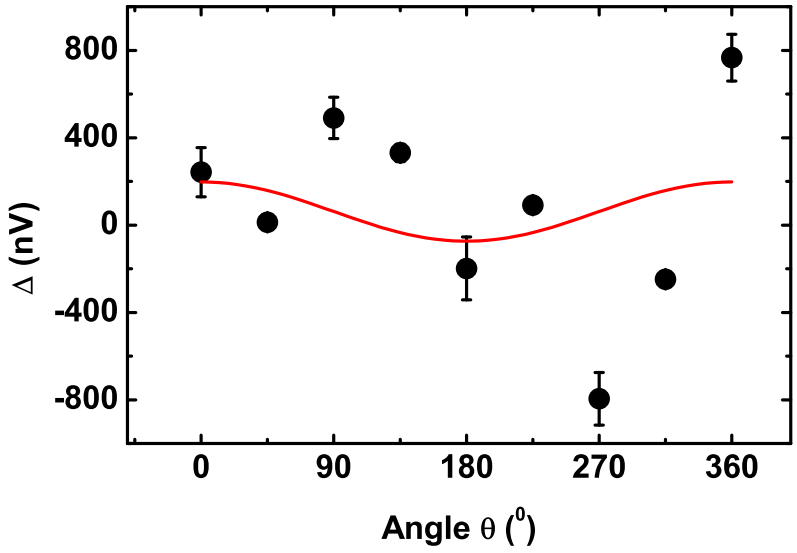

Figure 4.6: The black dots corresponds to data points collected as the difference between left and right average saturation values and the red curve is the $\cos\theta$ function according to the equation (4.4)

to a higher degree of sinusoidal function such as

$$\Delta(\theta) = D\cos\theta + F\sin(\theta+\delta 1)\cos(2\theta+\delta 2), \tag{4.8}$$

instead of with plain $\cos\theta$. This would then accommodate the effective angle between the effective magnetic field and applied temperature gradient direction with D, F, $\delta 1$ and $\delta 2$ being the fitting parameters. This fitting function works very well while fitting the observed $\Delta(H)$ signal for effective parasitic field of the values as small as 0.1 mT which is typical in the Helmholtz coil we used for our experiments.

In case of bulk MgO substrates, Shestakov *et al*., [170] carried out detailed experiment to understand the shape of the $\Delta(\theta)$. No such measurements with permanent magnets were done for the membrane samples. However, measurements were carried out at lower temperatures in a flow cryostat to have better a better understanding of this asymmetry signal observed in the membrane samples. Figure 4.7 shows the graph of $\Delta(\theta)$ vs angle, only for the membrane sample with gold point contacts, measured in a flow cryostat capable of measurement at lower temperatures. At a given value of heater current, the $\Delta(\theta)$ signal at different base temperatures of 60 K, 120 K, 180 K, 240 K and 300 K follow the same trace. Keeping the bath temperature fixed and applying different heater currents, it is observed that the overall amplitude of the signal varies linearly with heater current but non-linearly with θ. This observation signifies that the origin of this effect lies with the ΔT_x on the sample and a given external field contribution. The $\Delta(\theta)$ signal measured in the above membrane sample is then fitted to equation (4.8) and the plot is shown in Fig. 4.8. Notice that the shape of these graphs are different than the shape observed

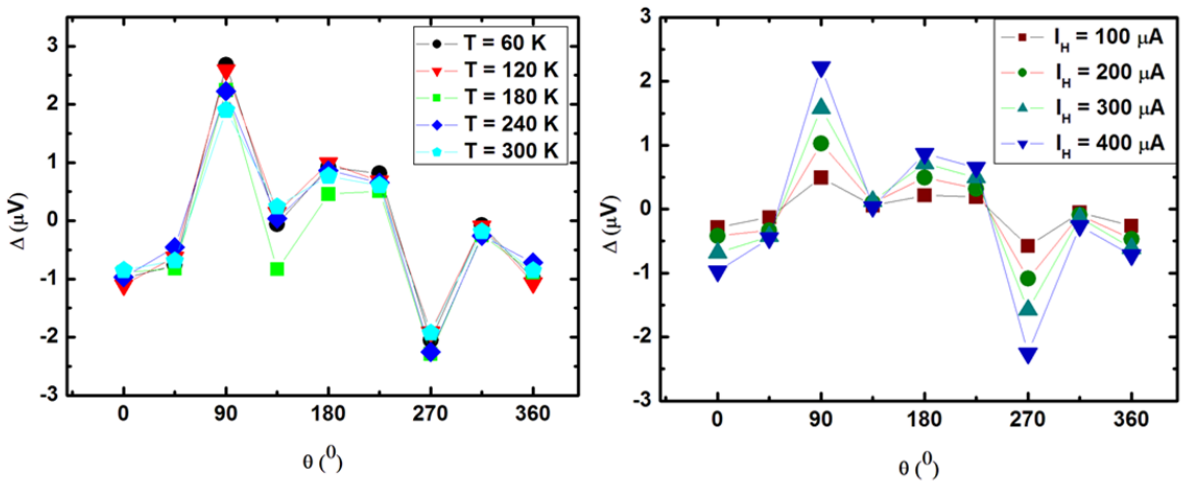

Figure 4.7: (A)The $\Delta(\theta)$ measured at different bath temperatures plotted Vs angle θ with applied heater current of 300 μA, (B) The $\Delta(\theta)$ for varying heater current, i.e., different ΔT as a function θ at 240 K.

in the same sample but measured in another set-up (Fig. 4.6). This difference can be attributed to the different parasitic magnetic field and misalignment in sample mounting.

4.2.5 Bulk sample result

The TSSE study was performed in Py/Pt bi-layer deposited on bulk MgO and GaAs substrates in collaboration with Schmid *et al*. [43, 62]. It was theorized that the phonons in the substrate were important in generating spin current in the magnetic layer [45]. Unlike the case of the membrane samples, the bulk substrates carry phonons and if indeed these phonons are responsible for the generation of TSSE as proposed in [45], then the observation of this effect will confirm the role played by phonons.

The transverse thermopower measured on Py on bulk MgO is as shown in the Fig. 4.9. We notice that the features observed in bulk sample are similar to the observation made on membrane sample i.e the $V_y(\vec{H})$ exhibits the same three features, first the peak and dip structures, second the background envelope taken at the saturation values $A(\theta)$ and finally the asymmetry in saturation values $\Delta(\theta)$. The data analysis done in the similar manner generates the amplitude of average voltage to be $A_0 = 1.2$ μV. This amplitude is almost 10 times smaller than that observed on membrane sample with (1/9)th the Pt detector strip width. This is accounted for by the fact that the ∇T is almost 77 times smaller in case of bulk substrate than the membrane sample. The bulk sample uses Peltier elements with limited output power to generate heat gradient and the substrate itself works as the heat sink. On the other hand, for the membrane, the etches made at the edges reduces the heat loss to the sink and is able to maintain higher ∇T values.

However, the $\Delta(\theta)$ signal on the bulk sample substrate could be fitted nicely to a cosine function with amplitude 50 nV which changes sign from hot to cold end. This could have been the contribution from TSSE

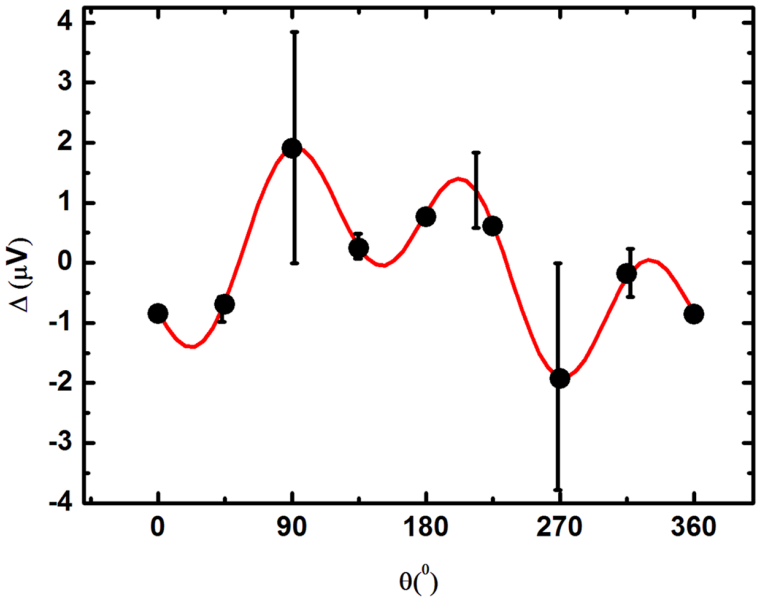

Figure 4.8: The $\Delta(\theta)$ fitted to equation (4.8).

though 2 orders of magnitude smaller than reported. Now it was necessary to verify whether this signal was actually TSSE or other competing effects such as the ANE which also follows $\cos\theta$ symmetry. Since the bulk sample can sustain an out of the plane temperature gradient ∇T_z, it was likely that this signal was purely ANE signal. A finite element COMSOL simulation taking radiation into consideration suggested that an anomalous Nernst coefficient of $\alpha_{ANE} = 2.6\ \mu$V/K was capable of generating voltages of the order of tens of nanovolts [62]. Hence at this stage the $\Delta(\theta)$ of 50 nV could be either from TSSE or ANE effect. In order to resolve this, further test measurements were performed on bulk substrates with copper strip instead of Pt strip. Copper has a very small spin Hall angle therefore no TSSE should have been observed but the 50 nV of $\Delta(\theta)$ was still observable indicating strongly that the 50 nV is the contribution from ANE. The reason behind the change of sign of $\Delta(\theta)$ signal from hot to cold end was found to be a set-up artifact, i.e., the uneven distance of the detector strip from the heater for the hot and cold ends of the bulk sample.

4.2.6 Possible influence of out of the plane magnetic field and transverse ∇T_y

A little discussion is dedicated here to other possible artifacts that could transform into measurable transverse voltage. We will discuss about the presence of out of the plane magnetization which could arise if there is error in mounting the sample, i.e., the sample plane does not coincide with X-Y plane and has a tilt. The consideration in this regard is the possible contribution of ∇T_y to transverse thermovoltage $V_y(\vec{H})$.

The sample misalignment with respect to the external magnetic field could give rise to anomalous Nernst signal $V_{ANE} = \alpha \nabla T_x l_{Pt} \sin(\theta + \phi)$, where ϕ is the sample tilt angle. Using Nernst coefficient of $\alpha = 2.6\ \mu$V/K and maximum $\phi = 2^\circ$, for membrane sample with l_{Pt}= 500 μm and ∇T_x=280 K/mm, the ANE contribution is

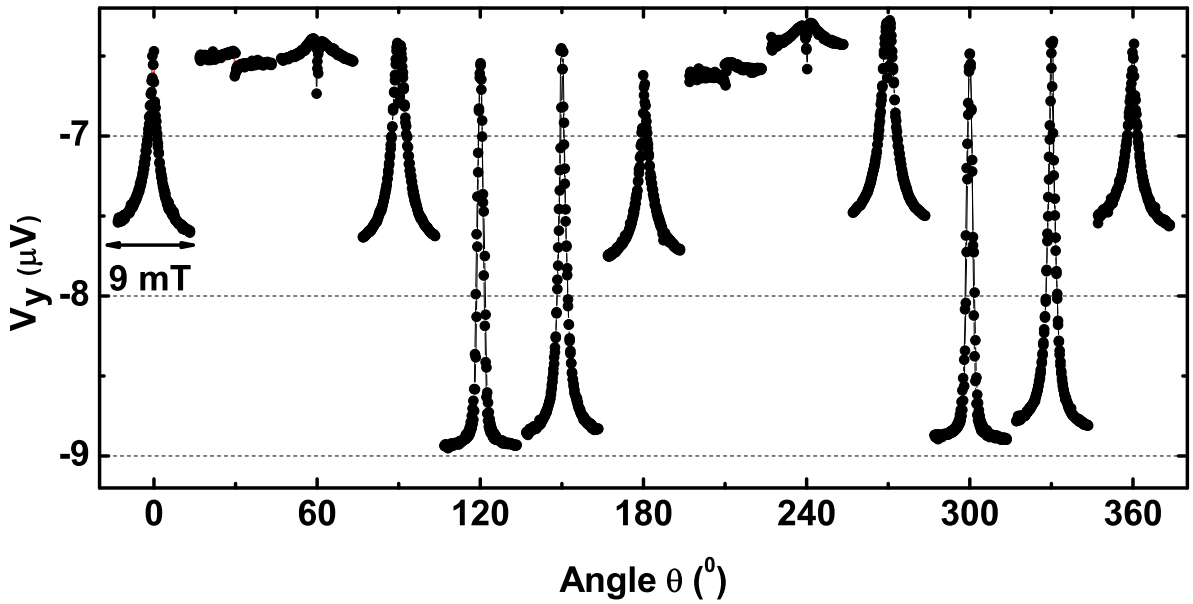

Figure 4.9: Transverse signal measured on Bulk Py/MgO sample.

estimated to be 54.2 nV which is way much smaller than the noise level of 200 nV in the $\Delta(\theta)$ signal. This together with the small thickness of the membranes eliminate the possibility of ANE voltage due to sample tilt. Also the origin of this 200 nV signal has been discussed in the context of parasitic magnetic field effect which arises due to the rotation of the sample and not tilt. Repeating the calculation for bulk MgO sample with $\phi = 2^\circ$, l_{Pt}= 4 mm and ∇T_{x}=3.6 K/mm yields an estimated ANE signal of 6.5 nV. The actual measured $\Delta(\theta)$ in this case is 50 nV. If at all there is a contribution to the Δ voltage due to tilt, it is small enough to be ignored.

In case of both membrane and bulk samples, the sample and the set-up are designed to perform experiment with temperature gradient perpendicular to the Pt strip (∇T_{x}). Even then the existence and influence of small ∇T_{y} persists. Intuitively the $\nabla T_{\mathrm{y}} \ll \nabla T_{\mathrm{x}}$, but if we take both into account then the transverse signal would carry the following expression

$$E_{\mathrm{y}} = S_{\mathrm{xy}} \nabla T_{\mathrm{x}} + S_{\mathrm{yy}} \nabla T_{\mathrm{y}}, \tag{4.9}$$

where

$$S_{\mathrm{xy}} = \frac{1}{2}(S_{\parallel} - S_{\perp}) \sin(2\theta), \tag{4.10}$$

$$S_{\mathrm{yy}} = \frac{1}{2}[(S_{\parallel} + S_{\perp}) + (S_{\parallel} - S_{\perp}) \cos(2\theta)]. \tag{4.11}$$

If the ∇T_y was substantial, a $\cos(2\theta)$ contribution should have appeared besides $\sin(2\theta)$ component in the AMTEP, i.e., the envelope function would have had an additional offset. On the existing data in Fig. 4.1, one could draw a line in the middle as a guide to the eye and this line would be horizontal. However, if the offset from ∇T_y were present, this line would no longer be horizontal but tilted at an angle. Due to the absence of this trait in our measurements, in both membrane as well as in bulk substrate samples, the parasitic contribution from ∇T_y has been ruled out.

4.2.7 Comparison with other experimental studies

The first report on the TSSE [38] generated a lot of interest in the magnetism community with various groups trying to reproduce or find the effect in other materials as well as trying to figure out the mechanism behind the effect. Our attempt was mainly motivated first of all to measure this effect and then find the role played by phonons present in the substrate. During this time, the observation of this effect was under some doubt with several groups not being able to reproduce this effect and also some disparities in the already published results [41, 162]. Our study follows the work of some other groups and their findings that we would like to discuss here including some other key issues.

In the experimental study by Huang *et al*. [41], TSSE was reported to have been observed on Py on silicon bulk substrate although the magnitude of TSSE signal was 10 times smaller than first reported. Furthermore the ANE effect was the most dominant effect in the transverse thermovoltage. Later attempt was also made in the study of Avery *et al*. [162], to find the effect on 500 nm SiN_x membranes and the measurement led to the observation of only AMTEP on such samples. Not surprisingly, this is quite similar to what we have observed on our 100 nm SiN_x membranes. After our work was published only one group has published their result on TSSE measured with the Pt strip embedded between the Py film and the substrate [40] but the origin of the effect was not clear and reproducibility of such experiments remains under question.

Among the publications which have reported TSSE, another such issue lies with the discrepancy in the spin Hall angle of Pt (θ_{Pt}). The spin Hall angle of Pt is an important input parameter in the evaluation of spin Seebeck coefficient. One way of calculating θ_{Pt} involves the following quantities

$$\theta_{SH} \propto \frac{V_{ISHE}\alpha_{Pt}t_{Pt}}{\lambda_{SD}g_{\uparrow\downarrow}\tanh(\frac{t_{Pt}}{2\lambda_{SD}})}, \tag{4.12}$$

where α_{Pt}, t_{Pt} and λ_{SD} are the conductivity, thickness and spin diffusion length of Pt whereas $g_{\uparrow\downarrow}$ stands for the spin mixing conductance at the interface between Pt and the underlying ferromagnetic film.

Unfortunately, the measured value of θ_{Pt} in various groups lacks agreement. What is more baffling is the fact that the spread in measured value of θ_{Pt} is more than factor 20, e.g., the θ_{Pt} measured at room temperature by Ando *et al*. is 0.08 [147] which is close to the value reported by Seki *et al*. of 0.113 [169], 0.12 by Obstbaum *et al*. [164], 0.08 by Azevedo *et al*. [171] and 0.056 by Rojas-Sanchez *et al*. [172] but is much larger than 0.0037 reported by Kimura *et al*. [160] and 0.013 by Mosendz *et al*. [173]. Recently Zang *et al*. [163] measured the θ_{Pt} on two different ferromagnetic films and they found the θ_{Pt} to be heavily dependent on the underlying film,

i.e., the θ_{Pt} for Pt/Py was measured to be 0.2 whereas it was 0.17 for Pt/Co sample. The average $\theta_{SHE(Pt)}$ value turns out to be 0.19 which is highest among any previously measured values of spin Hall angle of Pt. This high value for the θ_{Pt} has been attributed to the high interface transparency between the Pt and the ferromagnetic layer which is clearly not the case in all SSE studies.

Also the room temperature spin diffusion length of Pt is under debate with numbers varying from 7 nm by Ando *et al*. [147], 14 nm by Kurt *et al*. [174] to as low as 1.4 nm by Ralph *et al*. [175] and 1.2 nm by Zhang *et al*. [176]. The spin diffusion length measured by Azevedo *et al*. [171] and Rojas-Sanchez *et al*. [172] are 3.7 nm and 3.4 nm respectively. Such discrepancy raises the question on the ideal thickness of Pt strip.

In the first report on TSSE by Uchida *et al*. [38], special importance was attached to the interface between the ferromagnetic film and the Pt strip since it was the path for the pure spin accumulation to diffuse into the non-magnetic metal. In their work an etching step was involved between the Py deposition followed by lift-off and the Pt deposition step. This process was skipped in the study by Jaworski *et al*. [45] for the GaMnAs as well as by Meier *et al*. [22] and in our experiments by Schmid *et al*. [43]. Despite the clean interface no such effect was observed by us or in Bielefeld.

Continuing our discussion on interfaces, it was also suggested that the origin of the unique $\Delta(\theta)$ signal could have been a proximity effect. The issue of proximity effect is mostly discussed in relevance to the LSSE effect since it is proposed that the induced magnetism in Pt can generate ANE signal which could be disguised as SSE signal, nevertheless, it raises questions on the suitability of Pt as spin current detector as a whole as well as on the interpretation of the various spin induced effects. Huang *et al*. [16] published their experimental findings done in XMCD on Pt and showed that indeed magnetism is induced in Pt in proximity with magnetic insulator such as YIG and instead proposed diamagnetic gold as an alternative. Lim *et al*. [177] also observed temperature dependent proximity effect in thin Pt film sandwiched between two permalloy layers. Again SSE measurements on magnetite thin films by Ramos *et al*. [42] claim the SSE signal to be dominant over the ANE signal possibly caused due to proximity effect in Pt. However, the above results have been heavily contested by S. T. B. Gönnenwein and co-authors in Munich [178, 179], where no proximity induced effects were observed in Pt on insulating YIG substrates. Moreover detailed measurements were carried out by Kikkawa *et al*. [180] on Au/$Y_3Fe_5O_{12}$ (YIG) and Pt/Cu/YIG systems by varying magnetization and temperature gradient configurations and they ruled out any contribution of proximity effect to their observed LSSE signal. Also it has been claimed that the magneto-resistance at the interface could be due to an new effect called the spin magneto-resistance (SMR) and not due to proximity effect [181].

It is required to have a more comprehensive study and all the relevant parameters from various groups should be made available, in order to safely quantify SSE signal within an acceptable error range. Such an initiative has been taken by European Meteorology Research program already which conducts experiments on same samples in various groups across the globe and tests for reproducibility and error finding.

4.3 Summary

In conclusion, the transverse thermoelectric voltage in both membrane and bulk substrate samples is found to be dominated by anisotropic magneto thermoelectric power or planar Nernst effect and in case of bulk substrates the PNE is accompanied by anomalous Nernst effect signal. Disregarding the presence or absence of phonons in the substrate, our experiments find no evidence at all of the existence of TSSE at the level described in [38].

Chapter 5

Sample preparation, Characterization, measurement set-ups and methods for CoFe samples

5.1 Introduction

In this chapter, the device fabrication method for the transport property measurement samples are discussed. The transport study measurements were done primarily on 500 nm thick SiN_x membranes. Some of the earlier electrical transport property measurements have been performed on the 100 nm thin SiN_x membranes which we will discuss in detail in Chapter 6. Next the structural, com positional and magnetic characterization are discussed. All transport measurements are performed in a flow cryostat. Detail description of the measurement method and thermal platform model for the determination of thermal conductivity of thin films is described.

5.1.1 Transport study sample

The typical sample design for the transport coefficient measurement is as shown in Fig. 5.1. The basic sample structure involves two islands containing heater and thermometer structures on them while a SiN_x bridge connects these two islands. The bridge is where the CoFe film we are interested in studying is deposited.

The device fabrication steps are described in reference to Fig. 5.2. All the samples are cleaned in acetone and iso-propanol to begin with. For the electron-beam lithography, first a dose test is done since these membranes are thicker than the old ones used in the transverse thermoelectric power study in Py/Pt. Electron beam lithography is used to write a rectangular structure at the center of the membrane. The standard dimension of this strip is 116 μm $\times$ 60 μm (Fig. 5.1:A). In another kind of sample design, two bridges are fitted onto the chip and

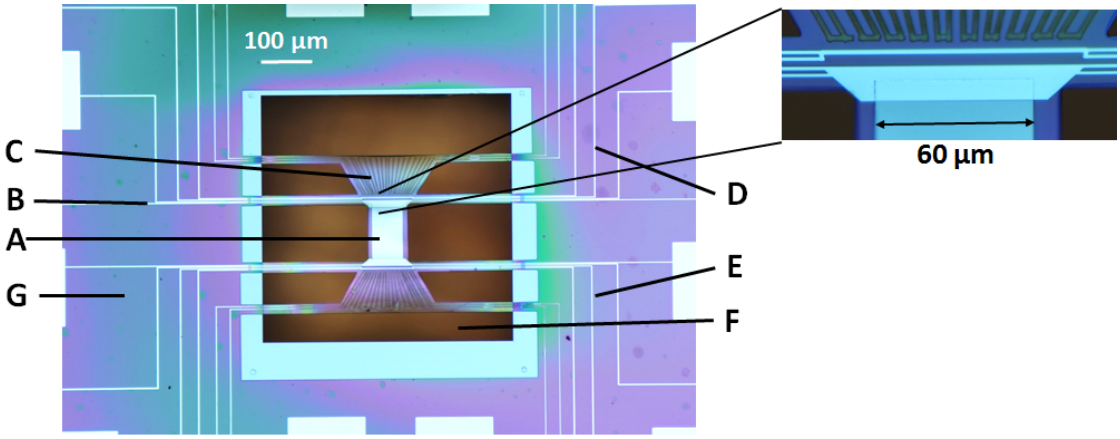

Figure 5.1: Optical image of transport coefficient measurement sample. (A) represents CoFe film on SiN_x forming the bridge, (B) is the leads in direct contact with the CoFe film for resistance and thermopower measurement. (C) is one of the two heater structures lying on the island structure on top of SiN_x, (D) and (E) represent the two thermometer lines designed between the heater and the bridge but not physically touching either and in a four-terminal measurement configuration. (F) shows the areas on the membrane etched away on which no structures has been made. Finally (G) shows the Si chip sink with the bond pads. The image on the right shows the zoomed in portion of one of the two trapezoidal pads.

the dimension of each bridge structure is 150 μm $\times$ 70 μm. On this rectangular structure(s), CoFe alloys are deposited via co-deposition from two different Knudsen cells at a base pressure of 2×10^{-11} mbar. These films include an additional capping layer of 4 nm of Au on top to prevent the CoFe surface from oxidation. The lift-off is done by placing the sample in warm acetone at 60° C for few minutes followed by cleaning in iso-propanol and blow drying with nitrogen. Post lift-off, the thickness of each film is measured in an atomic force microscope (AFM) system. After this is done, we continue the device fabrication steps with the heater structure. A meander heater structure (Fig. 5.1:C) caged in a trapezoidal structure is patterned in a second e-beam lithography step, placed symmetrically on the two islands on either end of the CoFe film. The total length of the meander structure is around 1.73 mm. At both ends of the meander structure, two contacts leads are designed, each leading upto the bonding pads on the silicon chip (Fig. 5.1:G). The four contact leads facilitate four terminal resistance measurement of the meander section of the heater. The width of the meander structure as well as the contact leads is 3 μm. For structures having smaller dimension such as the heater that are designed on the device, we have used two layer thin e-beam resist. First PMMA 50 K 3% resist has been spin coated, baked at 150° C for 6 minutes. Then as the top layer, 950 K 2% resist has been spin-coated and bakes at the same temperature for another 6 minutes. After the e-beam lithography, the sample is developed in NaOH:iso-propanol=1:3 solution for 10 seconds followed by a 30 seconds dip in iso-propanol. Next 40 nm thick $Au_{60}Pd_{40}$ along with 5 nm of Ti adhesion layer is deposited over this heater structure. In some of the older samples, gold has been deposited instead of $Au_{60}Pd_{40}$. The advantage of using $Au_{60}Pd_{40}$ alloy instead of pure Au heater is that not only the phonon drag effect present in pure metal is suppressed, higher resistivity value is achieved which in turn allows application of lesser current to the structure during heating experiments.

The thermometers (Fig. 5.1:D and E) and the contact leads (Fig. 5.1:B) on the ferromagnetic film are

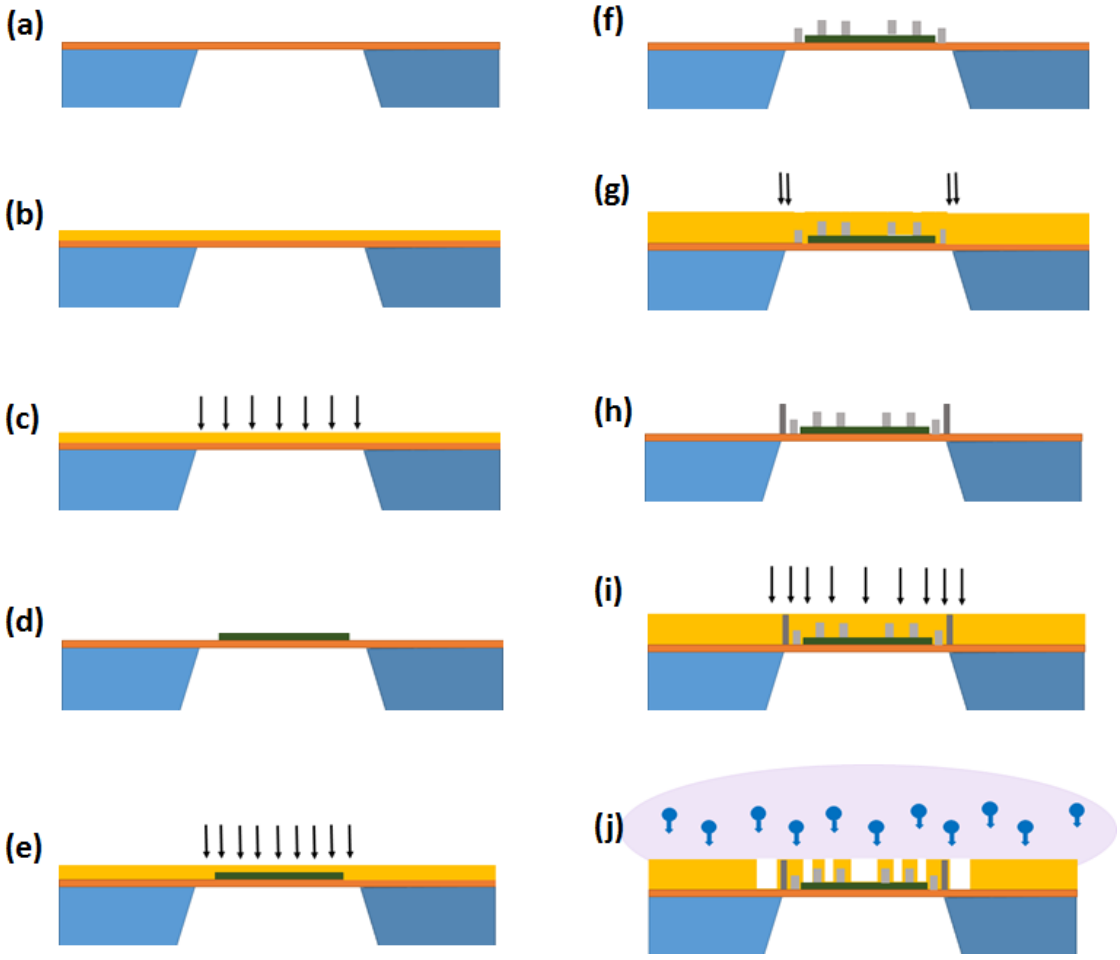

Figure 5.2: (a) chip after cleaning in acetone and propanol(b) thick layer e-beam resist coating (c) 1st e-beam lithography to define area where CoFe will be deposited (d) 60-80 nm CoFe (dark green)after deposition and lift-off (e) bi-layer e-beam resist coating and 2nd e-beam lithography step to define electric leads and thermometers (f) 50 nm Al after deposition and lift-off, thermometer lies outside the film region on the membrane (g) bi-layer resist coating and 3rd e-beam lithography to define heater structures (h) sample with all metal leads after deposition and lift-off of 40 nm AuPd on the heater structure. (i) thick e-beam resist coating and 4th and final e-beam lithography to define areas that need to be etched (j) etching in fluoride plasma (purple area).

patterned together in the third e-beam lithography step. Instead of making point contacts to the ferromagnetic film for resistance measurement, big trapezoidal pads (zoomed portion of the figure as shown to the right) are written at both top and bottom ends of the film. From these pads, two leads each go to the left and the right sinks. The two thermometer structures are designed so as to lie one on each island between the heater and the trapezoidal contact on the film, physically and hence electrically isolated from either structure. Each thermometer is a 100 μm long and 1.5 μm wide wire, designed in a 4 terminal resistance measurement layout. The thermometer structure lies 2 μm away from the heater and 3-4 μm away from the trapezoidal contact pad on the film. On these thermometer and contact lead patterns, after lithography, 50 nm thick aluminum is deposited with 5 nm of Ti adhesion layer in an ultra high vacuum chamber at a base pressure of 8 $\times 10^{-10}$ mbar. This is then followed by the usual process of lifted-off in acetone and cleaning in iso-propanol again.

As can be seen in the final product image in Fig. 5.1, one final step remains for the completion of the device fabrication. Areas on the membrane which have no structures on them need to be etched (Fig. 5.1:F) to carve out the planned bridge and island layout. For this final step of e-beam lithography, an e-draw file is designed in such a manner that after lithography and development, e-beam resist covers the bridge and the island areas only. Areas around these metal structures are removed in a subsequent etching step Fig. 5.2(j) using reactive ion etcher (RIE), following which we have our completed device.

A short discussion on the RIE etching method is provided here. This reactive ion etching technique involves a vacuum chamber with two electrodes, one of them is grounded and the other is connected to a high frequency mostly radio frequency (RF) source. These electrodes, facing each other, form the top and the bottom part of the reaction chamber. The sample that needs etching is placed on the bottom RF plate and chemical gas is injected into the chamber. Due to high frequency excitation, plasma is generated in the region between the plates. This plasma has equal number of electrons and ions and hence is inert. However, the electrons get repelled by the grounded electrode and start accumulating on the RF plate when a voltage bias is developed between the plates called the bias voltage. This bias voltage in turn attracts the ions which react with the material chemically. Additionally due to the high velocity with which these ions bombard on to the surface of the sample, material is also etched by simply getting knocked out. Hence the RIE method is a combination of both chemical and physical etching processes. A balance between the chemical and the physical etching can be achieved by adjusting the RF power, chamber pressure and the bias voltage to achieve suitable etch rate and selectivity. RIE method also has the advantage of providing most anisotropic etching option for insulators.

The SiN_x (Si_3N_4) in our case has been etched in reactive ion etcher (RIE) in the presence of fluorine plasma. In the literature [182, 183] various recipes are available for SiN_x etching using gases such as CCl_2F_2, SiF_4, CHF_3 and SF_6 where the chlorine or fluorine based ions react with Si in SiN_x to convert it to removable volatile products. The recipe we followed was CHF_3 with as little as 10% O_2, the oxygen provides selectivity over SiO_2 and anisotropy. Possible empirical reaction is given by

$$CHF_3 + Si_3N_4 \rightarrow SiF_4 + N_2, F_2, CHFN \tag{5.1}$$

The complete recipe includes chamber cleaning in 100 sccm oxygen plasma at 100 mTorr etch pressure, power

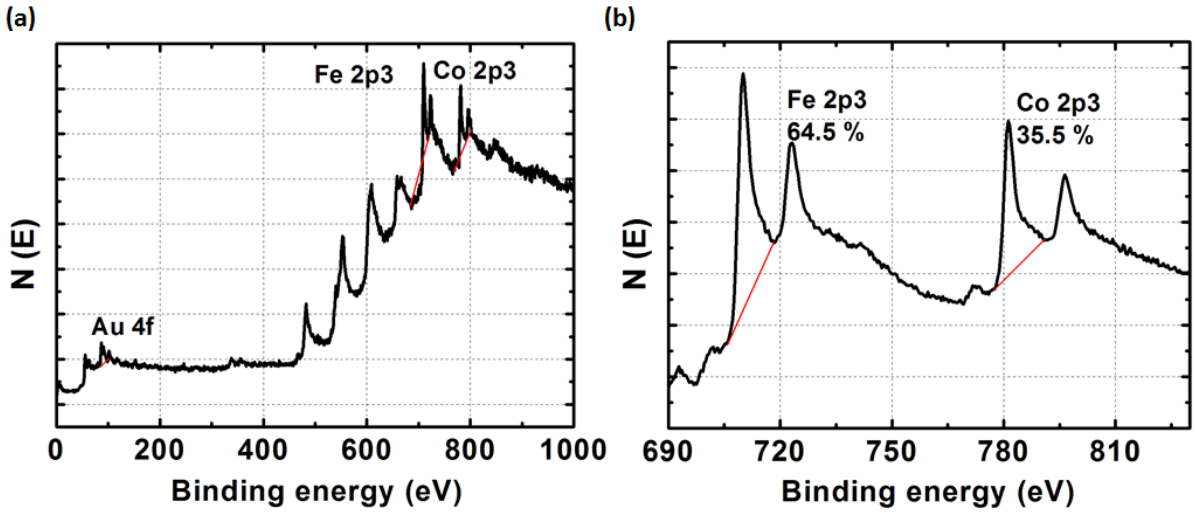

Figure 5.3: In XPS (a) after 50 minutes of sputter cleaning (b) average over 25 spectrum, prominent Co and Fe peaks visible.

200 W for 10 minutes followed by 50 sccm CHF_3, 5 sccm O_2, 150 W power for 12 minutes. After etching, the chamber is flushed and cleaned with N_2 gas. After 12 minutes of etching not only the unpatterned membrane is completely etched but also the residue resist from the rest of the structures is removed. This saves us an additional cleaning step in acetone otherwise needed to remove the leftover resist, which at this point is completely undesirable from structural fragility point of view.

5.2 Characterization of CoFe films

5.2.1 Composition determination

The CoFe alloys are deposited in a MBE chamber using two separate rate calibration curves for Fe and Co. Although the individual calibrations are very reliable, the composition of the alloy is affected by factors such as the power given to the source, the deposition rate, the volume of material present at that moment in each cell, temperature of the cells during evaporation and so on. Hence, after each deposition, the compositions of the ferromagnetic alloy films are detected using X-ray photo-electron spectroscopy (XPS). In our XPS system, first the Au capping layer is removed with Ar ion sputtering with 1.5 KeV source voltage and a raster of 7 mm $\times$ 7 mm. The concentration measurement is performed using a standard X-ray source with Magnesium anode and 250 W power. The error in composition was always found to be within 5% of the intended composition. Finally Au is deposited back on the film for future measurements.

Figure 5.3 illustrates a typical XPS characterization performed on a 80 nm film, intended to be $Co_{36}Fe_{64}$. At the beginning, only peaks corresponding to the Au capping layer appear on a graph of density of state vs binding energy graph. After sputter cleaning for 50 minutes, the carbon and oxygen from the surface of the film are removed and the Au peaks become smaller as seen in Fig. 5.3(a). The sample is now ready for exact

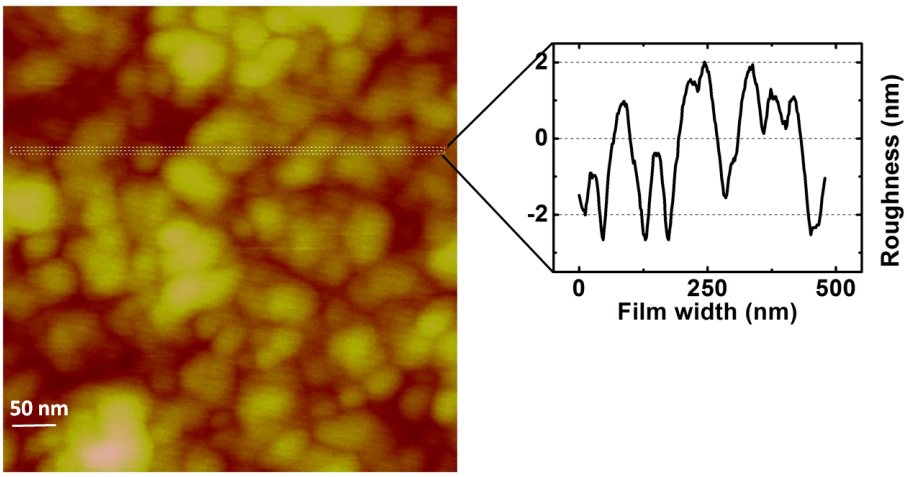

Figure 5.4: The surface roughness from AFM scanning mode image for 60 nm thick $Co_{70}Fe_{30}$ film.

determination of the concentration. The spectrum in Fig. 5.3(a) is repeated 25 times and the average is as shown in Fig. 5.3(b) with clear peaks of Co and Fe. The composition for this sample after measurement turned out to be $Co_{35.5}Fe_{64.5}$.

5.2.2 Thickness and surface roughness

The actual film thicknesses have been verified in AFM. The scanning mode of the AFM is used to make lateral scanning across the edge of the film and the average height difference measured across multiple points is used as the thickness of the film. In the MBE chamber, the deposition rate depends not only on the temperature of the cell but also on how much material is left in the cell. With so many varying parameters, we have observed that measuring the thickness of each and every sample in the AFM is much more precise than relying on the calibration curves for Fe and Co and this is what has been followed each time. Besides thickness the surface roughness has also been studied via AFM. As an example, for 60 nm thick $Co_{70}Fe_{30}$ film, Fig. 5.4 gives an upper limit to the surface roughness to be around 5 nm.

5.2.3 X-ray Crystallography

The crystal structure of the CoFe films is known to vary depending on factors such as deposition temperature, thickness, composition, annealing temperature etc. With change of lattice constant, the magnetic properties and the transport properties change too. In our experiments, we have used CoFe films with different compositions and it is important to know the crystal structure in each case. Therefore we have used X-ray diffraction (XRD) for thus purpose. However, the samples on which the transport measurements were performed could not be used directly for XRD as they were too small in dimension. Hence we prepared test samples that were deposited together with these samples (also used for XPS). The test samples were sent to Karlsruhe institute of technology

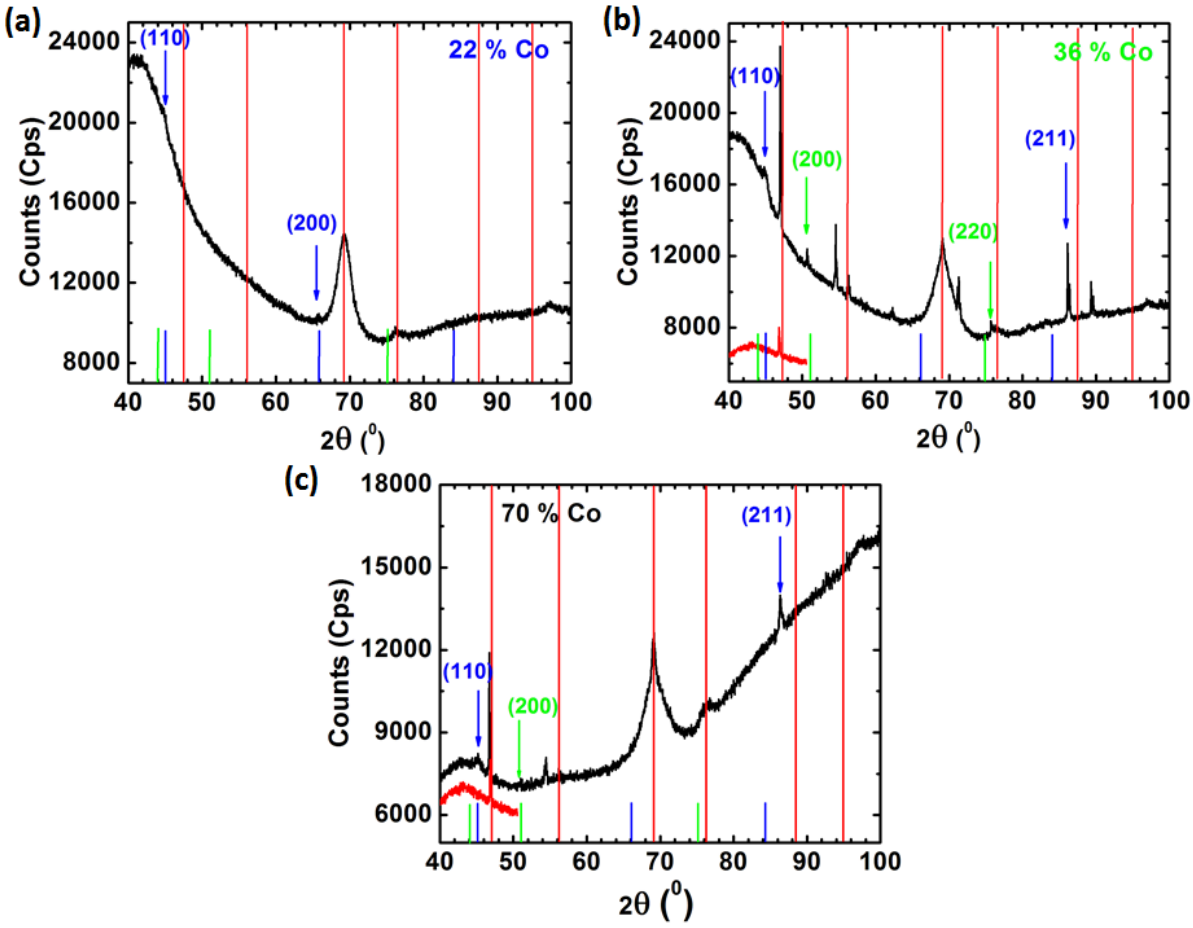

Figure 5.5: XRD spectrum. The red vertical lines indicate the background Si. XRD plot for sample with (a) $Co_{22}Fe_{78}$. The black arrow corresponds to bcc (110) peak (b) $Co_{36}Fe_{64}$ and $Co_{70}Fe_{30}$ .The blue arrows represent bcc (110) peaks and the green arrows represent fcc (200) and (220) peaks.

(KIT) for X-ray diffraction study by Prof. C. Sürgers. The XRD measurements were performed with Cu k-α radiation with wavelength 1.54184 $\AA$ and compared with JCPDS-international library for diffraction data.

Theoretically, the XRD peaks for bcc crystal structure are expected at angles (2θ) 45°, 66° and 84° for direction (110), (200) and (211) respectively. For fcc structure, peaks are expected at angles 44°, 51° and 75° in the respective direction of (111), (200) and (220). Figure 5.5 shows the XRD traces of three of the CoFe films namely, $Co_{22}Fe_{78}$, $Co_{36}Fe_{64}$ and $Co_{70}Fe_{30}$. The background contribution from the Si substrate has not been measured in the entire range of angles and thus not subtracted from these measurements. In the small range of angles where the diffraction contribution from Si was measured, the corresponding XRD measurement result has been shown in the figure as red trace. The expected XRD peak positions for Si are shown as red lines. The library data for expected bcc and fcc positions are indicated by blue and green lines respectively. The XRD image for 60 nm $Co_{22}Fe_{78}$ is shown in Fig. 5.5(a), for 80 nm thick $Co_{36}Fe_{64}$(Fig. 5.5(b)) and for 80 nm thick $Co_{70}Fe_{30}$ film is shown in Fig. 5.5(c). In principle, the bcc (110) peak at 45° should have the largest count, almost ten times the

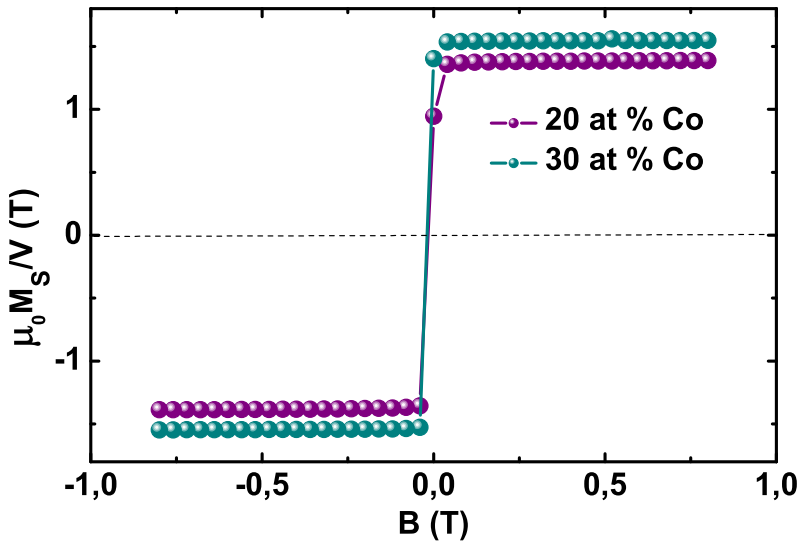

Figure 5.6: The saturation magnetization measured at room temperature in SQUID for samples with Co content of 20% (purple) and 30% (cyan) as a function of magnetic field swept between -800 mT and 800 mT.

peak at 66° corresponding to bcc (200). In all our films, the bcc (110) peak at 45° is visible. Notice no such peak feature in the XRD measurement of Si. In films with Co 36% and 70%, the bcc (211) peak at 84° is observed. However, the the bcc (200) peak at 66° is absent in all the samples. In case of $Co_{36}Fe_{64}$ film, small fcc (200) and (220) peaks can be discerned which are also faintly present in the $Co_{70}Fe_{30}$ film. One can therefore conclude that among our films, the higher Fe content samples are in single bcc phase while the rest are in a mixed bcc+fcc phase with the Fe bcc phase being dominant.

5.2.4 Magnetic properties

The magnetic characterization has been done in a static magneto-optic Kerr effect (MOKE) set-up or a superconducting quantum interference device (SQUID) set-up. The results in Fig. 5.6 indicate the absence of any out of the plane anisotropy. The saturation magnetization M_s is 1.39 T and 1.55 T for films with Co content 20% and 30% respectively. Anisotropic magneto resistance (AMR) measurements have also been performed to study the magnetization reversal for different composition of CoFe films at room temperature and a base pressure of 10^{-6} mbar.

In order to study the effect of external magnetic field on the resistance, the magneto resistance (MR) has also been measured on some of the compositions, mostly of thickness 20 nm. The MR shows the presence of anisotropy, i.e., the MR is always large when the applied current and the field are parallel to each other compared to when they are orthogonal. We have discussed the origin of AMR in Chapter 2 already. Figure 5.7 shows a

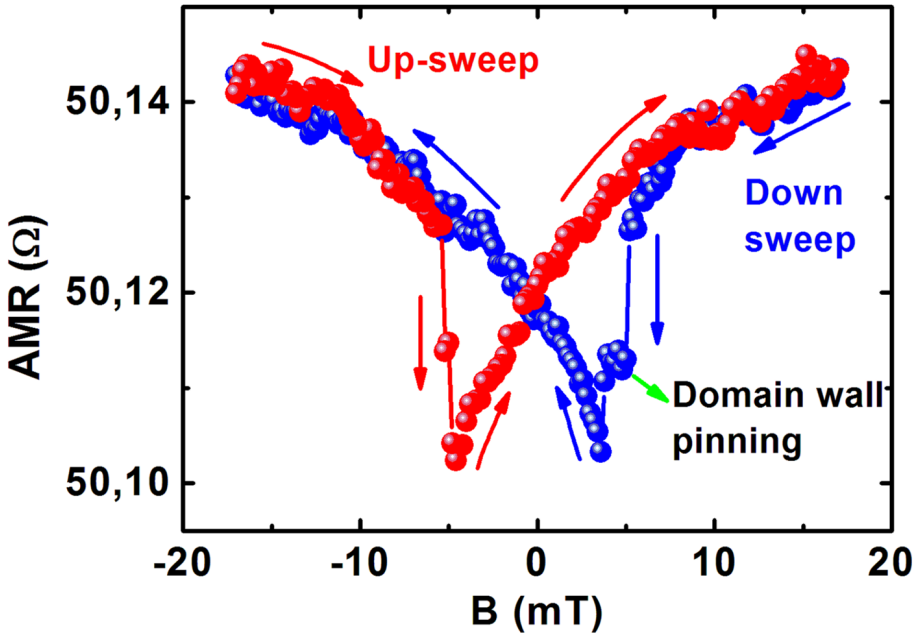

Figure 5.7: Anisotropic magneto resistance curves for 20 nm thick $Co_{20}Fe_{80}$ sample at room temperature and pressure of 10^{-6} mbar with applied bias current of 10 μA plotted as a function of magnetic field swept from -17 mT upto 17 mT (blue circle) and 17 mT to -17 mT (red circle), sweep directions indicated by arrows. Green arrow shows effect of pinned domain walls.

typical AMR curve for a 20 nm thick $Co_{20}Fe_{80}$ sample measured at room temperature and vacuum conditions. The arrows describe the direction in which the magnetic field has been swept. The red curve stands for the upward sweep and the blue curve for the corresponding down sweep, each sweep being an average of 4-6 such runs. At the beginning, when the field sweeping starts from -18 mT, the external magnetic field is in the left direction, hence, the magnetization in the film remains in a saturated state and lies in the direction of the external field. The magnetic field is slowly reduced but the internal anisotropy and exchange energy are not enough yet to completely overcome its effect. Therefore, the magnetization keeps rotating until the field value of 3.4 mT (black arrow). At this switching field, the magnetization hits the in plane direction of anisotropy and makes a sharp jump. After crossing this region, the magnetization starts to rotate until it begins to follow the external field in the right direction again. Small jumps at these regions (green arrow) may indicate the presence of domain walls that need to be overcome. The procedure repeats itself along the downward sweep direction as well. From these curves we see that the coercive field for these films are really low, around 0.1-0.4 mT, which is usual for the case of soft ferromagnet permalloy [184].

We know for polycrystalline films the AMR depends on the angle between the field and the current direction as

$$R(\theta) = R_{\perp} + \left(R_{\parallel} - R_{\perp}\right)\cos^2\theta, \tag{5.2}$$

where θ, $R_{\perp}$ and $R_{\parallel}$ are the angle between the applied field and current directions, MR with $\theta = 90^{\circ}$ and MR with $\theta = 0^{\circ}$ respectively. Hence if R(θ) is measured as a function of θ then the saturation values should be proportional to $\cos^2\theta$ as shown in the Fig. 5.8 with the normalized value, i.e., $R_{\theta}/R_{\parallel}$.

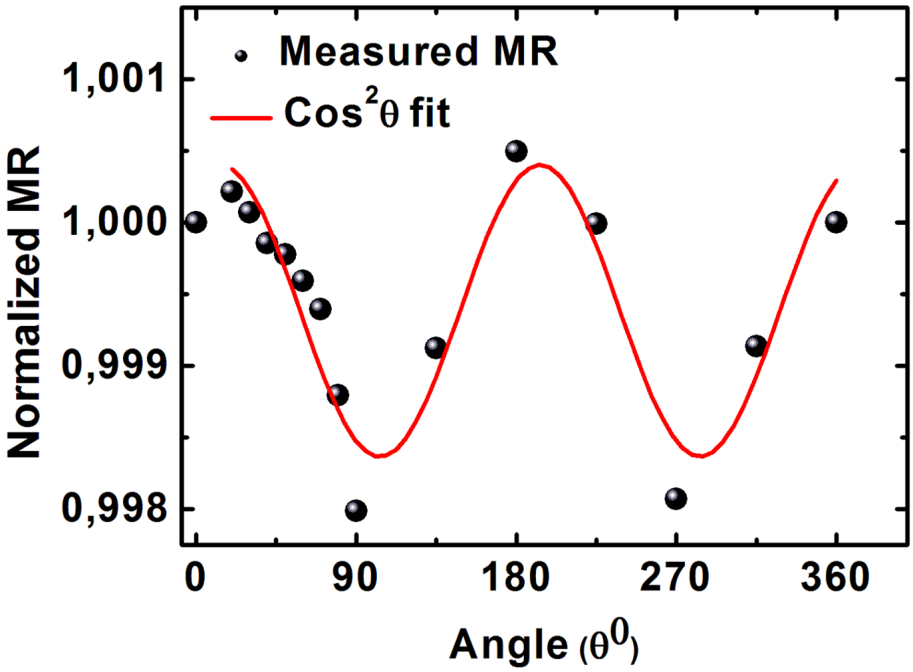

Figure 5.8: (a) Anisotropic magneto resistance normalized to 1 at saturation (filled circles), fit to $\cos^2\theta$ function (lines) from 0° to 360° at an interval of 90°.

The saturation magnetization of these films had been independently measured in SQUID earlier (see Fig. 5.6) and we know that for a 20 nm $Co_{20}Fe_{80}$ sample M_S was measured to be 1.39 T. In a simplistic picture, the maximum uniaxial anisotropy energy K_u for this film can be calculated using the relation,

$$K_u = H_C \times M_S. \tag{5.3}$$

The anisotropic energy for this polycrystalline film turns out to be -1.106 to -4.424 $\times 10^4$ erg/cm^3 which is one order of magnitude smaller than single crystalline $Co_{64}Fe_{36}$ bulk film deposited on GaAs in the study by Dumm *et al.*, [185].

One can notice Fig. 5.7, that the films are not in the saturation state at the highest applied field value. Hence, in Fig. 5.9, we present the AMR curves for 4 different compositions with Co contents 20%, 30%, 50% and 70% together with applied field values upto 200 mT in Fig. 5.9 $R_{\parallel}$ and $R_{\perp}$ are shown in black and red points and as expected we see that the $R_{\parallel}$ is always above the $R_{\perp}$. The AMR ratio can be calculated from,

$$AMR_{\text{ratio}} = \frac{R_{\parallel} - R_{\perp}}{\frac{1}{3}R_{\parallel} + \frac{2}{3}R_{\perp}}. \tag{5.4}$$

We have calculated this ratio for the above samples and plotted them as a function of Co content as shown in Fig. 5.10. The ratio seems to increase with increasing Co electron density and drops somewhere after 30% of Co. The monotonous increase of the AMR ratio with Co content does imitate the behavior exhibited by resistivity.

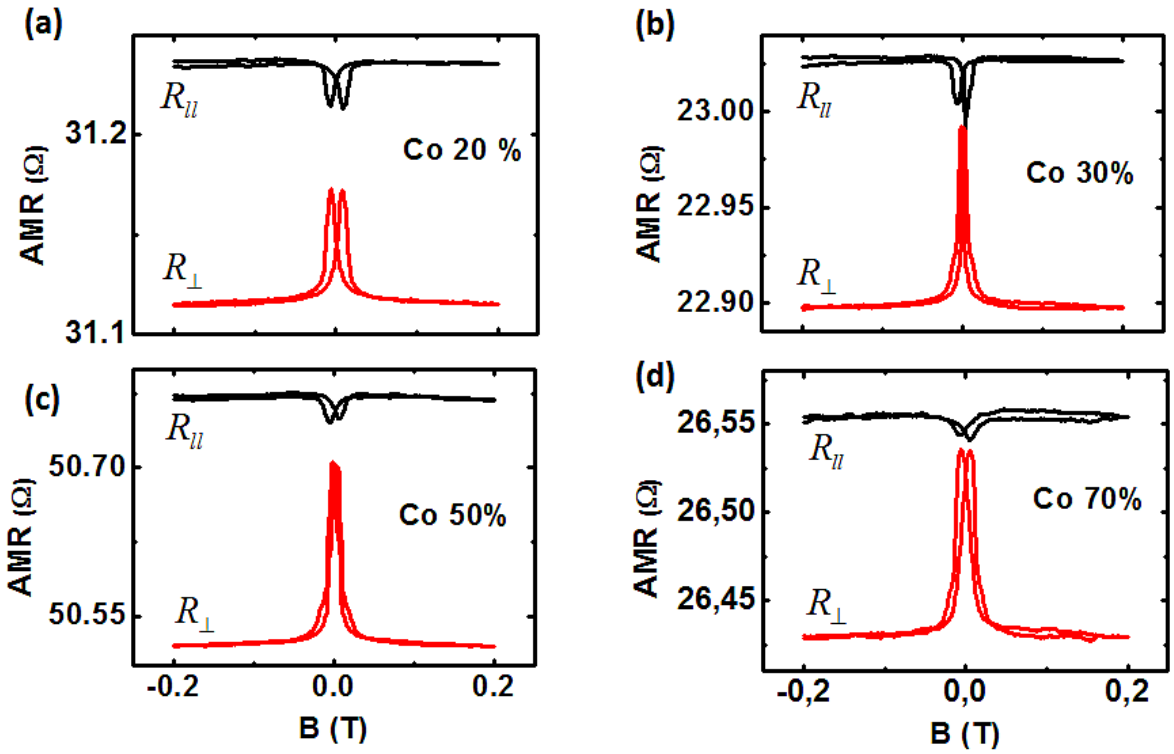

Figure 5.9: (a) Anisotropic magneto resistance curves plotted vs applied magnetic field swept from -200 mT to 200 mT for samples with Co contents (a) 20%, (b)30%, (c) 50% and (d) 70%. The black curve is with field parallel to applied current direction and red curve with field perpendicular to applied current direction.

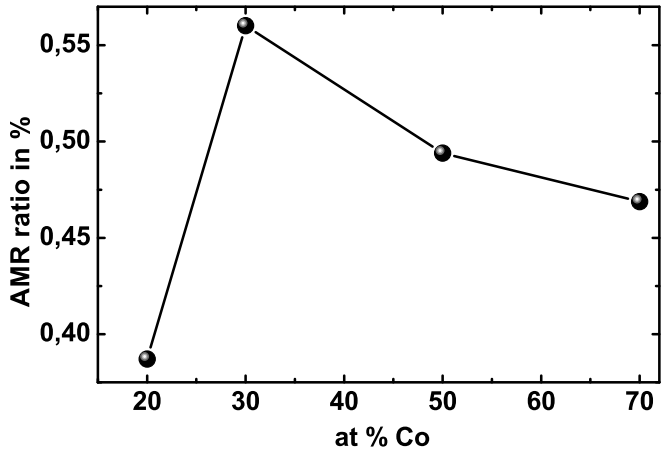

Figure 5.10: (a)Anisotropic magneto resistance ratio vs Co content in %.

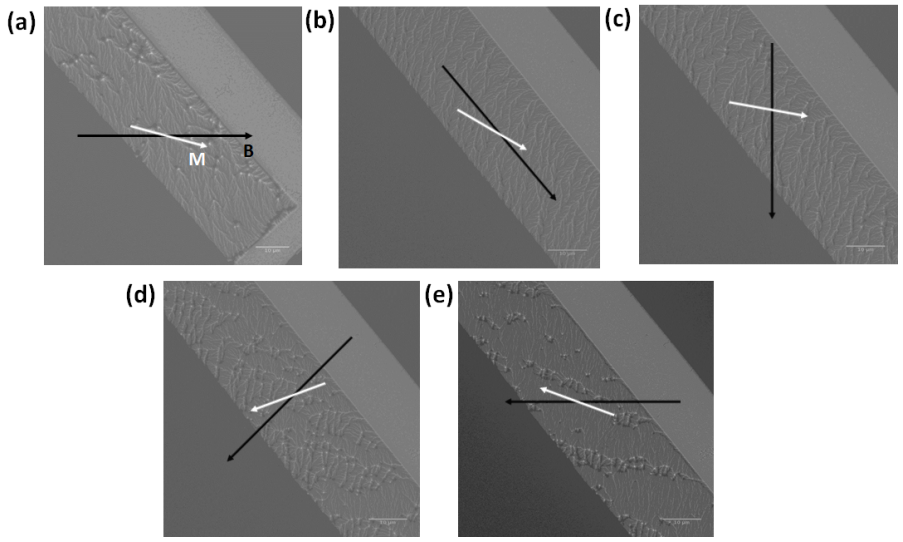

Figure 5.11: (a) The in-plane magnetization direction follows the external field direction at 0° with uniform domain patterns. (b) Field at angle 45°. (c) External field angle equal to 90° in the clockwise direction. (d) At field direction 135°, the domain patterns seem disarrayed, i.e., the eternal field in not sufficient to de-pin the domains to rotate. (e) The situation in (d) persists.

We lack data point for Co 22% film and hence we abstain from making direct correlation in terms of band theory but intuitively the two should hold correlations.

5.2.5 Domain pattern via Transmission electron microscope imaging

Additionally CoFe films were inspected by using Lorenz microscopy in transmission electron microscope (TEM) in the search for domain patterns in collaboration with Prof. J. Zweck. 20 nm of CoFe film was deposited onto 40 nm thick SiN_x membrane of dimension 30 μm $\times$ 100 μm. The images show wave like patterns as shown in the Fig. 5.11 which represent domain walls or boundaries and they become clearer after digitally enhancing the contrast of the images. The effect of the domain walls has already been observed in the AMR curve as shown in Fig. 5.7.

Following usual convention, the magnetization of the film lies in the direction perpendicular to the domain walls. In this technique, the domain patterns were varied by varying the external field generated by the microscope (stigmation) lenses. The white arrow represents the direction of the magnetic field and the red arrow represents the local direction of magnetization estimated manually by considering a direction perpendicular to the domain wall close to that region. We observe that for the direction of external magnetic field from 0° to 90°, the domain patterns follow the direction of the field but after this angle the domain depinning energy wins over the Zeemann energy and the patterns exhibit different direction of magnetization at different regions of the film.

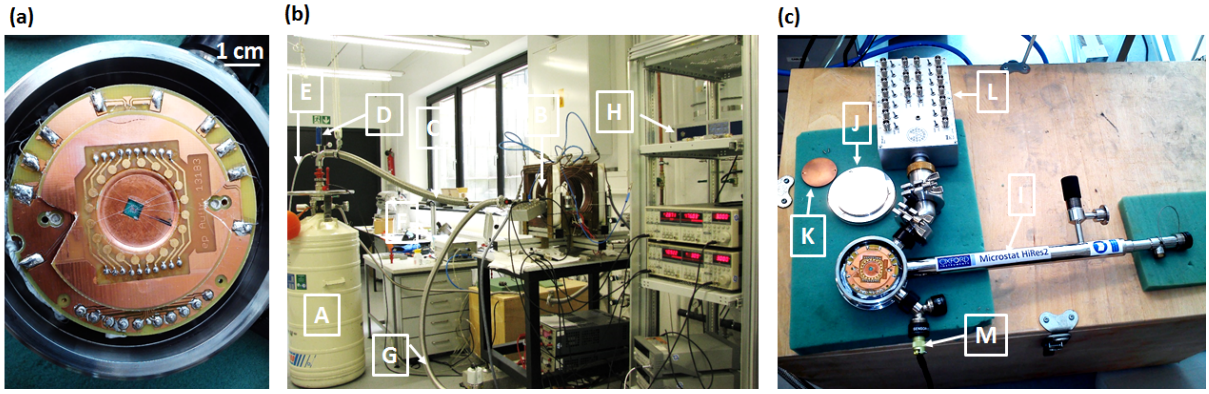

Figure 5.12: (a) Customized sample holder with a mounted sample, sitting on cryostat bottom plate which also acts as the radiation shield of the cryostat.Measurement set-up. (b) (A) helium dewar, (B) cryostat (C) helium transfer line (D) Motor for automatic needle-value inside the blue case (E) helium recovery line (F) helium flow controller (G) pumping line to the turbo pump (H) ITC temperature controller. (c) flow cryostat (I) leg of the cryostat (J) cryostat top cover (K) copper radiation shield (L) break-out box (M) connector to the ITC.

5.3 Transport coefficient measurement methodology

In this section, the measurement method and set-up are described for the measurement of the transport coefficients of 60-80 nm thick CoFe alloy films in a temperature range of 25-300 K in a helium flow cryostat without any external field. Only anisotropic magneto resistance measurements have been carried out at room temperature with the application of external field.

5.3.1 Set-up

The set-up for the measurement of transport coefficients are discussed in reference to Fig. 5.12. The transport properties have been studied in a custom made Oxford continuous flow cryostat (Fig. 5.12(c)) operable in a wide temperature range of 4 K - 500 K. Figure 5.12(b) shows the complete set-up while in Fig. 5.12(c), the image of the flow cryostat on its table is shown. The temperature stability read from the temperature controller (Fig. 5.12(b):H) was of the order of 30 mK at our lowest temperature of interest of 25 K. The sample holder is custom made particularly for this set-up as shown in Fig. 5.12(a). During wire-bonding the contacts, the contact pads on the sample holder are shorted together to protect the sample from sudden electrical shocks. While mounting the sample holder, a thin layer of silver paste is used between the bottom of the holder and the cold finger of the cryostat. A radiation shield (Fig. 5.12(c):K) is next placed on top of the holder with two screws going into the radiation shield of the cryostat so as to minimize the radiation effect. A breakout box (Fig. 5.12(c):L) is used between the electrical connections of the cryostat and the measurement instruments. For details on the operation procedure of the cryostat and the on the ITC temperature controller, refer to appendix-A.

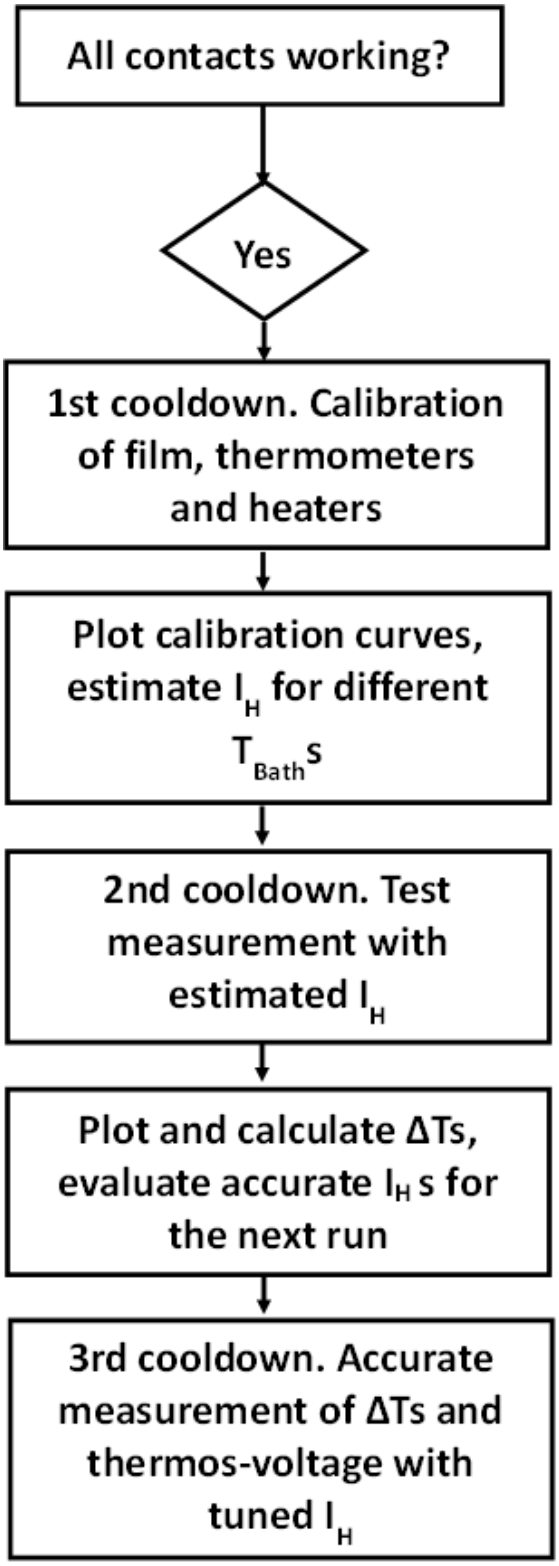

Figure 5.13: The transport coefficient measurement scheme as a flow chart.

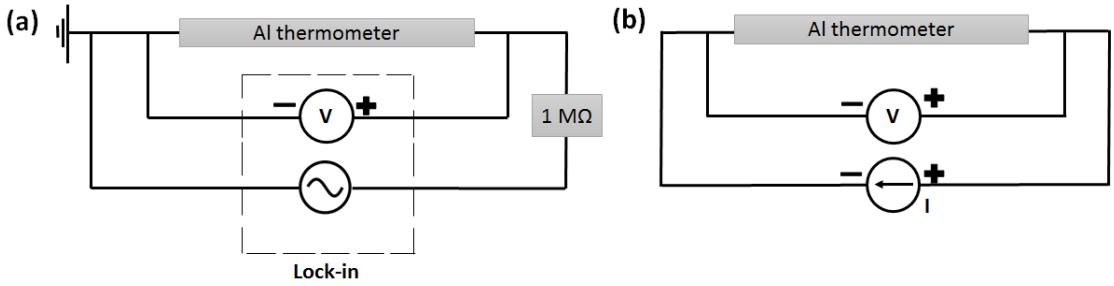

Figure 5.14: (a) Resistance measurement using lock-in amplifier (SR830) in ac method (b) In the dc method, current I is applied from a Yokogawa current source and voltage is measured using Agilent nanovoltmeter.

5.3.2 Measurement steps

In this set-up everything is automated, setting the temperature set point, applying current to the heater, acquiring data etc. are done using labview scripts. Always after a sample is mounted, the contacts are checked at room temperature. This is especially important for the thermometer structures which have to have all the 4 contacts working. Then the cryostat is evacuated to a minimum pressure of 8×10^{-6} mbar which takes about an hour using a turbo pump which keeps running during the whole measurement process. Then helium is let in and the cryostat is cooled to 25 K by doing proper adjustment of helium flow and heater power. At 25 K, a waiting time of 2-3 hours is set to allow proper thermalization. This required waiting time has been determined by taking measurement of resistance of one of the thermometers as a function of time. The resistance of the Al thermometers saturate below 25 K, rendering themselves useless at low temperature. The complete transport coefficients measurement scheme is displayed as a flow chart in Fig. 5.13.

In the first cool-down run, the resistance of the heaters, the thermometers and of the ferromagnetic film are measured while going up in the temperature. Measurement points are collected at each bath temperature (T_{Bath}) in every 6 K or 10 K. A minimum of 30 minutes is always spared between setting the T_{Bath} and starting any measurement to ensure proper thermal stabilization of the sample at that T_{Bath}. The resistances are measured either using dc method with Yokogawa current sources and nano-voltmeters or ac method with two SRS lock-ins or a combination of both. Figure 5.14 shows the schematic for ac or dc resistance measurement of one of the thermometer. The dc resistance is then calculated by using the equation

$$R = \frac{V_+ - V_-}{2|I|}, \tag{5.5}$$

where V_+ and V_+ are the measured voltages for both polarities of current flow, necessary to remove the dc offset from the instruments. The resistance values are plotted after this run is over. Especially the resistance of the heater provides with an idea of how much heater current is needed to be applied to do the thermal conductivity measurements starting with a guess value for it. This in turn is the purpose of the next cool down.

A second cool down run is done starting at 25 K at a T_{Bath} interval of 20 K upto 290 K. After stabilizing at each T_{Bath}, 3 to 4 different guess values of the heater current are applied and the thermometer resistances are

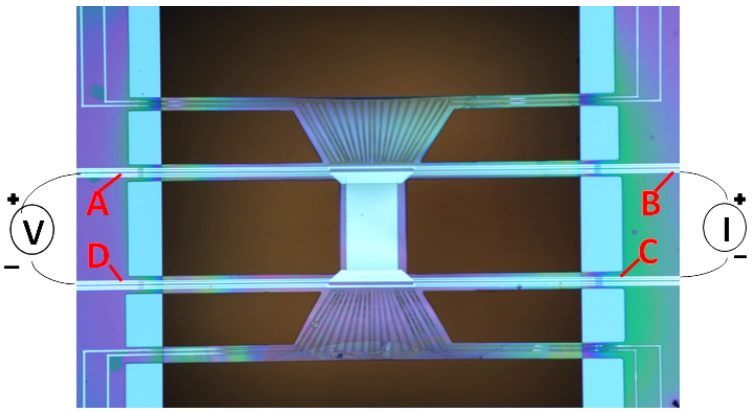

Figure 5.15: On an optical image of a typical sample with 60 nm thick CoFe film on 500 nm SiN_x membrane bridge, 4 leads out of the total 8 leads in direct contact with the film are labeled. Bias current from 1 - 10 μA is applied between contact leads B and C from a Yokogawa current source and the corresponding voltage is measured between the leads A and D using an Agilent nanovoltmeter. The resistance is then calculated using the offset cancellation method as described in the text.

recorded and plotted immediately. While at each bath temperature the resistances of the thermometers are being recorded, the thermo-voltages are also recorded. The objective here is to find out the required heater current which maintains a temperature difference ΔT that is close to 1% of the T_{Bath} between the two thermometers at any given T_{Bath}. As the thermal conductivity drops steeply at the lower temperature range, care is taken not to overshoot the ΔT range. Most of the times the required ΔT is even less than 1% of the T_{Bath}. Next we needed to have an idea of how much heater current is suitable at each temperature region. At each bath temperature, now we know the upper limit of the heater current that can be applied, which will generate linear thermovoltage vs ΔT plot. A third cool down is then performed from 25 K to 300 K at every 4 or 6 K, to provide the final full measurement for a given sample. In this run 8 to 12 different heater current values are applied to the heater at each T_{Bath}.

It is important that the three transport coefficients of a particular CoFe film are measured together without needing to unmount the sample from the holder. The simultaneous measurement of resistivity and thermal conductivity enables the study of the validity of Wiedemann-Franz law without any hesitation. The resistance of the film measured in the first cool down or measured in the third cool down barely show any difference.

Measurement geometry and method for the transport coefficients

Resistivity

The measurement geometry for the 4-terminal measurement of the resistance of the samples as shown in Fig. 5.15. These contacts are assigned the letters A, B, C and D. The resistance measurement is current biased, i.e., current is applied and resultant voltage is measured. In Fig. 5.15, DC current between 1-10 μA is applied from a Yokogawa instrument between contacts B and C and the dc voltage is measured using Agilent nanovoltmeter between contacts A and D. The known dimensions of the ferromagnetic film are used to calculate the resistivity

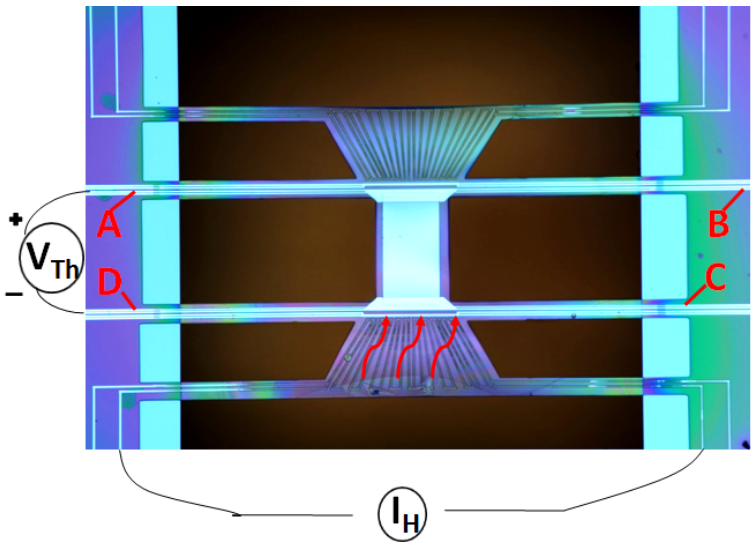

Figure 5.16: Heater current I_H is applied to the bottom heater. It generates temperature gradient along the film and the corresponding thermopower (V_{Th}) is measured between contacts A an D.

$\rho = R \times wt/l$ and plotted in a resistivity vs temperature curve. The whole process is then repeated for all the samples with different Fe content.

Thermopower

Figure 5.16 shows the configuration for the measurement of thermopower. For the measurement of thermal conductivity the knowledge of the absolute temperatures at the thermometers suffice. But the knowledge of the direction of the temperature gradient ∇T on the film is necessary to determine the sign of the Seebeck coefficient. The equation for the Seebeck coefficient, i.e., $S = \Delta V/\Delta T$ holds when the measurement is performed in the direction of ∇T at vanishing ΔTs values. Referring to Fig. 5.16 the dc current has been passed through heater structure which implies that the bottom island is the hot island (indicated by red arrows) and the top island is the cold island. The direction of ∇T is conventionally from cold region to hot region, hence the nanovoltmeter is connected between contacts A and D with the polarity assigned as shown in the Fig. 5.16.

As described previously, at all bath temperatures, ΔT has been kept below 1% of the corresponding bath temperature. The measured thermovoltage after subtraction of the 0 current dc offset is plotted against the calculated ΔT and the slope of such a curve gives the thermopower of the sample at that bath temperature. Fig. 5.17 represents an example of the thermovoltage vs ΔT graph for sample with Co content 36% at T_{Bath}=32 K. The uncertainty in thermovoltage comes from the error in ΔT and ΔV which is calculated by taking the standard deviation from the line fit to the thermovoltage vs ΔT curve.

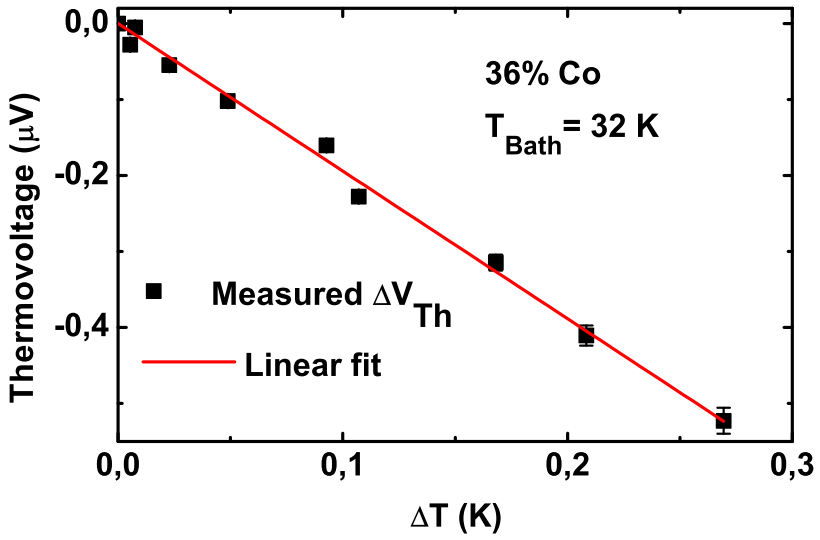

Figure 5.17: Measured thermovoltage (squares) between the contacts A and D in Fig. 5.13 for $Co_{36}Fe_{64}$ sample at bath temperature 32 K vs measured temperature difference (< 0.3 K) between the islands for 10 different applied heater currents. Straight line fit to the data (line). Error bar is the standard deviation from the linear fit.

Thermal conductivity

A typical thermal conductance measurement geometry is similar to the one used for thermopower as shown in Fig. 5.16. Out of the two heater structures only one is used at a time as the heat source. DC current is applied from a Yokogawa to the heater that increases the temperature of the patterned heater with Joule heating indicated by red color. This implies that the island with the active heater is now our hot island at temperature T_H and the second island becomes the cold island at temperature T_C. These temperatures T_H and T_C are noted by simultaneously measuring the resistances of the two thermometers using dc/ac method. The thermal conductance K is calculated from K=$P_H/\Delta T$. Here P_H is the applied heater power and ΔT is the measured temperature difference between the islands, i.e., $\Delta T = T_H - T_C$. The heater power is given by $P_H = I_H^2 R$, where I_H is the applied heater current and R is the heater resistance of the entire heater structure in the suspended region given by $R \approx 1.2R_{4T}$. R_{4T} is the measured four terminal resistance of the heater in the calibration cool-down. The scaling factor of 1.2 comes from COMSOL simulation which we determined by taking into account the known geometry of the structure.

5.3.3 Heater calibration and thermometry

The calibration curve for a typical AuPd heater structure in the temperature range 25-300 K is as shown in the R-T in curve Fig. 5.18. The heater resistance is of the order of 5-6 $\times 10^3 \Omega$ or the resistivity is of the order of 24-30 $\mu\Omega$ cm which is larger than the bulk resistivities of either Au (2.23 $\mu\Omega$ cm at room temperature) or Pd

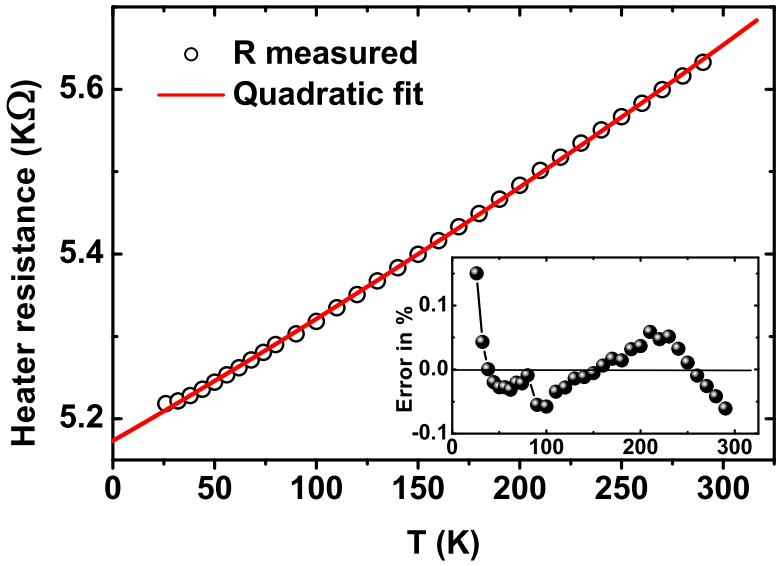

Figure 5.18: Resistance vs temperature curve for one of the heaters of sample with Co 22% (open circle), quadratic fit function to the measured data (line). Inset: Error in % between measured data and fit function vs temperature.

(10.5 $\mu\Omega$ cm at room temperature). For AuPd heater structures, the average resistivity ratio is slightly above one, i.e., $\rho_{\text{heater(300K)}}/\rho_{\text{heater(25K)}} = 1.075$. The resistance at each bath temperature is measured either using lock-in amplifier at low frequencies and bias current of $1-10$ μA or using DC method with similar bias currents. In some cases both the heaters are used, i.e., the temperature gradient direction is reversed and the thermopower is measured for consistency check. We have verified that the resistance of the two heaters on a given sample vary up to 3% of each other.

Additionally we have tested for possible overheating effect of the heater. In Fig. 5.19 we show V-I curves for a heater, which has a room temperature resistance of 5.7 $\times 10^3\Omega$ at two different bath temperatures, one at the low end of 30 K and other at the high temperature end of 296 K. The X axis represents the applied heater current. Red lines in the Fig. 5.19 represent ideal V-I plot in the absence of overheating effect. One can easily notice where the dots representing measured voltage start to deviate from linearity due to overheating. In this figure, the maximum acceptable heater currents are 60 μA and 84 μA at 30 K and 296 K respectively. In actual transport experiments on this sample, the applied heater currents had been less than 10 μA at bath temperatures of 30 K and less than 40 μA at 296 K. This justifies the fact that we have chosen to ignore non-linear contribution to the heater resistance in calculating thermal conductance.

Next we discuss the resistance of the thermometer structures. The thermometer structures are made of aluminum with very low room temperature electrical resistivity of between 2-3 $\mu\Omega$ cm. The typical resistivity ratio of aluminum thermometer between highest and lowest temperature is a little more than two, i.e.,

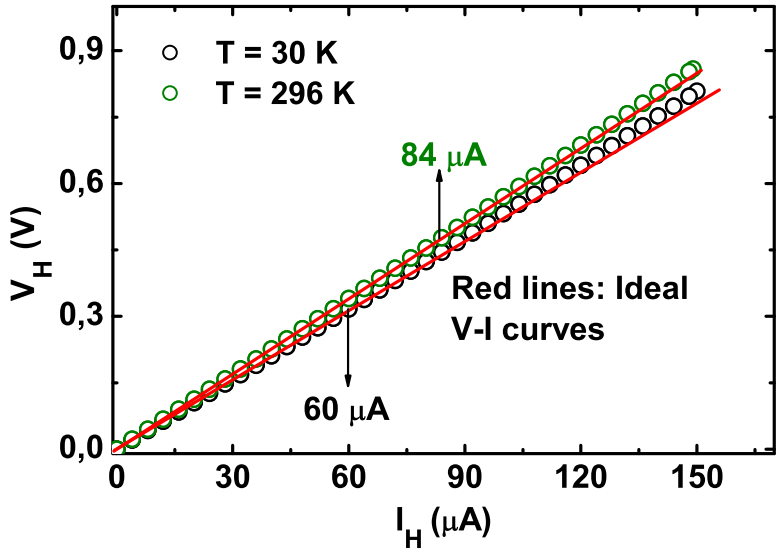

Figure 5.19: Heater V-I curves (filled circles) at bath temperatures of 30 K (black) and 296 K(green). The heater current at which the curves deviate from linearity are 60 μA and 84 μA respectively, indicated by arrows.

$\rho_{\mathrm{Al(300K)}}/\rho_{\mathrm{Al(25K)}} = 2.36$. The 4 terminal resistance is again measured using either ac or dc method but in both cases using a bias current between 1 μA to 10 μA. One has to adjust the bias current to avoid over heating effect in different temperature regime. We have two sets of R-T curves available. The first one is the resistance of the thermometers measured in the first cool down before applying any current to the heater. The second set is obtained in the third cool-down run with zero heater current, i.e., the first data set after every stabilization at a T_{Bath}. The difference between the two calibrations for a given thermometer is always smaller than 1.5% which is also of the order of magnitude of error between the same thermometer for repeated measurements. In most cases the resistances for both thermometers measured at zero heater current in the third cool-down are used for calibration purposes simply because they contain more data points. On a given sample, the resistance of the two thermometers for 0 heater current vary up to 2.5% of each other.

Next the process of determining ΔT between the thermometers is explained. In order to retrieve temperature values from resistance values, a given thermometer calibration curve is fitted to a polynomial function. The coefficients from this fit function are then used to invert thermometer resistance values during heating experiments to temperature values. The error between a calibration resistance data set and the corresponding fit function, i.e.,

$$\frac{\Delta R}{R} = \frac{R_{\mathrm{meas}} - R_{\mathrm{fit}}}{R_{\mathrm{meas}}}, \tag{5.6}$$

is always $< 1\%$ for the method of polynomial fit and this is reflected as the error of the same order in the temperatures between actual and calculated values.

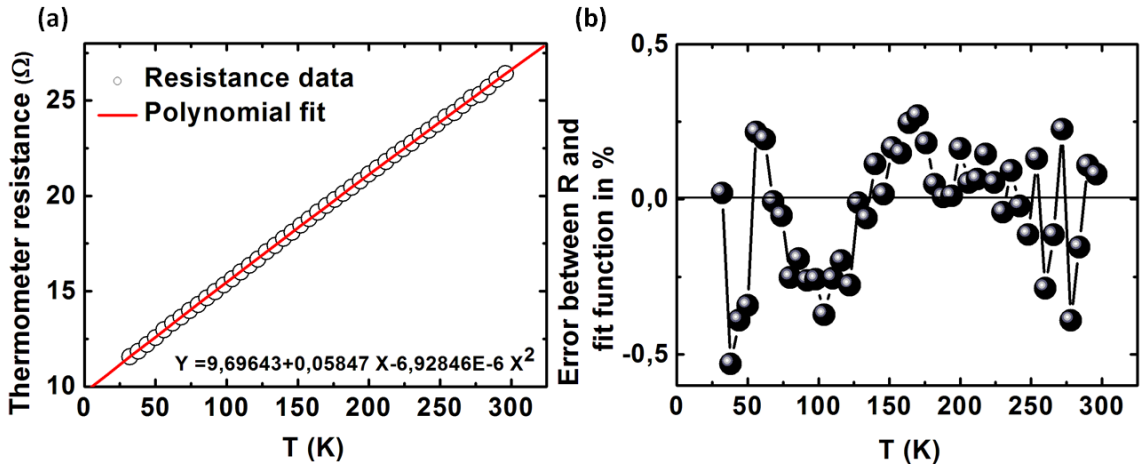

Figure 5.20: (a) Thermometer resistance calibration curve (open circles) with quadratic fit(line), (fit function on the graph). (b) Error between thermometer resistance calibration curve and the fit function in % vs T.

Figure 5.20 shows the measured thermometer calibration curve and the corresponding error between this curve and a polynomial fit to this curve respectively. Sometimes a single polynomial function may not fit the data in all temperature ranges, then two separate fitting functions are used in two different temperature ranges. For example, the temperature region starting at the lowest temperature where the thermometer resistance saturates upto the point where the resistance begins to follow linear behavior can be considered as one temperature range and fitted to a higher order polynomial. On the other hand, the remainder of the higher temperature region is easily fitted to linear or quadratic function.

With the application of heater current, i.e., in the presence of temperature gradient on the bridge, the resistance of the thermometers change. We can use this change in thermometer resistance to calculate change in island temperature as explained below. A resistance curve with non-zero heater current would get shifted in the upward direction from the calibration curve taken at zero heater current on a plot of resistance vs bath temperature. For each increase in heater current, the corresponding resistance gets more and more shifted in the upward direction. This shift of the R-T curve corresponds to the increase of temperature of that particular thermometer, in other words the change in the island temperature. For a given heater current, the resistance of the thermometer close to the heater has a larger upward shift from the calibration curve compared to the shift in the resistance of the colder thermometer from its corresponding calibration curve. This implies that the increase of the temperatures of the the two thermometers (ΔT_{H} and ΔT_{C}) is asymmetric, i.e., the increase of the temperature of the thermometer close to the heater is higher than the thermometer sitting on the other side of the bridge, i.e., $\Delta T_{\mathrm{H}} > \Delta T_{\mathrm{C}}$. The reason behind the asymmetry is the presence of a finite thermal conductance of the bridge. This difference between these two increments is the absolute temperature difference between the thermometers $\Delta T = \Delta T_{\mathrm{H}} - \Delta T_{\mathrm{C}}$, which is the temperature difference between the ends of the bridge. In Fig. 5.21(a) and (b), we show the temperatures of the hot and cold islands on a device after application of 5 μA of heater current. The straight line a linear fit to the temperature data. The absolute temperature difference between the two thermometers is shown as a function

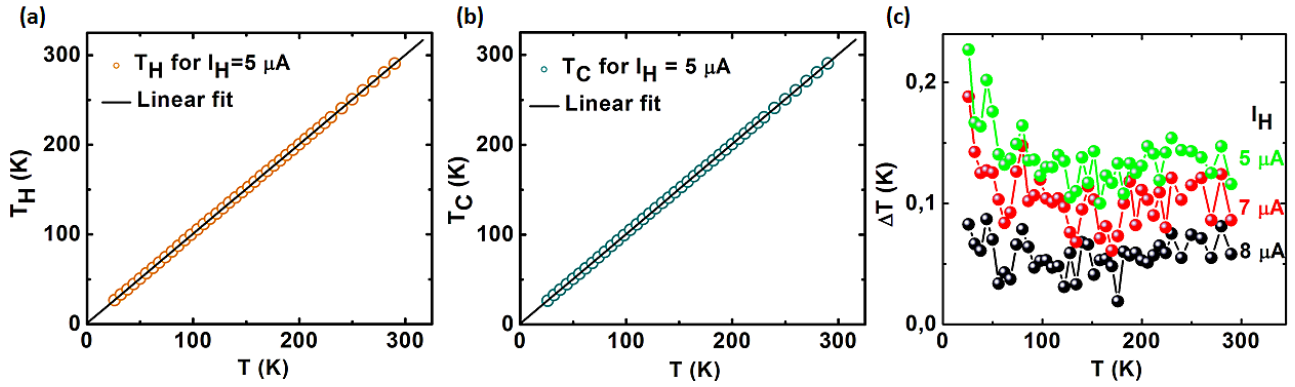

Figure 5.21: Extracted temperatures at the position of the hot (a) and the cold (b) thermometers with the applied heater current 5 μA, plotted vs bath temperature. The line represents linear fit to the data. (c) Temperature difference between the hot and the cold thermometer for applied heater currents of 5 μA (black circles), 7 μA (red circles) and 8 μA (green circles) vs temperature.

of bath temperature in Fig. 5.21(c) with the evolution of ΔT with the application of increasingly different heater currents.

5.3.4 Thermal platform and heat transfer model for transport property measurement

There exist several techniques for the determination of thermal conductivity of thin films [55] among which the most versatile techniques are the electrical heating or sensing techniques which include the very popular 3ω [56] technique, steady-state method and its variations, membrane method, bridge method etc. Other popular techniques include more specific facility-wise rather demanding techniques such as the optical heating technique and electro-optical techniques. The method that serves our purpose the best is the membrane technique while the design also enables us the simultaneous measurement of other transport coefficients on the very same sample. We will also point out a few of the advantages of the membrane technique over other techniques for in-plane thermal conductivity measurement. To begin with, the 3ω technique is quite popular since it discards any effect of radiation on the ΔT, however, it is mostly used for the cross plane thermal conductivity measurement and is model dependent. Besides the single transducer design does not help us in our goal of measuring all the transport properties together. Our membrane technique is a steady state technique, in which the heat loss to the sink is allowed only via the legs of the islands, hence, more accurate heat current profile and determination of ΔT is achieved.

The bridge and membrane techniques have been in use for the determination of thermal conductivity of carbon nanotube [186], other metals and SiN_x membranes [187, 188]. The schematic shows the model used in this technique [186, 189]. Although there are two heater structures, one on each island, during conductance measurement, the temperature gradient is created by using only one of them and in that case that particular island is called the 'Hot island' maintained at temperature T_H and the other one is called the 'Cold island' at the temperature T_C. The heater power input P_H at the hot island is then the Joule heating generated by applying DC current I_H to the heater structure and since no heat is generated at the cold island, $P_C = 0$. The total thermal conductance

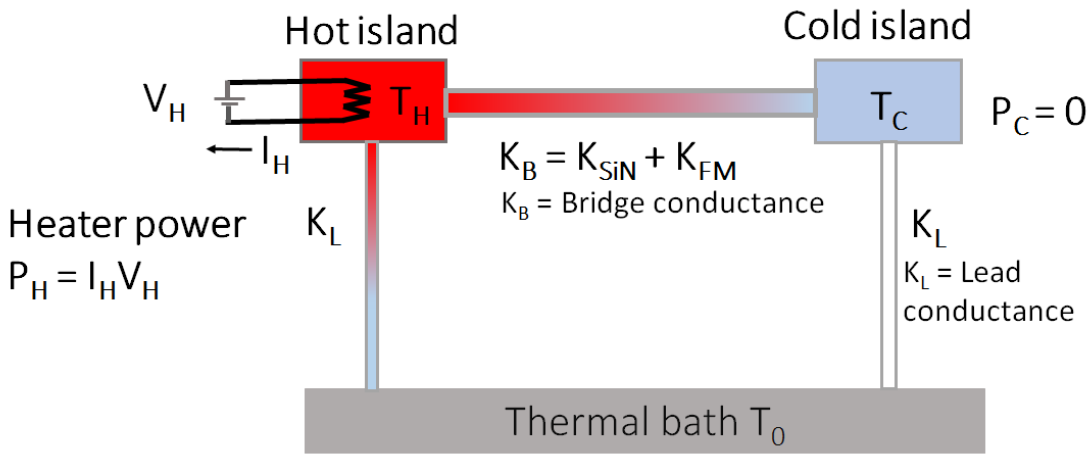

Figure 5.22: In the thermal model [186, 189], the two islands have been depicted as rectangles. The island with the active heater is on the left at a temperature of T_H, the temperature of the colder island on the right is T_C and both T_H and T_C are elevated from the sink temperature of T_0. The false color follows standard temperature distribution color scheme. The bridge connecting the islands is shown as two parallel lines, the bottom one stands for the SiN_x and the top for the ferromagnetic film, together have a total conductance of K_B. All the connecting leads have an effective thermal conductance of K_L. Due to the small area of the structures and the presence of high vacuum in the chamber, radiation effects have been neglected.

of the bridge connecting the two islands K_B is the parallel combination of conductance of the SiN_x membrane bridge and the ferromagnetic alloy film on top. The leg conductance K_L represents the effective conductance of the leads which includes the conductance of the aluminum leads of the thermometers, the aluminum leads to the ferromagnetic film and the AuPd heater leads upto where they meet the silicon substrate. The silicon chip acts as the thermal sink at the bath temperature of T_0, is the set temperature of the cryostat. This lead conductance going from both the islands in the model in Fig. 5.22 is represented by the same K_L owing to the symmetry in the sample design.

The model represents a closed system with two reservoirs at the hot and cold islands and at steady state the energy balance condition can be applied, i.e.,

$$\frac{\partial \varepsilon_{in}}{\partial t} = \frac{\partial \varepsilon_{out}}{\partial t}, \tag{5.7}$$

or

$$P_{in} = P_{out}. \tag{5.8}$$

Now the Fourier's law of heat conduction through a material with thermal conductivity κ states

$$\frac{\partial \varepsilon}{\partial t} = -\kappa A \nabla T, \tag{5.9}$$

where negative sign represents the direction of temperature gradient which is always from the cold to the hot

region. Now using the Fourier's law and equation 5.8 at the hot island we get

$$P_{\text{in}} = P_{\text{H}} = -\kappa_{\text{L}} A_{\text{L}} \frac{\Delta T_{\text{L}}}{\Delta x_{\text{L}}} - \kappa_{\text{B}} A_{\text{B}} \frac{\Delta T_{\text{B}}}{\Delta x_{\text{B}}}, \tag{5.10}$$

where A and Δx are the area of cross section and the length respectively. The subscripts L and B stand for the lead and the bridge respectively. These dimension factors can be taken care of by converting thermal conductivity to thermal conductance using the following relation

$$K = \frac{\kappa A}{\Delta x}. \tag{5.11}$$

Equation (5.10) can be now written as

$$P_{\text{H}} = -K_{\text{L}}(T_0 - T_{\text{H}}) - K_{\text{B}}(T_{\text{C}} - T_{\text{H}}). \tag{5.12}$$

The equation can be rewritten after rearranging the negative signs as

$$P_{\text{H}} = K_{\text{L}}(T_{\text{H}} - T_0) + K_{\text{B}}(T_{\text{H}} - T_{\text{C}}). \tag{5.13}$$

Similarly at the cold island the equation (5.8) in terms of thermal conductance values is given by

$$P_{\text{in}} = 0 = -K_{\text{L}}(T_0 - T_{\text{C}}) + K_{\text{B}}(T_{\text{C}} - T_{\text{H}}), \tag{5.14}$$

or

$$P_{\text{in}} = 0 = K_{\text{L}}(T_{\text{C}} - T_0) - K_{\text{B}}(T_{\text{H}} - T_{\text{C}}), \tag{5.15}$$

equations (5.13) and (5.15) can be solved simultaneously for T_{H} and T_{C} and they are written as follows

$$T_{\text{H}} = T_0 + P_{\text{H}} \frac{K_{\text{L}} + K_{\text{B}}}{K_{\text{L}}(K_{\text{L}} + 2K_{\text{B}})}, \tag{5.16}$$

$$T_{\text{C}} = T_0 + P_{\text{H}} \frac{K_{\text{B}}}{K_{\text{L}}(K_{\text{L}} + 2K_{\text{B}})}, \tag{5.17}$$

which are basically of the form $y = mx + c$. Hence at a fixed bath temperature, when the T_{H} and the T_{C} are measured and plotted against 8-10 P_{H} values, it yields straight lines where the bath temperature is given as the intercept of the straight lines and the slopes S_{H} and S_{C} contain the information on the K_{L} and K_{B}.

$$S_{\text{H}} = \frac{K_{\text{L}} + K_{\text{B}}}{K_{\text{L}}(K_{\text{L}} + 2K_{\text{B}})}, \tag{5.18}$$

$$S_{\text{C}} = \frac{K_{\text{B}}}{K_{\text{L}}(K_{\text{L}} + 2K_{\text{B}})}, \tag{5.19}$$

which can be simplified in order to calculate the conductance values as

$$K_{\mathrm{L}} = \frac{1}{S_{\mathrm{H}}+S_{\mathrm{C}}}, \tag{5.20}$$

$$K_{\mathrm{B}} = \frac{S_{\mathrm{C}}}{S_{\mathrm{H}}^2-S_{\mathrm{C}}^2}. \tag{5.21}$$

If the K_{SiN} value is known then the thermal conductance of any ferromagnetic alloy is then found by simply subtracting the K_{SiN} value from the total K_{B}, i.e., $K_{\mathrm{CoFe}} = K_{\mathrm{B}} - K_{\mathrm{SiN}}$. Later the thermal conductivity of the ferromagnetic film is determined by incorporating the known dimension of this film using equation $\kappa_{\mathrm{CoFe}} = K_{\mathrm{CoFe}} l/wt$.

The error in thus determined thermal conductivity can be calculated from the standard deviation of the slopes S_{H} and S_{C} denoted as ΔS_{H} and ΔS_{C}. From equation 5.21

$$\begin{aligned} K_{\mathrm{B}} &= \frac{S_{\mathrm{C}}}{S_{\mathrm{H}}^2-S_{\mathrm{C}}^2}, \\ &= \frac{S_{\mathrm{C}}}{(S_{\mathrm{H}}+S_{\mathrm{C}})(S_{\mathrm{H}}-S_{\mathrm{C}})}. \end{aligned} \tag{5.22}$$

The error in the bridge conductance can be calculated as

$$\frac{\Delta K_{\mathrm{B}}}{K_{\mathrm{B}}} = \sqrt{(\frac{\Delta S_{\mathrm{C}}}{S_{\mathrm{C}}})^2+(\frac{\Delta(S_{\mathrm{H}}+S_{\mathrm{C}})}{S_{\mathrm{H}}+S_{\mathrm{C}}})^2+(\frac{\Delta(S_{\mathrm{H}}-S_{\mathrm{C}})}{S_{\mathrm{H}}-S_{\mathrm{C}}})^2}, \tag{5.23}$$

$$= \sqrt{(\frac{\Delta S_{\mathrm{C}}}{S_{\mathrm{C}}})^2+(\frac{\Delta S_{\mathrm{H}}+\Delta S_{\mathrm{C}}}{S_{\mathrm{H}}+S_{\mathrm{C}}})^2+(\frac{\Delta S_{\mathrm{H}}-\Delta S_{\mathrm{C}}}{S_{\mathrm{H}}-S_{\mathrm{C}}})^2}. \tag{5.24}$$

In our measurements, the plots of T_{H} vs P_{H} and T_{C} vs P_{H} are never linear as shown in Fig. 5.23(a). The typical applied heater power for all our devices are of comparable magnitude. In this figure, the applied heater power is upto as low as 0.5 μW which corresponds to applied to heater current of as low as 10μA. The origin of this curvature is unclear however, the plot of temperature difference ΔT vs P_{H} as shown in Fig. 5.23(b) is always linear. This information is sufficient for the evaluation of our thermal conductance values.

5.3.5 SiN thermal conductivity κ_{SiN}

In the field of steady state thermal conductivity measurements, SiN_x based devices are at the heart of microcalorimetry, whether be it academic research or industry. To mention a few example-detection of melting in island of tin using high cooling rate differential scanning nanocalorimeter by Allen and co [190] or a microcalorimeter developed using poly-Si/Al thermopiles sensors by Sarro *et al*. [191], now being commercially produced by Xensor Integration [192], bolometers and microcalorimeters based on transition-edge sensors developed on SiN_x [193–195] and so on. Another place to take advantage of SiN_x microcalorimetry is in using the membrane as substrate for the measurement of thermal conductivity and specific heat of thin films or nano-wires

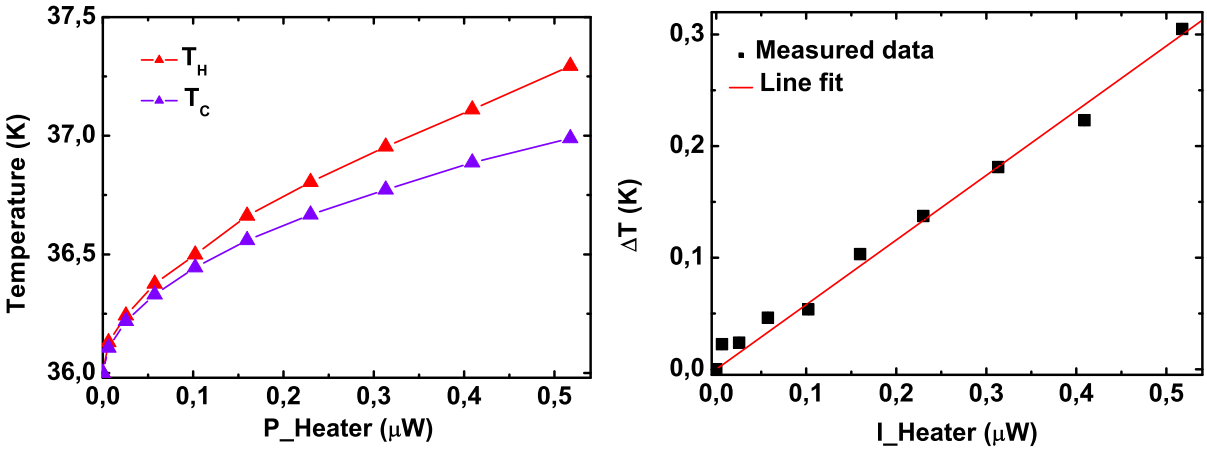

(a) (b)

Figure 5.23: a) Temperatures at the hot end (T_H) and the cold end (T_C) of a 80 nm thick $Co_{20}Fe_{80}$ film as a function of heater power. (b) The temperature difference between the ends of the CoFe film ($\Delta T = T_H$-T_C) as a function of applied heater power.

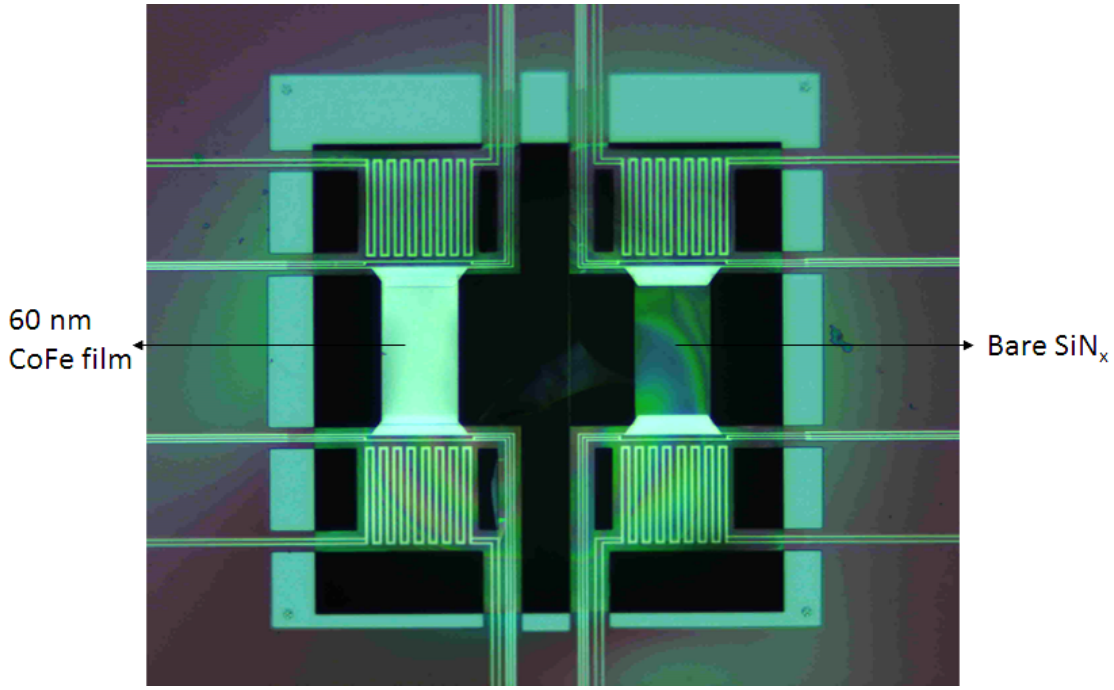

Figure 5.24: Optical image of double-bridges structure sample. The dimension of each bridge is 150 μm $\times$ 78 μm, bigger than rest of the measured devices.

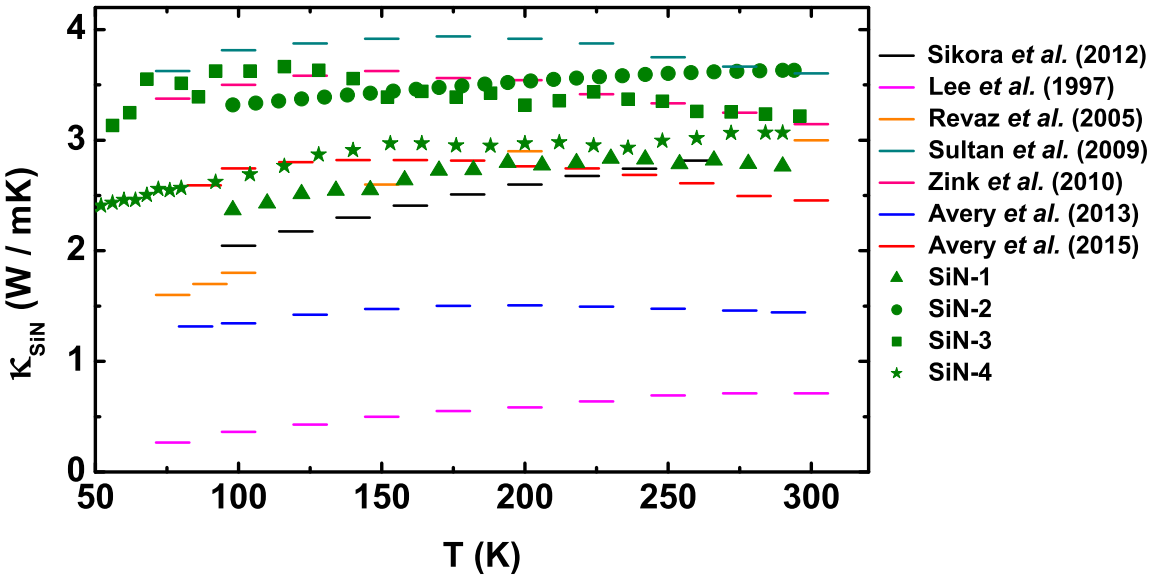

Figure 5.25: Thermal conductivity vs temperature for our SiN_x substrates along with literature values labeled by the group name. For details on literature sources follow table no. (5.1).

as experimentally carried out by Zink *et al*. and co-authors [188, 196–198] or by us for thermal conductivity of ferromagnetic alloy films. As it has been emphasized several times during the course of this thesis, only the proper subtraction of background contribution can yield precise thermal conductivity values for the films under study. With so much importance attached, the thermal transport properties of SiN_x membranes demand a special section for them. Hence this section is dedicated to the thermal conductivity of all the SiN_x membranes measured by us. Comparison with available literature is done and reasons for any deviations are discussed.

The thermal conductance of 500 nm thick bare SiN_x membrane K_{SiN} (platform without any metal film on the suspended region in Fig. 5.1 has been measured in the steady state technique method as described earlier in this Chapter. Three separately prepared samples SiN-1, SiN-2, SiN-3 and one sample device structure where two instead of one bridge structures are designed, are discussed. The last sample has two bridges, one meant for bare SiN_x, SiN-4 here, and the other for membrane plus film (60 nm thick $Co_{22}Fe_{78}$) structure on the same chip (see Fig. 5.24). The measured thermal conductivity of all 4 samples are plotted together as shown in Fig. 5.25 as filled circles, triangles, squares and stars respectively. In case of samples SiN-1 and SiN-2, larger ΔTs had been used between the two islands which implies that the data points below 100 K were probably over heated and hence have not been included in this graph. Sample SiN-3 has been measured 3 times, once with higher ΔT, the other two times with ΔT less than 10% and 1% of the bath temperature respectively. SiN-4 has been measured once with ΔT less than 1% of the bath temperature. We consider the third data set from SiN-3 and

then the average of all 4 κ_{SiN} for our background subtraction purposes and the uncertainty form highest to lowest value lies within $\pm 16\%$.

We now discuss the conductance at higher and lower temperatures separately where we can go over the scatter in κ_{SiN} for different samples. The κ_{SiN} for membrane sample SiN-1, SiN-2 and SiN-4 increase gradually with increasing temperature, reaching a small plateau around a higher temperature of around 200-250 K and then reduce very slightly or saturate. This is a typical behavior of amorphous solid (e.g for SiO_2 [56] and Si [199]). On the other hand for membrane sample SiN-3, the κ_{SiN} increases from 50 K, reaching a maximum around 90 K and then drops much faster before reaching values similar to the lower temperature values. This behavior has been observed before in the study of Zink and co-authors, where such feature had been assigned to the typical amorphous behavior plus the contribution from presence of micro- or nanocrystalline order in the films [197].

It is difficult to make direct comparison with available literature values since the thermal properties as well as the thermal transport properties depend on the technique with which the membrane is fabricated, on which surface is the SiN_x grown and how smooth or rough the surface is after etching the underlayer. The scattering at the boundaries or surfaces, thickness etc. have significant roles to play. We have seen already that there is a discrepancy among values of thermal conductivity for our 3 measured membranes purchased in the same batch. This would imply that either the membranes were not deposited and etched in the same run in the factory or the origin could lie in the induced surface roughness during patterning and etching steps.

Comparison of SiN_x thermal conductivity among groups				
Group	Technique	SiN_x thickness	T range	κ_{SiN} (W/mK)
Zink (2009)	Steady state membrane	500 nm	77 – 300 K	3.625 – 3.604
Zink (2010)	Steady state membrane	500 nm	77 – 300 K	3.375 – 3.145
Zink (2013)	Steady state membrane	500 nm	85 – 292 K	1.316 – 1.443
Zink (2015)	Steady state membrane	500 nm	88 – 300 K	2.591 – 2.456
Hellman(2003)	Steady state membrane	180 – 220 nm	3 – 300 K	0.06 – 1.996
Hellman(2005)	Relaxation method	200 nm	30 – 200 K	1.125 – 2.50
Cahill(1997)	3ω method	252 nm	77 – 400 K	0.305 – 0.7
Bourgeois(2012)	3ω method	100 nm	100 – 250 K	2.120 – 2.770
Our SiN 1	Steady state membrane	500 nm	104 – 294 K	3.327 – 3.633
Our SiN 2	Steady state membrane	500 nm	104 – 294 K	2.44 – 2.77
Our SiN 3	Steady state membrane	500 nm	46 – 296 K	2.964 – 3.214
Our SiN 4	Steady state membrane	500 nm	36 – 296 K	1.992 – 3.067

Table 5.1: SiN_x thermal conductivity (κ_{SiN}) values collected from literature from various experimental groups tabulated along with the measured thermal conductivity of 4 of our 500 nm SiN_x chips. The references are as follows. Zink (2009) [187], Zink (2010) [188], Zink (2013) [200], Zink (2015) [201], Hellman (2003) [202], Hellman (2005) [203], Cahill (1997) [204] and Bourgeois(2012) [205].

The deviation is of course dramatic at lower temperatures. Surface scattering from nitride films has been shown to deviate the thermal conductivity by 500% below 4 K by Holmes *et al*., [206]. According to the study by Zink *et al*., [196], below 10 K, these surface scattering makes the SiN_x based micro-calorimeters useless for the purpose of determining thermal conductivity of metals deposited on them . At such temperatures, phonon mean free path and eventually the κ_{SiN} can be reduced due to specular or diffusive scattering at the bottom or the top surface or both. This makes the precise determination of the thermal conductivity of any metal film deposited on top of the membrane problematic at these temperatures and hence needs to be handled very carefully. However, in our method we limit ourselves always above 25 K and due to the thickness of our membrane which is more close to the bulk value, such dramatic surface scattering effects are suppressed at all temperatures. Also in our sample design, the membrane and the metal film are suspended between the two islands which could make one wonder if mechanical stress has any adverse affect on the background thermal conductivity value. Recently, however, it was found out by Ftouni *et al*. [207] that such mechanical stress does not affect SiN_x thermal conductivity value hence we can safely rule this possibility out.

Scatter in the value of κ_{SiN} of SiN_x are common in the same research group preparing devices in different runs, e.g., as shown in Sultan *et al*., [197] or for example in our case even though we purchased batches of membranes from a single company. Errors introduced during modeling especially in the 3ω technique can also cause confusion sometimes [57, 207]. Hence to our understanding there exists a range of thermal conductivity values for SiN_x membrane rather a single value. In this regard we can say that we are safely within that range. But for the sake of completion in the table (5.1) we put the κ_{SiN} values measured in various groups (using different measurement techniques) in corresponding temperature ranges.

These available values of κ_{SiN} by various groups are shown together in Fig. 5.25 with our measured κ_{SiN} values to see how they compare. In our desired temperature range, the κ_{SiN} does compare with values available in literature. But in order to make more precise determination of the thermal conductivity of a metal film deposited on such membrane, which we do, it is necessary to know the exact background to subtract, which in our case is a precision limiting factor. However, as a verification step we have recently changed the structure to double bridges instead of one as in SiN-4 sample. This way we can know the exact background to subtract and more discussion on this is done later in Chapter 6.

Matlab heat distribution model

Matlab is equipped with a partial differential equation toolbox (PDEtool) which can be used to solve various partial differential equations in multiple dimensions using finite element analysis. The Matlab toolkit for solving 1-dimension heat equation was used to simulate the heat distribution profile on the sample on both the islands, along the bridge as well as along the legs going to the sink. With thermal conductivity of the materials involved and the input heater power as known parameters, the ΔT between the two thermometers can be estimated and then compared with the measured ΔT.

As a test, a simulation has been carried out for room temperature measurements performed on 60 nm $Co_{70}Fe_{30}$ sample. First of all for the modeling, a 2-D geometry was specified by manually drawing a design

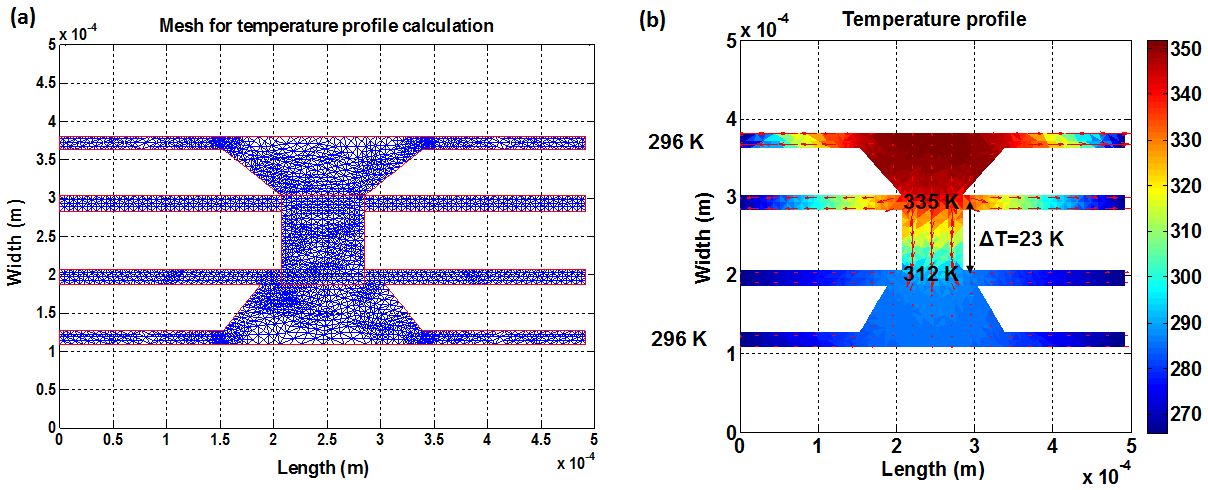

Figure 5.26: (a) Generated mesh for calculation (b) Temperature profile on the suspended region as a PDE solution at 296 K. The color bar represents the temperature from cold (blue) to cold region (red).

similar to the actual sample dimensions. Different segments have been drawn as separate closed structures, i.e., for example the leads going from the bridge to the sink have been considered as a single block with effective thermal conductance of the lead material and the underlying SiN_x together instead of considering each element separately. Next the boundary conditions have been set. For this simulation, at the boundaries linked to the sink, Dirichlet boundary condition, i.e., $a * T = T_r$ has been used where T_r is the temperature to be set which in this case is 296 K and $a = 1$. Next in the PDE mode, elliptic type of PDE has been solved for different segment in the design each with its own input parameters. This becomes clearer when we write down the PDE to be solved,

$$-\delta K \nabla T = Q + h * (T_{ext} - T), \tag{5.25}$$

where K is the total coefficient of heat conduction (acceptable value is the 2-dimensional heat conductivity $\kappa_{2D} = \kappa \times t$, t is the thickness), Q is the input from the source (total heater power per unit area of the heater), and h is the convective heat transfer coefficient ($h = 0$ in our case).

The entire segment containing the island with the active heater along with 2 leads to the sink is considered as the heat source where known values of the thermal conductivity of AuPd and Al are used together with the measured value of thermal conductance for the underlying SiN. One should remember that for calculating the heater power, the total resistance of the heater structure is the 4-terminal resistance of the heater portion lying on the island plus the resistance of the section of the leads going from the island to the sink. This is estimated using its known length. The same total thermal conductance value is used for the second island only with $Q = 0$. Finally for the bridge, $Q = 0$ and the thermal conductance value is the total measured thermal conductance of the film and the SiN_x together. The mesh for the calculation has been generated with growth rate of 1.7 and largest refinement method. Figure 5.26(a) shows the mesh before solving the PDE.

The solution of the PDE with input parameters corresponding to actual measurement heater power input and

the consequential thermal conductivity measurement is as shown in Fig. 5.26(b). The color code indicates dark blue for room temperature and towards the end of the rainbow color band with increasing temperature. As it is seen in the image, the temperature of the cold island does increase significantly due to the heat flow through the bridge. Hence it is important to measure the temperatures at both the thermometers to precisely ascertain the ΔT between the thermometers. Assuming the temperature of the cold island to be the same as the sink temperature will give faulty results.

As solution for this specific example, the ΔT indicated by Matlab simulation stands to be 23 K while the actual measured ΔT is 22 K at bath temperature of 296 K.

5.4 Sample yield and helium consumption

The sample yield in both the sections have been fairly good. During the second section, now that we had much experience in handling the membranes, in most cases we had 100 % yield including the working of the contacts. Some samples needed to be measured more than once that is why samples once mounted on a sample holder were stored intact so as to avoid unnecessary damage. For this purpose we have prepared a number of custom-made sample holders at our mechanical and electrical work shops.

The consumption of helium is as low as less than 1.5 lit/hr, which is the specified value given by the company. However, in actual practice with proper adjustment of helium flow percentage and operation mode of the temperature controller, the consumption could be lowered further. This also has to do with the fact that we did not work at the base temperature of 4.2 K which is where more helium is consumed rather we always worked at temperatures more than 25 K. To give an actual idea, measurement for one CoFe sample including 3 cool downs spanning over 4-5 days consumed at most 40 liters of helium. This enabled us measuring 2-3 samples per helium Dewar of 100 liter capacity.

5.5 Numerical calculation methodology in a nutshell

The transport coefficients measured are considered together with the values calculated numerically in order to draw a complete picture which facilitates the separation of the contribution from electrons, phonons and magnons to the respective coefficients. The numerical calculations are done in the group of H. Ebert in LMU, Munich.

Regarding the methodology, a first principle calculation has been performed utilizing multiple-scattering spin-polarized relativistic KorringaKohnRostoker method, using (SPRKKR) package developed by the group of Ebert in Munich [208]. The method utilizes relativistic 4-component Dirac formalism in the frame of spin density functional theory to calculate the band structure.

This scheme has been implemented quite successfully, importantly in calculating the Bloch-spectral function (BSF) for alloys [209], especially for ferromagnetic alloy e.g. in $Fe_{20}Ni_{80}$ [210]. This is also used to calculate the BSF for our CoFe alloys. The nice aspect of the formalism is that it includes the spin orbit coupling which

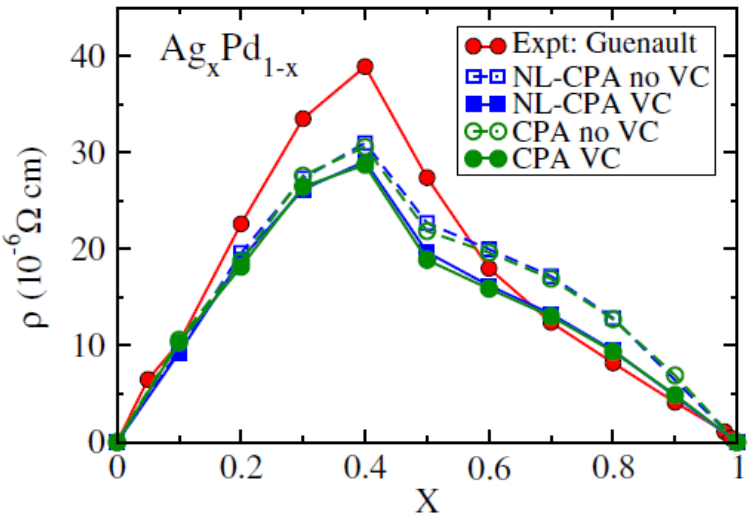

Figure 5.27: Residual resistivity of AgPd alloy as a function Ag concentration. The calculation and experimental result are explained in the text, sources [208, 213].

causes the spin-mixing of the spin-up and the spin-down channels. This is important for the calculation of the transport properties of ferromagnetic alloys.

The BSFs can be used in principle to calculate the electronic transport coefficients. The width of the BSF at Fermi surface can be used to calculate the $\vec{k}$-dependent lifetime and ultimately the group velocity of the electrons. This has been done by Stocks and Butler [211] to calculate the residual resistivity and thermopower within the semi-classical Boltzmann formalism. A more general method to calculate the transport properties is given by Kubo linear response formalism. This method calculates transport properties for pure systems. In both the above methods, the 'scattering in' term (see explanation in Boltzmann formalism derivation in Chapter 2) has not been taken care of. This term basically represents the electron-phonon scattering in which momentum is transferred from high velocity states (d-states for transition elements) to the low velocity states [211]. This term has been seen to affect the concentration dependent calculation of transport coefficients of alloys. Hence, in our case for the CoFe alloys, to account for this scattering in term, CPA over full concentration range is done including 'vertex corrections' (vc). This can be elaborated by referring to the work of Butler [212].

Figure (5.27) shows one such example taken from [208,213]. The residual resistivity of disordered Ag_xPd_{1-x} alloys has been calculated using CPA and Non-local CPA (NL-CPA) with and without vertex correction. These then have been compared with experimental result [214]. We focus on what interests us here, i.e., the calculated residual resistivity using Kubo formalism within CPA, with and without vertex corrections (green open and closed circles). The effect of vertex correction is clearly noticeable for Ag concentrations higher than 30%. In our CoFe films additionally the alloy analogy model was needed to be incorporated to include lattice vibrations and spin fluctuations in the calculation of the temperature dependent resistivity [215].

Concerning the thermoelectric and thermal transport coefficients, in our case they have been calculated via generalized Mott formula as has been previously demonstrated by Smrcka and Streda in 1977 [216] and Jonson

and Mahan in 1980 [217]. In summary, basically the transport coefficients are related to the response function (these functions connect the current density and the potential gradient as we have seen in the context of Onsager relations in Chapter 2) which in turn are calculated using Kubo Green's function formalism. The contribution of the electron-phonon interaction in the exact response function are done via the adiabatic phonon approximation. This method has already been used in the group of H. Ebert to calculate spin dependent thermoelectric [218] and galvanomagnetic [219] properties.

5.6 Summary

We have successfully developed the SiN_x platforms for the measurement of transport coefficients of CoFe in house with no prior experience. With bit of precaution 100% yield is achievable notwithstanding the several steps of lithography. The measurement of the transport coefficients especially thermal conductivity requires one to use proper waiting times for thermalization to take place. The total volume of the flow-cryostat is comparatively smaller than conventional systems and thus the actual time taken to cool all parts down to the bath temperature needs about 3 hours starting from cooling down the set-up. However, this is a small price to pay given the small helium consumption. Measurements were often repeated in order ensure data reproducibility so were the various fitting methods of converting resistance to temperature.

Chapter 6

Contribution of various quasi-particles to the transport coefficients of CoFe

6.1 Introduction

In this chapter, we discuss the results of our experiment on CoFe alloys. We study the transport coefficients namely resistivity, thermal conductivity and thermopower on 60-80 nm thick Co_xFe_{1-x} films of compositions x_{Co} = 0.2, 0.22, 0.36, 0.5 and 0.7 on suspended micro-calorimeter. The electron scattering contribution from phonons and magnons has been separated for each coefficient.

6.2 Electrical resistivity

We begin the discussion with the electrical resistivity ρ(T). In this section, the resistivity of the CoFe films measured in the temperature range of 26-300 K has been described. Comparison has been drawn between the measured resistivity result and theoretically calculated results. The scattering contribution from different quasi-particles such have been separated. Emphasis has been given to the high temperature magnon scattering contribution.

6.2.1 Resistivity measurement results and discussions

Experimental results

Figure 6.1(a) shows the results for the resistivity measurement plotted as a function of bath temperature T. The resistivity for all films increases with temperature. Also from top to bottom, resistivity shows a systematic decrease of magnitude for increasing Co content. It is noticeable that a change of ρ(T) of 4 $\mu\Omega$ cm takes place

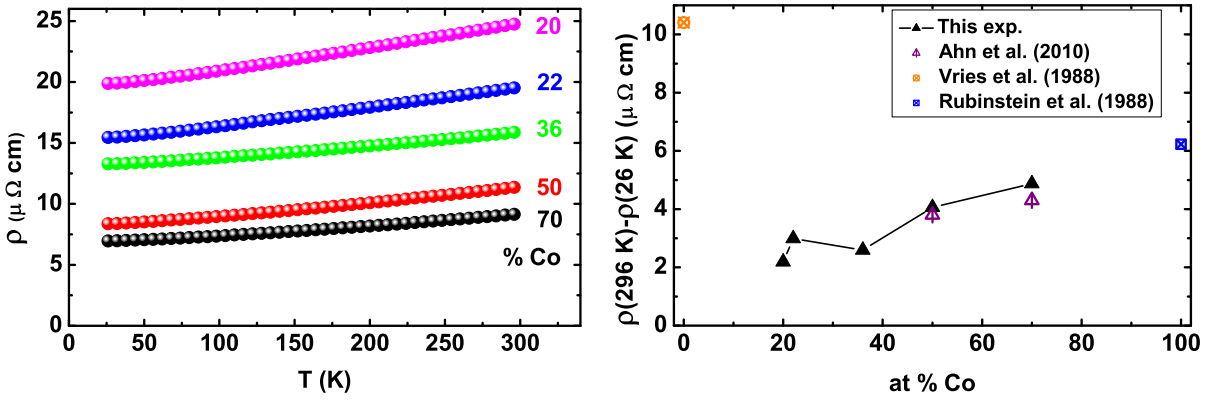

(a) (b)

Figure 6.1: a) Resistivity of five samples plotted together as a function of bath temperature labeled by Co content in %. (b) The temperature dependent part $\Delta\rho$(T) as a function of Co concentration. The literature values of $\Delta\rho$(T) for pure Fe (orange circle with cross), Co (blue square with cross) and CoFe (purple triangle with a line) are taken from the sources [221], [220] and [110] respectively.

at 296 K for a mere 2% change of Co content from 20% to 22%.

We write the total ρ as a sum of low temperature ρ_0 and temperature dependent $\Delta\rho$(T), i.e., ρ=ρ_0+$\Delta\rho$(T). The ρ_0 in our films vary within 6.965 $\mu\Omega$ cm - 19.88 $\mu\Omega$ cm at the lowest temperature. The temperature dependent part of the resistivity, i.e., the change of resistivity from the highest (296 K) to the lowest temperature (26 K), $\Delta\rho$(T)=ρ(296 K)-ρ(26 K) is of the order of 2-3 $\mu\Omega$ cm for films with Co content from 36% – 70% and 4-5 $\mu\Omega$ cm for films with Co content 20% – 22% as shown in Fig. 6.1(b).

To explore the dependence of ρ on Co composition, vertical cuts are made at 26 K and 290 K on Fig. 6.1(a) and the corresponding data are plotted vs Co content in Fig. 6.2. The low and high temperature date are plotted as black squares and red squares respectively. At both temperatures, the resistivity decreases quite monotonically at all temperatures with increase in x_{Co}. A peak structure is observed on at 20% Co content. At the high temperature of 290 K, a data point for measurement on pure Fe film is shown. Additional measurement on CoFe films with thickness of 20 nm and Co content of 20%, 30%, 50% and 70% deposited on 100 nm thin SiN_x membranes have been carried out. These resistivity values at 290 K have been added to this figure (green squares). The isotropic residual resistivity calculated theoretically is shown as a line for Co from 0% till 80%. It follows the shape of the measured ρ vs Co content traces. We have additionally shown literature values of ρ for pure Fe and Co and CoFe. The literature ρ value for 20 nm Fe measured at 26 K was obtained from the experiments by Rubinstein *et al*. [220] and the ρ data for 53 nm Co (at both 26 K and 296 K) have been obtained from the experiments by Vries *et al*. [221]. On the same figure we also show the literature value of the resistivity measured on bulk CoFe samples in the study by Freitas *et al*. [109] at liquid He temperature. The monotonic decrease of ρ with Co content with a pronounced peak around 20 % Co is unmistakable.

We also consider the effect of grain boundary scattering to ρ_0 in our alloys. In order to verify the contribution of such scatterings to ρ_0, we have measured the resistivity of a 60 nm thick $Co_{70}Fe_{30}$ test sample before and after

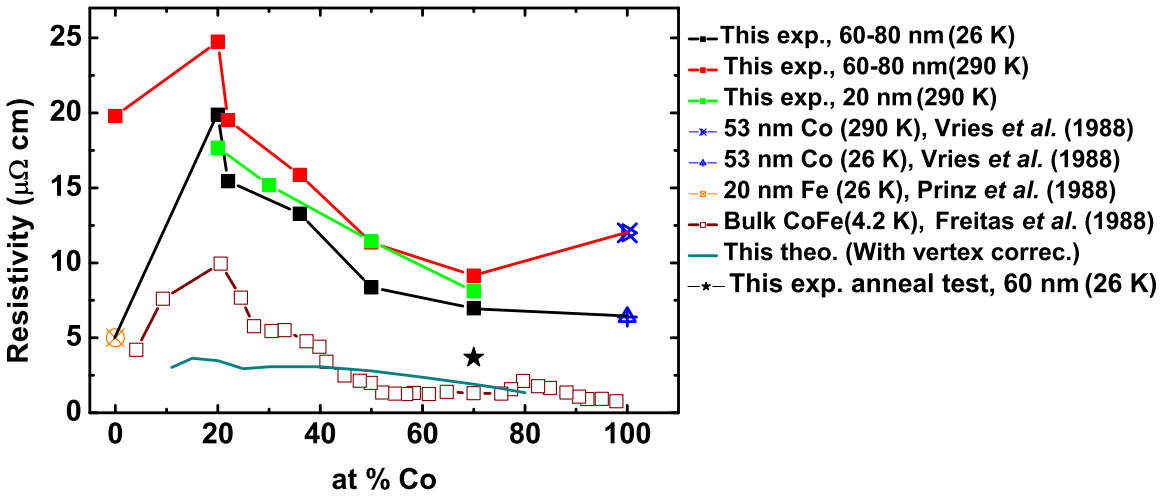

Figure 6.2: Resistivity plotted against Co content. Measured resistivity in this experimental work at 290 K for thick 60 nm film (red filled square) and thin 20 nm films (green filled square), at 26 K for thick films (black filled square). Annealed sample resistivity at 26 K (filled star). Experimental data from literature for bulk CoFe at 4.2 K [109](open squares) along with 20 nm Fe at 26 K [220] (circle with cross) and 53 nm Co at 26 K and 296 K [221] (right facing triangle and top facing triangles with cross respectively). Theoretically calculated resistivity due to chemical disorder only at 0 K (line).

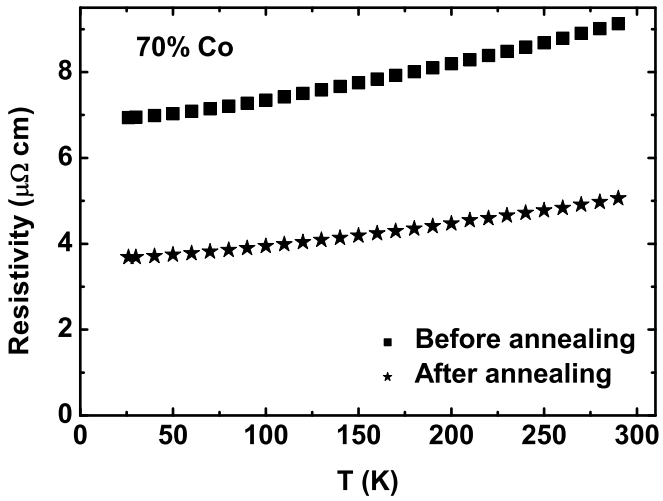

Figure 6.3: Resistivity of 60 nm thick $Co_{70}Fe_{30}$ test sample plotted as a function of temperature before (filled square)and after annealing (filled star) at 400° C for 5 minutes.

annealing in oven at 400 ° C for 5 minutes. The result is shown in Fig. 6.3 and also as a star in Fig. 6.2. The resistivity reduces from 6.94 $\mu\Omega$ cm to 3.68 $\mu\Omega$ cm at 26 K.

Theoretical calculation results

In order to understand the effect of electron bands on the measured resistivity, band structure calculations were carried out by H. Ebert and co-authors. Figure 6.4 shows the density of states (DOS) of majority spin up (in red) and minority spin down (in blue) states for CoFe alloys from Co content 20% till 70%. We notice that the DOS of the majority spins decreases with decrease in Co content (from bottom to top) and crosses the Fermi surface for $x_{\mathrm{Co}} = 0.2$.

Besides the calculation of ρ due to pure chemical alloying at 0 K, additional calculations were carried out including contribution from phonons (uncorrelated vibrations) and spin-fluctuations. This calculation is done for a 50% Co material in the temperature range of 100 K to 300 K. The result of the calculation is shown in Fig. 6.5. The black line corresponds to the isotropic resistivity calculated at 0 K, the purple for the calculated resistivity with the inclusion of uncorrelated vibrations which can be called the contribution from electron-phonon interaction, the green lines for the resistivity calculated by including spin fluctuations only. Finally the blue lines represent the resistivity calculation result including all the above contributions. Each contribution is calculated twice, one with a temperature independent potential (light color line) and the other with temperature dependent potential (dark color line). We notice very little difference between the two. The red triangles are the measured ρ for 50% Co film.

The red line in Fig. 6.5 includes the contribution from only temperature induced vibrational disorder which is 3.94 $\mu\Omega$ cm at 100 K and increases upto 7.86 $\mu\Omega$ cm at 300 K. The $\Delta\rho^{'}$(T) increases by 3.92$\mu\Omega$ cm as temperature is increased from 100 K to 300 K. Now calculating the contribution from temperature induced spin fluctuations only, the ρ jumps from 7.5 $\mu\Omega$ cm to 17.79 $\mu\Omega$ cm, i.e., the corresponding $\Delta\rho^{'}$(T) = 9.29 $\mu\Omega$ cm between 100 K and 300 K. Incorporating the above two contributions, the effective ρ is shown as blue line where the ρ jumps from 8.57 $\mu\Omega$ cm to 23.21 $\mu\Omega$ cm, an increase by 14.64 $\mu\Omega$ cm in the same temperature range.

Discussion

In this section, we discuss the experimental and theoretical results in detail. The resistivity for all compositions exhibit metallic behavior indicated from its temperature dependence. The low temperature ρ_0 values in our films are larger than the ρ_0 of 0.03 $\mu\Omega$ cm for pure Fe [220, 222] and 6.51 $\mu\Omega$ cm of pure Co [221]. They are also larger than ρ_0 of 1.67 $\mu\Omega$ cm for bulk $Co_{20}Fe_{80}$ sample measured at 4.2 K in the experiments by Freitas *et al*. [109]. The observation of such large magnitude of ρ_0 in comparison to pure metals as well as to alloys from other groups, indicate large contribution from grain boundary scattering.

Unlike most experimental work in the literature, the films in our study did not undergo any post deposition thermal treatment. This removes grain boundaries from where electrons can scatter and contribute to the larger ρ_0 compared to pure metals and annealed alloys. This is verified by the reduction of ρ_0 after the annealing test

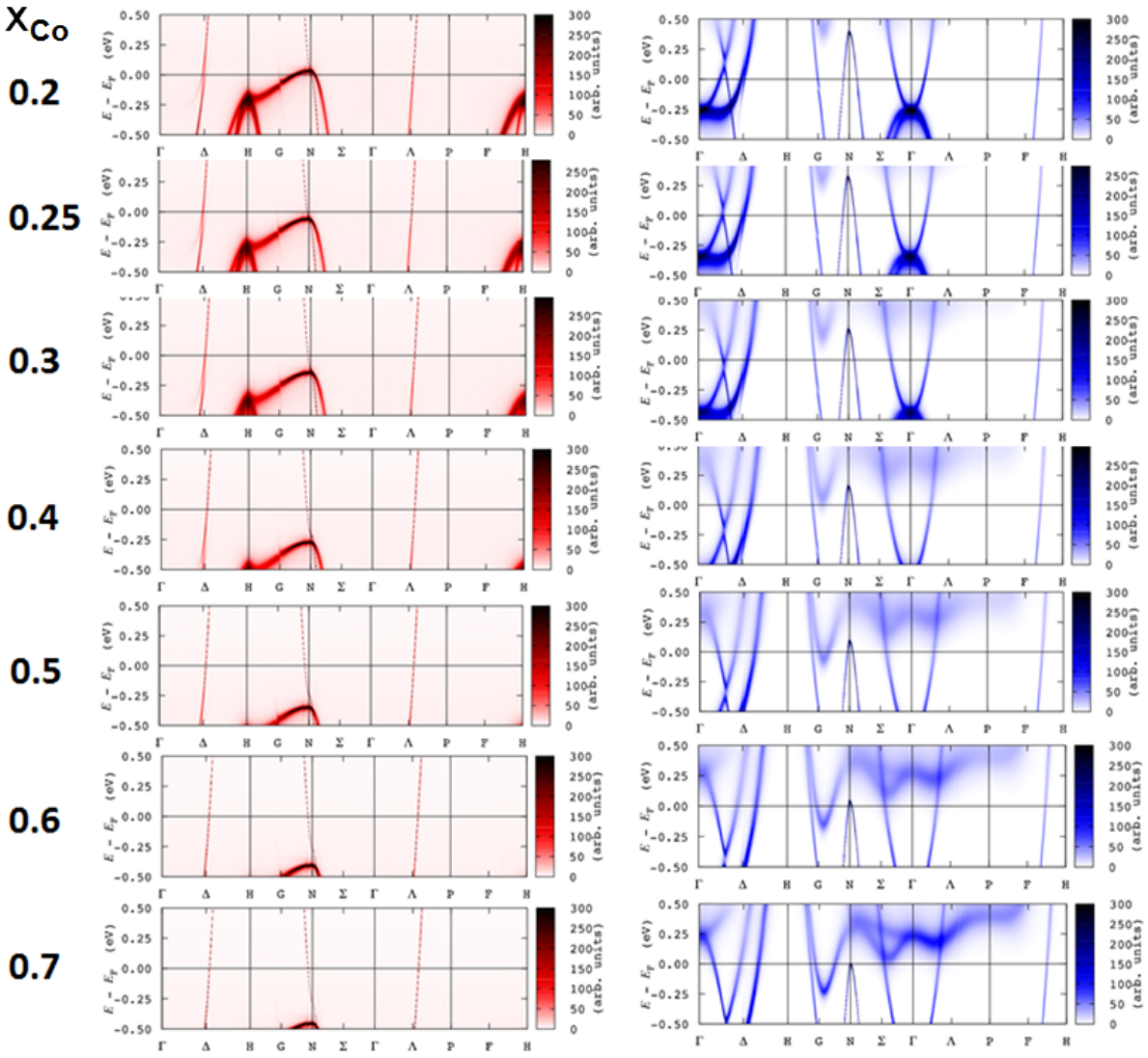

Figure 6.4: The density of states for majority spin up (red) and minority spin down (blue) states of CoFe with increasing Co content from top to bottom labeled by x_{Co}.

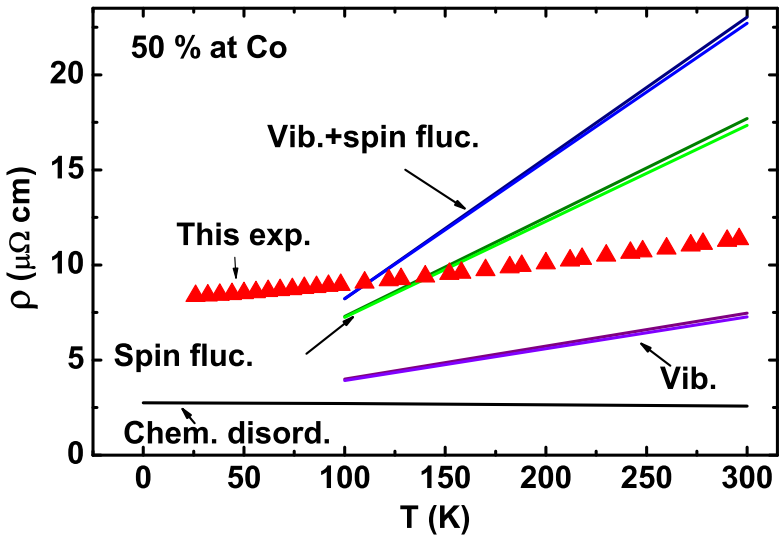

Figure 6.5: (a) Theoretically calculated resistivity as a function of temperature. With only chemical disorder (black line), with only uncorrelated vibrations or phonons (purple line), with only spin fluctuations (green line) and including all the above (blue line). For each calculation, dark color line stands for calculation with temperature dependent potential and light color line for without T dependent potential. Measured resistivity for 50 % Co film (red triangles).

as observed in Fig. 6.3.

The effect of the disorder is also manifested in the weaker temperature dependence of $\Delta\rho$(T) in comparison to pure Fe [220] and Co [221] metals. The $\Delta\rho$(T)=ρ(296 K)-ρ(26 K) for pure Fe [220] and Co [221] are reported to be 10.41 $\mu\Omega$ cm and 6.23 $\mu\Omega$ cm respectively which are larger than the $\Delta\rho$(T) observed in our films. In contrast, our measured ρ(T) and $\Delta\rho$(T) are quite comparable to the results studied experimentally by Ahn *et al*. [110] where resistivity has been measured for 200 nm $Co_{50}Fe_{50}$ and $Co_{70}Fe_{30}$ films between 4.2 K and 296 K. For the above two compositions, the room temperature absolute resistivity values are reported to be 11.3$\mu\Omega$ cm and 10.3$\mu\Omega$ cm and the $\Delta\rho$(T) to be 3.8 $\mu\Omega$ cm and 4.3 $\mu\Omega$ cm respectively.

Comparing the $\Delta\rho$(T) with the the phonon resistivities of polycrystalline Co (5.6 $\mu\Omega$ cm) or Fe (9.3 $\mu\Omega$ cm) [110], the deviation from these values can be attributed to the deviation from Matthiessen's rule. The deviation from Matthiessen's rule in our samples is rather small. In the work by Arajs *et al*. in [223], the residual resistivity and deviation from Matthiessen's rule have been discussed for solutes in bulk iron samples. It was shown there, that most transition metal solutes in iron, exhibit small $\Delta\rho$(T) and large deviation from Matthiessen's rule due to spin flip scattering among the spin up and down electrons in the two d bands. However, exceptions were observed for solutes of Co, Ni and Sn transition metals which observed not only small $\Delta\rho$(T) but also small deviation from Matthiessen's rule. Although the exact reason for such exception is not understood, the observations are quite consistent with what we have found in our samples.

Regarding the features of ρ vs Co content graph in Fig. 6.2, the shape of the graph is that of an isotropic alloy suggesting decreasing electron density effect with decreasing Co content. In a simplistic picture, Fe has one less electron than Co, hence with addition of more Fe, i.e., with reduction of Co content, the alloy conduction band depletes and the resistivity increases monotonically. This observation agrees with the theoretically calculated ρ as well as the experiments of Freitas *et al*. [109] in bulk CoFe (Fig. 6.2).

In regards to the thickness dependence of ρ, we observe no significant thickness dependent behavior as shown in Fig. 6.2. Here too the monotonous increase in resistivity with in crease in Fe amount maintains the trend exhibited by the relatively thick films as in the Fig. 6.2, including the sharp jump of resistivity close to 20% Co. Due to the grain boundary or in some cases surface scatterings of electrons [224], which reduce the electron mean free path in thin films, higher resistivity values are observed compared to their bulk counterparts. However, in our polycrystalline and highly diffusive system, the electron mean free path is comparable to atomic order at this temperature range and hence the change does not appear to be drastic from 20 nm to 60 nm.

The behavior of ρ vs Co content is also understood from the band structure calculation as shown in Fig. 6.4. From the majority spin state band structure we see band filling with decrease in Co concentration, i.e., decrease in density of state. With steady decrease in the density of state of the d bands the availability of states for the s electrons to scatter decreases and that results in the rise in the electrical resistivity. Again referring to the DOS figure, starting with the highest Co, with decreasing Co electron density, the d-bands below the Fermi level keep getting filled and after a certain composition, it hits the Fermi surface. Due to the flatness of the band, the Fermi velocity drops and thus generates a sharp jump in the resistivity. As more and more electron are added, the slope of the band changes with respect to the Fermi surface and the conductivity increases. This is one of the explanations for the peak observed in not only our measurements but also in the experiments by Freitas *et al*. [109] as shown in Fig. 6.2.

Next we discuss the temperature dependent calculation of the various contributions to ρ shown in Fig. 6.5. It appears that the Matthiessen's rule is followed in these resistivity calculations, i.e., the ρ from the only phononic contribution and from the only spin-fluctuation contribution add up to the ρ calculated taking both contributions into account. The magnitude of the resistivity at 100 K with the inclusion of only impurity and vibronic disorder is about 7-8 $\mu\Omega$ cm, which is shy by a small value to what we have measured at that temperature (triangles). This implies that the calculations provide good estimate of the contribution of electron-phonon scattering to ρ. However, the addition of spin-fluctuations grossly overestimates the $\Delta\rho^{'}$(T) value in comparison to measurement at all temperatures.

Keeping the various contributions from the theoretical calculation in mind, we proceed to separate the contribution of various scattering processes in our measured resistivity. As discussed in Chapter 2, in a non-ferromagnetic metal, the Bloch-Grüneisen function equation (2.26) with $n = 5$ is used to separate the contribution of electron-phonon interaction $\rho_{\mathrm{el-ph}}$ from the impurity scattering component. However, in a ferromagnetic film magnon scattering contribute to ρ at higher temperatures. Hence Bloch Wilson (BW) formula with $n = 3$ (for s-d scattering of electrons) is more suitable in the lower temperature region to separate $\rho_{\mathrm{el-ph}}$. Following the experiments by Kamalakar *et al*., [125], we make BW fit to our measured ρ from 26 K to 100 K and then

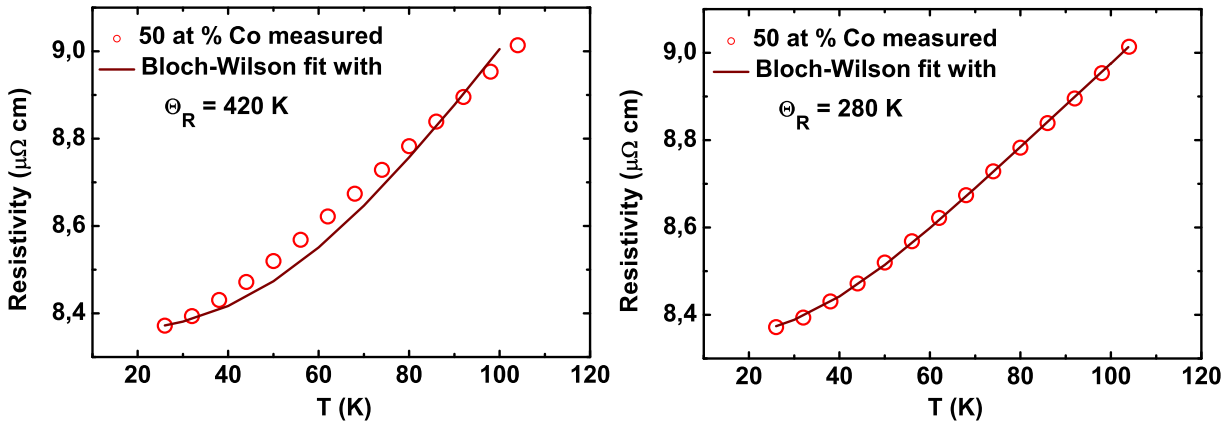

(a) (b)

Figure 6.6: Bloch-Wilson function fit (line) to measured data for 50 % Co sample (open circle) from 25 K upto 100 K, for fitting parameter (a) Θ_{Debye} = 420 K (b) Θ_{Debye} = 280 K.

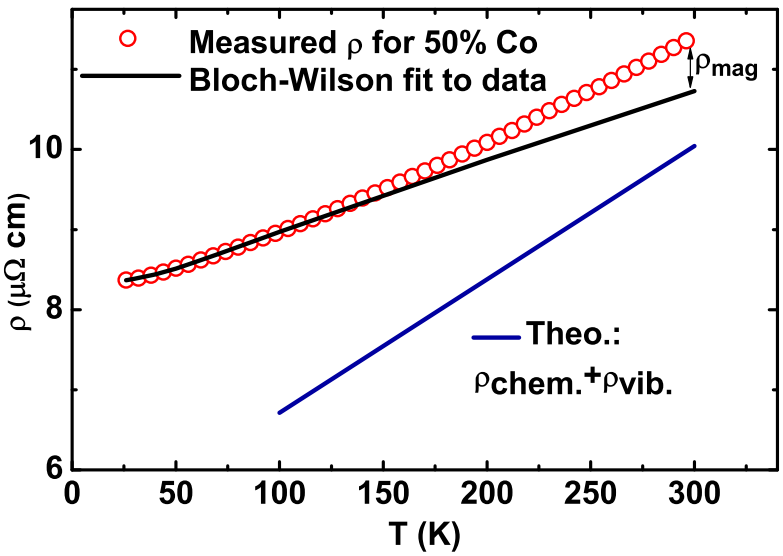

Figure 6.7: Resistivity as a function of temperature. Measured resistivity for 50 % Co sample (open circle), Bloch-Wilson fit upto 100 K and then extrapolated upto 296 K (black line). The difference between the measured and the fit data is resistivity due to magnon scattering (double headed arrow). Theoretically calculated resistivity taking only uncorrelated vibronics or phonons into consideration (blue line).

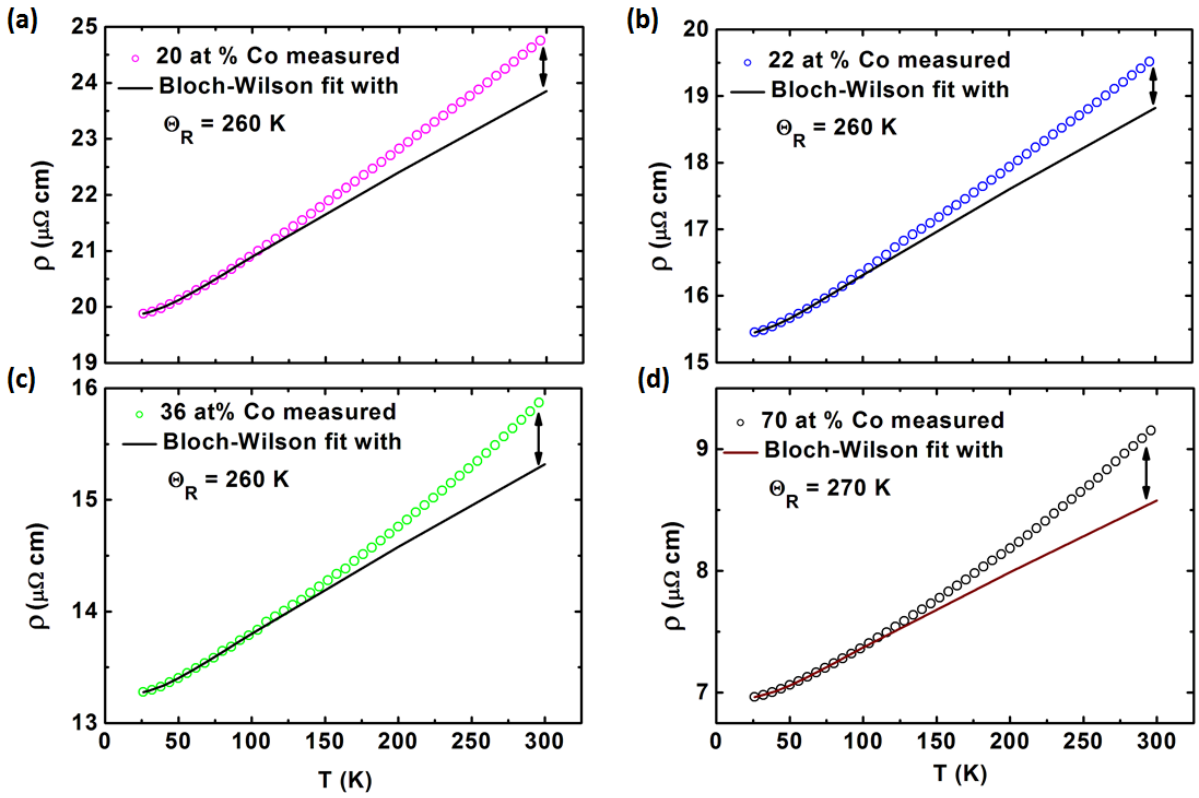

Figure 6.8: Bloch-Wilson function fit from 25 K to 100 K and then extrapolated to 296 K (line) on measured data (open circles) as a function of temperature at varying Θ_{Debye} for (a) 20 % Co, (b) 22 % Co, (c) 36 % Co and (d) 70 % Co. The resistivity due to magnon scattering (double headed arrow).

extrapolate this fit upto 300 K. The difference between the measured ρ and the extrapolated BW fit from 100 K to 300 K yields the contribution from magnon scattering ρ_{mag} to our measured ρ in the samples.

To fit our resistivity data with the BW function, we use ρ_0, $\alpha_{\text{el-ph}}$ and Θ_R as free parameters. As an initial guess for the Bloch-Wilson temperature Θ_R, we take 420 K. This is the average value of Θ_{Debye} for pure Fe and Co. We could not find any published values of Θ_{Debye} for CoFe alloy system. Figure 6.6(a) shows the BW fit with Θ_R=420 K to our 50% Co sample ρ data. We see that it fails to fit the data completely. A good fitting is possible by reducing the Θ_R to 280 K as shown in Fig. 6.6(b). In many instances changing the Θ_R, mostly by reducing it provides a good fit to the measured resistivity [225]. Additionally the disagreement between Θ_R and Θ_{Debye} is not very surprising since the Θ_{Debye} is an artifact of the Debye model.

Once proper fitting parameters upto 100 K has been established, extrapolation of this fit it carried upto 300 K. As an example, the BW fitting for the 50% Co film is shown in Fig. 6.7. The ρ_{mag} is shown as a double headed arrow and is smaller than the electron-phonon scattering contribution. At this point, comparison with theoretical calculation is made. The vibronic contribution from theory (blue line in Fig. 6.5) is comparable to our BW fit data. It is safe to state that the theoretical model is able to calculate electron-phonon scattering contribution to the charge transport to a good degree of accuracy. In Fig. 6.5, we have seen that the combination of theoretical

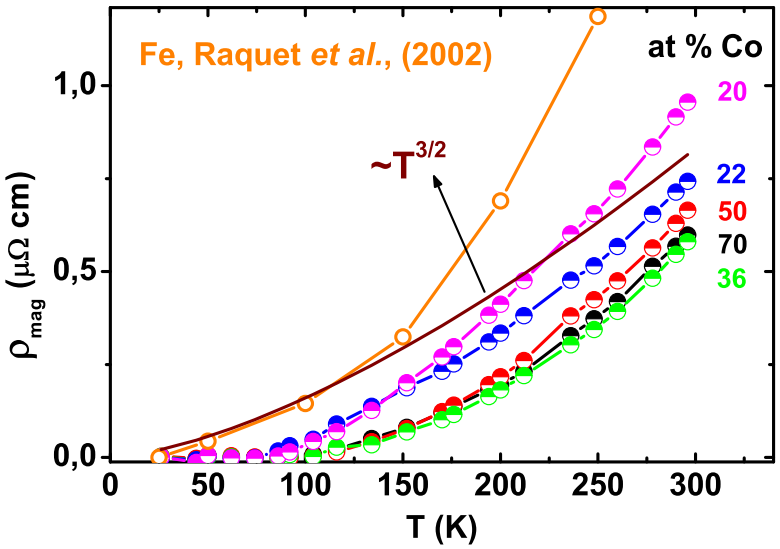

Figure 6.9: The resistivity due to magnon scattering as a function of temperature upto 296 K for all CoFe films labeled with Co content in %, from literature for bulk Fe [226] (open circles). The line represents f$\times T^{3/2}$ (f=0.0016) curve.

impurity scattering and phonon scattering stands little shy of the measured ρ but the inclusion of the measured spin fluctuation contribution overshoots the calculated ρ. Therefore only a smaller contribution from the spin fluctuations, i.e., from the electron-magnon scattering is all that is required to compensate for the difference. We have seen already that the Matthiessen's rule is followed by our samples, i.e., $\rho = \rho_{\text{el-imp}} + \rho_{\text{el-phonons}} + \rho_{\text{el-mag}}$. With the knowledge of electron-phonon scattering contribution, the electron-magnon scattering contribution from simple subtraction from the total ρ is justified.

The BW fitting to the resistivity of the rest of the films is shown in Fig. 6.8(a)-(d). The Θ_R values vary within the range of 260 K - 270 K. The ρ_{mag} is collected and plotted together as a function of temperature in Fig. 6.9. We observe an increase in the magnon scattering contribution with the increase in temperature and also with increase in Fe content. The origin of lower ρ_{mag} for 36% Co is from the fact that the CoFe system has maximum magnetization about 30% Co [75]. AT 200 K, the ρ_{mag} varies between 0.195 $\mu\Omega$ cm for 70% Co upto 0.412 $\mu\Omega$ cm for 20% Co which correspond to 2.38% and 1.89% of the total ρ respectively. Similarly at 296 K the corresponding numbers are 0.598 $\mu\Omega$ cm and 0.955 $\mu\Omega$ cm which correspond to 6.53% and 3.86% of the total ρ respectively. All ρ_{mag} values are tabulated in table 6.2. This magnon scattering contribution is compared with what magnons contribute to the the total ρ of pure Fe and Co in the contribution by Raquet *et al*., [226]. The ρ_{mag} for bulk Fe is shown as open circles in Fig. 6.9. The values agree with our measured ρ_{mag} with maximum contribution of 1.6 $\mu\Omega$ cm from pure Fe at 300 K (not shown in the figure).

As discussed previously in Chapter 2, at the low temperature limit, the magnon number is given by equation 2.35, i.e., it has a $T^{3/2}$ dependence. Intuitively, if the resistivity due to magnon scattering is dominated by the

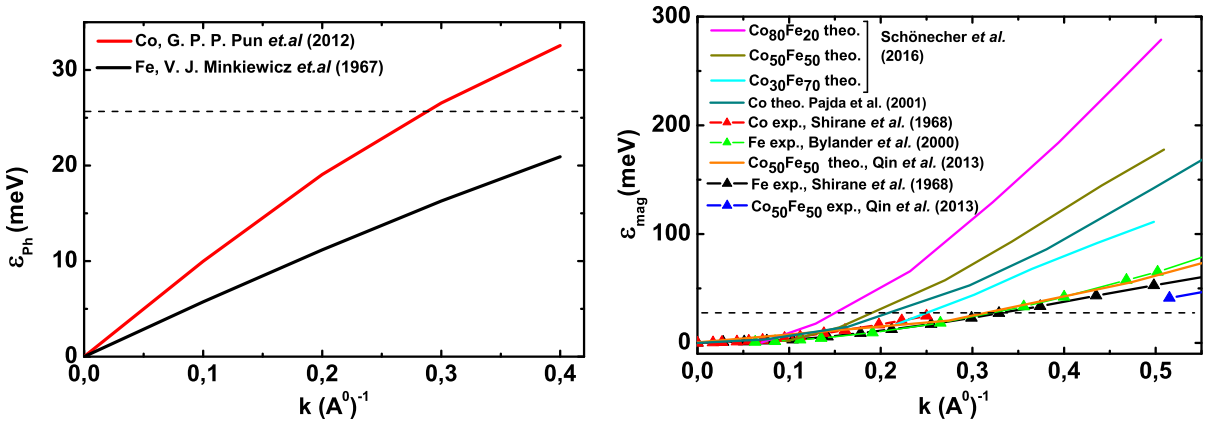

(a) (b)

Figure 6.10: a) Literature phonon dispersion for Fe [227] (black line) and Co [228] (red line), dashed line stands for room temperature. (b) Literature magnon dispersion for theoretical $Co_{30}Fe_{70}$ (light blue line), $Co_{50}Fe_{50}$ (dark yellow line) and $Co_{80}Fe20$ (magenta line) [232], theoretical Co [237] (blue line), experimental Fe [229] (green triangle), [230] (black triangle), Co [230] (red triangle), theoretical $Co_{50}Fe_{50}$ [231] (orange line), experimental $Co_{50}Fe_{50}$ [231] (blue triangle) .

electron-magnon scattering time, which varies with the magnon number density, then the ρ_{mag} should have a $T^{3/2}$ dependence. That is why in fig 6.9, we have additionally plotted a line denoting theoretical ρ_{mag} given by f$\times T^{3/2}$, where f=0.0016 is a scaling factor required to fit the calculated value in our range of data. This line appears to agree with the result for Fe ρ_{mag} from the work of Raquet *et al*., [226] but only upto 150 K. Above this temperature, the theoretical ρ_{mag} is suppressed and agrees in magnitude with our measured result. However a $T^{3/2}$ dependence fails to fit our measured ρ_{mag} data in the entire temperature range. In fact the data can not be fitted to any single power law function. This suggests that the ρ_{mag} does not have a simple power law dependence on temperature rather it is a more complicated function. One can refer to the theoretical model calculation of ρ_{mag} in the work of Raquet *et al*. which suggests a complicated temperature dependent function (see equation (8) in [226]).

In order to further ensure that the magnons are indeed involved in the scattering process with electrons and contribute to the resistivity, we discuss the phonon and magnon dispersion of Fe, Co and their alloys. Fig. 6.10(a) shows the phonon dispersion relations for Fe and Co. We see that the Θ_{Debye} for these metals are close to or above room temperature (dashed line at 28.86 meV) indicating that at this point, all the high temperature phonon modes are excited and participating in the scattering processes. However, in the corresponding magnon dispersion relation as shown in Fig. 6.10(b), the energy scales are much higher. The magnon energy corresponding to the Θ_{Debye} for phonons, i.e., Θ_{mag} for Fe and Co are at 280 meV and 730 meV respectively which are at least 10 to 20 times larger than the Θ_{Debye}. The theoretical magnon dispersion for CoFe alloys in a wide range of composition [229, 230, 233, 234], lie above the dispersion of pure Fe but around the dispersion curve of pure Co. Furthermore the available values of spin wave stiffness constant ($D^{'}$ defined in equation 2.32) for Fe, Co and their alloys from literature have been collected and tabulated in table 6.1. We see that the $D^{'}$ of Fe is the lowest

(250 meV $\AA^2$) and of the Co is the highest 808 meV $\AA^2$. The $D^{'}$ of the CoFe alloys lie in between these two ranges. Additionally some of the literature values of $D^{'}$ from Table 6.1 are shown in Fig. 6.11. In this figure, the different color of the legends represent different literature from were the $D^{'}$ values have been collected. The $D^{'}$ for bcc Fe from experiments by Shirane *et al*. [230], Bylander *et al*. [229] and theory by Pajda *et al*. [237] agree quite well. Similarly good agreement is also observed for $D^{'}$ of fcc Co from experiments by Shirane *et al*. [230] and theory by Pajda *et al*. [237]. Pajda *et al*. [237] have additionally calculated $D^{'}$ of intermediate CoFe alloys which follows the magnetization vs Co concentration trend of these alloys(represented by dashed line as a guide to the eye). In these theory calculations, a clear discrepancy is observed for 50% Co film, the reason of which according to the authors, is unclear. Nevertheless the collected $D^{'}$ values from literature indicates that in our range of measurement temperature, only low energy magnons have been excited and we can safely take low temperature magnon number (equation 2.35) into consideration for interpreting our result.

Spin wave stiffness constant $D^{'}$		
Material	$D^{'}_{\text{Exp.}}$ (meV $\AA^2$)	$D^{'}_{\text{Theo.}}$ (meV $\AA^2$)
Co (fcc)	340([230])	-
Co (fcc)	466 ± 16([233])	808([233])
Co (bcc)	325 ± 40([234])	-
Co (fcc)	580, 510 [237]	663([237])
Fe (bcc)	286([229])	-
Fe (bcc)	280, 330 [237]	250 ± 7([237])
$Co_{30}Fe_{70}$ (bcc)	470 ± 14 ([234])	-
$Co_{37}Fe_{63}$ (bcc)	530 ± 17 ([234])	-
$Co_{47}Fe_{53}$ (bcc)	800 ± 50 ([234])	-
$Co_{50}Fe_{50}$ (bcc)	-	560, 465, 289 ([84])
$Co_{68}Fe_{32}$ (bcc)	476 ± 15 ([234])	-

Table 6.1: Collected spin wave stiffness constant, both experimental or ab-initio values, for Fe, Co and their alloys. The values of spin wave stiffness constant for Fe are always for Fe in bcc crystal structure while for Co, both bcc and fcc values are collected. The source citation number is written beside each value in square bracket.

We return to the electron-phonon contribution to ρ. From the Bloch-Wilson fitting, we are able to collect the electron-phonon interaction parameter, α_{e-ph}. The parameter α_{e-ph} decreases with decreasing Co content except for the film with 36%. The purpose of studying this coefficient is that the α_{e-ph} is proportional to the electron-phonon coupling constant λ_{BW} via the relation (2.28) in Chapter 2. The coupling constants can be calculated using available parameters for pure Fe, i.e., m^*=8 $\times$ m=8 $\times$ 9.1×10^{-31} Kg, n_e=8.5×10^{28} m^{-3} and υ_s=5900 m/s since the corresponding values for CoFe are not available yet. The extracted λ_{BW} values are as shown in the table 6.2.

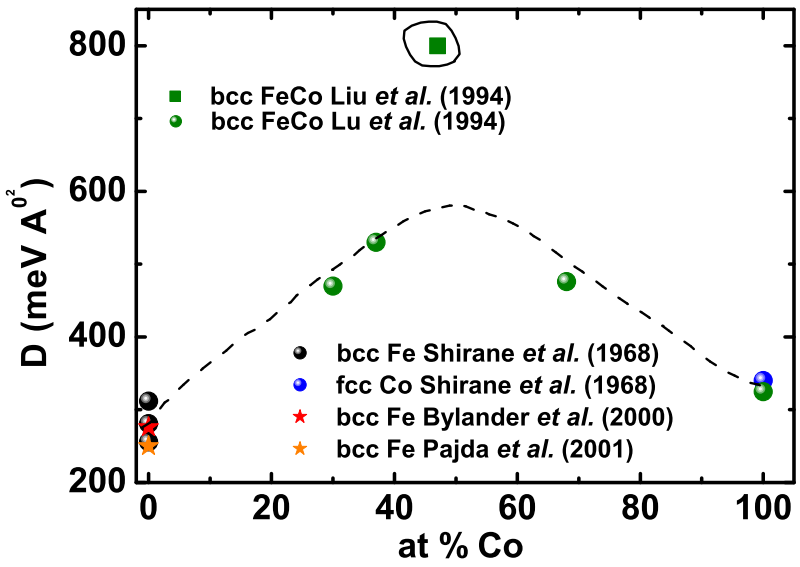

Figure 6.11: The spin wave stiffness constant D' of CoFe as a function of Co concentration, collected from literature. The $D'_{Exp.}$ for bcc Fe are from Shirane *et al*. [230] (black circle), Bylander *et al*. [229] (red star) and $D'_{Theo.}$ from Pajda *et al*. [237] (orange star). The $D'_{Exp.}$ for a series of bcc CoFe alloys are from Liu *et al*. [234] (green circle) where a discrepancy is observed for 47% Co film (green square with a free hand circle around it), the reason for which is unclear according to the authors. The $D'_{Exp.}$ for fcc Co (blue circle) is taken from Shirane *et al*. [230]. The dashed line is a guide to the eye.

Parameters in Bloch-Wilson fit to ρ					
% Co	$\rho_0(\mu\Omega$ cm)	Θ_R (K)	$\alpha_{e-ph}(\mu\Omega$ cm)	λ_{BW}	$\rho_{mag}(\mu\Omega$ cm)
20	19.83	260 – 270	7.2	0.436	0.9549
22	15.41	260 – 270	6.1	0.514	0.741
36	13.25	260 – 270	3.7	0.848	0.5513
50	8.345	270 – 280	4.5	0.697	0.6298
70	6.944	260 – 270	3.04	1.032	0.5977

Table 6.2: Bloch-Wilson fit parameters ρ_0, Θ_R and α_{e-ph} to the resistivity of the CoFe films and the extracted electron-phonon coupling parameter λ_{BW}. The extracted magnon scattering resistivity at 296 K.

Temperature coefficient of resistivity

The temperature coefficient of resistivity (*TCR*) is an intrinsic property of a material which signifies the resistivity change factor with change in temperature. *TCR* is given by equation 2.29, mostly for linear T dependence of ρ (in our case above 50 K). The *TCR* for all our 5 CoFe samples have been calculated using numerical differentiation of ρ from Fig. 6.1(a) over corresponding ρ_0 and plotted together as a function of temperature in the Fig. 6.12.

The *TCR* shows interesting features which can be expressed via comparison with the resistivity data in Fig. 6.1(a). What seems apparent from the very first look is the absence of strict composition dependence. The *TCR* for sample with Co content 50% shows highest value followed by film with Co 70% forming a group with each other and staying above the rest. Film with Co content 36% has the least *TCR* at all temperatures and film with Co 22% clearly breaks the symmetry. Until 120 K, the Co 22% film *TCR* keeps close to Co 70% film but later deviates. After around 120 K, the *TCR* for films with Co 20% and 22% seem almost independent of temperature. The slight dip in the *TCR* around 240 K for all samples could be due to some systematic error present in the set-up since there seems no physical significance attached at this particular temperature.

The *TCR* at room temperature for pure bulk Fe is 5.6 $\times 10^{-3}$/C$^\circ$ while for pure Co it is 7 $\times 10^{-5}$/C$^\circ$. The *TCR* for most novel pure metals such as Pt, Au, Ag etc is in the order of magnitude range of 3 - 4 $\times 10^{-3}$/C$^\circ$. In comparison, the *TCR* for our films is one order of magnitude smaller. This again is an indicator of increased degree of disorder due to alloying as well as grain boundary scattering effects.

6.3 Thermal conductivity

The whole design of the membrane platform has been done keeping in mind the challenging task of measuring the thermal conductivity (κ) of thin films. The contribution from SiN_x background has been taken into account while calculating the κ of the CoFe films. In the resistivity section, we have seen how the various scattering processes have contributed to the transport of electrons in the films. In this section, the measurement

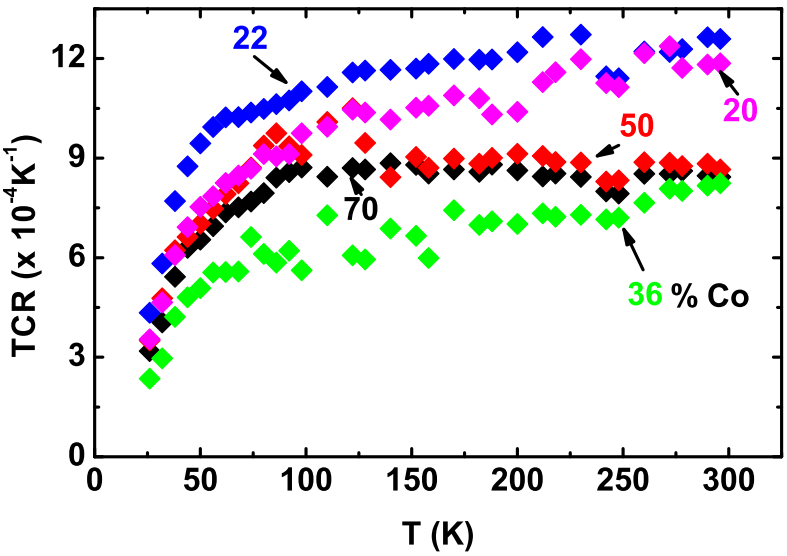

Figure 6.12: Temperature coefficient of resistivity for samples labeled with Co contents in % plotted vs temperature

results of the thermal conductivity has been elaborated and the contributions from scattering among various quasi-particles is discussed.

6.3.1 Thermal conductivity of CoFe films

Results

Figure 6.13 shows the total thermal conductance K_B of all 5 CoFe films and the average K_{SiN} as a function of bath temperature. The error bars on the CoFe curves are obtained from the uncertainty of the slopes from T_H vs P_H and T_C vs P_H curves as explained in the error analysis section in Chapter 4.

Each conductance trace increases rapidly starting from 26 K and then becomes flat at higher temperatures. At $T > 50$ K, K_{SiN} is much smaller than the total K_B, hence after subtraction, the measured K_{CoFe} should be quite acceptable. However, the uncertainty arises at lower temperatures when the K_{SiN} and the K_{CoFe} become comparable and thus these data are not discussed any further.

We are interested to see if any patterns emerge in the behavior of thermal conductivity vs temperature curves of our samples. In Fig. 6.14, we notice that minimum κ at high temperatures is exhibited by the 20% Co sample upto 150 K. However, at 150 K, the curve for 20% Co sample crosses over the 36% Co sample curve and therefore below this temperature minimum κ is exhibited by 36% Co sample. The κ values for 50% and 70% Co films remain close to each other. Thus with an exception of the film with 36% Co, we can state that the samples follow the same pattern of behavior as exhibited by resistivity.

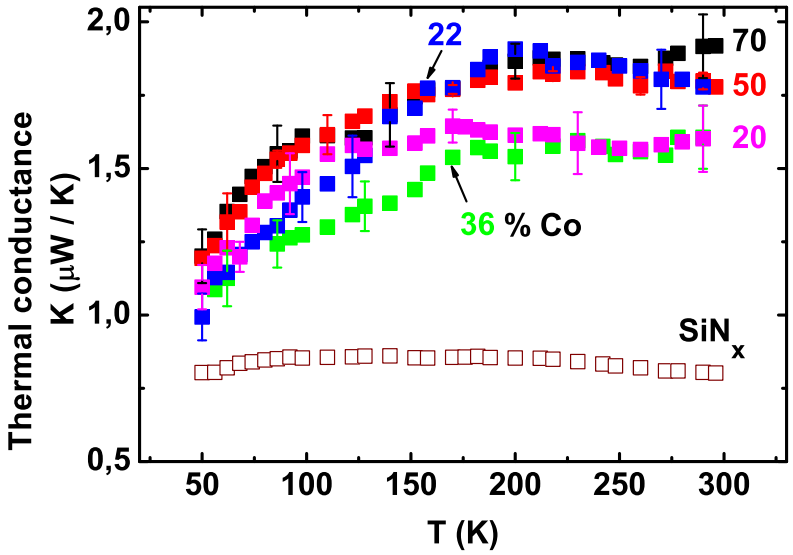

Figure 6.13: The bridge with CoFe film thermal conductance (filled squares) labeled with Co content in % and the SiN_x thermal conductance (open squares) as a function of temperature. The error bar calculated from the uncertainty in the slopes of T_H and T_C vs P_H.

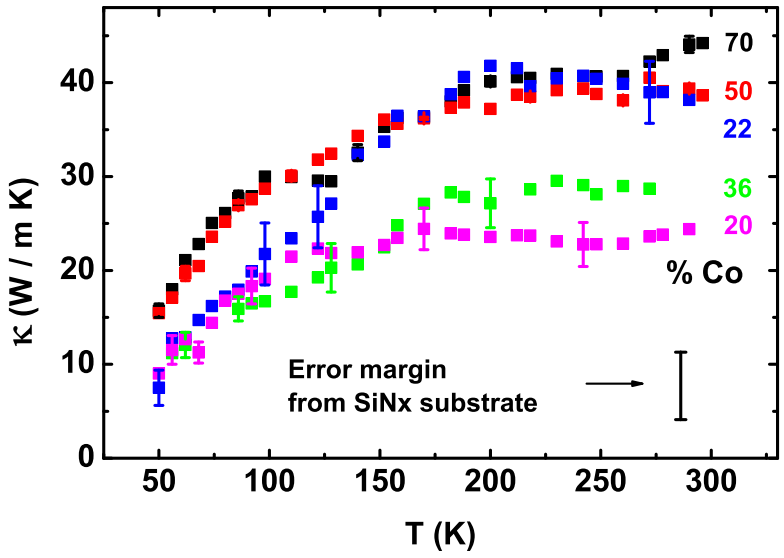

Figure 6.14: The thermal conductivity for CoFe films (filled squares) with Co content in % vs temperature. The big error bar represents the maximum error range incurred by scatter in background SiN_x substrate thermal conductivity.

The error from the background contribution from different SiN_x membranes has been shown as the error bar beside the κ values of the CoFe films in Fig. 6.14. In case the κ values of the CoFe films happen to lie very close to each other, then an error of the order of 7.5 W/m K could disturb this pattern. For example, if we take a closer look at the κ values for films with Co 70% and 50% then we see that an error of an order one W/m K introduced by wrong background subtraction could have caused the two curves to lie so close to each other at all temperatures which is not the case for electrical resistivity values. But then this much background error fails to explain the huge deviation from the behavior exhibited by samples with Co 22% and 36%.

Moreover, the thermal conductivity data in Fig. 6.14 closely resembles the behavior that we have observed for the temperature coefficient of resistivity for our films. We can make qualitative comparison between Fig. 6.12 and 6.14. We see that in both the cases the films with Co content 50% and 70% are above the rest of the curves and close to each other. The 36% Co content sample is at the bottom in case of TCR and partly at the bottom in case of κ. Film with Co 22% lie above the rest in both cases. In Fig. 6.14 the κ value for the 22% Co sample is close to the values for Co 50% and 70%. While as far the TCR is concerned, the value for film with Co 22% is closer to the 50% and 70% films below 120 K and closest to 20% Co film. Finally, the κ values for films with Co 20% and 36% are more or less temperature independent at higher temperatures. Similar behavior was observed for 20% Co film in its TCR vs temperature plot (Fig. 6.12).

Discussion

To begin the discussion, the qualitative high temperature behavior of κ is not surprising. The measured ρ at these temperatures vary almost linearly with temperature as we have seen in Fig. 6.1(a). This implies that the linear temperature dependence of ρ cancels out and the κ turns out to be T-independent. At high temperatures, the phonon population grows and the strong electron-phonon and phonon-phonon scattering suppresses the high temperature κ. We also have to consider the inelastic electron-phonon and electron-magnon vertical scatterings which contribute to thermal transport but not to pure electronic transport.

Next is the discussion on the separation of the contributions of electrons, phonons and magnons to the total κ. The first quasi-particle to consider are the electrons. The Wiedemann-Franz expectation of the electronic thermal conductivity (κ_e) is calculated from the measured electrical resistivity. This has been made possible in our measurement technique since all the transport coefficients have been measured simultaneously. Here the κ_e has been calculated from our measured ρ values using the Sommerfeld value for the Lorenz number $L_0 = 2.45 \times 10^{-8}$ W Ω/ K^2. The $\kappa_e = L_0 T/\rho$ is shown as lines in Fig. 6.15(a) together with the total measured κ.

We see that at temperature below 150 K, the electronic thermal conductivity almost agrees with the measured total κ for all samples with Co content $\geq$ 36%. For samples with Co 20% and 22%, the κ_e values are underestimated. At higher temperatures the κ deviates strongly from the Wiedemann-Franz expectation where the estimated κ_e keeps increasing while the actual total κ flattens out. The exception being film with Co 22% where the estimated κ is underestimated at all temperatures. For films with Co 50% and 70%, the estimated κ_e is almost twice the measured κ values. This indicates that we have gross violation of Wiedemann-Franz law for

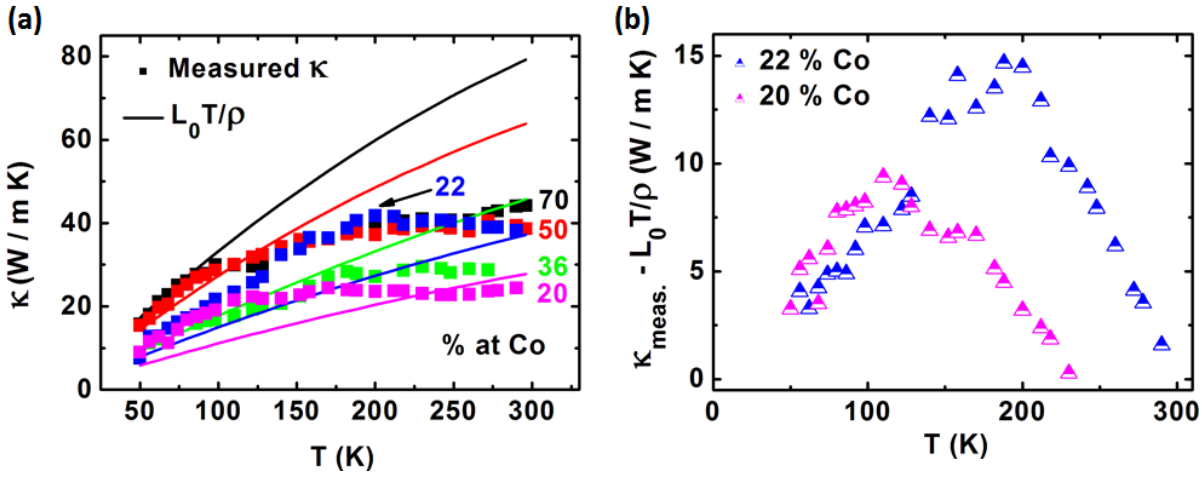

Figure 6.15: (a) Measured thermal conductivity (filled squares) and Wiedemann-Franz expectation calculated from the measured resistivity values (lines) vs temperature labeled with Co content in %. L_0=2.45 × W Ω/K^2 is the Sommerfeld value of the Lorenz number. (b) Difference between measured and calculated (from ρ) thermal conductivity (half filled triangles) for films with Co content 20 % (magenta) and 22 % (blue).

all compositions.

First for a positive deviation from Wiedemann-Franz expectation, as observed for films with Co 20% and 22%, we can express the deviation as an additional contribution to thermal conductivity from quasi-particles other than electrons. This non-electronic contribution to κ for these two films is calculated using $\kappa - \kappa_e$ and plotted in Fig. 6.15(b). It has been observed in the XRD measurements that these two films are in a single bcc phase. Therefore significant contribution from phonons to the thermal conductivity is expected in these films. This contribution has the typical shape of κ_{ph} which initially increases sharply with temperature and then drops as the population of phonons increases at higher temperatures. The peak structure in κ_{ph} resembles the well known Umklapp peak. However, the temperature at which the peaks appear in our case between 100-220 K can not represent the Umklapp peak which ideally should be below 100 K for this material.

For negative deviation from Wiedemann-Franz law, we discuss the likely reason, the presence of in-elastic electron scatterings. As we have discussed in the introduction to thermal conductivity in Chapter 2, at higher temperatures, the population of phonons increases. An electron-phonon interaction can force the electrons to undergo several elastic and inelastic scatterings and to relax via both horizontal and vertical jumps [118]. We refer to the work of Klemens in 1956 [238] to describe the deviation from Wiedemann-Franz law upon alloying. According to Klemens, the electronic thermal conductivity κ_e follows Matthiessen's rule analogous to the electrical resistivity in terms of electronic thermal resistivity (W), i.e., $1/\kappa_e = W_e = W_0 + W_i$. Here W_0 is the residual electronic thermal resistivity which follows Wiedemann-Franz law with residual electric resistivity ρ_0 due to scattering at defects and W_i due to the scattering of electrons by phonons. He showed that the deviation of the Fermi distribution function f from equilibrium distribution function f^0 is $\propto f(k_1)\left(df^0/d\varepsilon\right)$ and $\propto f(k_1)\varepsilon\left(df^0/d\varepsilon\right)$ for electrical and thermal conduction respectively. Hence the sign of f changes with sign of

$df^0/d\varepsilon$ involving electrons scattering with phonons with large change of wave vector across the Fermi surface, i.e., via horizontal scattering. On the other hand the sign of f depends on both the sign of $df^0/d\varepsilon$ and of ε for thermal conduction. The W_i then can involve electrons scattered from phonons in both large and small angles, i.e., via both horizontal and vertical motion of electrons across the Fermi surface, approximately $W_i = W_{Hi} + W_{Vi}$. According to his previous work in 1954 [239], Klemens argued that the horizontal movement includes large distances on the Fermi surface and hence is more sensitive to band structure compared to vertical movement which involves only local property of the Fermi surface. In most cases the W_{Vi} is negligible in comparison to W_{Hi} and then the Wiedemann-Franz law holds. In alloys if it so happens that the W_{Vi} is not negligible then deviation from the Wiedemann-Franz law should arise and κ_e would get suppressed. However, such simple considerations have limitations in alloys, due to the fact that the W_i's not directly observed and often calculated from parent materials. On top of that the lattice contribution to the total thermal resistivity W_{ph} has also to be accounted for and it may not be negligible compared to W_e.

Regarding the contribution of electron-magnon scattering, it is present in the resistivity but it is known that this scattering contribution is small in thermal conductivity above 5 K [240].

Finally the other reason for the deviation of W-F law is the deviation of Lorenz number from the Sommerfeld value in our films. As we have discussed in Chapter 2, the Lorenz number which is an intrinsic quantity for a material can also vary from the Sommerfeld value owing to the presence of mechanisms that degrade thermal current but not the charge current, i.e., excess of phonons or magnons, grain or surface scattering or inelastic scatterings.

Phonon thermal conductivity κ_{Ph} from literature

For cases of $\kappa > \kappa_e$ in our films, the deviation from Wiedemann-Fran law is attributed to the significant contribution of phonons to κ. In the work by Ho *et al*. [241], the electronic and phononic contributions to the total thermal conductivity of a few binary alloys have been discussed. As a guide we look at such contributions to κ from those alloys whose components are neighbors as in the case of Fe and Co, i.e., with a difference of one electron in the electronic configuration and have their Debye temperatures are close to the Θ_{Debye} of Fe and Co. We find FeNi (due to the unavailability of CoNi data) as a ferromagnetic and PdAg, PdCu, CuZn as the non-ferromagnetic suitable candidates.

In case of FeNi we have collected and plotted the κ_e and κ_{ph} for a wide range of compositions in Fig. 6.16. We see that the deviation of Wiedemann-Franz law occurs, i.e., the κ_e calculated from the measured resistivity is larger than the total κ in these films. The deviation is largest for the lowest Fe content film of 30% Fe at T $>$ 70 K, and is the smallest for 80% Fe film and for T $>$ 130 K. This picture is quite close to what we have seen in our films for similar Fe content. Although the reason for this behavior has not been discussed in this literature, the suppression of the total κ here too can also be attributed to inelastic scattering of electrons.

The κ_{ph} of PdAg, PdCu and ZnCu are shown in Fig. 6.17. The range of κ_{ph} values here is comparable to the κ_{ph} in our measured films with Co 20% and 22% as shown in Fig. 6.15(b).

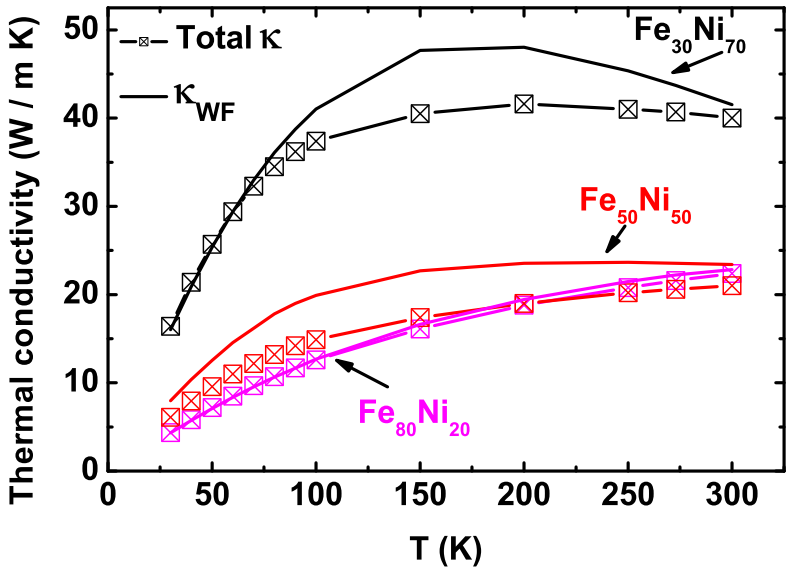

Figure 6.16: Literature values of the total thermal conductivity of Fe_xNi_{1-x} (square with cross) [241] and electronic thermal conductivity calculated from literature resistivity values (lines) [242] vs temperature for Fe content 30%(black), 50% (red) and 80% (magenta).

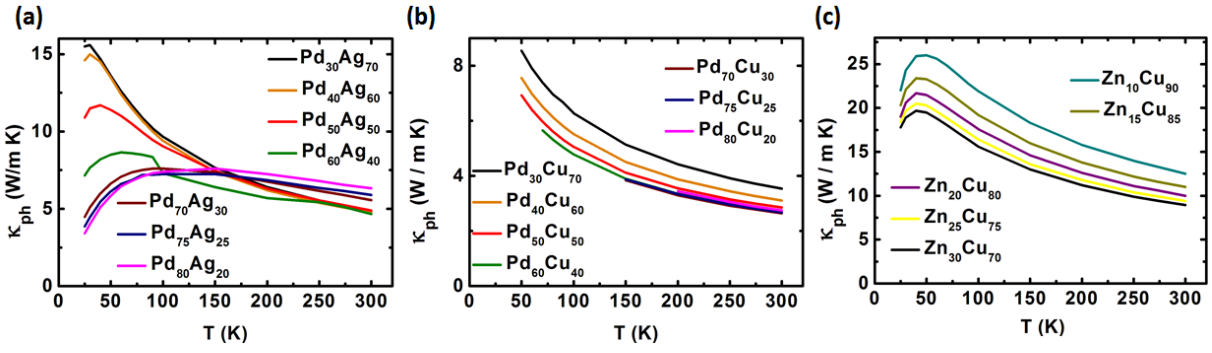

Figure 6.17: Lattice thermal conductivity from literature [241] vs temperature for alloys of (a) PdAg (b)PdCu and (c)ZnCu.

6.3.2 Modeling the temperature distribution

In our sample design, the heat source lies on one island and the heat current transmits through the bridge creating a temperature gradient across it to arrive at the other island, observed as the temperature rise at the thermometer positions. Simultaneously heat also flows through the leads and goes to the sink owing to the small but finite thermal conductance of the leads. In our measurement scheme, using the thermal transfer model the thermal conductance of the bridge and the leads are separated. Only after this the thermal conductivity of the film can be calculated if the background thermal conductance is known. As we have pointed out earlier, the background contribution is not known with precision for individual samples since the conductance of bare SiN_x lying at the bottom of each CoFe films has not been measured separately. Fortunately there exist heat distribution models which solve the 1-D heat distribution equation to simulate such temperature profile across the structures. Such models use the thermal conductivity as an input parameter. Hence this can be used as a good confirmation check for our measurements, i.e., by using our final κ values for the films and membranes, the heat distribution across the structures can be simulated and then compared to the measured temperatures at the thermometers. A huge disagreement between these 2 numbers will be an indicator of a larger deviation of the membrane conductance from the averaged conductance that we use in our analysis. Additionally the temperature profile distribution along the length and width of the bridge can be visualized. Therefore we have used finite element COMSOL simulation method.

COMSOL temperature distribution profile

This simulation has been carried out in the group of Prof. Back. The sample design has been directly imported from the e-draw file, i.e., the dimensions used during lithography are exactly copied. The heater resistance and thermal conductivity κ values for $Co_{70}Fe_{30}$ sample has been used to produce its temperature profile, simulation results this time at a lower bath temperature of 50 K. The mesh size distribution has been made non-uniform so that the exact temperature at the intricate and smaller structure regions are better captured. Figure 6.18(a) and Fig. 6.18(b) show the temperatures at the hot and the cold thermometers respectively for applied heater voltage from 0.01-0.03 V at bath temperature of 50 K. We observe that across the length of the thermometer which is 100 μm in our case, the temperature forms much flatter plateau and then it drops faster towards the sink.

The distribution of temperature across the length of the film is shown in Fig. 6.19(a) on the CoFe film on SiN_x bridge for applied heater power of 0.02 V. The temperature profile on the entire structure can be seen in Fig. 6.19(b) with a high heater voltage of 0.1 V which raises the temperature of the hot island by almost 20 K to gain a pictorial overview.

We have taken this opportunity to calculate the ratio of the heater power dissipated along the total length of the heater structure from one sink to the other and along the portion of the structure lying on the island. This ratio turns out to be around 1.2. This is the same scaling factor representing the ratio of the lengths of the above said heater segments which we have used to correct our input heater power, i.e., $P_H = I_H^2(1.2R_{4T})$ for calculating

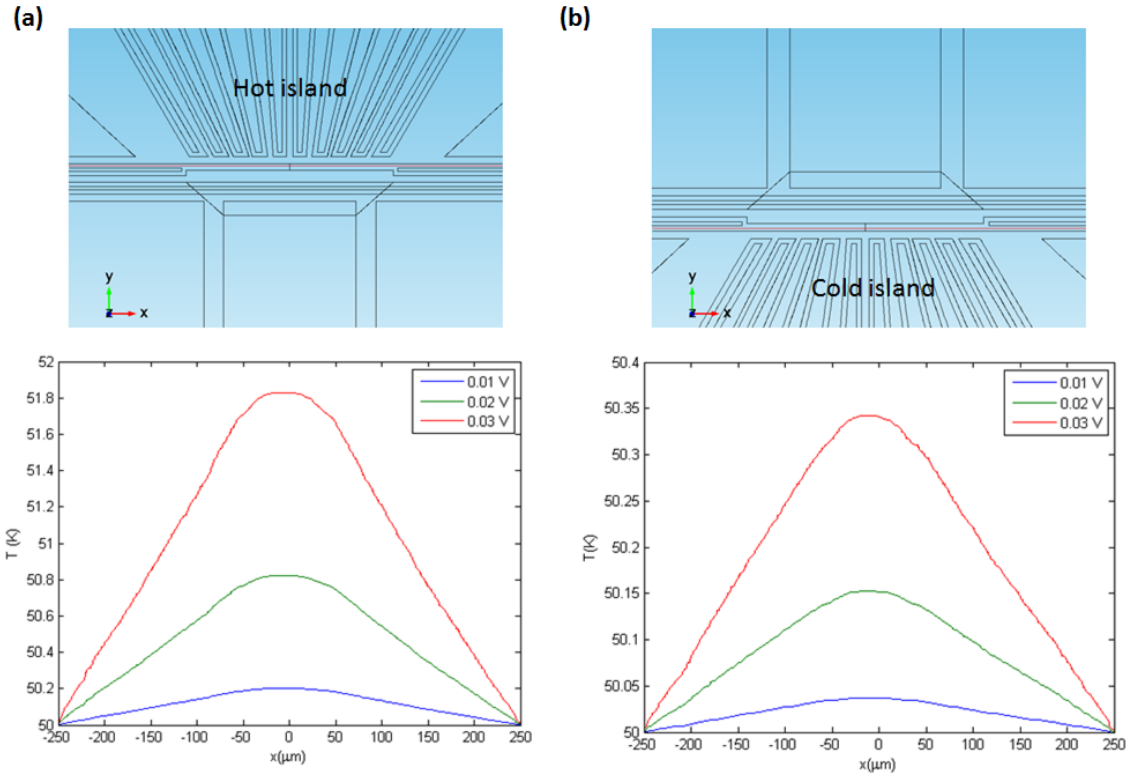

Figure 6.18: (a) Island temperature as a function of lateral distance with 0 at the center of the thermometer for applied heater voltages 0.01 V (blue line), 0.02 V (green line) and 0.03 V (red line) (a) at hot island and (b) at cold island at bath temperature of 50 K.

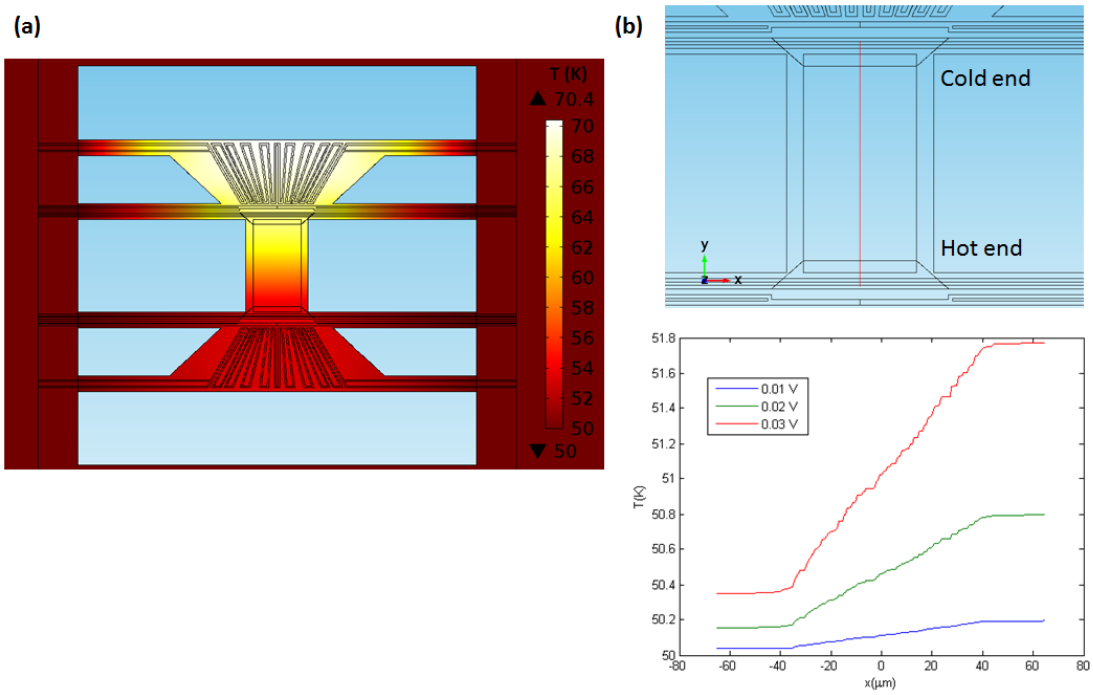

Figure 6.19: (a) Temperature profile across the entire membrane structure at bath temperature of 50 K and heater voltage of 0.1 V. (b) temperature distribution along the length of the film. Temperature from cold to hot end for heater voltage of 0.01 V (blue line), 0.02 V (green line) and 0.03 V (red line) at bath temperature of 50 K.

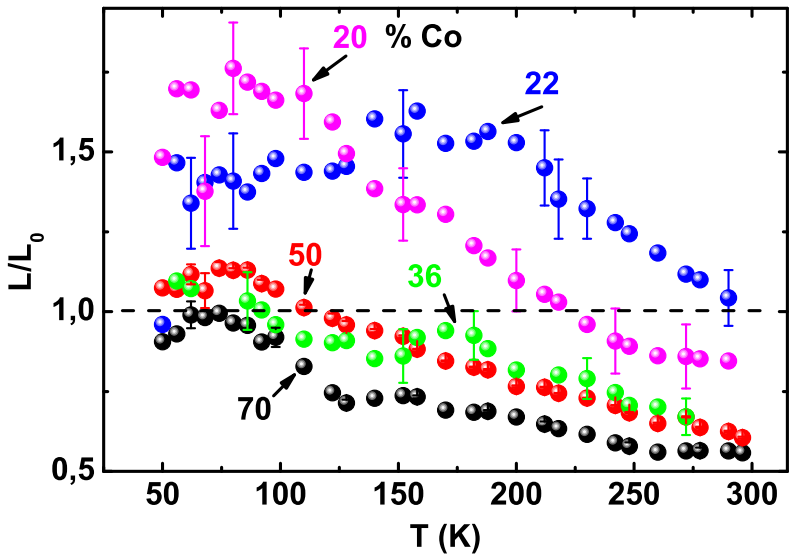

Figure 6.20: Lorenz ratio as function of temperature for this experimental work for films with Co content in %. Error bars calculated from error in thermal conductivity. Dashed line represents Sommerfeld Lorenz number L_0.

thermal conductance.

6.3.3 Lorenz ratio

Results

The Lorenz ratio has been calculated as

$$\frac{L}{L_0} = \frac{1}{2.45 \times 10^{-8}} \frac{\kappa\rho}{T} \tag{6.1}$$

The Lorenz ratio is plotted as a function of temperature in Fig. 6.20. At temperatures above 100 K, for films with Co from 36-70 %, the Lorenz ratio is below the Sommerfeld value. Below 100 K however, the Lorenz ratio is comparable or little higher than the Sommerfeld values L_0 with a small bump visible around 70 K. On the other hand for samples with Co 20% and 22%, the corresponding Lorenz ratio lies above L_0 at all temperatures, above 220 K for Co 20% sample and reaches a maximum upto 46% for 22% Co sample.

Discussion

We discuss the possible causes for the positive and the negative deviation of Lorenz ratio one by one. Observation of Lorenz number larger than L_0 is common and the reasons have been attributed to various factors.

Examples are the large contribution of phonons to the thermal conductivity [243], gain boundary enhancement of Lorenz number in polycrystalline films of Au and Pt nano-films [244, 245] or in silver nanowires [246]. In our case, from XRD measurement we know that films with Co content $\leq$ 22 % are in single bcc phase. In these films we have observed significant contribution from phonons to the thermal conductivity (Fig. 6.15(b)). The large positive deviation of the Lorenz ratio is then attributed to the large phononic thermal conductivity .

On the other hand, experimental observations of Lorenz number smaller than L_0 are also available. In the work [225] on Ag nanowire, the Lorenz number deviates from the Sommerfeld number by 15-68% with lowering in temperature and has been attributed to material purity, independent of surface scattering. The deviation of Lorenz number from L_0 in Ni nanowire [247, 248] has been attributed to the strong surface scattering. Also in case of thin films of pure ferromagnets and normal metals in the work of Zink and co-authors, the Lorenz number has been found to be smaller than L_0 for all materials. The possible causes are electron-phonon scattering at the grain or surface boundaries [201] or inelastic scattering [201, 249]. In our measurements, from XRD spectrum we know that films with Co content $\geq$ 36 % are in a mixed bcc+fcc phase. In these films, the presence of inelastic scattering from phonons and magnons degrade the thermal current but not the electric current, thus lowering the L from L_0.

6.3.4 Double-bridges sample

Results

As discussed in the κ_{SiN} section in Chapter 4, an additional sample was prepared with two identical bridges prepared on the sample chip (Fig. 5.24), one is the bare SiN_x and the other has 60 nm thick $Co_{22}Fe_{78}$ deposited on the bridge area. The purpose was to measure the thermal conductance of both the bridges so that we know the exact background κ_{SiN} to subtract for the determination of κ of the CoFe film. The measurement results for resistivity and thermal conductivity are shown in Fig. 6.21.

Figure 6.21(a) shows the resistivity of the $Co_{22}Fe_{78}$ film in dark cyan plotted along with the resistivity (blue) of the previously measured standard sample of similar Co content (ρ in Fig. 6.1(a). The resistivity of the double-bridges device is larger than than the single bridge device at temperature lower than 100 K and smaller in the rest of the temperature range. The temperature dependent part of the resistivity, i.e., $\Delta\rho$(T)= 2.09 $\mu\Omega$cm, is smaller than 4.07 $\mu\Omega$cm of the standard device film.

Figure 6.21(b) shows the total bridge thermal conductance (K_B in olive green), the thermal conductance of the 2nd bare SiN_x bridge (K_{SiN} in wine) and the difference between them which represents the thermal conductance of the CoFe film alone (in dark cyan). The K_{SiN} is smaller in magnitude and with little temperature dependence in comparison to both K_B and K_{CoFe}. In order to compare with the single bridge device, we plot both the κ values in Fig. 6.21(c). The two κ values agree in the intermediate temperature range between 130 - 200 K and the double-bridge film has a maximum κ of 60 W/mK at ambient temperature. While the κ of the single-bridge film almost saturates after 200 K, the κ of that of the double-bridge film keeps on increasing until 250 K before saturating to a nearly temperature independent value.

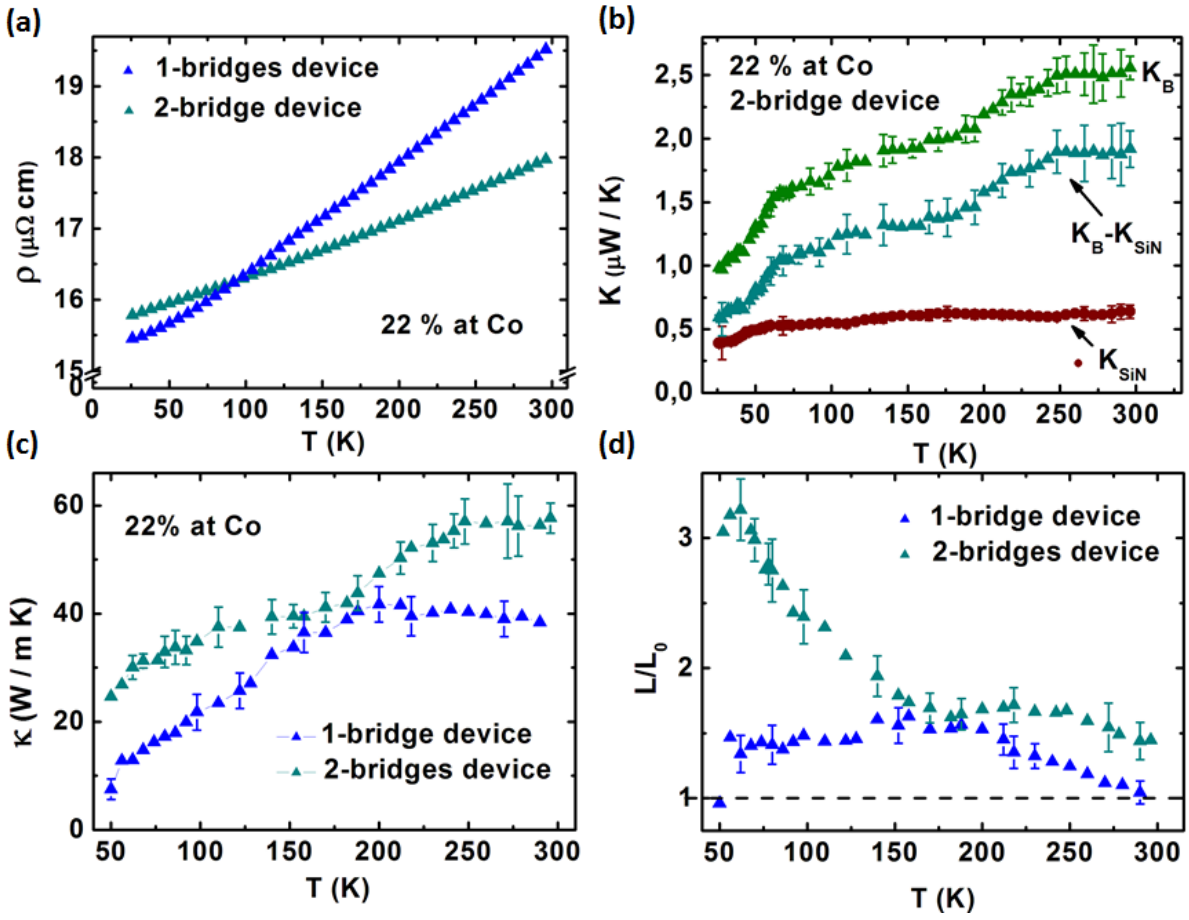

Figure 6.21: Transport coefficients measured on sample with Co 22% shown in Fig. 5.24 vs temperature. The coefficients for this sample are plotted in dark cyan and the corresponding quantities in standard single bridge device in blue. (a) resistivity, (b) total thermal conductance (green), background SiN_x thermal conductance (wine) and the film thermal conductance. (c) thermal conductivity and (d) Lorenz ratio with L_0 (dashed line).

Finally, we take a look at the Lorenz ratio L/L_0 values calculated from its measured ρ and κ. The L is larger than the L_0 in the entire temperature range, as was the case for the single-bridge device film but here we are surprised by the steep rise in L towards the lower temperature range. The highest L value is around 8×10^{-8} WΩ/K^2 which is twice the highest value for the single bridge film.

Discussion

The double-bridge samples were deposited in the same MBE chamber as were the rest of the films but almost after a year, several chamber service and maintenance steps later. Even though the composition is quite similar to the other film, it is possible that the quality and grain size are different. This is a possible cause for the shape of the resistivity curve.

Since the resistivity lies for most part below the resistivity of the single-bridge device film, it is expected that the thermal conductivity should be larger and this is what we observe. In the XRD study we have found that film with Co 22% deposited alongside this device is in single bcc phase. Hence we observe a large phonon contribution to the thermal conductivity. However, such large L even in comparison to film of same composition and same thickness indicates that there are other mechanisms which enhance heat conduction but not charge conduction. The κ values of the two films agree with each other within an error margin of upto 35% while the error in single-bridge device film on account of false background subtraction leads to only upto 16% error. One candidate is the presence of grain boundary scattering. In the experiments by Wang *et al*. [244], grain boundary scattering has been shown to raise the L of Au and Pt thin polycrystalline films to value as high as 10 $\times10^{-8}$ WΩ/K^2 at 77 K. In our experiments, we have done an annealing test on a 60 nm thick $Co_{70}Fe_{30}$ film and have observed the reduction of resistivity upon annealing. This has proved the substantial presence of grain and surface scattering contribution to our films.

In conclusion, the purpose of the double-bridge device is partially satisfied. The resistivity values of this film and the previously deposited and measured film are comparable and we have verified that the subtraction of the correct background leads to κ_{CoFe} being not too off. However, different film quality and asymmetric device design prevents us from doing a direct comparison of the κ and L values between the films.

6.4 Thermopower or Seebeck coefficient

It is known that the charge current can also be generated by temperature gradient dependent on the so called Seebeck coefficient (S) or in vice versa temperature gradient can be generated via charge current dependent on the Peltier coefficient (Π). The S and Π are related through a linear temperature dependence, therefore no independent knowledge can come out of them. That is why for our purposes, we have measured and will study only one of the two coefficients S. The thermoelectric power measured for Co_xFe_{1-x} films for compositions x_{Co} = 0.2, 0.22, 0.36, 0.5 and 0.7 in the temperature range of 25-300 K are presented along with the measurement technique. Magnon drag and phonon drag contributions are discussed. Theoretical calculations performed in the group of Prof. H. Ebert in Munich is included in the analysis.

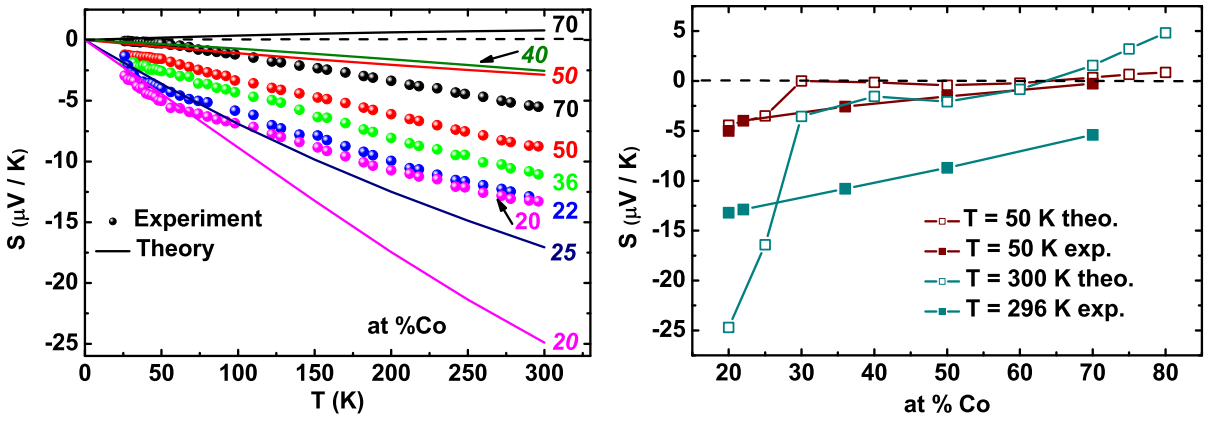

(a) (b)

Figure 6.22: (a)The measured thermopower (filled sphere) vs temperature with Co contents in %. The lines represent theoretically calculated thermopower. (b) Measured S (filled squares) and S_{Theo} (open squares) at 50 K (wine) and 296 K (300 K for S_{Theo}) (blue) vs % of Co. The 0 value on the thermopower axis is shown as a dashed line.

6.4.1 Seebeck coefficient results and discussions

Results

The measured thermopower vs temperature curves for all CoFe samples are as shown in Fig. 6.22(a) as filled spheres. The sign of the thermopower for all our compositions is negative except the sample with Co 70 % which shows a small positive thermopower at the lowest temperature but then reverts to the negative sign as the temperature is raised. The pattern of behavior with varying composition is the same as shown by the resistivity data, i.e., the absolute value of the thermopower increases or in other words the thermopower decreases negatively with increase of Fe. The range of S at room temperature is between -5.8 μV/K for the 70% Co sample and -13.8 μV/K for the 20% Co film.

In Fig. 6.22(a), at high temperatures, the curves for all compositions vary almost linearly with temperature but as the lower temperature is approached, a change of curvature is unmistakably visible. The curves change their slopes in an attempt to come to 0 value at even lower temperatures, as required by 3rd law of thermodynamics.

Next the theoretically calculated thermopower (S_{Theo}) is compared with the measured thermopower as shown in Fig. 6.22(a). We see that the curves are quite nicely reproduced considering only the elastic scattering contribution to the thermopower. S_{Theo} has been obtained by evaluating the generalized Mott relation (equation 2.44) for Co content 20%, 25%, 40%, 50%, 60%, and 75%. Here too the calculation for Co 70% produces small positive thermopower but unlike our measured data, this coefficient remains positive at all temperatures but for all other compositions with Co less than 70%, the S is negative. The S_{Theo} for 50% Co is -3 μV/K at the room temperature which is smaller than the value we measured. The magnitude and direction of curvature for Co 25%

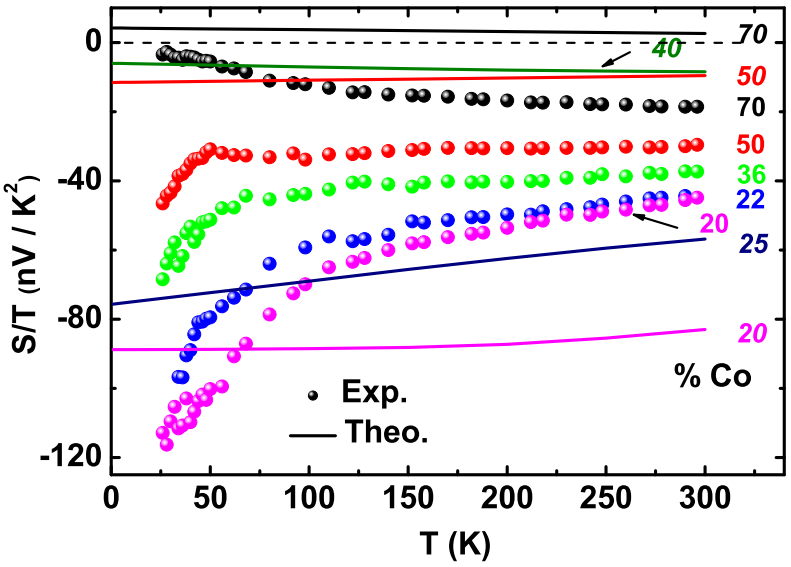

Figure 6.23: The thermopower/temperature plotted vs temperature for *S* curves shown in Fig. 6.22(a). The measured (filled circles) and calculated *S*/T (lines) are labeled by Co content in %. Dashed line shows 0 on the *S* axis.

is closest to what we have measured for Co 22%. The exception is then exhibited by samples with 20% Co where the S_{Theo} is as large as -25 μV/K at room temperature compared to measured thermopower of -15 μV/K around the same temperature while at the lowest temperature they agree with each other quite well. S_{Theo} curves for 50% and 40% Co in Fig. 6.22(a) seem to have their places interchanged and the 30% Co thermopower curve crosses most of the high Co content thermopower curves.

The comparison of S_{Theo} vs measured *S* is better visualized by plotting the thermopower against Co content at two different bath temperatures of 50 K and 290 K as shown in Fig. 6.22(b). Between 30-70% Co, the measured and calculated Seebeck coefficient trend seem to agree well with an offset, the agreement being very good at 50 K in terms of magnitude but the S_{Theo} clearly shows huge offset for lower Co content films especially at the higher temperature. The discrepancy between them is as high as -25 μV/K for S_{Theo} compared to -13.9 μV/K for the measured thermopower for composition of 20% Co.

In Fig. 6.22(a), the striking feature in the measured thermopower is the change of slope, not present in calculated thermopower, S_{Theo}. The sign changes from positive for Co 50-70 % to negative for Co 20-22 %. In order to explore this region further, we re-plot Fig. 6.22(a) with thermopower divided by temperature (*S*/T) on the y-axis vs temperature on the x-axis. Now we see in Fig. 6.23 that at higher bath temperatures, the thermopower for most films are linear with temperature. The curves for Co 20-22% appear to not have yet reached saturation and will strictly follow linear temperature dependence at a further higher temperature. Moving in the direction of decreasing temperature, the curvatures change significantly. There is no dramatic effect observed as the Co

content is decreased from 22% to 20% rather the curves follow each other quite closely. We also notice that the onset temperature at which the bending of the curvature takes place is composition dependent, i.e., the sample with the lowest Co content changes curvature from linear to non-linear T dependence at an earlier temperature and then the others follow suit until sample with Co content of 70%, in which case the sign of the curvature itself changes with slight positive magnitude at the lowest temperature region. On the same graph we have additionally plotted S_{Theo}/T. At no temperature range do we find agreement between S/T and S_{Theo}/T.

Discussion

We now proceed to the discussion part of the above observations. The systematic increase of thermopower with electron number indicates significant contribution from electron diffusion to the thermopower. The calculated S_{Theo}, which is nothing but the diffusion thermopower, does not agree with the measured S. Fig. 6.22(b) clearly shows the deviation between the measurement and calculation. Also the diffusion contribution according to Mott is linear in temperature (equation.2.15). However, a straight line traced through the data points at the high temperatures neither fits the low temperature data nor meets the 0 on y-axis at 0 K. This indicates that in our measured S, there are non-negligible contributions other than diffusion alone.

Taking a careful look at the S_{Theo} in Fig. 6.22(a), one finds that for those calculations with Co $\geq$ 40%, the lines are pretty straight, quite Mott like linear dependence in temperature but for calculation with Co 20% and 22%, the lines bend inward. The reason is that the solutions have been arrived by solving the generalized Mott relation and not the classical Mott relation. Hence via the Fermi-Dirac distribution, the redistribution of carriers is taken into account i.e the more asymmetric the energy dependence of the conductivity around the Fermi level, the stronger the deviation from linearity. The classical Mott formula on the other hand contains only the slope at the Fermi level and is therefore strictly only valid for low temperatures or very simple, s-type band structures where the slope is constant over a larger energy range.

We have already established the presence of contributions other than diffusion to our measured thermopower. In our samples, the contribution from phonons or magnons or yet other different scattering mechanisms are present which are capable of overshadowing the only electronic band structure and elastic electron-phonon scattering contribution to the thermopower. The mechanism that can make such large deviations possible, is the scattering from spin wave system or magnons since we are working with ferromagnetic alloys here. Also we have already observed the presence of magnon scattering contribution to the resistivity in our films (Fig. 6.9). Such larger magnitude of thermopower indicates contribution from magnon drag effects. The magnon drag effect in pure single crystalline Fe had been reported in early 70s' [135] and also recently in both pure Fe and Co by [138] (See Chapter 2 for details).

In order to separate the electron diffusion and magnon drag contributions, the measured thermopower has been fitted to a function

$$S = S'_{\mathrm{D}}T + S'_{\mathrm{M}}T^{3/2} \tag{6.2}$$

at high temperatures from 100 K to 300 K. Here $S_{\mathrm{D}} = S'_{\mathrm{D}} \times T$ is the electron diffusion contribution which

varies linearly with temperature. Secondly $S_M = S'_M \times T^{3/2}$ is the contribution from magnon drag where $T^{3/2}$ dependence comes from the magnon specific heat dependence on temperature. The $T^{3/2}$ fit is valid upto the magnon drag peak. The magnon drag peak usually appears at a temperature around one half to one fifth of the Curie temperature of the material. As discussed in Chapter 2, CoFe has a high Curie temperature, even higher than Co [83]. It has been observed that the magnon drag peak for pure Fe and pure Co take place around 200 K and 400 K respectively [138]. This implies that the magnon drag peak in our films is expected to take place at a temperature higher than room temperature.

Fitting parameters for fit to S		
% Co	$S'_D(V/K^2)$	$S'_M(V/K^{5/2})$
20	$-9.04 \times 10^{-8} \pm 1.82 \times 10^{-9}$	$2.63 \times 10^{-9} \pm 1.13 \times 10^{-10}$
22	$-7.96 \times 10^{-8} \pm 1.52 \times 10^{-9}$	$2.08 \times 10^{-9} \pm 9.57 \times 10^{-11}$
36	$-5.51 \times 10^{-8} \pm 1.58 \times 10^{-9}$	$1.04 \times 10^{-9} \pm 9.83 \times 10^{-11}$
50	$-3.48 \times 10^{-8} \pm 9.54 \times 10^{-10}$	$2.86 \times 10^{-10} \pm 5.95 \times 10^{-11}$
70	$-8.84 \times 10^{-9} \pm 7.01 \times 10^{-10}$	$-5.72 \times 10^{-10} \pm 4.37 \times 10^{-11}$

Table 6.3: Parameters to the fit of thermopower from 100-300 K. S'_D is the coefficient for diffusion contribution and S'_M is the coefficient for contribution from magnon drag.

Once the data fitting has been done, the coefficients S'_D and S'_M can be used to parameterize the diffusion and magnon drag terms at all temperatures. These coefficients are tabulated in table (6.3). We have verified that the fitting is independent of the temperature range of choice, i.e., the coefficients obtained from fitting from 200-300 K, yield similar values to what we have obtained already.

Figure 6.24 shows an example of the separation of the contributions for film with 70% Co. The black circles represent the measured thermopower and the fit function as a line on top of the measured thermopower between 100 K and 300 K. The diffusion thermopower is shown as squares (cyan), is linear in temperature. The magnon-drag thermopower is shown as triangles (orange) and has a $T^{3/2}$ temperature dependence. Finally contribution other than diffusion and magnon drag is shown as upside-down triangles (dark yellow) and has small non-zero value at the low temperature. The dashed line indicated 0 on the y-axis. For this sample, the magnon drag contribution surpasses the diffusion contribution at high temperature. The coefficients S'_D and S'_M for all 5 films are tabled in table 6.3.

First we discuss the diffusion terms. Figure 6.25(a) shows the S_D for all the 5 samples together with the S_{Theo}. The coefficient S'_D is shown in the inset and we see that it is negative for all our films. Since S_{Theo} represents the elastic diffusion part of the thermopower, it is fitting that this should be compared with our extracted S_D. The agreement between measured and theoretically calculated diffusion thermopower is excellent for film with Co 20 % and close for 22%. This indicated that the difference between them ($S - S_D$) can be assigned mostly to the magnon contribution S_M. This is also seen in the S_D vs Co content plot in Fig. 6.25(b) at both high and low temperatures. This is in stark contrast with similar plot in Fig. 6.22(b) where especially at high temperature,

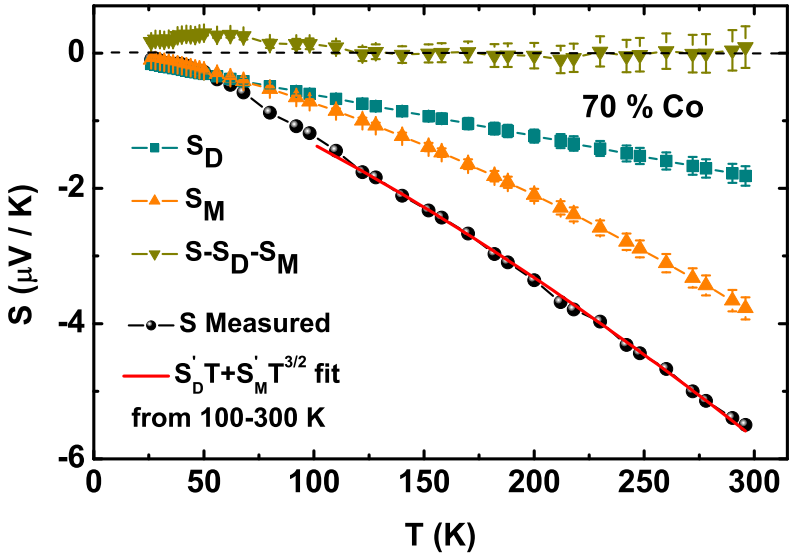

Figure 6.24: An example of fitting of measured thermopower (in circles) from 100 K to 300 K with function (line) from equation 6.2 for film with Co 70%. Separation of diffusion thermopower S_D (blue), magnon drag thermopower S_M (orange) and residual thermopower $S - S_D - S_M$ (dark yellow) contributions. Dashed line shows 0 on the thermopower axis.

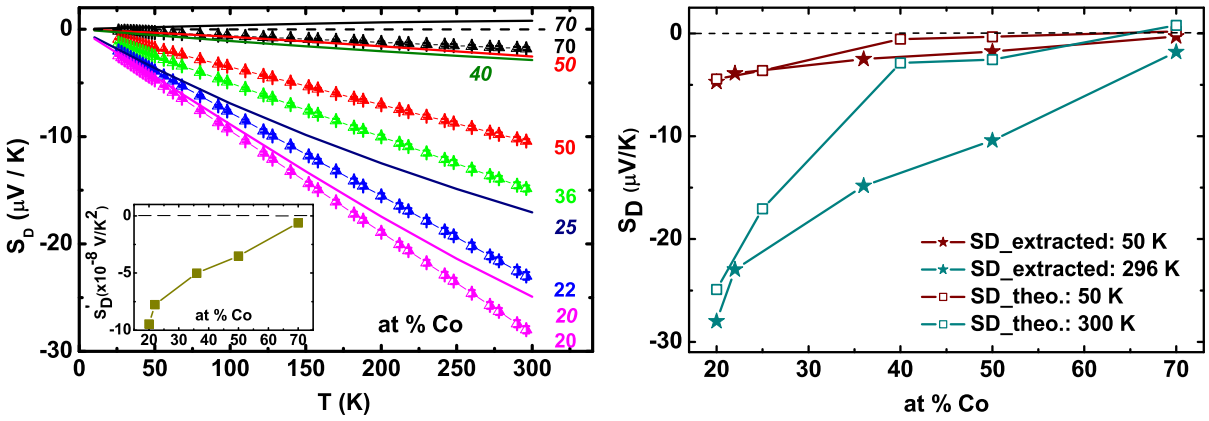

(a) (b)

Figure 6.25: (a)Diffusion thermopower vs temperature (half filled triangles), comparison with theoretically calculated thermopower (lines). (Inset: Coefficient S_D' vs Co content in %). (b) Diffusion thermopower vs Co content in % from measurement (star) and calculation (open square) at temperatures of 50 K (wine) and 296 K (300 K for theory)(blue). Dashed lines in (a) and (b) show 0 on the thermopower axis.

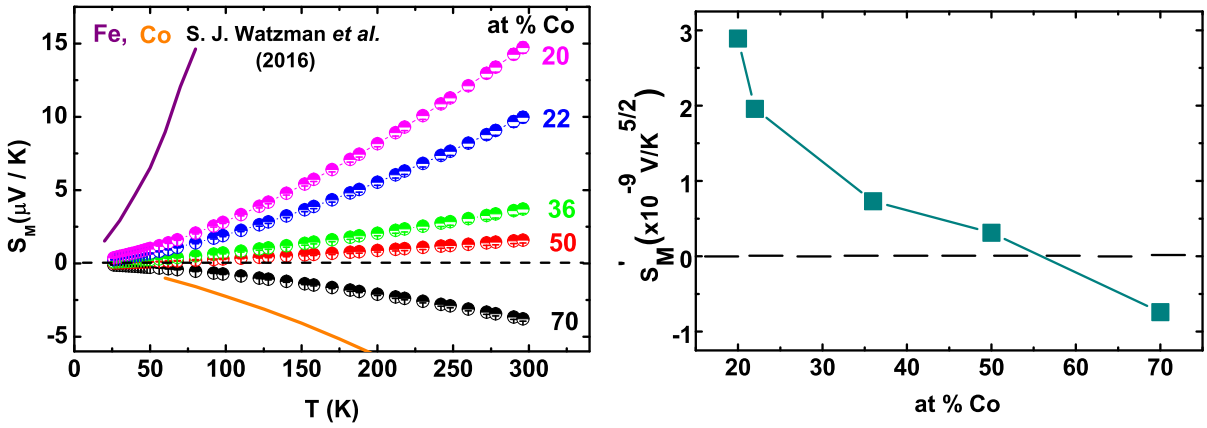

(a) (b)

Figure 6.26: (a) Magnon drag thermopower vs temperature. Extracted from measured thermopower (half filled circles), from literature (lines) for bulk Fe (purple) and bulk Co (orange) [138].(b) Coefficient $S_M^{'}$ vs Co content in %. In (a) and (b) dashed line shows 0 on the thermopower axis.

there was huge disagreement between the measured and calculated thermopower.

For the rest of the samples, the S_{Theo} is significantly smaller than the extracted S_D. For film with Co 70%, the sign of S_{Theo} and S_D are opposite. One possible explanation for the disagreement is that the calculations assume bcc phase for all compositions while in our XRD data as stated in Chapter 5, only films with Co 20-22 % are in pure bcc phase while the films with Co $\geq$ 36% are in a mixed phase of bcc and fcc. The crystal phase indicates different phonon spectrum and thereby different electron-phonon scattering rates.

In order to ensure that the $T^{3/2}$ fit for the magnon-drag contribution is not a simple artifact, we additionally calculate the thermoelectric parameter 'η' for the 20% Co content sample from $S_D = -\pi^2 k_B \eta / 3eT_F$ where T_F is the Fermi temperature. We compare with the available data for bulk Fe. The T_F for bulk Fe considering the effective mass m^*=8$\times$ m_e [64] is 1.04 $\times$ 10^6 K. Using this T_F, the η for our film turns out to be 5.4. This is close to the calculated $\eta = 7.6$ in literature by Hirata *et al*. [250] for liquid Fe with $m^* = 0.8\ m_e$.

Next we discuss the features of magnon-drag thermopower as observed in our films, as shown in Fig. 6.26(a). The magnon contribution is first of all small at low temperatures and becomes significant after 100 K, which is consistent with what we have seen in case of resistivity. Also the coefficient $S_M^{'}$ has negative sign for Co concentration of 70 % and positive for rest of the samples as shown in Fig. 6.26(b). The signs are consistent with the signs for the magnon-drag thermopower for pure Co and pure Fe bulk films [138], also shown in Fig. 6.26(a) together with our measured S_M . This captures the evolution of S_M with composition as we move from iron-rich to Co-rich material and also with temperature. This magnon-drag contribution explains the deviation of measured thermopower from theoretically calculated thermopower in Fig. 6.22(a) for Co 20-22 %, where owing to the larger positive S_M, the measured thermopower values lie below the S_{Theo}.

Finally we discuss contribution besides diffusion and magnon drag, i.e., $S_{\text{residue}} = S - S_D - S_M$ as shown in

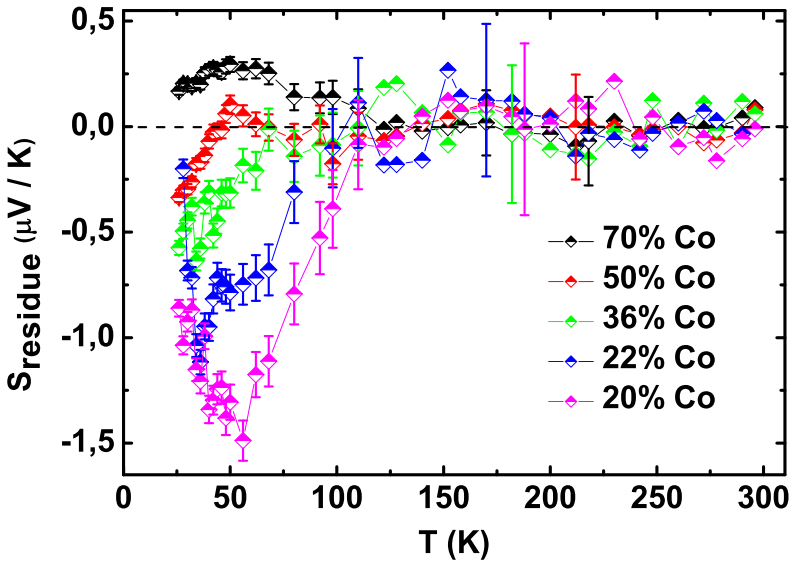

Figure 6.27: Residual thermopower vs temperature with Co content in %. 0 thermopower is indicated by dashed line.

Fig. 6.27. The S_{residue} is at least an order of magnitude smaller in comparison to the diffusion and magnon drag contributions. For films with Co contents 20% ans 22%, troughs are observed around temperature of 50 K. These two films are in single bcc phase and these structures are the reminiscent of phonon drag effect. On the other hand for films with Co $\geq$ 36 %, which are in a mixed crystal phase, contribution from vertical scattering of electrons from phonons and low energy magnons are observed in the thermal conductivity. Hence such contribution should also affect the thermopower. The theoretical argument of the contribution of in-elastic scattering to thermopower has been discussed in the work by Gunault *et al*. [251] and recently has been observed to have a huge contribution in graphene thermopower as reported by Ghahari *et al*. [252]. According to the theoretical study by Durczewski *et al*. [253], the contribution of in-elastic collision to the S shows up as a peak at the lower temperatures with linear T dependence both before and after this peak. Such a small peak is still visible in the thermopower of samples with Co 50% and 70%. But since both phonon drag peak and inelastic collision contribution to S have similar temperature dependence, we assign the term $S - S_{\text{D}} - S_{\text{M}}$ as a manifestation of both the effects i.e $S_{\text{ph+inela}}$.

Besides we have to take into consideration that being transition metals, inter-band scatterings are present even though it has been argued that this contribution should be small due to large DOS associated with the d-bands and small mass difference between such metals. Recalling Fig. 6.4, in the minority spin channel, before Co 50%, the minority s-band appears to cross the corresponding d-band. Hence a possible spin mixing contribution of inter-band spin scattering to thermopower is also expected.

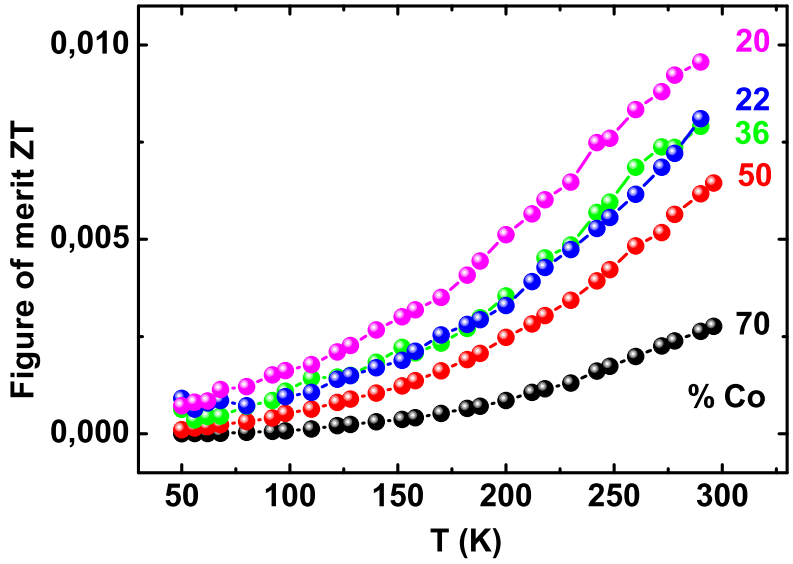

Figure 6.28: Thermoelectric figure of merit values for all CoFe samples as a function of temperature labeled with Co content in %.

6.5 Thermometric figure of merit ZT

The thermometric figure of merit of a material characterizes how efficient the material is in power generation or refrigeration. This dimensionless quantity is calculated using the transport coefficients ρ, κ and S as indicated by equation (2.47).

The thermoelectric materials are engineered to have larger thermopower and smaller thermal conductivity especially smaller lattice thermal conductivity to achieve ZT greater than unity. In our experiments we have measured the above transport coefficients with our thermal conductivity strongly suppressed at temperatures close to the room temperature and hence we can calculate the ZT for our CoFe alloys and see where they fall in terms on themoelectric properties. The calculated ZT values are now plotted as a function of temperature for our five CoFe samples in Fig. 6.28.

The ZT values for our samples at room temperature are well under 0.01 for all our samples indicating them as not very good thermoelectric materials for practical applications. However, from Fig. 6.28 we see that the ZT for our samples exhibit interesting trend with composition. The ZT increases with increase in Fe content and lie very close to other for samples with Co 22% and 36%. There is a significant increase in the room temperature ZT value for increase of Co content from 20% to 70%. But an educated extrapolation of the curves at higher temperatures can not be made since it is not clear how the thermal conductivity and thermopower will behave at those temperatures but we know that the ZT value is unlikely to reach any significant number for our materials.

6.6 Conclusion

The transport coefficients have been discussed individually one after the other and in each case the possible contribution from various quasiparticles such as electrons, phonons and magnons and scattering mechanisms have been discussed. This has been made possible by using existing theories and possible comparison with other literature values. The calculation done in the theory group helps unravel some of the intricacies especially concerning the band structure of the alloys.

The contributions from electron-phonon scattering and magnons, which contribute significantly to resistivity and thermopower at the higher temperatures, have been separated using both measured and theoretical calculations. The measured S is understood qualitatively as a competitive effect of diffusion, magnon drag, inelastic collision of electron and even phonon drag effects. For all compositions, the Wiedemann-Franz law is violated. The phonon contribution to L in single phased lower Co content samples raise the L above L_0. While the inelastic scattering of the electrons with the magnon and phonons cause L smaller than L_0 in the samples with mixed phase.

It is also clear that separation of the contribution of different scattering processes to the transport coefficients is not so trivial. More realistic model is therefore required to address this issue which has been attempted although total success is far from being achieved.

Chapter 7

Conclusions

7.1 Summary

Transport phenomena is one of the most fundamental fields of research in solid state physics, an area which has been studied for decades if not centuries. With evolving technology newer materials are in ever increasing demand, more so are the methodologies to go beyond classical level to the quantum where spin degree of freedom plays an important part. Attempts are being made by several research groups to keep up the pace with fast evolving technology and at the same time develop a basic understanding of the interactions and contribution of various quasi particles and their scattering mechanism have remained ignored or unexplored at the ground level. In this thesis work, not only have we tried to work hand in hand with the current progress but also to address the need for the understanding the part played by the particles through their contribution to transport coefficients. The electrical and thermal transport property study has been done on CoFe films with varying Fe contents whereas the magneto-thermal transport properties have been performed on thin Py films. For both the studies, SiN_x membrane based microcalorimeters have been developed and duly implemented.

The research done in this thesis can be broadly divided into two parts. In part one, we have studied the transverse magneto-thermoelectric effect on Py/Pt bi-layer. For this work, 100 nm thick SiN membranes have been utilized to fabricate suspended structures. The suspension design not only facilitates low heat loss to the heat sink but also guides the direction of temperature gradient. We have carried out experiments in membrane samples as well as bulk substrate samples in collaboration with Schmid *etal*. [43, 62]. Comparison of the results from both sets of experiments allows us to propose resolution to several outstanding questions regrading the proposed transverse spin Seebeck effect in metals. However, the bulk of our thesis work is done in part two of the thesis. In this part, we have carried out extensive experiments to measure the transport coefficients such as resistivity, thermopower and thermal conductivity of CoFe thin films. For this purpose we have used suspended micro-calorimeters prepared on 500 nm thick SiN. The use of the suspended structure minimizes the contribution of background thermal conductance but also allows the measurement of all transport coefficients together on the same sample. The experimental results are complimented by theoretical simulations which allows us to

differentiate between the contributions of electrons, phonons and magnons to each transport coefficient.

The experiments and results pertaining to part one of the thesis are described in Chapter 3 and 4. On 100 nm thick suspended device, heaters and thermometers are patterned using e-beam lithography. The thin substrate and the micro-designs allow the application of large temperature gradient on the Py film and its accurate determination. In-situ deposition of Py/Pt bi-layer further ensures transparent interface for spin pumping purposes. Transverse thermovoltage has been measured in the presence of in-plane magnetization and temperature gradient. Together with the results from bulk substrate samples, the following conclusions have been derived. The transverse thermopower is dominated by planar Nernst effect. In bulk substrates, the planar Nernst effect is accompanied by anomalous Nernst effect due to the thickness of the substrate that can sustain out-of plane temperature gradients. In both sample types, no transverse spin Seebeck effect was detected, irrespective of the presence or absence of phonons in substrate. Our results is one of the few conclusive works on the topic of proposed transverse spin Seebeck effect which had been misinterpreted in its first report.

The biggest part of our research has been invested in studying the electrical and thermal transport properties of CoFe films. From XRD crystallography measurement of our samples, we found that the films 20-22 % Co content are in single bcc phase while the rest of the films have small traces of fcc mixed with largely bcc phase. This crystal structure has important implication for the thermal transport properties of the films. Our films are polycrystalline and ferromagnetically soft. The results for measurements of various transport coefficients results are described in detail in Chapter 6 and are summarized here briefly. The transport coefficients resistivity, thermopower and thermal conductivity have been measured for Co_xFe_{1-x} films with Co contents x= 0.2, 0.22, 0.36, 0.5 and 0.7. We have found that with increasing Co content, the resistivity of the films decreases monotonically until Co 22% and then makes a downward jump. This behavior is consistent with numerical simulations which have been performed taking into account band theory. The absolute values of the resistivity for all CoFe films were found to be larger than their pure counterparts owing to the presence of disorder which reduces the electron mean free path in the material. The different contributions to the total resistivity can be written as, $\rho = \rho_0 + \rho_{\mathrm{el-ph}} + \rho_{\mathrm{mag}}$, where ρ_0, $\rho_{\mathrm{el-ph}}$ and ρ_{mag} are contributions from the scattering from defects, electron-phonon and electron-magnon interactions respectively. The contributions have been separately estimated using Bloch-Wilson fitting function and theoretical calculations. The magnon scattering contribution is negligible below 100 K but increases not only with temperature but also with Fe content (i.e., with increasing electron number). The maximum contribution from magnon scattering is of about 6.5% to the total resistivity at room temperature for sample with Co 20%. The ρ_{mag} at room temperature is almost around half of what the magnon would contribute in pure Fe [226] indicating the effect of alloying on electron-magnon scattering. After subtraction of magnon contribution from the total resistivity, the electron-phonon scattering component agrees with what has been calculated theoretically. Therefore in case of this transport coefficient, the separation of contribution from impurity scattering, electron-phonon and magnons could be done using both measured and calculated results.

We found that the thermal conductivity of our samples is influenced by a combination of factors, the major contribution coming from the electron-phonon interactions and inelastic scattering of electron with phonons and magnons, as evidenced by the observed deviation from Wiedemann-Franz law or the large deviation of the Lorenz

number from the Sommerfeld value. In the films with single crystal structure, namely, films with Co 20% and 22%, the phonons contribute significantly to the thermal conductivity in almost entire range of temperature and the Lorenz ratio goes up by as high as 46 %. However, for the mixed phase films, the inelastic electron scattering from phonons or low energy magnons hinder the transport of thermal energy by the electrons and the Lorenz ratio drops to about 30% of the Sommerfeld value. The contribution of magnons to the thermal conductivity is negligible in our temperature range. Therefore it is desirable to consider more complicated modeling which includes all the temperature dependent potentials belonging to each quasi-particle to truly do the separation and especially interesting would be the contribution from in-elastic scattering effect.

Finally we briefly discuss the results of our thermopower (S) experiments on CoFe. The thermopower decreases with decreased Co content which is consistent with the behavior exhibited by resistivity. Since we observed non-zero contribution of electron-magnon scattering to resistivity, we expect similar contribution here to the thermopower. The thermopower is found to have two major components and can be written as $S = S_{\mathrm{D}} + S_{\mathrm{M}}$ where S_{D} denotes the diffusion part and S_{M} is the contribution from magnon drag effect. Taking into account the temperature dependence of these contributions, the thermopower can be written as, $S = S_{\mathrm{D}}^{'} T + S_{\mathrm{M}}^{'} T^{3/2}$. These coefficients $S_{\mathrm{D}}^{'}$ and $S_{\mathrm{M}}^{'}$ allow us to parameterize the diffusion and the magnon drag contributions in the entire temperature range. We found out that only in case of low Co content samples with Co 20-22 %, does the diffusion thermopower extracted from the total thermopower agree with the theoretically calculated thermopower. This is an indicator that indeed there are significant magnon drag contribution together with possibly other contributions to the thermopower present in our films. Our calculations were done done using generalized Mott relation, however, to truly and precisely separate the various contributions, more sophisticated calculations are required. That said, our findings are significant nonetheless. The fact that the magnon drag contribution (S_{M}) has negative sign only for sample with Co 70 % is consistent with the results for pure Fe films. Furthermore the sign of S_{M} is positive for the rest of the films which have high Co content. The contribution of magnon drag to the total thermopower is was found to be high as 14.7 μV/K at room temperature. After subtracting the S_{D} and S_{M} from the total S, in all our samples we found small but non-zero contribution from either phonon drag effect or electron in-elastic scattering effect or both.

We conclude with an outlook of future research that can be done based on our work. One of the missing factors in our measurements were the data points below 25 K. Unfortunately we were limited by our material choice for the thermometers. At much lower temperatures, the effect of the phonon is expected to die out and the contribution from from magnon scattering is likely to be higher. This could be explored further by going to even lower temperatures. The effort to build a thermometer specifically for lower temperature measurements requires considerable redesigning and sample preparations which were beyond the scope of our project. At temperatures lower than 25 K, the contribution to the thermal conductance coming from the SiN substrate is comparable to that of the metallic film of interest. Additionally below 4 K, the surface scattering from the nitrides is significant. Together this makes the steady state measurement method untenable at lower temperatures. However, this is being pursued in our group in another project which we would like to discuss briefly here. Instead of continuing with the steady state method of thermal conductivity measurements, we are developing the 3-Omega method for membrane systems. The 3 Omega method has been used for measurement of thermal

conductivity for bulk and thin films on bulk substrates since 1987 originally developed by Cahill *et al*. [56]. Only recently has been this method been extended to membrane systems since the membranes are advantageous in experiments involving small heat currents. The advantage of using the 3-Omega technique on membranes is that the thermal conductance of both the bare SiN and metallic film can be measured on the same sample, additionally thermal diffusion constant can be also determined.

In pursuit of this thesis we have developed from scratch membrane based micro-calorimetry devices which can be used not only to effectively measure the various transport properties but also to separate the various contributions to them from the scattering mechanisms of different quasi-particles involved. Furthermore, we could determine whether or not Wiedemann-Franz law is valid in our films in the temperature regime of our interest. One of the most important conclusions that can be drawn from our research is that magnon scattering plays a significant role especially in generating thermoelectric effects. We expect that understanding the role played by magnons in generation and transmission of heat and spin currents will remain crucial in the context of research and development of future generation thermoelectric devices.

Appendix A

Flow cryostat operation details

A.1 Oxford flow cryostat operation

A small description is dedicated to the design and the working principle of this cryostat. The cylindrical vacuum chamber of the cryostat has the diameter of 9 cm and height of 4-5 cm. A removable top cover enables sample replacement. During the entire operation, a turbo pump maintains low pressure inside the chamber. On one side of the vacuum chamber exists a leg with length around 40 cm, meant to hold a transfer line from a helium dewar. One leg of the transfer tube rests completely inside the dewar with a needle valve at the bottom of this let. A motor attached at the top of this part automates the needle valve during operation. Beyond the motor section, the transfer line is a double coaxial tube. Helium from the dewar flows through the inner tube to the cryostat. Inside the cryostat helium flows through a small tube spiraling around a copper cold finger and heat exchanger and exits along the outer tube of the transfer line to a flow meter and controller box. From the flow-meter, helium flows to a diaphragm pump which continuously sucks helium hence enabling the continuous helium circulation. From there helium flows back to the flow-meter again which calculates the helium flow rate in lit/hr unit. The system is a low consumption system since ideally the flow rate is only 1.5 lit/hr. From the second port on the flow-meter helium finally makes its way to the in-house helium recovery line eventually leading to the university helium liquifier. Due to the small volume of the set-up, the temperature of the cryostat goes from 300 K to the base temperature of 4.2 K in only 8 minutes.

During the operation we noticed the freezing of the needle-vale on several occasions. We figured out the proper operation steps to avoid this inconvenience. The trick is to keep adequate pressure inside the dewar before inserting the transfer line into the transfer leg of the cryostat. Follow the procedure mentioned in the manual for the system. Only remember to close the recovery valve of the dewar halfway through the insertion of the transfer line into the dewar so as a maintain a pressure of around 100-200 mbar inside the dewar before inserting the cryostat end of the transfer line into the leg of the cryostat. Open this valve and release the pressure when the temperature controller shows drop in the chamber temperature.

For a second cool-down run on the same mounted sample with the transfer line still inside the leg of the

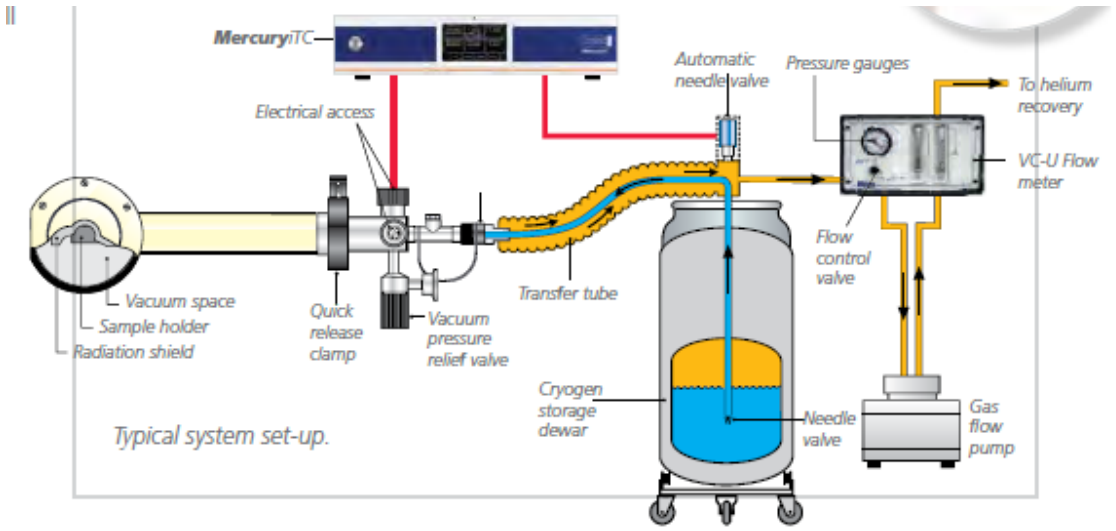

Figure A.1: The Schematic has been taken from the website of Oxford Instruments. During the operation, the continuous running membrane pump G4 creates enough pressure inside the helium can for the helium to flow through the transfer line to the cryostat. After passing through the heat exchanger, it flows back to the helium flow-meter and controller, then to the membrane pump and back to the flow-meter from where finally ti is released to the recovery.

cryostat, the procedure of cooling down is easier and explained here. At this point the membrane pump is running and the valve on the flow controller is open. So just open the needle valve and the cool down should take place within 10 minutes.

To remove the cryostat end of the transfer line, again follow the instruction written in the manual line by line.

As a third option, if the sample needs to be changed which can be done in 1 day time, removing the transfer line from the dewar is a waste of helium. So we leave that end inside the dewar, the other end dangling outside, while we mount another sample. After the sample has been mounted and the chamber has been evacuated, we are ready to do the cool down. First close the recovery valve of the dewar and use the balloon to create pressure of around 100 mbar inside the dewar. Turn on the membrane pump without opening the flow controller valve. Now check for helium flow on the other end of the transfer line by putting it in a dish with a little iso-propanol. If bubbles form in the iso-propanol that implies that the needle valve is clean and we are ready to follow the instructions in the manual. If the valve is clogged or the user forgets to create gas pressure inside the dewar, it is likely that the valve will freeze. Then the user has to remove the entire transfer line out from the dewar, warm it completely before attempting inserting it in helium again.

A.2 Oxford ITC temperature controller automation and operation

The flow cryostat that I used for my measurement is paired with the intelligent temperature controller (ITC) from Oxford. We have no previous experience with this particular instrument. The default instrument we re-

ceived was communicable only via serial port which had issues of getting jammed or being unavailable from time to time. The instrument had to be turned off and on again several times in order to access the port again. Hence it became necessary to purchased a GPIB card from Oxford Instruments and then with the use parallel port continuous communication could be maintained. First thing is to ensure that the system system is available for talking, one has to go to NI-MAX explorer and see if the address of the instrument is scan-able. Also the GPIB address can not be set in the configuration page on the screen, the default address 0 had to be used. For the purpose of automation the driver for the instrument is down-loadable from Oxford website along with some sub VIs to write a measurement script. But unfortunately these sub-VIs do not work because they come with in-built 'call by reference' and this reference is not only missing but also can't be reset by other users.

The instrument does not respond to standard $^{*}IDN?$ query instead to $^{*}IDN?\backslash n$ and the output gives the instrument model number followed by its current software version. For example the device id for our ITC is OXFORD INSTRUMENTS.MERCURY ITC:65:1.4.40. In order to automate the device using labview it is then recommended to use the 'Basic Serial Write and Read.vi' from the labview provided examples and change the serial port to GPIB port at then beginning of the block diagram. It has to be kept in mind to change the command setting from Legacy to SCPI (Signal Oriented Measurement Commands) on the device screen when the device is received from factory. Now the SCPI commands supplied by Oxford Instruments can be used for the device. In the next paragraph we give simple examples of writing to and reading from the ITC.

Each instrument has one mother board and several daughter boards and each board has several devices with unique device identifier named UIDs. These UIDs can be retrieved by executing 'READ:SYS:CAT' command using the basic serial write and read vi from labView. The reply to this command may not necessarily look exactly like as mentioned in the manual for the device but nevertheless the device IDs can be recognized. For example the answer to 'SYS:CAT' for our device is 'STAT.SYS.CAT.DEV.GRPX.PSU.DEV.MB1:T1.TEM P.DEV.GRPY.PSU.DEV.GRPZ.PSU.DEV.DB4:G1:AUX:DEV:MB0.H1:HTR' This implies that we have 2 mother boards 'MB1' and 'MB0' with thermometer and heater devices with UIDs 'MB1.T1' and 'MB0.H1' respectively. The one daughter board 'DB4' has an auxiliary device 'DB4.G1' for helium flow control. Now the standard SCPI command structure of <VERB>:<NOUN>:<NOUN> from the manual can be used to either 'SET' or 'READ'. As an illustration, the command to set the set temperature to 30 K will be written as 'SET:DEV:MB1.T1:TEMP:LOOP:TSET:30 \ n' and so on. Oxford instruments provides a list of SCPI commands for the users of this device as well as the software for updating.

Now I describe how the operation of the instruments falls within the entire measurement run scheme. First using the sub-vi 'NeedleValve_ New' the needle valve is opened 100 % and let the system cooldown all the way down to the base temperature, this takes about 10 minutes. Then the set temperature is set via the sub-vi 'T_Set_New_13Feb'. Since I use temperatures above 20 K now is the time for the trick to save helium. It is done by first closing the needle valve to 30%. After this has been done, the heater inside of the instrument which was kept inactive so far is turned on by running 'ON' on the sub-vi 'Set_Heater_Auto_New'. This then operates the heater in the automatic mode while we can then readjust the needle valve manually to an even lower % such that when the measurement starts at 25 K, the heater voltage at the instrument display is close to 5 V. From this temperature onwards, the only parameter needed to be incorporated in the bigger measurement script is the

set the set-temperature sub-vi. The heater takes care of itself automatically. Finally when the measurement is finished, the needle-valve can be closed by setting the valve to be at 0%, 'OFF' on the 'Set_Heater_Auto_New' vi for the heater to be operated in manual mode and setting the heater percentage to be 0 by running the sub-vi 'Heaterpercent_new', all included in the script.

Appendix B

Labview scripts for measurement

B.1 TSSE measurement

The TSSE was originally measured in the set-up in Prof. Back's chair, but it is not available anymore. For the sake of reproducibility of data, I have implemented the vis to measured TSSE in our flow cryostat. Hence I describe the vis and sub-vis needed to do transverse signal measurement in this set-up. All the relevant vis are placed in Desktop\For measurement.

The heater current can be rampped-up using the vi 'Yoko_ set_ output_ current.vi' situated in the Desktop\For measurement\Yoko folder. The inputs are the GPIB address of the Yokogawa instrument, initial and final currents together with the current ramping-up speed. The unit of current is A, hence e.g. if user wants to apply 100μA current then 100E-6 has to be typed in.

For the measurement of transverse voltage, vi 'diff_ angle_ PNE' is used. The angles from 0° to 360° are split to 9 parts i.e. at interval of 45°. These angles are defined within individual flat-sequence structures. Inside each case, sub-vi 'V_ H_ copy.vi' is run. The angles, initial and final field values with field step, magnetic field calibration files are set as constants. The field value constants can be edited if required. The inputs are the of number of loops to take average over and the GPIB address of the nanovoltmeter. GPIB 22 is usually the default number I have used. The data are plotted live on each page designated for the corresponding angle on the front panel of the labView script. The data are saved after run on each angle is finished and in the file and folder assigned by the user. If a file name is repeated the said file is overwritten.

If measurement at only 1 angle is needed then 'V_ H_ copy.vi' can be run alone. In this case, the inputs are the initial, final field values, field steps, nanovoltmeter GPIB address, number of loops to take average over, field hysteresis loop required or not and the names of the files to save the data. Inside the block diagram of the script, the 1st case initializes the instrument and applies the magnetic field related inputs. In the next case comes the 'while loop', the condition for which is set by the number of loops to take average over. Inside the while loop, the magnetic field is set by the sub-vi 'mag_ field_ set.vi' followed by a waiting time of 1 second between set

field values and start of the voltage reading. The voltage is acquired by the voltmeter using sub-vi 'Read_ dcV_ nanovoltmeter.vi'. This voltage is then averaged over the total number of loops and plotted live vs applied field in V vs H plot. The 3rd case contains the data saving option which is done after the end the complete run of the program. This case also includes the 'mag_ field_ set.vi' which sets the field to be 0.

A quick note on the sub-vi 'mag_ field_ set.vi'. It uses NI-USB6215 DAQ card to apply voltage to the kepco which then supplies current to the Helmholtz coils. The DAQ channels and field calibration files are set as default. For maximum output of $\pm$ 10 V for each channel, the maximum field values for the inner circular coil is $\pm$17.5 mT and is $\pm$9.5 mT for the outer rectangular coil. The program calculates the currents needed to each coil so that $H = \sqrt{h^2_{circular} + h^2_{rectangular}}$, where H is the effective field value set by user and uses the given field calibration curves 'circ.txt' and 'rect.txt' available also in the same folder i.e. Desktop\For measurement, for the said purpose.

At the end, the current to the heater structure can be reduced to 0 using the vi 'Yoko_ reduce_ output_ current'.

B.2 Transport measurement

B.2.1 Film and heater Calibration

At the beginning of every sample, the first step is to measure the film resistance and the heater resistance. In folder Desktop\For measurement\with measure thermo R, there are several example files which have been used e.g. 'Cali_ 25July_ SFM33.vi' or 'Cali_ SFM30_ 21Aug_ ver1.vi', indicating the sample name, date and the purpose here is heater and/or film calibration. The front panel of the script has 4 pages. Page 1 allows setting the GPIB address of the ITC temperature controller, 2nd page asks for the number of temperature steps, 3rd page allows user to set file name to save data and finally 4th page shows the ITC closing sequence which need not be changed.

Over on the block diagram side, there are several flat sequence structures which allows the flow of the script. 1st case allows user to set a waiting time (for cooldown) before the user decides to start the measurement. This waiting time is also a fail safe if the user wants to stop the script and change something or simply forgot something. The 1st data point is acquired at the 1st set temperature of usually around 25 K. Since the temperature has been set sometime ago, now it only needs to carry out the resistance measurement. For dc method, use 'Thermometer_ cali_ ver4.vi'. How much current one needs to apply to either film or heater can be edited inside 'Set_ positive.vi' or 'Set_ positive_ ver2.vi'. The current sources are only Yokogawas or Yokogawa with analog output channels of lock-in amplifier. Of course values inside 'Set_ negative.vi', 'Set_ negative_ ver2.vi', 'Set_ positive_ zero.vi', 'Set_ negative_ zero.vi' have to be edited accordingly. These tasks are intuitive if one takes a look at the scripts. Each data point is averaged over 30 loops. For ac method, one has to replace 'Thermometer_ cali_ ver4.vi' with '2_ Rlockin_ woMag_ array.vi'. Then the GPIB addresses are already plugged in and saved as constants and the user has to give the sensitivity as input depending on the temperature range. If more diverse sensitivity are required then the temperature range can be split using additional case structures.

The next case includes the calibration sub-vi inside a for loop for the rest of the temperature range. The number of temperature steps is set in the condition of the for loop. 1st the temperature is set by sub-vi 'T_ set_ new_ 13Feb.vi', followed by waiting time, next the 'Thermometer_ cali_ ver4.vi', saving the data and finishes with the ITC closing sequence which has been described in chapter 4.

Example 'Calibration_ 23April_ ver1.vi' shows how to calibrate film, heater and both the thermometers together using both dc and ac methods.

B.2.2 Measurement for S and κ

After the calibration of the heater and the film resistance, there will be 2 more cooldowns as described in chapter 4. 2nd cooldown to estimate the optimal heater current before the 3rd and final long measurement. The scripts for the last 2 runs are similar except for the number of temperature steps all inside Desktop\For measurement\with measure thermo R folder. For the 3rd run, the entire temperature range is split into several ranges for example 25-36 K, 38-50 K, 56-74 K etc. For each temperature range different heater currents are applied via specific sub-vis meant for that range. The heater currents are increasing from smaller values at lower temperature to larger at the highest temperatures since we already know that in our materials the thermal conductivity increases with temperature. From instrumentation side, in these runs, we need one Yokogawa for the heater structure, 2 lock-ins for the thermometers for ac or 1 Yokogawa and 1 lock-in analog output for dc method and finally 1 nanovoltmeter channel for the measurement of thermopower.

One example script is 'Delta_ SFM33_ 3Feb.vi'. On the front panel, we have 6 pages. The 1st page has indicators for the set temperature at what T we are at during any given time during the run. The second page contains some numerical controls, each indicating at how many temperatures we will make our measurement in a given temperature range. For example, in the range from 182-224 K, we want to make measurements at every 6 K hence the controller input (Numeric 4) has to be 8 and so on. The next 3 pages allows user to put file names for data saving and on the final page are the ITC closing sequences with default inputs.

The block-diagram is a cascade structure with repeating sequences allowing the user to input different sub-vis for different temperature ranges. Always the first case has the waiting time constants. Nest comes the elaborate run for the 1st set temperature which is 26 K in this case. We have chosen 26-36 K as one T range here. The sub-vi is called 'Delta_ sub_ 3Feb_ 26-36.vi' followed by the file saving commands in the immediate next case. In this T range we want to make measurements at every 2 K steps hence in the next case the numeric controller input will be 5. After the measurement at 26 K is over the, the temperature shall be set to 28 K according to the next case followed by a waiting time of 25 minutes before the sub vi'Delta_ sub_ 3Feb_ 26-36.vi' is run again. After this T range is completed the next temperature range of 38-54 K begins and the run continues now with another sub-vi of 'Delta_ sub_ 3Feb_ 38-54.vi'. This process takes place until all the ranges are completed. In this particular measurement, the data are taken at every 2 K steps from 26 K to 74 K and at every 6 K steps from 80 K upto 296 K. Finally when all the T ranges are exhausted, the ITC closing sequence runs.

Now coming to the sub-vis part, we take a look at one of the sub-vis say 'Delta_ sub_ 3Feb_ 38-54.vi'. It begins with the sub-vi 'Thermometer_ calibration_ array_ ver1' while no heater current has been applied yet. This

is similar to the 'Thermometer_ cali_ ver4.vi' sub-vi with one Yokogawa and 1 lock-in analog output channel as the current sources to the two thermometers. The 4 output array elements represent the 2 voltages measured once with positive output currents and next with current polarities reversed and averaged over 30 such runs. The next case contain the sub-vi '1VH_ 22_ nano_ woMag_ ch1_ array.vi'. This sub-vi collects the thermo-voltage and averages again over 30 runs. Hence at this point we have the thermometer resistances for calibration purpose and the 0 heater current dc offset thermovoltage. Up next comes the 'build array' structure where user has to give the 8-10 heater current values one needs to apply at that temperature range. Here for example in this range of 38-54 K, we have used 11 different heater currents i.e. from 2μA - 10μA at 1μA steps along with 12μA and 14μA. Of course these values are not random, are guessed from the heater resistance for the 2nd run and finally optimized for the 3rd run. In the next case these heater current arrays are indexed and fed to the 'Yoko_ set_ output_ current' sub-vi. After each such heater current is applied, the program commands to wait for 90 s before the sub-vis 'Thermometer_ calibration_ array_ ver1' and '1VH_ 22_ nano_ woMag_ ch1_ array.vi' are run one after the other. When the measurement steps in this sub-vi 'Delta_ sub_ 3Feb_ 38-54.vi' at 38 K is finished, it ramps the heater current back to 0 in the next case using the sub-vi 'Yoko_ reduce_ output_ current' and waits 2 minutes, sends the save data command and then moves to the next temperature of 40 K where it repeats itself again.

Appendix C

Sample detail

C.1 Sample detail

The description of all the samples mentioned in this thesis chapter 6 are given in the following table.

Table of samples				
Device name	Material	Thickness	Property measured	Comments
SFM4	$Co_{45}Fe_{55}$	20 *nm*	AMR	FIB contamination
SFM18	$Co_{50}Fe_{50}$	20 *nm*	AMR	–
SFM19	$Co_{20}Fe_{80}$	20 *nm*	AMR, ρ	–
SFM21	$Co_{20}Fe_{80}$	20 *nm*	AMR, ρ	–
SFM23	$Co_{50}Fe_{50}$	20 *nm*	AMR, ρ	–
SFM24	$Co_{70}Fe_{30}$	20 *nm*	AMR, ρ	–
SFM29	$Co_{70}Fe_{30}$	60 *nm*	ρ, S, κ	–
SFM30	$Co_{50}Fe_{50}$	60 *nm*	ρ, S, κ	–
SFM31	$Co_{70}Fe_{30}$	60 *nm*	AMR	–
SFM32	$Co_{50}Fe_{50}$	60 *nm*	ρ	–
SFM33	$Co_{20}Fe_{80}$	80 *nm*	ρ, S, κ	–
SFM35	$Co_{36}Fe_{64}$	60 *nm*	ρ, S, κ	–
SFM37	$Co_{22}Fe_{78}$	60 *nm*	ρ, S, κ	–
SFM38	$Co_{0}Fe_{100}$	60 *nm*	ρ at RT	Broke during cooldown
SFM41	$Co_{22}Fe_{78}$	60 *nm*	ρ, S, κ	2-bridges device
SFM42	$Co_{70}Fe_{30}$	60 *nm*	ρ, κ	Annealed device
SM11	SiN	500 *nm*	κ_{SiN}	SiN-1
SM13	SiN	500 *nm*	κ_{SiN}	SiN-2
SM15	SiN	500 *nm*	κ_{SiN}	SiN-3
SFM41	SiN	500 *nm*	κ_{SiN}	SiN-4
SFC-2	$Co_{36}Fe_{64}$	60 *nm*	XRD	bcc+fcc peaks
SFC-2	$Co_{22}Fe_{78}$	60 *nm*	XRD	bcc peaks
SFC-3	$Co_{30}Fe_{70}$	20 *nm*	XRD	no relevant peaks
SFC-4	$Co_{20}Fe_{80}$	20 *nm*	XRD	small bcc peaks
SFC-5	$Co_{36}Fe_{64}$	80 *nm*	XRD	bcc+fcc peaks
SFC-6	$Co_{70}Fe_{30}$	80 *nm*	XRD	bcc+fcc peaks

Bibliography

[1] Th. J. Seebeck, Magnetische Polarisation der Metalle und Erze durch Temperatur-Differenz '1822-1823', A. J. v. Oettingen (1895);

[2] H. J. Goldsmith, Introduction to thermoelectricity, Springer series in materials science, **121** (2009);

[3] V. Zlatic and A. Hewson, Properties and applications of thermoelectric materials, Springer science and bussiness media, (2009);

[4] D. C. Brock, 'Understanding Moore's law: Four decades of innovation'*Philadelphia, Pa: Chemical Heritage Press* ISBN 0941901416 (2006);

[5] G. E. Moore, 'Cramming more components onto integrated circuits'*IEEE Solid-State Circuits Newsletter* **38** 114 (1965);

[6] see the 'International Technology Roadmap for Superconductors' http://www.itrs.net/;

[7] I. Zutic, J. Fabian and S. D. Sarma, 'Spintronics: Fundamentals and applications'. *Rev. Mod. Phys.* **76** 323 (2004)

[8] C. Chappert, A. Fert and F. N. Van Dau, 'The emergence of spin electronics in data storage'. *Nature Mater.* **6** 813-823 (2007)

[9] A. Fert and I. A. Campbell, Electrical resistivity of ferromagnetic nickel and iron based alloys. *J Phys. F: Metal Phys.* **6**, 5 (1976).;

[10] J.M. Slaughter, Materials for Magnetoresistive Random Access Memory. *Annu. Rev. Mater. Res.*, **39**, 277-296(2009). ;

[11] International Technology Roadmap for Semiconductors, 2007 Edition Emerging Research Devices, http://www.itrs.net (accessed October 2011).;

[12] J-G. Zhu, Magnetoresistive Random Access Memory: The Path to Competitiveness and Scalability. *Proceedings of the IEEE* **96** 11 (2008).;

[13] K. Uchida, J. Xiao, H. Adachi, J. Ohe, S. Takahashi, J. Ieda, T. Ota, Y. Kajiwara, H. Umezawa, H. Kawai, G. E. W. Bauer, S. Maekawa and E. Saitoh, Spin Seebeck insulator. *Nature Mater.* **9**, 894-897 (2010).

[14] H. Adachi, K. Uchida, E. Saitoh, J. Ohe, S. Takahashi and S. Maekawa, Gigantic enhancement of spin Seebeck effect by phonon drag. *Appl. Phys. Lett.* **97**, 252506 (2010).;

[15] D. Meier, D. Reinhardt, M. van Straaten, C. Klewe, M. Althammer, M. Schreier, S. T. B. Goennenwein, A. Gupta, M. Schmid, C. H. Back, J.-Michael Schmalhorst, T. Kuschel and G. Reiss., Longitudinal spin Seebeck effect contribution in transverse spin Seebeck effect experiments in Pt/YIG and Pt/NFO. *Nature Commun.* **6**, 8211(2015).;

[16] S. Y. Huang, X. Fan, D. Qu, Y. P. Chen, W. G. Wang, J. Wu, T. Y. Chen, J. Q. Xiao, and C. L. Chien, Transport Magnetic Proximity Effects in Platinum. *Phys. Rev. Lett.* **109**, 107204 (2012).;

[17] D. Qu, S. Y. Huang, Jun Hu, Ruqian Wu, and C. L. Chien, Intrinsic Spin Seebeck Effect in Au/YIG. *Phys. Rev. Lett.* **110**, 067206 (2013).;

[18] A. Kehlberger, G. Jakob, M. C. Onbasli, D. H. Kim, C. A. Ross and M. Klui, Investigation of the magnetic properties of insulating thin films using the longitudinal spin Seebeck effect . *J. Appl. Phys.* **115**, 17C731 (2014).;

[19] M. Schreier, G. E. W. Bauer, V.I. Vasyuchka, J. Flipse, K. Uchida, J. Lotze, V. Lauer, A. V Chumak, A.A. Serga, S. Daimon, T. Kikkawa, E. Saitoh, B. J. van Wees, B. Hillebrands, R. Gross, and S. T. B. Goennenwein, Sign of inverse spin Hall voltages generated by ferromagnetic resonance and temperature gradients in yttrium iron garnet platinum bilayers . *J. Phys. D: Appl. Phys.* **48**, 025001 (2015).;

[20] K. Uchida, H. Adachi, T. Ota, H. Nakayama, S. Maekawa and E. Saitoh, bservation of longitudinal spin-Seebeck effect in magnetic insulators. *Appl. Phys. Lett.* **97**, 172505 (2010).;

[21] G. Siegel, M. C. Prestgard, S. Teng and A. Tiwari, Robust longitudinal spin-Seebeck effect in Bi-YIG thin films. *Scientific Reports* **4**, 4429 (2014).;

[22] D. Meier, T. Kuschel, L. Shen, A. Gupta, T. Kikkawa, K. Uchida, E. Saitoh, J.-M. Schmalhorst, G. Reiss, Thermally driven spin and charge currents in thin NiFe2O4/Pt films. *Phys. Rev. B.* **87** 054421 (2013).;

[23] K. Uchida, T. Nonaka, T. Kikkawa, Y. Kajiwara, and E. Saitoh1, Longitudinal spin Seebeck effect in various garnet ferrites. *Phys. Rev. B* **87**, 104412 (2013).;

[24] K. Uchida, T. Nonaka, T. Ota and E. Saitoh, Longitudinal spin-Seebeck effect in sintered polycrystalline (Mn,Zn)Fe2O4 . *Appl. Phys. Lett.* **97**, 262504 (2010).;

[25] G.E.W. Bauer, A. H. MacDonald and S. Maekawa, 'Spin Caloritronics'. *Sol. Stat. Commun.* **150** 459 (2010).;

[26] S. R. Boona, Vlaminck, R. C. Myers and J. P. Heremans, Spin caloritronics. *Energy Environ. Sci.* **7**, 885 (2014).;

[27] A. Kirihara, K.-i. Uchida, Y. Kajiwara, M. Ishida, Y. Nakamura, T. Manako, E. Saitoh, and S. Yorozu, Spin-current-driven thermoelectric coating. *Nature Mater.* **11(8)**, 686-689 (2012).;

[28] A. B. Cahaya, O. A. Tretiakov, and G. E.W. Bauer, Spin Seebeck Power Conversion . *IEEE Trans. Magn.* **51**, 0800414 (2015).;

[29] A. V. Chumak, V. I. Vasyuchka, A. A. Serga and B. Hillebrands, Magnon spintronics. *Nat. Phys.* **11**, 453-461 (2015).;

[30] R. Bogue, 'Nanoscale fabrication: techniques, limitations and future prospects'*Assembly Automation* **31** Iss:4 304-308 (2011).;

[31] G. J. Snyder and E. S. Toberer, Complex thermoelectric materials. *Nature Mater.* **7**, 105-114 (2008).;

[32] M. S. Dresselahaus, G. Chen, M. Y. Tang, R. Yang, H. Lee, D. Wang, Z. Ren, J.-P. Fleurial and P. Gogna, New Directions for Low-Dimensional Thermoelectric Materials. *Adv. Mater.* **19**, 1043 (2007).;

[33] P. Pichanusakorn and P. Bandaru, Nanostructured Thermoelectrics. *Mater. Sci. Eng.: R* **67**, Iss:2-4, 19-63 (2010).;

[34] I. Chowdhury, R. Prasher, K. Lofgreen. G. Chrysler, S. Narasimhan, R. Mahajan, D. Koester. R. Alley and R. Venkatasubramanian, On-Chip cooling by Superlattice-based Thin-Film Thermoelectrics. *Nature Nanotech.* **4**, 1, 235 (2009);

[35] T. M. Tritt and M. A. Subramanian, Thermoelectric Materials, Phenomena and Applications: A bird's eye view *MRS Bulletin* **31**, (3) 188 (2011).;

[36] J. E. Cornett and O. Rabin, Thermoelectric figure of merit calculations for semiconducting nanowires. *Appl. Phys. Lett.* **98**, 18, 182104 (2011).;

[37] D. Narducci, Do we really need high thermoelectric figures of merit?, A critical appraisal to the power conversion efficiency of thermoelectric materials. *Appl. Phys. Lett.* **99**, 102104 (2011).;

[38] K. Uchida, S. Takahashi, K. Harii, J. Ieda, W. Koshibae, A. Ando, S. Maekawa and E. Saitoh, Observation of the spin Seebeck effect. *Nature* **455**, 778-781 (2008).;

[39] S. Bosu, Y. Sakuraba, K. Uchida, K. Saito, T. Ota, E. Saitoh and K. Takanashi, Spin Seebeck effect in thin films of the Heusler compound Co2MnSi. *Phys. Rev. B.* **83**, 224401 (2011).;

[40] S. H. Wang, L. K. Zou, J. W. Cai, B. G. Shen, and J. R. Sun, Transverse thermoelectric effects in platinum strips on permalloy films. *Phys. Rev. B* **88**, 214304(2013).;

[41] S.Y. Huang, W. G. Wang, S. F. Lee, J. Kwo, and C. L. Chien, Intrinsic Spin-Dependent Thermal Transport. *Phys. Rev. Lett.* **107**, 216604 (2011).;

[42] R. Ramos, T. Kikkawa, K. Uchida, H. Adachi, I. Lucas, M. H. Aguirre, P. Algarabel, L. Morelln, S. Maekawa, E. Saitoh and M. R. Ibarra, Observation of the spin Seebeck effect in epitaxial Fe3O4 thin films. *Appl. Phys. Lett.* **102**, 072413 (2013).;

[43] M. Schmid, S. Srichandan, D. Meier, T. Kuschel, J.-M. Schmalhorst, M. Vogel, G. Reiss, C. Strunk, and C. H. Back, Transverse Spin Seebeck Effect versus Anomalous and Planar Nernst Effects in Permalloy Thin Films. *Phys. Rev. Lett.* **111**, 187201 (2013).;

[44] K. Uchida, T. Ota, K. Harii, K. Ando, H. Nakayama and E. Saitoh, Electric detection of the spin-Seebeck effect in ferromagnetic metals. *J. Appl. Phys.* **107**, 09A951 (2010).;

[45] C. M. Jaworski, J. Yang, S. Mack, D. D. Awschalom, J. P. Heremans and R. C. Myers, Observation of the spin-Seebeck effect in a ferromagnetic semiconductor. *Nature Mater.* **9**, 898-903 (2010).;

[46] K. Uchida, T. Ota, H. Adachi, J. Xiao, T. Nonaka, Y. Kajiwara, G. E. W. Bauer, S. Maekawa and E. Saitoh, Thermal spin pumping and magnon-phonon-mediated spin-Seebeck effect. *J. Appl. Phys.* **111**, 103003 (2012).;

[47] C. M. Jaworski, J. Yang, S. Mack, D. D. Awschalom, R. C. Myers and J. P. Heremans, Spin-Seebeck Effect: A Phonon Driven Spin Distribution. *Phys. Rev. Lett.* **106**, 186601 (2011).

[48] V. D. Ky, Planar Hall and Nernst Effect in Ferromagnetic Metals. *Phys. Stat. Sol.* **22**, 729 (1967).;

[49] W. Nernst, *ber die electromotorischen Krfte, welche durch den Magnetimus in von einem Warmstorme durchflossenen Metallplatten geweckt werden; von Walter Nernst . Ann. Phys.(Leipzig)* **267**, 760 (1887).;

[50] A. Slachter, F. L. Bakker, J-P. Adam and B. J. van Wees, Thermally driven spin injection from a ferromagnet into a non-magnetic metal. *Nature Phys.* **6**, 879-882 (2010).;

[51] J. Flipse, F. L. Bakker, A. Slachter, F. K. Dejene and B. J. van Wees, Direct observation of the spin-dependent Peltier effect. *Nature Nanotech.* **7**, 166-168 (2012).;

[52] J. Xiao, G. E. W. Bauer, K.-i. Uchida, E. Saitoh and S. Maekawa, Theory of magnon-driven spin Seebeck effect. *Phys. Rev. B* **81**, 214418 (2010).;

[53] M. Schreier, A. Kamra, M. Weiler, J. Xiao, G. E. W. Bauer, R. Gross and Sebastian T. B. Goennenwein, Magnon, phonon, and electron temperature profiles and the spin Seebeck effect in magnetic insulator/normal metal hybrid structures. *Phys. Rev. B* **88**, 094410 (2013).;

[54] S. Geprägs, A. Kehlberger, F. D. Coletta, Z. Qiu, E.-J. Guo, T. Schulz, C. Mix, S. Meyer, A. Kamra, M. Althammer, H. Huebl, G. Jakob, Y. Ohnuma, H. Adachi, J. Barker, S. Maekawa, G. E. W. Bauer, E. Saitoh, R. Gross, S. T. B. Goennenwein and M. Klüi, Origin of the spin Seebeck effect in compensated ferrimagnets. *Nature Commun.* **7**, 10452 (2016).;

[55] T. M. Tritt (edited by), 'Thermal Conductivity: Theory, properties and Applications'. Kluwer Academic / Plenum Publishers, (2004).;

[56] D. G. Cahill, Thermal conductivity measurement from 30 K to 750 K: the 3 omega method *Rev. Scint. Instr.* **61(2)**, 802-808 (1990).;

[57] H. Ftouni, C. Blanc, A. Sikora, J. Richard, M. Defoort, K. Lulla, E. Collin and O Bourgeois, Thermal conductivity measurement of suspended Si-N membranes from 10 K to 275 K using the 3ω-Vlklein method. *Jour. of Phy.: Conference Series* **395**, 012109 (2012).;

[58] F. Völklein and E. Kessler, A Method for the Measurement of Thermal Conductivity, Thermal Diffusivity, and Other Transport Coefficients of Thin Films. *Phys. Stat. Sol.* **81**, 585 (1984).;

[59] F. Völklein, H. Reith, and A. Meier, Measuring methods for the investigation of in-plane and cross-plane thermal conductivity of thin films. *Phys. Status Solidi A* **210** 1, 106-118 (2013).;

[60] D. G. Cahill, W. K. Ford, K. E. Goodson, G. D. Mahan, A. Majumdar, H. J. Maris, R. Merlin and S. R. Phillpot, Nanoscale thermal transport *J. Appl. Phys.* **93**, 793 (2003);

[61] D. G. Cahill, P. V. Braun, G. Chen, D. R. Clarke, S. Fan, K. E. Goodson, P. Keblinski,W. P. King, G. D. Mahan, A. Majumdar, H. J. Maris, S. R. Phillpot, E. Pop, and L. Shi, Nanoscale thermal transport. II. 20032012. *Appl. Phys. Rev.* **1**, 011305 (2014);

[62] Schmid Maximilian (2015) *Magnet-thermoelectric effects in NiFe thin films.* Dissertationsreihe der Fakultät für Physik der Universität Regensburg 46, Dissertation, Universität Regensburg.

[63] E. C. Stoner ,Collective electron ferromagnetism. *Proc. Roy. Soc. London A* **165**, 372 (1938).;

[64] N. W. Ashcroft and N. D. Mermin, *Solid State Physics*, Thomson Learning, Inc. (1976);

[65] J. Hubbard, Calculation of partition functions. *Phys. Rev. Lett.* **3**, 77 (1959).;

[66] J. Hubbard, Collective electron ferromagnetism. *Proc. Roy. Soc. London* **84**, 455 (1964).;

[67] A. Lichtenstein, Emergent Phenomena in Correlated Matter. *Lecture Notes of the Autumn School Correlated Electrons Jülich* **3**, (2013).;

[68] A. Preuss, *Magnetic properties of FeCo alloys at different temperatures*, dissertation, University of Zurich, (1912).;

[69] P. Weiss, The magnetic properties of the alloys of the ferromagnetic metals: iron-nickel, nickel-cobalt, cobalt-iron . *Trans. Faraday Soc.* **8**, 149-156 (1912).;

[70] W. C. Ellis, *Renselaer Polytech. Inst. Bull. Eng. Sci. Ser* **16**, 1-57 (1927).;

[71] G. W. Elmen, U.S. Patent 1 739 752, (1929).;

[72] R. Bozorth. *Ferromagnetizm*, Moscow (Translated from Russian) (1956).;

[73] G. K. White and R. J. Tainsh, Lorenz Number for High-Purity Copper. *Phys. Rev.* **119**, 1869 (1960).;

[74] H. L. B. Gould and D. H. Wenny, Supermendur: A new rectangular-loop magnetic material. *Electrical Engineering* **76**, 3 (1957).;

[75] K. Schwarz, P. Mohn, P. Blaha and J. Kübler, Electronic and magnetic structure of BCC Fe-Co alloys from band theory. *J. Phys. F: Met. Phys.* **14**, 2659-2671 (1984).;

[76] J. M. MacLaren, T. C. Schulthess, W. H. Butler, R. Sutton and M. McHenry, Electronic structure, exchange interactions, and Curie temperature of FeCo. *J. Appl. Phys.* **85**, 8 (1999).;

[77] S.E. Kulkova, D.V. Valujsky, J. S. Kim, G. Lee and Y.M. Koo, The electronic properties of FeCo, Ni3Mn and Ni 3Fe at the orderdisorder transition. *Physica B* **322**, 236-247 (2002).;

[78] D. I. Bardos, Mean Magnetic Moments in bcc FeCo Alloys. *J. Appl. Phys.* **40**, 1371 (1969).;

[79] L. Berger, Electronic Specific Heat and Saturation Magnetization of Cr-Fe and Fe-Co Alloys. *Phys. Rev.* **137**, 1A (1965).;

[80] M. E. McHenry, M. A. Willard and D. E. Laughlin , Amorphous and nanocrystalline materials for applications as soft magnets. *Prog. Mater. Sci.* **49:291**, 433 (1999).;

[81] T. Burkert, L. Nordström, O. Eriksson and O. Heinonen, Giant Magnetic Anisotropy in Tetragonal FeCo Alloys. *Phys. Rev. Lett.* **93**, 2 (2004).;

[82] T. Sourmail, Near equiatomic FeCo alloys: Constitution, mechanical and magnetic properties. *Prog. Mater. Sci.* **50**, 816 (2005).;

[83] R. S. Sundar and S. C. Deevi, Soft Magnetic FeCo Alloys. Alloy Development, Processing, and Properties. *Int. Mater. Rev.* **50**, 157 (2005).;

[84] E. Sasioglu, C. Friedrich and S. Blügel, Strong magnon softening in tetragonal FeCo compounds. *Phys. Rev. B* **87**, 020410(R) (2013).;

[85] M. Walter, J. Walowski, V. Zbarsky, M. Mnzenberg, M. Schäfers, D. Ebke, G. Reiss, A. Thomas, P. Peretzki, M. Seibt, J. S. Moodera, M. Czerner, M. Bachmann and C. Heiliger, Seebeck effect in magnetic tunnel junctions. *Nature Mater.* **10**, 1038 (2011).;

[86] D. Hunter, W. Osborn, K. Wang, N. Kazantseva, J. Hattrick-Simpers, R. Suchoski, R. Takahashi, M. L. Young, A. Mehta, L. A. Bendersky, S. E. Lofland, M. Wuttig and I. Takeuchi, Giant magnetostriction in annealed $Co_{1x}Fe_x$ thin-films. *Nat. Commun.* **2:518**, doi: 10:1038/ncomms1529 (2011).;

[87] R. C. Hall, Single Crystal Anisotropy and Magnetostriction Constants of Several Ferromagnetic Materials Including Alloys of NiFe, SiFe, AlFe, CoNi, and CoFe. *J. Appl. Phys.* **30**,816 (1959).;

[88] C. W. Chen, *Magnetism and metallurgy of soft magnetic materials.* North- Holland Publishing Company, Amsterdam, (1977).;

[89] R. H. Yu, S. Basu, Y. Zhang, and J. Q. Xiao, Magnetic domains and coercivity in FeCo soft magnetic alloys. *J. Appl. Phys.* **85**, 6034 (1999).;

[90] A. Daz-Ortiz, R. Drautz, M. Fhnle, H. Dosch, and J. M. Sanchez, Structure and magnetism in bcc-based iron-cobalt alloys. *Phys. Rev. B* **73**, 224208 (2006).;

[91] M. D. Cooke, L-C Wang, R. Watts, R. Zuberek, G. Heydon, W. M. Rainforth and G. A. Gehring, The effect of thermal treatment, composition and substrate on the texture and magnetic properties of FeCo thin films. *J. Phys. D: Appl. Phys.* **33**, 1450-1459 (2000).;

[92] S. Blizak, G. Bihlmayer and S. Blgel, Ab initio investigations of magnetic properties of FeCo monolayer alloy films on Rh(001). *Phys. Rev. B* **86**, 094436 (2012).;

[93] C. J. Gutierrez, J. J. Krebs, and G. A. Prinz, Epitaxial bcc FexCo1-x alloy films on ZnSe(001). *Appl. Phys. Lett.* **61**, 2476 (1992).;

[94] P. S. Galepov, Magnetoresistivity of single-crystal films of iron, cobalt, and nickel binary alloys. *Soviet Physics Journal* **17**, 9 (1974).;

[95] K. Shikada, M. Ohtake, F. Kirino, and M. Futamoto, Microstructure and magnetic properties of FeCo epitaxial thin films grown on MgO single-crystal substrates. *J. Appl. Phys.* **105**, 07C303 (2009).;

[96] D. Z. Bai, J.-G. Zhu, W. Yu and J. A. Bain, Micromagnetic simulation of effect of stress-induced anisotropy in soft magnetic thin films. *J. Appl. Phys.* **95**, 6864 (2004).;

[97] P. Pain, J. P. Eymery, M. Cahoreau, M. F. Denanot and J. F. Dinhut, Structural and magnetic properties of Fe-Co thin films elaborated by ion-beam sputtering. *J. mag. and mag. mater.* **133**, 493-496 (1994).;

[98] J. F. Dinhut and J. P. Eymery, Spin orientation in Fe and Fe-Co thin films. *J. mag. and mag. mater.* **93**, 252-256 (1991).;

[99] I. Ohnuma , H. Enokia, O. Ikeda , R. Kainuma , H. Ohtani , B. Sundman and K. Ishida, Spin orientation in Fe and Fe-Co thin films. *J. mag. and mag. mater.* **93**, 252-256 (1991).;

[100] R. S. Liu, S.-H. Yang, X. Jiang, X.-G. Zhang, C. Rettner, L. Gao, T. Topuria, P. M. Rice, W. Zhang, C. M. Canali, and Stuart S. P. Parkin, CoFe alloy as middle layer for strong spin dependent quantum well resonant tunneling in MgO double barrier magnetic tunnel junctions. *Phys. Rev. B* **87**, 204411 (2013).;

[101] J. Alonso, H. Khurshid, V. Sankar, Z. Nemati, M. H. Phan, E. Garayo, J. A. Garca and H. Srikanth, FeCo nanowires with enhanced heating powers and controllable dimensions for magnetic hyperthermia. *J. Appl. Phys.* **117**, 17D113 (2015).;

[102] R. Ruer and K. Kaneko, *Ferrum* **2**, 33 (1911).;

[103] H. Masumoto, *Sci. Rep.* Tohoku Imp. Univ. **15**, 449 (1926).;

[104] T.Kase. *ibid.* **16**, 491 (1927).;

[105] Z. Turgut, J. H. Scott, Q. Huang, S. A. Majetich, and M. E. McHenry., Magnetic properties and ordering of C-coated Fe_xCo_{1x} alloy nanocrystals. *Jour. Appl. Phys.* **83**, 6468-6470 (1998).;

[106] Y. Ustinovshikov and S. Tresheva., Character of transformations in Fe-Co system. *Mat. Sci. Eng. A* **A248**, 238-244 (1998).;

[107] A. S. Normanton, P. E. Bloomfield, F. R. Sale, and B. B. Argent., A calorimetric study of iron-cobalt alloys. *Metal. Sci.* **9**, 510-517 (1975).;

[108] R. W. Fountain and F. Libsch., Development of mechanical and magnetic hardness in a 10% v-co-fe alloy. *trans. AIME.* **197**, 349-356 (1953).;

[109] P. P. Freitas and L. Berger, Effect of atomic order on the electrical resistivity of CoxFe100x alloys. *Phys. Rev. B* **37**, 6079 (1988).;

[110] C. Ahn, K.-H. Shin, R. Loloee, J. Bass, and W. P. Pratt, Jr., Current-perpendicular-to-plane spin transport properties of CoFe alloys: Spin diffusion length and scattering asymmetry. *J. Appl. Phys.* **108**, 023908 (2010).;

[111] M. S. Seehra and P. Silinsky, Order-disorder and α-γ transitions in FeCo. *Phy. Rev. B* **13**, 12 (1976).;

[112] D.B. Downie and J.F. Martin, Heat capacity of FeCo in the range 5 to 3OO K. Analysis of entropy contributions. *Scripta Metallurgica* **16**, 139-143 (1982).;

[113] P. Drude, *Annalen der Physik* **1**, 566 and **3**, 369 (1900).;

[114] G. Wiedemann and R. Franz, Ueber die Wrme-Leitungsfhigkeit der Metalle. *Ann. Phys.* **89**, 497 (1853).;

[115] W. Thomson, On the dynamical theory of heat, part V Thermoelectric currents. *Philosophical Transactions of the Royal Society of Edinburgh* **21**, 123-171 (1854).;

[116] L. Onsager, Reciprocal relations in irreversible processes. I. *Phys. Rev.* **37**, 405-426 (1931).;

[117] G. S. Kumar, G. Prasad and R. O. Pohl, 'Experimental determinations of the Lorenz number' *Journal of Materials Science* **28**, 4261-4272 (1993);

[118] J. M. Ziman, Electrons and Phonons. Oxford University, London (1960).;

[119] P. B. Allen in *Quantum Theory of Real Materials* edited by J. R. Chelikowsky and S. G. Louie (Kluwer Academic Publishers, Boston, 1996), pp. 219250.;

[120] A. Nassour, V. Mauchamp, W. Yu, T. Cabioch, L. Piraux, V. Gauthier-Brunet, and S. Dubois, Key role of electron-phonon interactions in the electronic conductivity of Ti_3SiC_2: Experiment and ab initio calculations. *Phys. Rev. B* **93**, 085119 (2016).;

[121] N. F. Mott, The electrical conductivity of transition metals. *Proc. R. Soc. Lond. A* **153**, 699 (1936).;

[122] N. F. Mott, The resistance and thermoelectric properties of the transition metals. *Proc. R. Soc. Lond. A* **156**, 368 (1936).;

[123] N. F. Mott and K. W. H. Stevens, The band structure of the transition metals. *Philosophical magazine* **2:23**, 1364-1386 (1957).;

[124] I. Mannari, Electrical Resistance of Ferromagnetic Metals. *Prog. Theor. Phys.***22**-3, 335-343 (1959) ;

[125] M. V. Kamalakar, A. K. Raychaudhuri, X. Wei, J. Teng and P. D. Prewett, Temperature dependent electrical resistivity of a single strand of ferromagnetic single crystal nanowire, *Appl. Phys. Lett.* **95**, 013112 (2009).;

[126] H. S. Carslaw and J. C. Jaeger, Conduction of heat in Solids. Oxford university press, 36, (1959).;

[127] G. E. Childs, L. J. Ericks and R. L. Powell, Thermal conductivity of solids at room temperature and below - review and compilation of literature. *NBS Monograph* M131:1608 (1973).;

[128] E. H. Sondheimer, The mean free path of electrons in metals., *Adv. in Phys.*, **50**, 499(2001);

[129] S. Arajs, B. F. Oliver and G. R. Dunmyre, Thermal conductivity of high-purity iron at low temperatures. *Jour. Appl. Phys.* **36**, 2210 (1965).;

[130] W. R. G. Kemp, P. G. Klemens and G. K. White, Thermal and electrical conductivities of Iron, Nickel, Titanium, and Zirconium at low temperatures. *Australian Journal of Physics* **9**(2), 180-188 (1956).;

[131] W. R. G. Kemp, P. G. Klemens and R. J. Tainsh, Thermal and electrical conductivities of Rhodium and Iron. *Annalen der Physik* **460**, 35-41 (1959).;

[132] H. M. Rosenberg, The thermal conductivity of metals at low temperatures. *Phil. Trans. Roy. Soc. A* London **247**, 441 (1955).;

[133] S. Kasap, Thermoelectric effects in metals: thermocouples. *Thermoelectric Effects in Metals: Thermocouples (S. O. Kasap) An e-Booklet* (1997 - 2001).;

[134] M. Cutler and N. F. Mott, Observation of Anderson Localization in an Electron Gas. *Phys. Rev.* **181** 1336 (1969).;

[135] F. J. Blatt, D. J. Flood, V. Rowe, P. A. Schroeder and J. E. Cox, Magnon-Drag Thermopower in Iron. *Phys. Rev. Lett.* **18**, 395 (1967).;

[136] G. N. Grannemann and L. Berger, Magnon-drag Peltier effect in a Ni-Cu alloy. *Phys. Rev.B* **13**, 2072 (1976).;

[137] M. V. Costache, G. Bridoux, I. Neumann and S. O. Valenzuela, Magnon-drag thermopile. *Nature Materials* **11**, 199-202 (2012).;

[138] S. J. Watzman, R. A. Duine, Y. Tserkovnyak, H. Jin, A. Prakash, Y. Zheng, J. P. Heremans, Magnon-drag thermopower and Nernst coefficient in Fe, Co and Ni. *Phys. Rev. B* **94**, 144407 (2016).;

[139] C. Kittel. *Quantum Theory of Solids* (Wiley, New York)(1963).;

[140] D. Y. Chung,T. Hogan, J. Schindler, L. Iordarridis, P. Brazis, C. R. Kannewurf, Baoxing Chen, C. Uher and M. G. Kanatzidis, Complex bismuth chalcogenides as thermoelectrics. 16th International conference of thermoelectrics, *Proceedings ICT '97. XVI International Conference, Dresden* (1997).;

[141] S. N. Girard, T. C. Chasapis, J. He, X. Zhou, E. Hatzikraniotis, C. Uher, K. M. Paraskevopoulos, V. P. Dravidc and M. G. Kanatzidis, PbTePbSnS2 thermoelectric composites: low lattice thermal conductivity from large microstructures. *sci.* **5**, 8716-8725 (2012).;

[142] J. P. Heremans, V. Jovovic, E. S. Toberer, A. Saramat, K. Kurosaki, A. Charoenphakdee, S. Yamanaka and G. J. Snyder, Enhancement of Thermoelectric Efficiency in PbTe by Distortion of the Electronic Density of States. *Science* **321**, 5888 (2008).;

[143] A. D. LaLonde, Y. Pei, H. Wang and G. Jeffrey Snyder ,Lead telluride alloy thermoelectrics. *materiasltoday* **14**, 11 (2011).;

[144] M. I. Fedorov, Y. Pei, H. Wang and G. Jeffrey Snyder ,Thermoelectric silicides: past, present and future. *Jour. of Thermoelectricity* **2**, 51 (2009).;

[145] B. C. Sales, C. Uher , In *Recent Trends in Thermoelectric Materials Research II, Semiconductors and Semimetals*. T. M. Tritt, Ed; Academic Press: San Diego, **69**, 1-36, 139-253 (2000).;

[146] E. Hall, On a new action of the magnet on electric currents. *American jour. of Math.* **2**(3), 287-292 (1879).;

[147] K. Ando, S. Takahashi, K. Harii, K. Sasage, J. Ieda, S. Maekawa and E. Saitoh, Electric Manipulation of Spin Relaxation Using the Spin Hall Effect. *Phys. Rev. Lett.* **101**, 36601 (2008).;

[148] M. I. Dyakonov and V. I. Perel, Possibility of Orienting Electron Spins with Current. *Sov. Phys. JETP Lett.* **13**, 467 (1971).;

[149] M.I. Dyakonov and V.I. Perel , Current-induced spin orientation of electrons in semiconductors. *Phys. Lett. A* **35** (6), 459 (1971).;

[150] S. O. Valenzuela and M. Tinkham, Direct electronic measurement of the spin Hall effect. *Nature* **442**, 176-179 (2006).;

[151] J. E. Hirsch, Spin Hall Effect. *Phys. Rev. Lett.* **83**, 1834 (1999).;

[152] V. Vlaminck, J. E. Pearson, S. D. Bader, and A. Hoffmann, Dependence of spin-pumping spin Hall effect measurements on layer thicknesses and stacking order. *Phys. Rev. B* **88**, 064414 (2013).;

[153] J. Sinova, S. O. Valenzuela, J. Wunderlich, C.H. Back, and T. Jungwirth, Spin Hall effects. *Rev. Mod. Phys.* **87**, 1213 (2015).;

[154] L. Berger, Side-jump mechanism for the hall effect of ferromagnets. *Phys. Rev. B* **2**, 4559-4566 (1970).;

[155] E. Saitoh, M. Ueda, H. Miyajima and G. Tatara, Conversion of spin current into charge current at room temperature: Inverse spin-Hall effect. *Appl. Phys. Lett.* **88**, 182509 (2006).;

[156] E. H. Sondheimer and A. H. Wilson , The Theory of the Magneto-Resistance Effects in Metals . *Proc. Roy. Sco. London. Series A, Math. and Phys. Sciences* **190**, 1023, 435-455 (1947).;

[157] M.Kohler, The Theory of the Magneto-Resistance Effects in Metals . *Ann. Phys., Lpz.* (6) **6**, 18 (1949).;

[158] T. R. Mcguire and R. I. Potter , Anisotropic Magnetoresistance in Ferromagnetic 3d Alloys . *IEEE Trans. on Magn.* **Mag-11**, 4 (1975).;

[159] R. H. Silsbee, A. Janossy and P. Monod, Coupling between ferromagnetic and conduction-spin-resonance modes at a ferromagneticnormal-metal interface. *Phys. Rev. B* **19**, 4382 (1979).;

[160] T. Kimura, Y. Otani, T. Sato, S. Takahashi and S. Maekawa, Room-Temperature Reversible Spin Hall Effect. *Phys. Rev. Lett.* **98**, 156601 (2007).;

[161] N. Nagaosa, J. Sinova, S. Onoda, A. H. MacDonald, and N. P. Ong, Anomalous Hall effect . *Rev. Mod. Phys.* **82**, 1539 (2010).;

[162] A. D. Avery, M. R. Pufall and B. L. Zink, Observation of the Planar Nernst Effect in Permalloy and Nickel Thin Films with In-Plane Thermal Gradients. *Phys. Rev. Lett.* **109**, 196602 (2012).;

[163] W. Zhang, W. Han, X. Jiang, S.-Hun Yang and S. S. P. Parkin, Role of transparency of platinumferromagnet interfaces in determining the intrinsic magnitude of the spin Hall effect. *Nature Phys.* **11**, 496 (2015).;

[164] M. Obstbaum, M. Härtinger, H. G. Bauer, T. Meier, F. Swientek, C. H. Back, and G. Woltersdorf, Inverse spin Hall effect in Ni81Fe19/normal-metal bilayers. *Phys. Rev. B* **89**, 060407(R) (2014).;

[165] D. Wei, M. Obstbaum, M. Ribow, C. H. Back and G. Woltersdorf, Spin Hall voltages from a.c. and d.c. spin currents. *Nat. Commun.* **5**, 3768 (2014).;

[166] Y. Tserkovnyak and A. Brataas, Enhanced Gilbert Damping in Thin Ferromagnetic Films. *Phys. Rev. Lett.* **88**, 11 (2002).;

[167] M. Isasa, E. Villamor, L. E. Hueso, M. Gradhand, and F. Casanova, Temperature dependence of spin diffusion length and spin Hall angle in Au and Pt. *Phys. Rev. B* **91**, 024402 (2015).;

[168] G. Mihajlovi, J. E. Pearson, M. A. Garcia, S. D. Bader, and A. Hoffmann, Negative Nonlocal Resistance in Mesoscopic Gold Hall Bars: Absence of the Giant Spin Hall Effect. *Phys. Rev. Lett.* **103**, 166601 (2009).;

[169] Takeshi Seki, Yu Hasegawa, Seiji Mitani, Saburo Takahashi, Hiroshi Imamura, Sadamichi Maekawa, Junsaku Nitta and Koki Takanashi, Giant spin Hall effect in perpendicularly spin-polarized FePt/Au devices. *Nat. Mater.* **7**, 125-128 (2008).;

[170] A. S. Shestakov, M. Schmid, D. Meier, T. Kuschel and C. H. Back, Dependence of transverse magnetothermoelectric effects on inhomogeneous magnetic fields. *Phy. Rev. B* **92**, 224425 (2015).;

[171] A. Azevedo, L. H. Vilela-Leo, R. L. Rodrguez-Surez, A. F. Lacerda Santos and S. M. Rezende, Spin pumping and anisotropic magnetoresistance voltages in magnetic bilayers: Theory and experiment. *Phys. Rev. B* **83**, 144402 (2011).;

[172] J.-C. Rojas-Snchez, N. Reyren, P. Laczkowski, W. Savero, J.-P. Attan, C. Deranlot, M. Jamet, J.-M. George, L. Vila, and H. Jaffrs, Spin Pumping and Inverse Spin Hall Effect in Platinum: The Essential Role of Spin-Memory Loss at Metallic Interfaces. *Phys. Rev. Lett.* **112**, 106602 (2014).;

[173] O. Mosendz, V. Vlaminck, J. E. Pearson, F. Y. Fradin, G. E. W. Bauer, S. D. Bader, and A. Hoffmann, Detection and quantification of inverse spin Hall effect form spin pumping in permalloy/normal metal bilayers. *Phys. Rev. B* **82**, 214403 (2010).;

[174] H. Kurt, R. Loloee, K. Eid, W. P. Pratt Jr. and J. Bass, Spin-memory loss at 4.2 K in sputtered Pd and Pt and at Pd/Cu and Pt/Cu interfaces. *Appl. Phys. Lett.* **81**, 4787 (2002).;

[175] L. Liu, R. A. Buhrman and D. C. Ralph, Review and Analysis of Measurements of the Spin Hall Effect in Platinum. *arXiv* 1111.3702 (2012).;

[176] W. Zhang, V. Vlaminck, J. E. Pearson, R. Divan, S. D. Bader and A. Hoffmann, Determination of the Pt spin diffusion length by spin-pumping and spin. *Appl. Phys. Lett.* **103**, 242414 (2013).;

[177] W. L. Lim1, N. Ebrahim-Zadeh1, J. C. Owens, H. G. E. Hentschel and S. Urazhdin, Temperature-dependent proximity magnetism in Pt. *Appl. Phys. Lett.* **102**, 162404 (2013).;

[178] S. Geprägs, S. Meyer, S. Altmannshofer, M. Opel, F. Wilhelm, A. Rogalev, R. Gross, and S. T. B. Goennenwein., Investigation of induced Pt magnetic polarization in Pt/Y3Fe5O12 bilayers. *Appl. Phys. Lett.* **101**, 262407 (2012).;

[179] S. Geprägs, S. T. B. Goennenwein, M. Schneider, F. Wilhelm, K. Ollefs, A. Rogalev, M. Opel, and R. Gross., Pt magnetic polarization on Y3Fe5O12 and magnetotransport characteristics. *ArXiv e-prints*, 1307.4869 (2013).;

[180] T. Kikkawa,K. Uchida,Y. Shiomi,Z. Qiu,D. Hou, D. Tian, H. Nakayama, X.-F. Jin, and E. Saitoh, Longitudinal Spin Seebeck Effect Free from the Proximity Nernst Effect. *Phys. Rev. Lett.* **110**, 067207(2013).;

[181] Y. M. Lu, Y. Choi, C. M. Ortega, X. M. Cheng, J. W. Cai, S. Y. Huang, L. Sun, and C. L. Chien, Pt Magnetic Polarization on Y3Fe5O12 and Magnetotransport Characteristics. *Phy. Rev. Lett.* **110**, 147207 (2013).;

[182] B. D. Pant and U. S. Tandon, Etching of Silicon Nitride in CCl_2F_2, CHF_3, SiF_4, and SF_6 Reactive Plasma: A Comparative Study. *Plasma Chemistry and Plasma Processing* **19**, 4 (1999).;

[183] T. C. Mele, J. Nulman, and J. P. Krusius, Selective and anisotropic reactive ion etch of LPCVD silicon nitride with CHF3 based gases . *Journal of Vacuum Science & Technology B* **2**, 684 (1984).;

[184] S. F. Cheng, P. Lubitz, Y. Zheng, and A. S. Edelstein, Effects of spacer layer on growth, stress and magnetic properties of sputtered permalloy film. *J. Magn. Magn. Mat.* **282**, 109 (2004).;

[185] M. Dumm, M. Zölfl, R. Moosbühler, M. Brockmann, T. Schmidt, and G. Bayreuther, Magnetism of ultrathin FeCo(001) films on GaAs(001). *J. Appl. Phys.* **87**, 9 (2000).;

[186] P. Kim, L. Shi, A. Majumdar and P. L. McEuen, Thermal Transport Measurements of Individual Multiwalled Nanotubes. *Phys. Rev. Lett.* **87**, 21 (2001).;

[187] R. Sultan, A. D. Avery., G. Stiehl and B. L. Zink, Thermal conductivity of micromachined low-stress silicon-nitride beams from 77 to 325 K. *J. Appl. Phys.* **105**, 043501 (2009);

[188] B. L. Zink, A. D. Avery., R. Sultan, D. Bassett and M. R. Pufall, Exploring thermoelectric effects and wiedemann-franz violation in magnetic nanostructures via micromachined thermal platforms. *Sol. Stat. Commun.* **150**, Iss: 11-12, 514-518 (2010);

[189] L. Shi, D. Li, C. Yu, W. Jang, D. Kim, Z. Yaoh, P. Kim, and A. Majumdar, Measureming Thermal and Thermoelectric Properties of One-Dimensional Nanostructures Using a Microfabricated Device. *J. Heat. Tranfer* **125**, 881 (2003).;

[190] S. L. Lai, J. Y. Guo, V. Petrova, G. Ramanath, and L. H. Allen, Size-Dependent Melting Properties of Small Tin Particles: Nanocalorimetric Measurements. *Phys. Rev. Lett.* **77**, 99 (1996).;

[191] P.M. Sarro, A.W. van Herwaarden and W. van der Vlist, A silicon-silicon nitride membrane fabrication process for smart thermal sensors. *Sensors and Actuators A* **41-42**, 666-671 (1994).;

[192] http://www.xensor.nl/. ;

[193] J. M. Gildemeister, Adrian T. Lee, and P. L. Richards, A fully lithographed voltage-biased superconducting spiderweb bolometer. *Appl. Phys. Lett.* **74**, 6, 868-870 (1999).;

[194] M. Kenyon, P.K. Day, C.M. Bradford, J.J. Bock and H.G. Leduc, Electrical properties of backgroundlimited membraneisolation transitionedge sensing bolometers for farIR/submillimeter directdetection spectroscopyr. *Jour. Low Temp. Phys.* **151**, Iss:1, 112-118 (2008).;

[195] K. D. Irwin and G. C. Hilton, Transition-Edge Sensors. *Cryogenic Particle Detection (Topics Appl. Phys.)* **99**,C. Enss eds., (Springer-Verlag, Berlin), 63, (2005).;

[196] B. L. Zink, B. Revaz, J. J. Cherry, and F. Hellman, Measurement of thermal conductivity of thin films with a Si-N membrane-based microcalorimeter. *Rev. Sci. Instr.* **76**, 024901 (2005).;

[197] R. Sultan, A. D. Avery, J. M. Underwood, S. J. Mason, D. Bassett and B. L. Zink, Heat transport by long mean free path vibrations in amorphous silicon nitride near room temperature. *Phys. Rev. B* **87**, 214305 (2013).;

[198] A. D. Avery, R. Sultan, D. Bassett, D. Wei and B. L. Zink, Thermopower and resistivity in ferromagnetic thin films near room temperature. *Phys. Rev. B* **83**, 10 (2011).;

[199] B. L. Zink, R. Pietri and F. Hellman, Thermal Conductivity and Specific Heat of Thin-Film Amorphous Silicon. *Phys. Rev. Lett.* **96**, 055902 (2006).;

[200] A. Avery, Thermal and Electrical Transport in Ferromagnetic Metal Thin Films. *Electronic Theses and Dissertations* Page 38. (2013).;

[201] A. D. Avery, S. J. Mason, D. Bassett, D. Wesenberg, and B. L. Zink, Thermal and electrical conductivity of approximately 100-nm permalloy, Ni, Co, Al, and Cu films and examination of the Wiedemann-Franz Law. *Phys. Rev. B* **92**, Phys. Rev. B (2015).;

[202] B. L. Zink and F. Hellman, Specific heat and thermal conductivity of low-stress amorphous SiN membranes. *Sol. State Commun.* **129**, 199-204 (2003).;

[203] B. Revaz, B.L. Zink and F. Hellman, Si-N membrane-based microcalorimetry: Heat capacity and thermal conductivity of thin films. *Thermochimica Acta* **432**, 158-168 (2005).;

[204] S.-M. Lee and D. G. Cahill, Heat transport in thin dielectric films. *J. Appl. Phys.* **81**, 2590 (1997).;

[205] A. Sikora, H. Ftouni, J. Richard, C. Hbert, D. Eon, F. Omns and O. Bourgeois, Highly sensitive thermal conductivity measurements of suspended membranes (SiN and diamond) using a 3-Völklein method . *Rev. Sci. Instrum.* **83**, 054902 (2012).;

[206] W. Holmes, J. M. Gildemeister, P. L. Richards and V. Kotsubo, Measurements of thermal transport in low stress silicon nitride films *Appl. Phys. Lett.* **72**, 2250 (1998).;

[207] H. Ftouni, C. Blanc, D. Tainoff, A. D. Fefferman, M. Defoort, K. J. Lulla, J. Richard, E. Collin and O. Bourgeois, Thermal conductivity of silicon nitride membranes is not sensitive to stress. *Phys. Rev. B* **92**, 125439 (2015).;

[208] H. Ebert, D. Kdderitzsch and J, Minr, Calculating condensed matter properties using the KKR-Greens function methodrecent developments and applications. *Rep. Prog. Phys.* **74**, 096501 (2011).;

[209] J. S. Faulkner and G. M. Stocks, Calculating properties with the coherent-potential approximation. *Phys. Rev. B* **21**,3222 (1980).;

[210] H. Ebert, A. Vernes and J. Banhart, Relativistic bandstructure of disordered magnetic alloys. *Sol. State. Commun.* **104**, 4(1997).;

[211] G. M. Stocks and W. H. Butler, Mass and Lifetime Enhancement due to Disorder on Ag_cPd_{1c} Alloys. *Phys. Rev. Lett.* **48**, 55(1982).;

[212] W. H. Butler, Theory of electronic transport in random alloys: Korringa-Kohn-Rostoker coherent-potential approximation. *Phys. Rev. B* **31**,3260(1985).;

[213] P. R. Tulip, J. B. Staunton, S. Lowitzer, D. Kdderitzsch, and H. Ebert, Theory of electronic transport in random alloys with short-range order: Korringa-Kohn-Rostoker nonlocal coherent potential approximation. *Phys. Rev. B* **77**, 165116 (2008).;

[214] A. M. Gué anault, Low-temperature thermoelectric power of palladium-silver alloys. *Philos. Mag.* **30**, 641-649 (1974).;

[215] H. Ebert, S. Mankovsky, K. Chadova, S. Polesya, J. Minr, and D. Kdderitzsch, Calculating linear-response functions for finite temperatures on the basis of the alloy analogy model. *Phys. Rev. B* **91**, 165132 (2015).;

[216] L. Smrcka and P. Streda, Transport coefficients in strong magnetic fields. *J. Phys. C: Solid State Phys.* **10**, 12 (1977).;

[217] M. Jonson and G. D. Mahan, Mott's formula for the thermopower and the Wiedemann-Franz law. *Phys. Rev. B* **21**, 4223 (1980).;

[218] S. Wimmer, D. Kdderitzsch, K. Chadova, and H. Ebert, First-principles linear response description of the spin Nernst effect. *Phys. Rev. B* **88**, 201108(R) (2013).;

[219] S. Wimmer, D. Kdderitzsch and H. Ebert, Galvanomagnetic and thermogalvanomagnetic transport effects in ferromagnetic fcc Co_xPd_{1x} alloys from first principles. *Phys. Rev. B* **89**, 161101(R) (2014).;

[220] M. Rubinstein, F. J. Rachford, W. W. Fuller, and G. A. Prinz, Electrical transport properties of thin epitaxially grown iron films. *Phys. Rev. B* **37**, 15 (1988).;

[221] J. W. C. De Vries, Temperature and Thickness Dependence of the Resistivity of Thin Polycrystalline Aluminium, Cobalt, Nickel, Palladium, Silver and Gold Films. *Thin Solid Films* **167**, 25-32 (1988).;

[222] G. R. Taylor, A. Isin, and R. V. Coleman, Resistivity of Iron as a Function of Temperature and Magnetization. *Phys. Rev.* **165**, 2, (1968).;

[223] S. Arajs, F. C. Schwerer and R. M. Fisher, Residual Resistivities of Binary Iron Alloys. *Phys. Stat. Sol.* **33**, 731 (1969).;

[224] A. F. Mayadas and M. Shatzkes, Electrical-resistivity model for polycrystalline films: the case of arbitrary reflection at external surfaces. *Phys. Rev. B* **1**, 1382 (1970).;

[225] D. Kojda, R. Mitdank, M. Handwerg, A. Mogilatenko, M. Albrecht, Z. Wang, J. Ruhhammer, M. Kroener, P. Woias, and S. F. Fischer, Temperature-dependent thermoelectric properties of individual silver nanowires. *Phys. Rev. B* **91**, 024302 (2015).;

[226] B. Raquet, M. Viret, E. Sondergard, O. Cespedes, and R. Mamy, Electronmagnon scattering and magnetic resistivity in 3d ferromagnets. *Phys. Rev. B* **66**, 024433 (2002).;

[227] V. J. Minkiewicz, G. Shirane and R. Nathans, Phonon dispersion relation for iron. *Phys. Rev.* **162**, 3 (1967).;

[228] G. P. P. Pun and Y. Mishin, Embeded-atom potential for hcp and fcc cobalt. *Phys. Rev. B* **86**, 134116 (2012).;

[229] D. M. Bylander, Q. Niu L. Kleinman, Fe magnon dispersion curve calculated with frozen spin-wave method. *Phys. Rev. B* **61**, 18 (2000).;

[230] G. Shirane, V. J. Minkiewicz and R. Nathans, Spin waves in 3d metals. *Jour. Appl. Phys.* **39**, 380-390 (1968).;

[231] H. J. Qin, Kh. Zakeri, A. Ernst, T.-H. Chuang, Y. -J. Chen, Y. Meng and J. Kirschner, Magnons in ultrathin ferromagnetic films with a large perpendicular magnetic anisotropy. *Phys. Rev. B* **88**, 020404(R) (2013).;

[232] S. Schönecker, X. Li, B. Johansson and L. Vitos, Atomic long-range order effects on Curie temperature and adiabatic spin-wave dynamics in strained fe-Co alloy films. *Phys. Rev. B* **94**, 064410 (2016).;

[233] X. Liu, M. M. Steiner, R. Sooryakumar, G. A. Prinz, R. F. C. Farrow and G. Harp, Exchange stiffness, magnetization, and spin waves in cubic and hexagonal phases of cobalt. *Phys. Rev. B* **53**, 18 (1996).;

[234] X. Liu, R. Sooryakumar, C. J. Gutierrez and G. A. Prinz, Exchange stiffness and magnetic anisotropies in bcc Fe1-x Cox alloys. *Jour. Appl.Phys.* **75**, 7021 (1994).;

[235] M. Sperl, W. Kipferl, M. Dumm and G. Bayreuther, Spin-wave excitations in epitaxial ultrathin FeCo with zero magnetocrystalline anisotropy. *Jour. Appl. Phys.* **99**, 08J703 (2006).;

[236] Y. Hanlumyuang, P. R. Ohodnicki, D. E. Laughlin and M. E. McHenry, Bragg-Williams model of Fe-Co order-disorder phase transformations in a strong magnetic field. *Jour. Appl. Phys.* **99**, 08F101 (2006).;

[237] M. Pajda, J. Kudrnovsky, I. Turek, V. Drchal and P. Bruno, Ab initio calculations of exchange interactions, spin-wave stiffness constants, and Curie temperatures of Fe, Co, and Ni. *Phys. Rev. B* **64**, 174402 (2001).;

[238] P. G. Klemens, Deviation from Matthiessen's Rule and Lattice Thermal Conductivity of Alloys. *Aus. Jour. Phys.* **12**, 199 (1956).;

[239] P. G. Klemens, The Electrical and Thermal Conductivities of Monovalent Metals. *Aus. Jour. Phys.* **7**(1), 70-76 (1954).;

[240] Y. Hsu and L. Berger, Magnon heat conduction and magnon lifetimes in the metallic ferromagnet $Fe_{68}Co_{32}$ at low temperatures. *Phys. rev. B* **14**, 9 (1976).;

[241] C. Y. Ho, M. W. Ackerman, K. Y. Wu, S. G. Oh and T. N. Havill, Thermal conductivity of ten selected binary alloy systems. *J. Phys. Chem. Ref. Data* **7**, 3 (1978).;

[242] C. Y. Ho, M. W. Ackerman, K. Y. Wu, T. N. Havill, R. H. Bogaard, R. A. Matula, S. G. Oh and H. M. James, Electrical resistivity of ten selected binary alloy systems. *J. Phys. Chem. Ref. Data* **12**, 2 (1983).;

[243] D. Daniel, J. F. Gregg, S. M. Thompson, J. M. D. Coey, A. Fagan, K. Ounadjela, C. Fermon and G. Saux, Thermal conductivity of a giant magnetoresistive mechanical alloy. *J. Mag. and Magnetic Mater.* **140-144**, 493-494 (1995).;

[244] H.-D. Wang, J.-H. Liu, X. Zhang, Z.-Y. Guo, K. Takahashi, Experimental study on the influences of grain boundary scattering on the charge and heat transport in gold and platinum nanofilms. *Heat Mass Transfer* **47**, Heat Mass Transfer(2011).;

[245] Q. G. Zhang, B. Y. Cao, X. Zhang, M. Fujii and K. Takahashi, Influence of grain boundary scattering on the electrical and thermal conductivities of polycrystalline gold nanofilms. *Phys. Rev. B* **74**, 134109 (2006).;

[246] Z. Cheng, L. Liu, S. Xu, M. Lu and X. Wang, Temperature Dependence of Electrical and Thermal Conduction in Single Silver Nanowire. *Scientific Reports* **5**, 10718 (2015).;

[247] M. N. Ou, T. J. Yang, S. R. Harutyunyan, Y. Y. Chen, C. D. Chen, and S. J. Lai, Electrical and thermal transport in single nickel nanowire. *Appl. Phys. Lett.* **92**, 063101 (2008).;

[248] X. Zheng, D. Cahill, P. Krasnochtchekov, R.Averback, and J.-C. Zhao, High-throughput thermal conductivity measurements of nickel solid solutions and the applicability of the WiedemannFranz law. *Acta Mater.* **55**, 5177 (2007).;

[249] P. Nath and K. Chopra, Thermal conductivity of copper films. *Thin Solid Films* **20**, 53 (1974).;

[250] K. Hirata, Y. Waseda, A. Jain and R. Srivastava, Resistivity of liquid transition metals and their alloys using the t matrix. *J. Phys. F: Metal Phys.* **7**, 3 (1977).;

[251] A. M. Gué nault and D. K. C. Macdonald, A note on thermoelectric power and inelastic scattering. *Philosophical Magazine* **6:70**, 1201-1206 (1961).;

[252] F. Ghahari, H.-Y. Xie, T. Taniguchi, K. Watanabe, M. S. Foster, and P. Kim, Enhanced Thermoelectric Power in Graphene: Violation of the Mott Relation by Inelastic Scattering. *Phys. Rev. Lett.* **116**, 136802 (2016).;

[253] K. Durczewski and M. Ausloos, Inelastic-phonon-scattering effect on the behavior of the thermoelectric power of metals. *Phys. Rev. B* **49**, 18 (1994).;